SYNTHETIC, SPECTROSCOPIC AND STRUCTURAL STUDIES OF CHALCOGEN PERI-SUBSTITUTED HETEROCYCLES: A SOLID-STATE NMR PERSPECTIVE

Paula Sanz Camacho

A Thesis Submitted for the Degree of PhD
at the
University of St Andrews

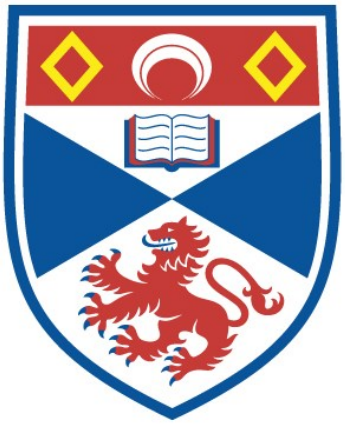

2016

Synthetic, Spectroscopic and Structural Studies of Chalcogen *Peri*-Substituted Heterocycles: A Solid-State NMR Perspective

Paula Sanz Camacho

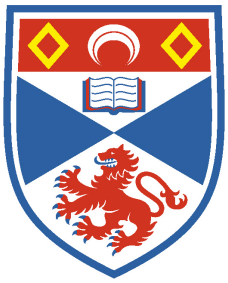

University of
St Andrews

This thesis is submitted in partial fulfilment for the degree of

Doctor of Philosophy (PhD)

at the
University of St Andrews

27th of June 2016

Declarations

I, Paula Sanz Camacho, hereby certify that this thesis, which is approximately 65000 words in length, has been written by me, and that it is the record of work carried out by me, or principally by myself in collaboration with others as acknowledged, and that it has not been submitted in any previous application for a higher degree.

I was admitted as a research student in September 2012 and as a candidate for the degree of Philosophy in August 2013; the higher study for which this is a record was carried out in the University of St Andrews between 2012 and 2016.

Date Signature of candidate

I hereby certify that the candidate has fulfilled the conditions of the Resolution and Regulations appropriate for the degree of Doctor in Philosophy in the University of St Andrews and that the candidate is qualified to submit this thesis in application for that degree.

Date signature of supervisor

Date signature of supervisor

In submitting this thesis to the University of St Andrews I understand that I am giving permission for it to be made available for use in accordance with the regulations of the University Library for the time being in force, subject to any copyright vested in the work not being affected thereby. I also understand that the title and the abstract will be published, and that a copy of the work may be made and supplied to any bona fide library or research worker, that my thesis will be electronically accessible for personal or research use unless exempt by award of an embargo as requested below, and that the library has the right to migrate my thesis into new electronic forms as required to ensure continued access to the thesis. I have obtained any third-party copyright permissions that may be required in order to allow such access and migration, or have requested the appropriate embargo below.

The following is an agreed request by candidate and supervisor regarding the publication of this thesis:
No embargo on print copy, but embargo on all or part of electronic copy for a period of one year on the following ground:

- Publication would preclude future publication

Date Signature of candidate

Date signature of supervisor

Date signature of supervisor

Acknowledgements

Firstly, and most importantly, I wish to thanks the persons that brought me to St Andrews in first place and welcome me in their respectively groups, my two supervisors, Prof J. Derek Woollins and Prof Sharon E. Ashbrook. They introduced me to the exciting word of selenium and J couplings, providing me with their knowledge, guidance and support through these three and a half years. I am also grateful for their encouragement and enthusiasm towards this research and for the opportunity they gave me to develop my skills in multiple discussion and conference that I truly enjoyed.

I will also like to thanks the past and present Woollins and Ashbrook group members but also Slawin and Kilian group, for making the days enjoyable in the lab and offices and for the help they have given me over the years. Special mention goes in Ashbrook group, to Valery Seymour, and to Daniel Dawson for his excellent experimental advice and his guidance over the years and for being a great office mate over the last months of my PhD. Daniel is also thanked for proof reading part of this manuscript as well as Scott Sneddon and Dave McKay. In Woollins, Slawin and Kilian group I would like to thanks Andreas Nordheider, Brian Chalmer, Kasun A. Arachchige and Fergus Knight for their patience and help specially at the beginning of my PhD, and more lately to Phillip Nejman for the help in the lab, proof reading part of this thesis, and especially for his constant supply of funny moments. Brian Chalmer and Phillip Nejman are also thanked for doing the NMR fill every time I forget to do it (that it was quite often!). Special thanks go also to Martin Stanford for his enthusiasm and dedication in his undergraduate project and to Christin Kirst for her dedication in her master thesis.

I owe thanks to the National Mass Spectrometry Facility in Swansea, Mr Stephen Boyer in London Metropolitan University for elemental analysis, Dr Tomáš Lébl and Mrs Melanja Smith for the NMR services provided. I will also like to thanks the UK 850 MHz solid-state NMR Facility used in this research was funded by EPSRC and BBSRC, as well as the University of Warwick including via part funding through Birmingham Science City Advanced Materials Projects 1 and 2 supported by Advantage West Midlands (AWM) and the European Regional Development Fund (ERDF). I am also indebted to the crystallographers, Kasun Athukorala, David Cordes and Alexandra Slawin that provided me with great and abundant crystal structures, but especially for their patient, help and dedication in the search for missing polymorphs and in contributing discussion about it. Moreover, Alexandra Slawin is also thanked for her guidance and for her support in low moments.

Many people also helped me not only in a scientific way but also in a personal way through this intense but exciting experience. From St Andrews, I would like to thanks my Spanish community, specially Diego, Richard, Alba, Juanma and Rosa and Silvia and Danila the Italian annex, for their help in the many high and low points and for lots of great moments. In Dundee I also met great people that I wish to thank like Miriam, Tamara, Jorge, Abraham, Salva, Carlos, Marilo, Michael and also my waterpolo team (menzieshill), that makes living in Dundee enjoyable. My friends and family are also thanks for their support, specially my parents, Magdalena Camacho and Julio Sanz, for their constant belief and encouragement. Last but not least, I will like to thank my co-pilot in this adventure, Julien Verget, for his constant encouragement that helped me going during the most difficult stages of this work.

To my parents and to Julien

This page intentionally left blank.

Abstract

Chalcogen-containing materials are an area of increasing interest for spintronic applications. The synthesis, structures and reactivity of these novel compounds are normally studied by solution-state nuclear magnetic resonance (NMR) spectroscopy, density functional theory (DFT) calculations and single-crystal X-ray diffraction. In this thesis, a range of chalcogen-containing heterocycles has been explored, focussing on the solid-state nature and exploring the bulk samples. Therefore, all materials were studied by powder X-ray diffraction and solid-state NMR, in addition to conventional solution-state NMR and single-crystal X-ray diffraction. DFT calculations were also used to interpret the solid-state NMR spectra and to gain insight into the NMR parameters. In the first chapter of results, a series of mixed Te, Se acenaphthenes is investigated. ^{77}Se and ^{125}Te NMR parameters are explored to determine whether changes in the Te aryl-group have an impact on the local environments of both nuclei. Dynamics and the requirement to consider relativistic effects for calculations of NMR parameters of heavy atoms is discussed. In the second results chapter, a series of novel P-S and P-Se six-membered heterocycles are described in terms of their synthesis, reactivity, and ^{31}P and ^{77}Se local environments. We observed and measured some unusual "through-space" couplings that occur between molecules and which mechanism and pathways are supported by DFT calculations. In the third results chapter, these heterocycles are oxidised with O, S and Se and the NMR parameters are discussed in terms of the structure. Polymorphism, phase transitions and weak interactions are some of the phenomena present in these novel compounds. This thesis demonstrated that solid-state NMR is a very good probe to study Se- and Te-containing materials.

This page intentionally left blank.

Publications

1. M. W. Stanford, F. R. Knight, K. S. Athukorala Arachige, **P. Sanz Camacho**, S. E. Ashbrook, M. Bühl, A. M. Z. Slawin and J. D. Woollins, "Probing Interactions Through Space using Spin-Spin Coupling", *Dalton Trans*., **2014**, 43, 6548-6560.

2. K. S. Athukorala Arachchige, **P. Sanz Camacho**, M. J. Ray, B. A. Chalmers, F. R. Knight, S. E. Ashbrook, M. Bühl, P. Kilian, A. M. Z. Slawin and J. D. Woollins, "Sterically Crowded Tin-Phosphines, Stabilized by Weak Intramolecular Donor-Acceptor Interactions", *Organometallics,* **2014**, 33, 2424-2433.

3. **P. Sanz Camacho**, K. S. Athukorala Arachchige, A. M. Z. Slawin, T. F. G. Green, J. R. Yates, D. M. Dawson, J. D. Woollins, S. E. Ashbrook, "Unusual Intermolecular "Through-Space" J Couplings in P–Se Heterocycles", *J. Am. Chem. Soc*., **2015**. 137, 6172-6175.

4. L. S. Konstantinova, I. E. Bobkova, Y. V. Nelyubina, E. A. Chelanova, I. G. Irtegova, N. V. Vasilieva, **P. Sanz Camacho**, S. E. Ashbrook, G. Hua, A. M. Z. Slawin, J. D. Woollins, A. V. Zibarev and O. A. Rakitin, "[1,2,5]Selenadiazolo[3,4-*b*]pyrazines: Synthesis from 3,4-Diamino-1,2,5-selenadiazole and Generation of Persistent Radical Anions", *Eur. J. Org. Chem*., **2015**, 25, 5585-5593.

5. L. S. Kostantinova, E. A Knyazeva, A. A. Nefydov, **P. Sanz Camacho**, S. E. Ashbrook, J. D. Woollins, A. V. Zibarev and O. A. Ratkin, "Direct

Synthesis of Fused 1,2,5-selenadiazoles from 1,2,5-thiadiazoles",*Tet. Lett*., **2015**, 56, 1107-1110.

6. A. Nordheider, E. Hupf, B. A. Chalmers, F. R. Knight, M. Bühl, S. Mebs, L. Checinska, E. Lork, **P. Sanz Camacho**, S. E. Ashbrook, K. S. Athukorala Arachchige, D. Cordes, A. M. Z. Slawin, J. Beckmann and J. D. Woollins, "Peri-Substituted Phosphorus-Tellurium Systems – an Experimental and Theoretical Investigation of the P···Te Through-Space Interaction", *Inorg. Chem*., **2015**, 54, 2435-2446.

7. F. R. Knight, L. M. Diamond, K. S. Athukorala Arachchige, **P. Sanz Camacho**, R. A. M. Randall, S. E. Ashbrook, M. Bühl, A. M. Z. Slawin and J. D. Woollins, "Conformational Dependence of Through-Space Tellurium-Tellurium Spin-Spin Coupling in Peri-Substituted Bis(Tellurides)", *Chem. Eur. J*., **2015**, 21, 3613-3627.

Table of contents

Abbreviations

General Abbreviations

3c-4e	three-centre four-electron
Å	Angstrom (10^{-10} metres)
Ani-p	4-methoxyphenyl
Ani-o	2-methoxyphenyl
Acenap	Acenaphthene-5,6-diyl
APIs	Active pharmaceutical ingredients
APCI	Atmospheric-pressure chemical ionisation
calc	Calculated
$CDCl_3$	Deuterated chloroform
Δ	Difference
DCM	Dichloromethane
EA	Elemental analysis
e.g.	Latin: *exempli gratia* ("for example")
EI	Electron Ionisation
Et	Ethyl
exp	experimental
Fp	4-fluorophenyl
i.e.	Latin: *id est* ("That is", "in other words")
in vacuo	Latin: "*within a vacuum*"
IR	Infrared
iso	Isotropic
^{i}Pr	Isopropyl
K	Kelvin
kcal	Kilocalorie
kJ	Kilojoule

M	Molar (mol/L)
Me	Methyl
Mes	Mesityl (2,4,6-trimethylphenyl)
mol	moles
m.p.	Melting point
Nap	1-naphthyl
$NapS_2$	Naphtho[1,8-cd]1,2-dithiole
$NapS_2P^iPr$	Naphtho[1,8-cd]1,2-dithiole *iso*propylphosphine
$NapS_2P^tBu$	Naphtho[1,8-cd]1,2-dithiole *tert*butylphosphine
$NapS_2PPh$	Naphtho[1,8-cd]1,2-dithiole phenylphosphine
$NapSe_2$	Naphtho[1,8-cd]1,2-diselenole
$NapSe_2P^iPr$	Naphtho[1,8-cd]1,2-diselenole *iso*propylphosphine
$NapSe_2P^tBu$	Naphtho[1,8-cd]1,2-diselenole *tert*butylphosphine
$NapSe_2PPh$	Naphtho[1,8-cd]1,2-diselenole phenylphosphine
$NapE_2$	Naphtho[1,8-cd]1,2-diselenole or Naphtho[1,8-cd]1,2-dithiole
NSI	Nano-electrospray
Ph	Phenyl
Superhydride	lithium triethylborohydride
θ	Steric parameter
Tip	2,4,6-triisopropanylphenyl
^{t}Bu	*Tertiary*-butyl
Tp	4-*tert*butylphenyl
Tol	Tolyl (4-methylphenyl)
TCTTN	Tetrachlorotetrathionaphthalene
THF	Tetrahydrofuran
TMEDA	N,N,N′,N′-tetramethylethylene-1,2-diamine
vdW	van der Waals

VT	Variable Temperature
XRD	X-ray diffraction

DFT Abbreviations

ADF	Amsterdam density functional
AO	Atomic orbitals
CDD	Coupling deformation density
DFT	Density functional theory
GIPAW	Gauge-induced PAW
GGA	Generalized gradient approximation
GTO	Gaussian-type orbitals
HF	Hartree fock
LCAO	Linear combination of atomic orbitals
LDA	Local density approximation
PAW	Projector augmented wave
PBE	Perdew-Burke-Ernzerhof
rel	relativity
STO	Slater-type orbitals
ZORA	Zeroth order regular approximation

NMR Spectroscopy Abbreviations

ArH	Aromatic hydrogen
ArC	Aromatic carbon
COSY	Correlation spectroscopy
δ	chemical shift
σ	chemical shielding
CP	Cross polarization
CPMG	Carl-Purcell-Meiboom-Gill
C_q	Quaternary carbon

CSA	Chemical shift anisotropy
CW	Continuous wave
d	Doublet
dd	Doublet of doublets
DSO	Diamagnetic spin-orbit
FC	Fermi contact
FID	Free induction decay
HMBC	Heteronuclear multiple bond coherence
HSQC	Heteronuclear single quantum coherence
Hz	Hertz
J	Scalar coupling constant
κ	Skew
kHz	Kilohertz
m	Multiplet
MAS	Magic angle spinning
NMR	Nuclear magnetic resonance
Ω	Span
PAS	Principal axis system
ppm	Parts per million
PSO	Paramagnetic spin-orbit
rf	Radio frequency
RS-HEPT	Rotor-synchronized Hahn echo pulse train
s	Singlet
SNR	Signal-to-noise ratio
SD	Spin dipolar
SSBs	Spinning sidebands
t	Triplet

TPPM	Two-pulse phase-modulation

IR Abbreviations

ν	Stretch
m	Medium
s	Strong
w	Weak

This page intentionally left blank.

Outline

Chapter 1. An Introduction to *peri*-substituted systems

In this chapter, an overview of the studies performed in *peri*-substituted systems is given, focussed on solution-state NMR and X-ray diffraction.

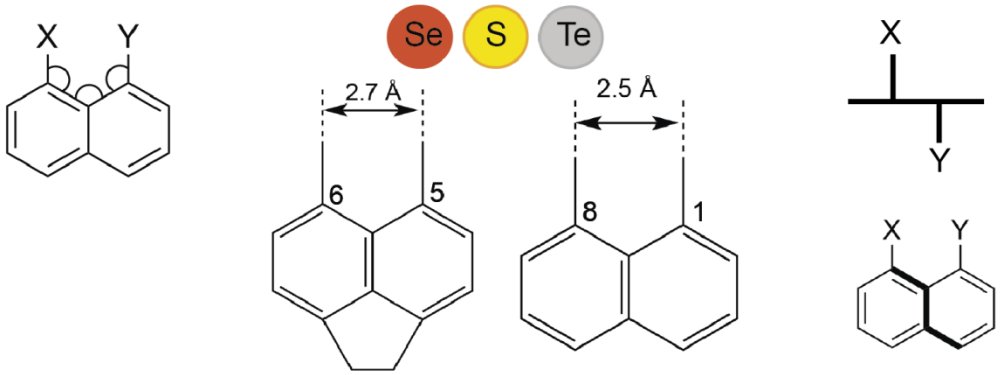

Chapter 2. Methods

A basic description of the three main techniques used in this thesis (solid-state NMR spectroscopy, X-ray diffraction and density functional theory (DFT) calculations) is given in this chapter.

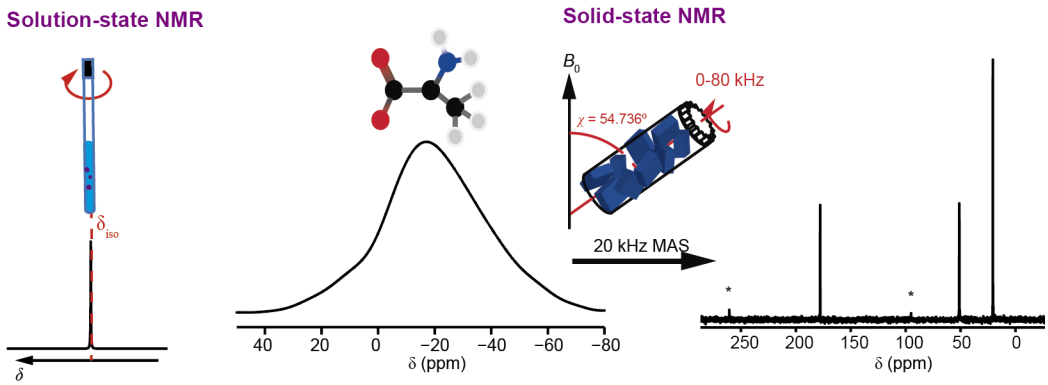

Chapter 3. ^{77}Se and ^{125}Te solid-state NMR studies of *peri*-substituted acenaphthene systems

This chapter deals with the ^{77}Se and ^{125}Te NMR study of a series of nine mixed *peri*-substituted acenaphthenes and their local environments.

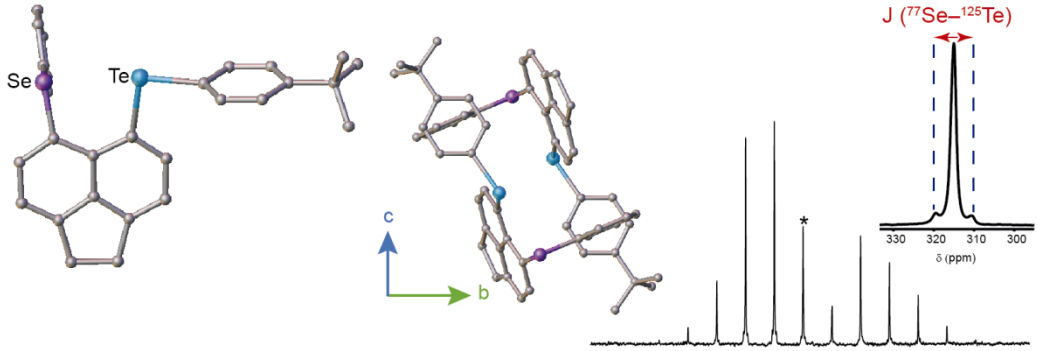

Chapter 4. Studying interactions in chalcogen-phosphorus heterocycles

The subject of this chapter is the synthesis and characterisation of novel six-membered P-S and P-Se heterocycles. Their local environments, reactivity and packing motifs are described in a series of six compounds.

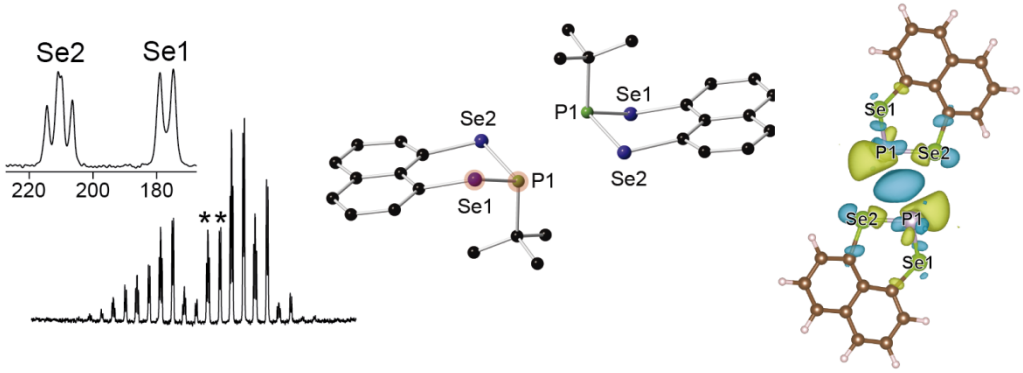

Chapter 5. Synthesis and spectroscopic studies of oxidised S-P and Se-P heterocycles

The oxidation of compounds described in Chapter 4 with different chalcogens (O, S, Se) are described here. Their synthesis and NMR parameters are compared with the parent compounds in order to determine trends in the series of compounds.

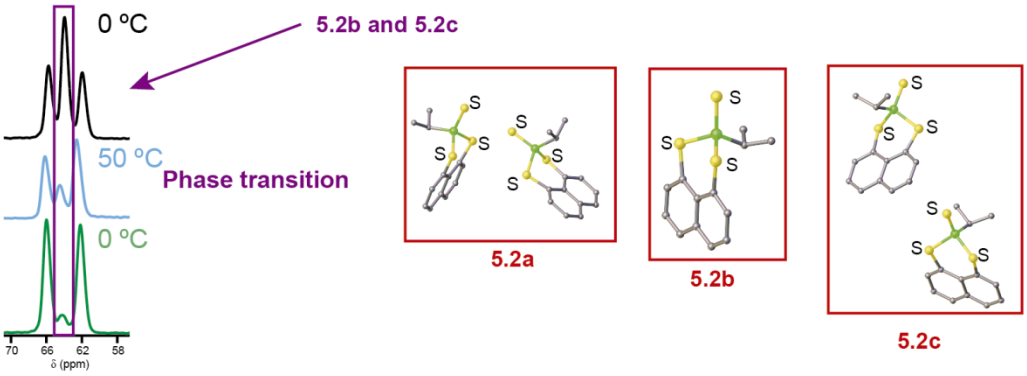

Chapter 6. Experimental procedures

All the experimental procedures followed to synthesized compounds described in Chapter 4 and 5 are given here with the microanalysis, solution-state NMR, mass spectrometry and IR data.

This page intentionally left blank.

Chapter 1: An introduction to *peri*-substituted systems

1.1 *Peri*-substitution

Peri-substitution is defined as a double substitution that occurs in organic molecules with rigid backbones, such as naphthalene and acenaphthene, in *peri*-positions (*i.e.,* positions 1 and 8 in the naphthalene and 5 and 6 in the acenaphthene)[1] as shown in Figure 1.1. This term derives from the Greek *peri*, meaning around, or near about. The unsubstituted ("ideal") naphthalene (*i.e.,* with two hydrogen atoms in the *peri*-positions) is a rigid planar molecule with all internal angles being ~ 120° and with only small variations in the C-C bond lengths within the structure.[2] This results in the exocyclic *peri*-bonds being aligned parallel to each other at a *peri*-distance of ~2.5 Å.[1] In the acenaphthene ring, owing to the CH_2-CH_2 bridge at position 1 and 2 of the acenaphthene backbone, a slight deviation from planarity is found in the system, together with a longer *peri*-distance of ~2.7 Å and some variation in the angles, the smallest being the C1-C1a-C2 of 112.4(1)° and the largest the C5-C5a-C6 of 128.4 (1).[3]

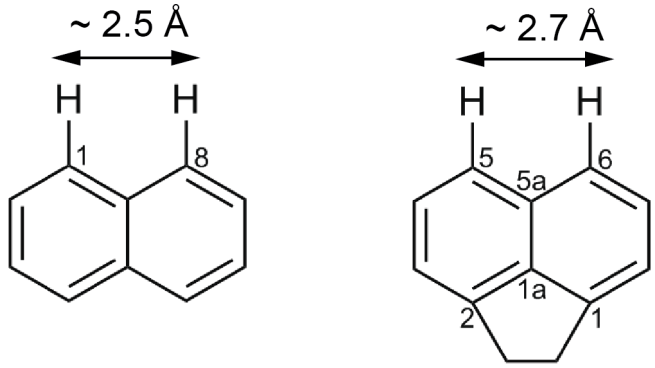

Figure 1.1.Naphthalene and acenaphthene structures with the *peri*-distances shown.

Only hydrogen atoms can fit comfortably in the *peri*-positions as the sum of their van der Waals (vdW) radii is smaller than the *peri*-distance. Substitution of the hydrogen atoms by any other atom will result in greater steric strain in the system, particularly for heavy atoms, unless there is a bonding interaction between the *peri*-atoms, as shown in Figure 1.2, where the *peri*-distance in compound **A** is 1.914(3) Å while, the *peri*-distance in compound **B** is 3.1332(9) Å.[4, 5]

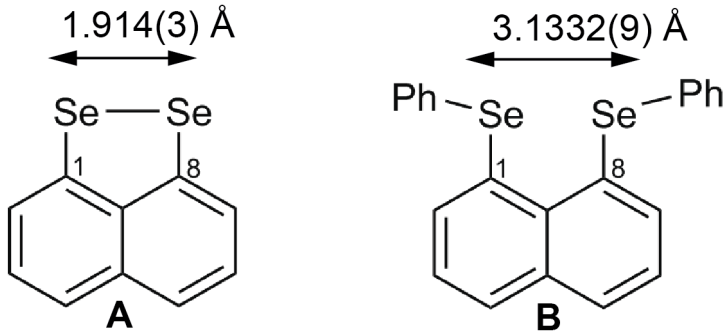

Figure 1.2. Illustration of the *peri*-distance in two different compounds. In compound **A**, a bonding interaction shortens the distance between the two Se atoms while, in compound **B**, where there is no bonding interaction, the distance between Se atoms is larger.

1.2 X-ray crystallography

For systems, where the *peri*-atoms are not formally bonded together, the steric strain introduced in the system by heavy atoms occupying the *peri*-position can be released *via* a distortion of the rigid carbon skeleton through elongation of the *peri*-atoms bonds, in plane distortions (Figure 1.3b), out-of-plane displacements (Figure 1.3c) and/or buckling of the naphthalene backbone (Figure 1.3d),[1,6] or *via* attractive interactions between the two *peri*-atoms.[7]

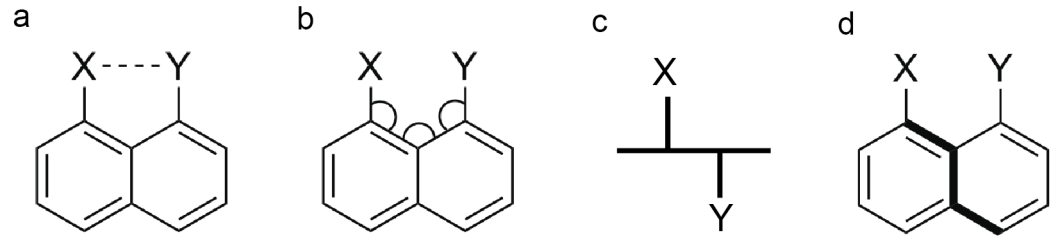

Figure 1.3. Illustration of the various ways of measuring the degree of steric strain and naphthalene deformation by analyzing (a) *peri*-distances, (b) in-plane distortions or splay angle, (c) out-of-plane displacements and (d) torsion angles.

To try to gain insight into the steric strain in these molecules, X-ray crystallography is widely used, as it can measure the distortion in the backbone, and any changes in bond length and bond angles in the *peri*-region that may occur when substituting the hydrogen atoms in the *peri*-positions by different groups.

Of the various ways to relieve the steric strain, the elongation of the *peri*-bond lengths is really uncommon, owing to the typically large amount of energy associated with this change.[8] However, some or all of remaining modes of relief can be present, depending on the degree of steric strain for the molecule. The *peri*-distance (Figure 1.3a) is a good (although indirect) indicator of the forces (bonding or non-bonding) acting between the *peri*-atoms, and can also indicate the degree of distortion away from an ideal geometry. The in-plane distortion can be analysed by considering the sum of the *peri*-angles (as shown in Figure 1.3b) subtracted from 360° (the ideal value). This is also called the splay angle, and this will be the name used throughout this thesis. The splay angle can be a positive value, implying a repulsive (nonbonding) interaction between the *peri*-atoms is present, or it can be a negative value indicating an attractive

(bonding) interaction. The out-of-plane displacements, shown in Figure 1.3c, are a measure of how far the *peri*-atoms deviate from the naphthalene or acenaphthene plane (*i.e.,* as a consequence of the steric repulsion the atoms prefer to be more distant from each other). In addition to the in- and out-of-plane distortions, the backbone can also undergo a twisting in order to relieve the strain in the system. This can be measured by analysing the torsion angles, as shown in Figure 1.3d. In an unsubstituted ring the torsion angle is 180/0° and so any change indicates the level of buckling within the planar ring system.

1.3 Weak interactions

As previously mentioned, the considerable steric hindrance that results from two large heteroatoms constrained in the *peri-* positions of a rigid organic backbone can be relieved either by bond formation or weak interaction between the *peri*-atoms, or by significant distortion of the geometry. Understanding these weak interactions has been the focus of some controversy as they are typically poorly understood and certainly not as extensively studied as strong covalent and ionic bonding interactions. The Woollins and Kilian research groups have carried out extensive work on naphthalene- and acenaphthene *peri*-substituted systems mainly focused on group 15 (P, As, Sb, Bi)[1, 9] and 16 (S, Se, Te),[1, 10] but also halogen-chalcogenides functionalities have been studied[11, 12] and even group 14 (Sn).[13, 14]

The existence of weak donor-acceptor interactions between the *peri*-atoms has been recognised for some of the systems studied by Woollins and Kilian groups. These donor-acceptor interactions, termed three-centre four-electron,[11] derive from the lone-pair orbital of one of the heteroatoms

(E) interacting with the empty σ*(E′-C) anti-bonding orbital of the adjacent heteroatom, under appropriate geometric conditions. DFT calculations have been important in the understanding of these weak interactions.[15]

1.4 The use of J coupling to study weak interactions

X-ray diffraction is usually used in *peri*-substituted systems to determine the presence or otherwise of weak interactions between the *peri*-atoms, by measuring the *peri*-distance. Although bond lengths, molecular conformations and interatomic distances offer some information on weak interactions, these indirect structural parameters are not very sensitive probes of electronic interactions. In contrast, NMR spectroscopy offers an extremely sensitive probe of the local, atomic-scale environment, through both the chemical shift and the indirect J coupling between two spins. The magnitude of the J coupling typically decreases as the number of bonds that connect two atoms increases, and coupling through more than four bonds is often too small to be observed.[16] However, significant J couplings have been observed in solution-state NMR spectra between nuclei that are joined by a large number of bonds, but are in close spatial proximity. Several examples appeared in the literature during the period 1970 – 2000, and the J coupling in these systems was termed "through-space" suggesting it occurs between formally non-bonded atoms in close spatial proximity.[17] Figure 1.4a shows some examples of "through-space" J coupling in *peri*-substituted naphthalene and acenaphthene compounds. Mallory *et al.*, reported a J(F,F) of between 59 – 85 Hz in several 1,8-difluoronaphthalenes (**A**, in Figure 1.4) while a smaller value (J(F,F) of 28 Hz) was found in the acenaphthene analogues (**B**, in Figure 1.4). The J(F,F) were found to directly depend on the F···F distance.[18]

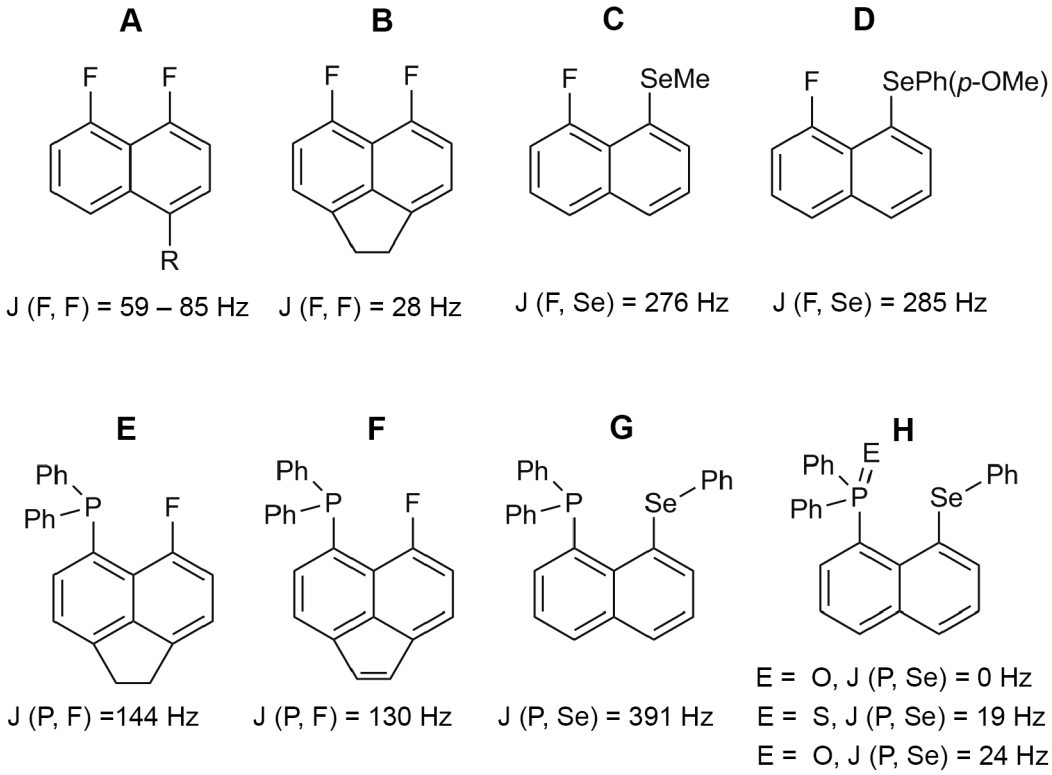

Figure 1.4. Naphthalene and acenaphthene *peri*-substituted compounds presenting "through-space" couplings between the *peri*-atoms.[7, 18, 19, 20]

Typical coupling magnitudes of ~144 and ~130 Hz have also been observed between *peri*-substituted P and F atoms in acenaphthene systems (**E** and **F**, in Figure 1.4) by Mallory *et al*.[18] In all these studies, Mallory proposed that the origin of the J coupling is the overlap between lone-pairs orbitals on the crowded elements.[19] Nakanishi *et al.*, studied *peri*-substituted F and Se atoms in naphthalene systems (**C** and **D**, in Figure 1.4) and J couplings between 276 and 285 Hz were observed. Nakanishi proposed a linear alignment of F···Se-C to be responsible for the J coupling interaction.[20] In more recent work from Woollins and co-workers, a J(^{31}P, ^{77}Se) coupling of ~391 Hz was observed between *peri*-substituted P and Se

in naphthalene systems (**G**) while, smaller values are found for the oxidised versions (**H**).[7]

1.5 Solid-state NMR studies of *peri*-substituted systems

Only a few examples of the study of *peri*-substituted system by solid-state NMR spectroscopy are known in the literature. Griffin *et al.*, studied a series of inorganic and organoselenium compounds (**A** – **D1**, in Figure 1.5) by ^{77}Se solid-state NMR and first-principles calculations.[21] In this study, good agreement was found between the experimental and calculated NMR parameters. However, a second study by the author of mixed *peri*-substituted acenaphthenes salts (**E** – **F,** in Figure 1.5) shows a poorer agreement between experimental and calculated NMR parameters.[22]

In additions to those studies, collaborations between the Woollins and Ashbrook groups produced four more recent studies on acenaphthenes systems using solid-state NMR. One of these studies will be described in Chapter 3 in full detail. The other three are not described in this thesis, and therefore brief mention of these will be given here. A series of Sn and P *peri*-substituted acenaphthenes (**G1**-**G3**) with a through-space J(^{31}P, ^{119}Sn) coupling were investigated by solid-state NMR. The J coupling and chemical shifts were in relatively good agreement with the solution-state NMR values, with slight deviations observed.[23] A mixed *peri*-substituted acenaphthene (**H1**) was also studied by ^{125}Te and ^{31}P solid-state NMR and a through-space J(^{31}P, ^{125}Te) coupling of 1336 Hz was unambiguously determined by the doublet observed in the ^{125}Te MAS NMR spectrum.[24]

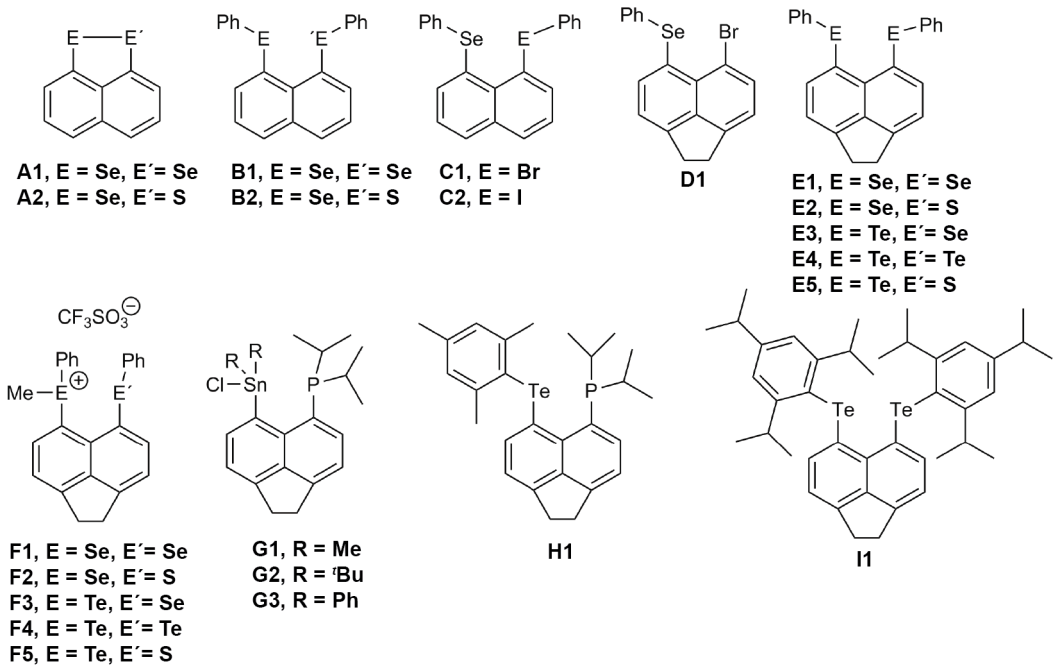

Figure 1.5. Naphthalene and acenaphthene *peri*-substituted compounds Studied by solid-state NMR.

Although, the through-space J(^{125}Te-^{125}Te) coupling in compound **I1** can be, in principle, unambiguously determined by ^{125}Te solid-state NMR (*i.e.*, both Te atoms in the *peri*-position are crystallographically inequivalent in the solid state) owing to the large chemical shift anisotropies and the observation of J(^{125}Te, ^{125}Te) as satellites in the spectrum, it was very difficult to obtain an accurate and precise value for compound **I1** (*i.e.*, an estimate of the J(^{125}Te, ^{125}Te) was between 3600 – 4000 Hz).[25]

1.6 References

1. P. Kilian, F. R. Knight and J. D. Woollins, *Chem. Eur. J.*, **2011**, 17, 2302-2328.

2. C. A. Coulson, R. Daudel and J. M. Robertson, *Proc. R. Soc. London Ser. A*, **1951**, 207, 306-320.

3. H. W. W. Ehrlich, *Acta. Crystallogr.*, **1957**, 10, 699-705.

4. S. M. Aucott, H. L. Milton, S. D. Robertson, A. M. Z. Slawin and J. D. Woollins, *Heteroat. Chem.*, **2004**, 15, 530-542.

5. F. R. Knight, A. L. Fuller, M. Bühl, A. M. Z. Slawin and J. D. Woollins, *Chem. Eur. J.*, **2010**, 16, 7503-7516.

6. P. Wawrzyniak, A. L. Fuller, A. M. Z. Slawin and P. Kilian, *Inorg. Chem.*, **2009**, 48, 2500-2506.

7. F. R. Knight, A. L. Fuller, M. Bühl, A. M. Z. Slawin and J. D. Woollins, *Chem. Eur. J.*, **2010**, 16, 7503-7516.

8. V. Balasubramaniyan, *Chem.Rev.*, **1966**, 66, 567-641.

9. B. A. Chalmers, M. Bühl, K. S. Athukorala Arachchige, A. M. Z. Slawin and P. Kilian, *J. Am. Chem. Soc.*, **2014**, 136, 6247-6250.

10. P. Kilian, F. R. Knight and J. D. Woollins, *Coord. Chem. Rev.*, **2011**, 255, 1387-1413.

11. L. K. Aschenbach, F. R. Knight, R. A. M. Randall, D. B. Cordes, A. Baggott, M. Buhl, A. M. Z. Slawin and J. D. Woollins, *Dalton Trans.*, **2012**, 41, 3141-3153.

12. L. M. Diamond, F. R. Knight, K. S. Athukorala Arachchige, R. A. M. Randall, M. Bühl, A. M. Z. Slawin and J. D. Woollins, *Eur. J. Inorg. Chem.*, **2014**, 2014, 1512-1523.

13. K. S. Athukorala Arachchige, L. M. Diamond, F. R. Knight, M. L. Lechner, A. M. Z. Slawin and J. D. Woollins, *Organometallics*, **2014**, 33, 6089-6102.

14. B. A. Chalmers, K. S. Athukorala Arachchige, J. K. D. Prentis, F. R. Knight, P. Kilian, A. M. Z. Slawin and J. D. Woollins, *Inorg. Chem.*, **2014**, 53, 8795-8808.

15. M. Bühl, F. R. Knight, A. Křístková, I. Malkin Ondík, O. L. Malkina, R. A. M. Randall, A. M. Z. Slawin and J. D. Woollins, *Angew. Chem.*, **2013**, 52, 2495-2498.

16. L. Ernst and P. Sakhaii, *Magn. Reson. Chem*., **2000**, 38, 559-565.

17. J. C. Hierso, *Chem. Rev.,* **2014**, 114, 4838-4867.

18. F. B. Mallory, C. W. Mallory, K. E. Butler, M. B. Lewis, A. Q. Xia, E. D. Luzik, L. E. Fredenburgh, M. M. Ramanjulu, Q. N. Van, M. M. Francl, D. A. Freed, C. C. Wray, C. Hann, M. Nerz-Stormes, P. J. Carroll and L. E. Chirlian, *J. Am. Chem. Soc.,* **2000**, 122, 4108-4116.

19. F. B. Mallory and C. W. Mallory, "Coupling Through Space in Organic Chemistry", *eMagRes*, John Wiley & Sons, Ltd, USA, **2007**. DOI: 10.1002/9780470034590.emrstm0099.

20. W. Nakanishi, S. Hayashi, A. Sakaue, G. Ono and Y. Kawada, *J. Am. Chem. Soc.,* **1998**, 120, 3635-3640.

21. J. M. Griffin, F. R. Knight, G. Hua, J. S. Ferrara, S. W. L. Hogan, J. D. Woollins and S. E. Ashbrook, *J. Phys. Chem. C,* **2011**, 115, 10859-10872.

22. F. R. Knight, R. A. M. Randall, K. S. Athukorala Arachchige, L. Wakefield, J. M. Griffin, S. E. Ashbrook, M. Bühl, A. M. Z. Slawin and J. D. Woollins, *Inorg. Chem.,* **2012**, 51, 11087-11097.

23. K. S. Athukorala Arachchige, P. Sanz Camacho, M. J. Ray, B. A. Chalmers, F. R. Knight, S. E. Ashbrook, M. Bühl, P. Kilian, A. M. Z. Slawin and J. D. Woollins, *Organometallics,* **2014**, 33, 2424-2433.

24. A. Nordheider, E. Hupf, B. A. Chalmers, F. R. Knight, M. Bühl, S. Mebs, L. Chęcińska, E. Lork, P. S. Camacho, S. E. Ashbrook, K. S. Athukorala Arachchige, D. B. Cordes, A. M. Z. Slawin, J. Beckmann, J. D. Woollins, *Inorg. Chem.,* **2015**, 54, 2435-2446.

25. F. R. Knight, L. M. Diamond, K. S. A. Arachchige, P. Sanz Camacho, R. A. M. Randall, S. E. Ashbrook, M. Bühl, A. M. Z. Slawin and J. D. Woollins, *Chem. Eur. J.,* **2015**, 21, 3613-3627.

Chapter 2: Methods

In this chapter, the principles of the three characterisation techniques (NMR, X-ray diffraction and DFT) used in this thesis will be discussed. A more detailed description of NMR will be provided, as it is the most used technique in this thesis. However, it must be noted that although the principles of crystallography and DFT methodologies are relevant to the content of this work, it is beyond the scope of this thesis to give a full description of these techniques. More information can be found elsewhere.[1]

2.1 NMR spectroscopy theory

2.1.1 Basic principles of NMR

All atomic nuclei possess an intrinsic angular momentum, **I**, with a magnitude that is described by the nuclear spin quantum number I. Only nuclei with a non-zero nuclear spin quantum number are considered NMR active. These species have a nuclear magnetic dipole moment, **μ**, given by:

$$\boldsymbol{\mu} = \gamma \mathbf{I} \quad , \qquad [2.1]$$

where γ is the gyromagnetic ratio, characteristic of a given nuclide. In the absence of an external magnetic field, the projection of **I**, along an arbitrary axis, typically defined as the z-axis, is quantized in units of ħ:

$$I_z = m_I \hbar \quad , \qquad [2.2]$$

where m_I is the magnetic quantum number, and takes values between +I and –I in integer steps, leading to 2I + 1 degenerate spin states. The z component of **μ** is given by:

$$\mu_z = \gamma I_z = \gamma m_I \hbar \quad . \qquad [2.3]$$

An external magnetic field, of magnitude B_0, which lies along the z-axis by convention, lifts the degeneracy of the nuclear spin states. The splitting of the nuclear energy levels is known as the Zeeman interaction and will depend on the angular momentum, **I**. The Zeeman energy level is given by:

$$E_{m_I} = -\gamma I_z B_0 = -\gamma m_I \hbar B_0 \quad . \qquad [2.4]$$

Only transitions with $\Delta m_I = \pm 1$ are observable in NMR spectroscopy. A nucleus with spin quantum number I = 1/2 has only one possible transition, at a frequency ω_0, while a nucleus with spin quantum number I > 1/2, known as a quadrupolar nucleus, has more possible transitions (*e.g.*, I = 1 has two observable transitions degenerate with frequency ω_0 as shown in Figure 2.1), given by:

$$\omega_0 = -\gamma B_0 \quad , \qquad [2.5]$$

where ω_0 is the Larmor frequency, in units of rad s^{-1} or $\nu_0 = -\omega_0 / 2\pi$ in Hz.

In a macroscopic sample, at thermal equilibrium, the nuclei occupy energy levels according to the Boltzmann distribution:

$$N = \frac{N_{upper}}{N_{lower}} = e^{-\Delta E/kT} \quad , \qquad [2.6]$$

where N is the population difference, T is the temperature in Kelvin, k is the Boltzmann´s constant and ΔE is the energy difference between two spins states under the influence of an external magnetic field.

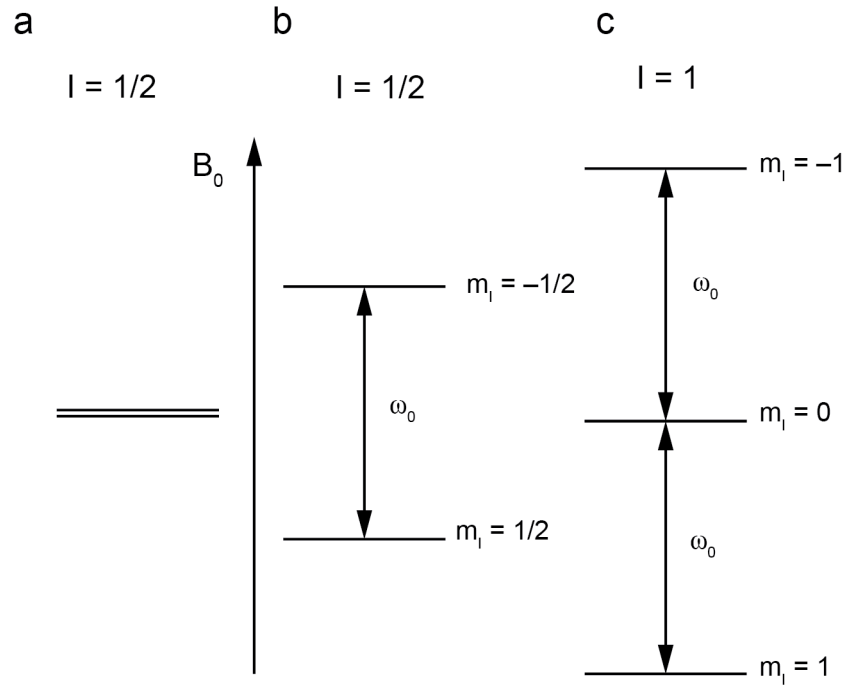

Figure 2.1. Schematic energy level diagram for (a) I = 1/2 nucleus in the absence of a magnetic field, (b) I = 1/2 and (c) I = 1 nuclei in the presence of a magnetic field of magnitude B_0.

This population difference gives rise to an equilibrium bulk nuclear magnetisation, represented by a vector, $\mathbf{M_0}$, aligned with B_0. The magnitude of $\mathbf{M_0}$ depends upon the field applied and the Larmor frequency, and so is much larger for nuclei with higher γ and, for a given nucleus, the magnitude of $\mathbf{M_0}$ will increase with the field strength, as shown in Equation 2.7.

$$\mathbf{M_0} = \frac{N(\gamma h)^2 B_0}{16\pi^2 kT} \quad . \qquad [2.7]$$

2.1.2 Basic NMR experiments

Although spins are inherently quantum mechanical, an ensemble of spins can be treated classically. The vector model[2] can be used to understand basic concepts of NMR spectroscopy, such as, the manipulation of the bulk magnetisation for spin I = 1/2 nuclei under the influence of a "pulse", a radiofrequency (rf) electromagnetic irradiation. An alternative approach is to use the density operator formalism, which can describe more complex NMR experiments. However, it is more complicated to describe mathematically and, thus, is beyond the scope of this thesis.

In the simplest NMR experiment, a short pulse of high-power (rf) electromagnetic irradiation with frequency ω_{rf}, which is at or near the Larmor frequency, is applied in order to perturb $\mathbf{M_0}$ from its equilibrium position along z-axis.

All NMR experiments are performed in the static or "laboratory" frame shown in Figure 2.2a, however, it is easier to consider the effect of pulses on $\mathbf{M_0}$ in a "rotating frame"; a coordinate system where the z-axis remains aligned with B_0 but the xy-plane rotates around the z-axis at a frequency of ω_{rf}. In the laboratory frame, a pulse appears as two counter-rotating components with angular frequencies of $\pm\omega_{rf}$, while in the rotating frame, the component rotating at $+\omega_{rf}$ appears static, interacting with the nuclear spins, while the second component now, rotates at $-2\omega_{rf}$ in the rotating frame and its effects can be ignored. The pulse, can now be considered as a fixed magnetic field, of magnitude B_1, applied in the xy-plane of the rotating frame, as shown in Figure 2.2b. This static magnetic field, B_1, will affect the bulk magnetisation, $\mathbf{M}$, which then nutates about B_1 at a frequency of:

$$\omega_1 = -\gamma B_1 \ , \qquad [2.8]$$

for the duration of the pulse, τ_p.

The direction in which B_1 is applied in the rotating frame is described by the phase of the pulse, φ, and the "flip angle",defined as the angle through which **M**, nutates during the pulse. This flip angle, β, depends on the duration of the pulse and the nutation frequency with:

$$\beta = \omega_1 \tau_p \ . \qquad [2.9]$$

All pulses can be described by "β_{φ}" notation where, in this thesis, β will be described in degrees and φ will be given in degrees or defined as being applied along the Cartesian axes (x, y and z).

After the pulse is applied, **M** then precesses about the z-axis with a frequency of:

$$\Omega = \omega_0 - \omega_{rf} \ , \qquad [2.10]$$

as shown in Figure 2.2c. If the pulse is "on resonance", $\omega_{rf} = \omega_0$ and $\Omega = 0$. In this case, **M** is static in the rotating frame. It is this precession that generates an oscillating current in a detector coil that can be recorded. When a pulse with $\beta = 90°$ is applied to the system, transverse magnetisation is created in the xy-plane giving rise to a maximum detectable signal. In contrast, when a pulse with $\beta = 180°$ is applied to the system, **M** is then aligned along –z-axis, resulting in no observable magnetisation in the xy-plane, and thus no signal is observed.

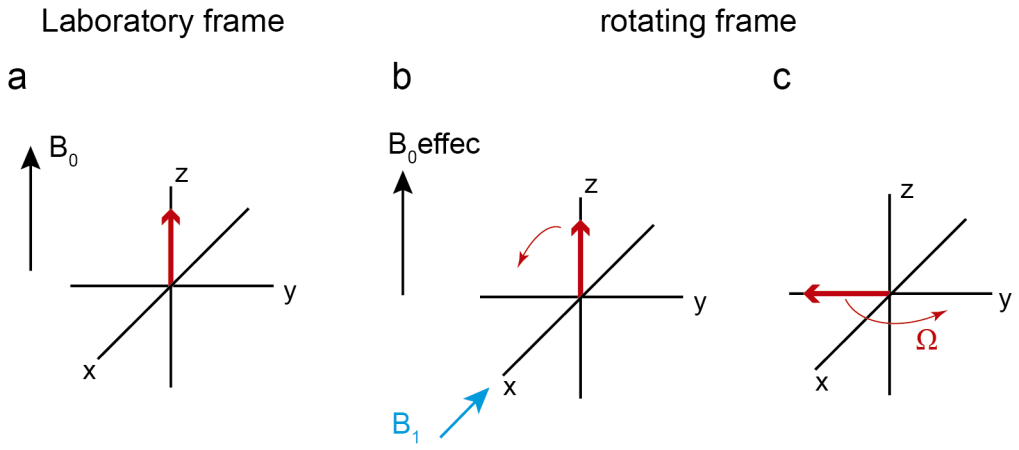

Figure 2.2. Schematic representation of the bulk magnetisation (represented by a red arrow) (a) in the laboratory frame under the effect of B_0; (b) effect by applying a magnetic field, of magnitude B_1 in the xy-plane of the rotating frame (c) effect after the application of the magnetic field where **M** then precesses about the z-axis in the xy plane with a frequency of Ω. It is assumed a nucleus with positive Larmor frequency.

The precession of **M** is damped by relaxation processes, described in more detail below, leading to a complex time-dependent signal, S(ω), known as the free induction decay (FID). Fourier transformation of this time-domain signal yields the frequency-domain spectrum, as explained below.

In most experiments, "signal averaging" is required in order to obtain a good sensitivity, and therefore, a good signal-to-noise ratio (SNR) in the NMR spectrum. This is carried out by repeating the experiment N times and co-adding the FIDs. The signal increases linearly with N, whereas random noise ensures that the SNR increases with $\sqrt{N}$. Signal averaging is extremely important and typically 100 – 10000 FIDs are coadded for low-sensitivity nuclei, such as ^{77}Se or ^{29}Si.

2.1.3 Relaxation

The bulk magnetisation (**M**) returns to equilibrium ($\mathbf{M_0}$) through a number of relaxation processes. Longitudinal or spin-lattice relaxation, characterized by a time constant T_1, describes the return of the z component of the magnetisation to equilibrium. T_1 Values are sample dependent and, for solid samples, can be extremely long (minutes to hours), which can result in very long experimental times, as it is assumed that the equilibrium is restored after ~$5T_1$.

Transverse or spin-spin relaxation is described by a time constant T_2, and defines the loss of magnetisation in the xy-plane that occurs through interactions between the spins. Typically, in solids, T_1 is much greater than T_2, unless significant dynamics are present.

2.1.4 Fourier transformation

The FID is composed of a number of different oscillating signals, each described by a frequency and phase. In order to determine both the frequency and the phase, quadrature detection (*i.e.*, the use of two detectors) is employed, allowing the measurement of two separate components (*i.e.*, a real and imaginary part) of the FID.[3] These two components can be described by a cosine function and a sine function of the offset frequency, Ω, and are 90° out of phase. These signals give the real and imaginary parts of a complex time-domain signal, S(t) respectively, given by:

$$S(t) = [\cos \Omega t + i \sin \Omega t] \exp(-t/T_2) , \qquad [2.11]$$

$$S(t) = \exp(i\Omega t)\exp(-t/T_2) \quad t \geq 0 \ , \qquad [2.12]$$

$$S(t) = 0 \quad t < 0 \ . \qquad [2.13]$$

Fourier transformation of the time-domain signal results in a frequency-domain spectrum, S(ω), given by:

$$S(\omega) = \int_0^\infty S(t)e^{-i\omega t}dt \ , \qquad [2.14]$$

The frequency-domain spectrum also has two components, one real and one imaginary. A(Δω) and D(Δω) represent the absorptive and dispersive Lorentzians, respectively, that describe the frequency-domain signal and are given by:

$$S(\omega) = A(\Delta\omega) - iD(\Delta\omega) \ , \qquad [2.15]$$

where

$$A(\Delta\omega) = \frac{1/T_2}{(\frac{1}{T_2})^2 + (\Delta\omega)^2} \ , \qquad [2.16]$$

$$D(\Delta\omega) = \frac{\Delta\omega}{(\frac{1}{T_2})^2 + (\Delta\omega)^2} \ . \qquad [2.17]$$

In reality, the real component of the frequency-domain is a combination of absorptive (A) and dispersive (D) lineshapes and in order to obtain the purely absorptive-lineshape usually reported in NMR, a process called "phasing" must be performed post Fourier transformation.

2.1.6 Interactions in solid-state NMR

In solid-state NMR, in addition to the Zeeman interaction described in section 2.1.1, there are a number of other interactions between nuclear spins and the local magnetic fields arising from the surroundings of the nucleus. These interactions can provide detailed information about bonding, interatomic distances and local structure of the nucleus studied. In solid-state NMR, most of these internal interactions have an isotropic (orientation-independent) and an anisotropic (orientation-dependent) component. In solution, owing to the isotropic tumbling of molecules, only the isotropic components are generally observed. Although the Zeeman interaction is normally the dominant interaction in solid-state NMR, the effects of the other interactions can usually be treated as perturbations of the Zeeman energy levels, and can still result in significant changes to the NMR spectrum.

The main interactions that will be considered in this thesis are chemical shielding, dipolar coupling and J coupling, all described more in detail below. However, it must be noted that a number of other interactions can affect the spectrum in solid-state NMR, such as quadrupolar, paramagnetic and Knight shift.[4]

2.1.6.1 Chemical shift anisotropy (CSA)

The magnetic field experienced by an isolated nucleus differs from the applied magnetic field owing to the electrons circulating around the nucleus, creating a small magnetic field, B'. In a molecule, this magnetic field can oppose or augment the applied field resulting in a shielding or

deshielding effect. The effective magnetic field felt by the nucleus can be considered as:

$$B_{eff} = B_0 - B' . \quad [2.18]$$

The observed Larmor frequency is then given by:

$$\omega_{obs} = -\gamma B_{eff} = -\gamma B_0(1-\sigma) , \quad [2.19]$$

where σ is the field-independent shielding parameter. The value of σ depends on the local chemical environment (*i.e.*, the local distribution of electrons in bonds). Therefore, different chemical environments will result in different resonances within the spectrum. The absolute value of σ is hard to measure experimentally and so it is more convenient to define a chemical shift, δ, which is measured relative to a known frequency of a reference compound, ω_{ref}, and typically reported in ppm, given by:

$$\delta = 10^6(\omega_{obs} - \omega_{ref})/\omega_{ref} . \quad [2.20]$$

It can be seen that δ and σ are opposite in sign and, therefore, σ is a measure of shielding, while δ is a measure of deshielding. However, the electron density distribution around the nucleus is rarely spherical and σ is not a scalar quantity, but is defined by a tensor **σ**. The interaction then has an isotropic and an anisotropic component.

The anisotropic broadening arises as a consequence of the presence of different crystallites with all possible orientations forming the powder sample. If just one crystallite is present, a single resonance in the spectrum is observed for each different orientation of the isolated crystallite respect to the magnetic field, as shown in Figure 2.3. However, in most cases the sample is a powder, with all possible crystallite orientations present simultaneously, resulting in a broadened "powder-pattern" lineshape.[5]

Mathematically, the shielding is described as a second-rank tensor (a 3 × 3 matrix), **σ**, which, when expressed in the laboratory frame, contains 9 independent components:

$$\sigma^{lab} = \begin{pmatrix} \sigma_{xx} & \sigma_{xy} & \sigma_{xz} \\ \sigma_{yx} & \sigma_{yy} & \sigma_{yz} \\ \sigma_{zx} & \sigma_{zy} & \sigma_{zz} \end{pmatrix} . \quad [2.21]$$

In the laboratory frame, B_0 is applied along the z-axis and two angles, θ and φ, can be used to describe the orientation of the tensor with respect to the magnetic field for any individual crystallite as shown in Figure 2.4. However, **σ** can also be described in its principal axis system (PAS), a coordinate frame where the tensor is diagonal such that:

$$\sigma^{PAS} = \begin{pmatrix} \sigma_{11} & 0 & 0 \\ 0 & \sigma_{22} & 0 \\ 0 & 0 & \sigma_{33} \end{pmatrix} , \quad [2.22]$$

where σ_{11}, σ_{22} and σ_{33} are described as the principal components of the chemical shielding tensor. It should be noted that more generally rotation between different frames can be expressed using three Euler angles (α, β, γ).[6]

There are three different conventions used to define the chemical shift anisotropy: the standard[7], the Herzfeld-Berger[8] and the Haeberlen convention.[9] In the standard convention,[7] shown in Figure 2.5a, the chemical shift components are labelled in order of their magnitude, with $\delta_{11} \geq \delta_{22} \geq \delta_{33}$. The isotropic value, δ_{iso}, is given by:

$$\delta_{iso} = \frac{(\delta_{11} + \delta_{22} + \delta_{33})}{3} , \quad [2.23]$$

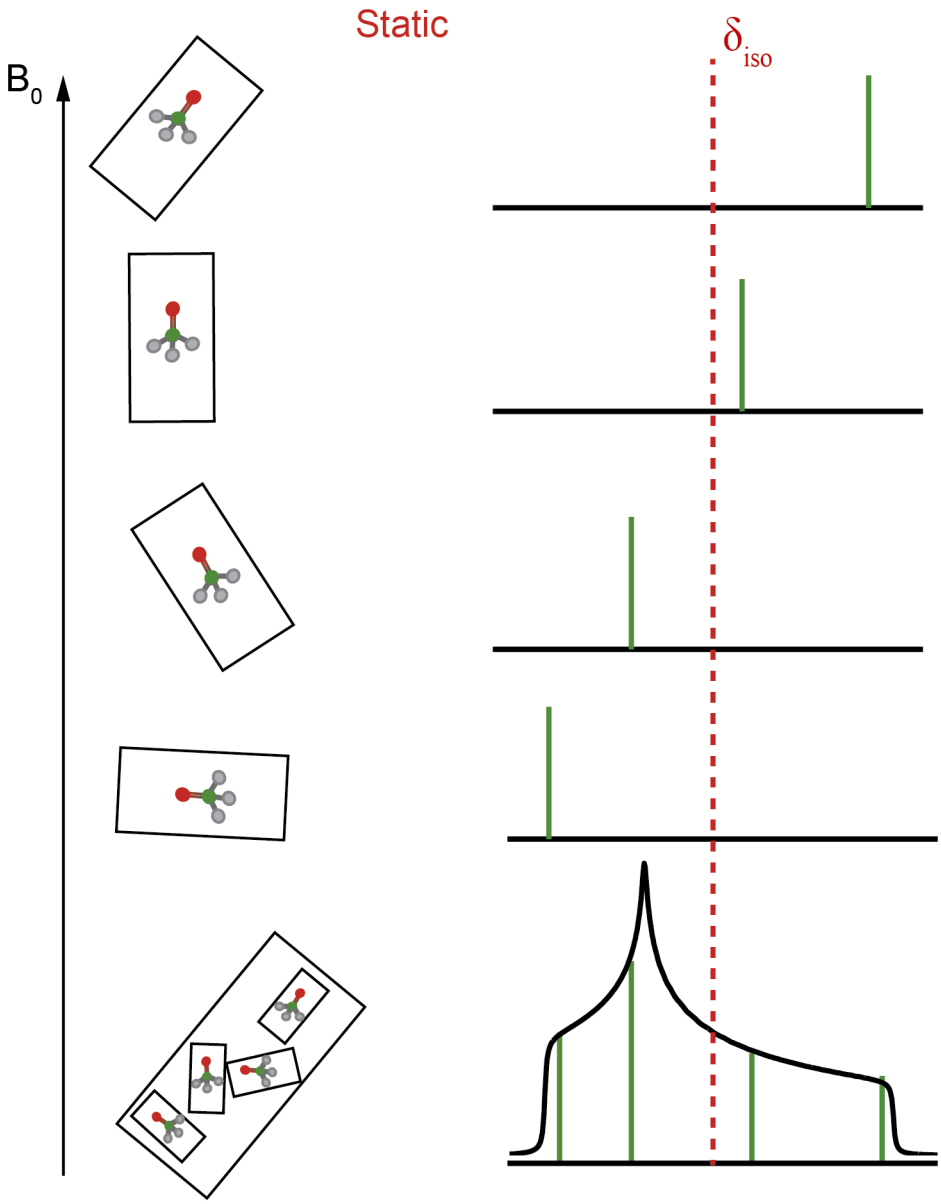

Figure 2.3. Schematic representation of the NMR spectrum when affected by the CSA, with an isolated molecule in an isolated crystallite, and in a powdered sample where all possible crystallites orientation are present.

and corresponds to the centre of gravity of the lineshape. The Herzfeld-Berger convention,[8] shown in Figure 2.5b, is most frequently used in this thesis to describe the CSA.

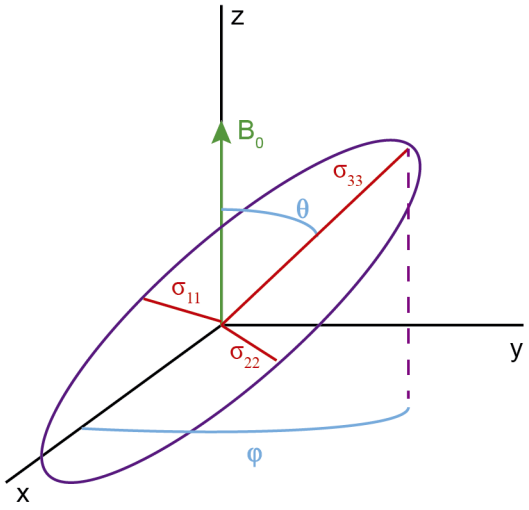

Figure 2.4. Schematic representation of the shielding tensor in the laboratory frame, where the principal components (σ_{11}, σ_{22} and σ_{33}) are related to B_0 by θ and φ angles (in blue).

To describe the anisotropy, in the Herzfeld-Berger convention, two parameters are used; the span, Ω:

$$\Omega = \delta_{11} - \delta_{33} \ , \qquad [2.24]$$

which represents the maximum width of the powder pattern, and the skew,κ:

$$\kappa = \frac{3(\delta_{22} - \delta_{iso})}{\Omega} = \frac{3a}{\Omega} \ , \qquad [2.25]$$

which is a measure of the shape or asymmetry of the tensor. The skew can take negative or positive values ($-1 \leq \kappa \leq 1$), depending on the position of δ_{22} with respect to δ_{iso}, while the span can only be positive.

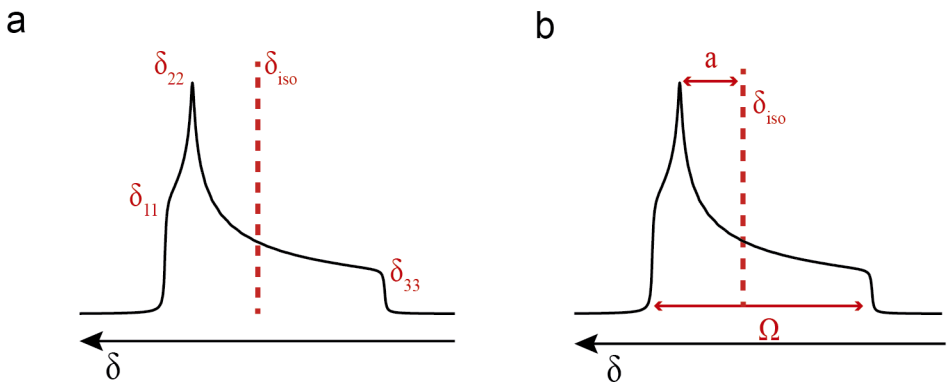

Figure 2.5. Schematic static lineshape for a spin I = 1/2 nucleus broadened by the CSA, labelled using (a) the standard convention, (b) the Herzfeld-Berger convention.

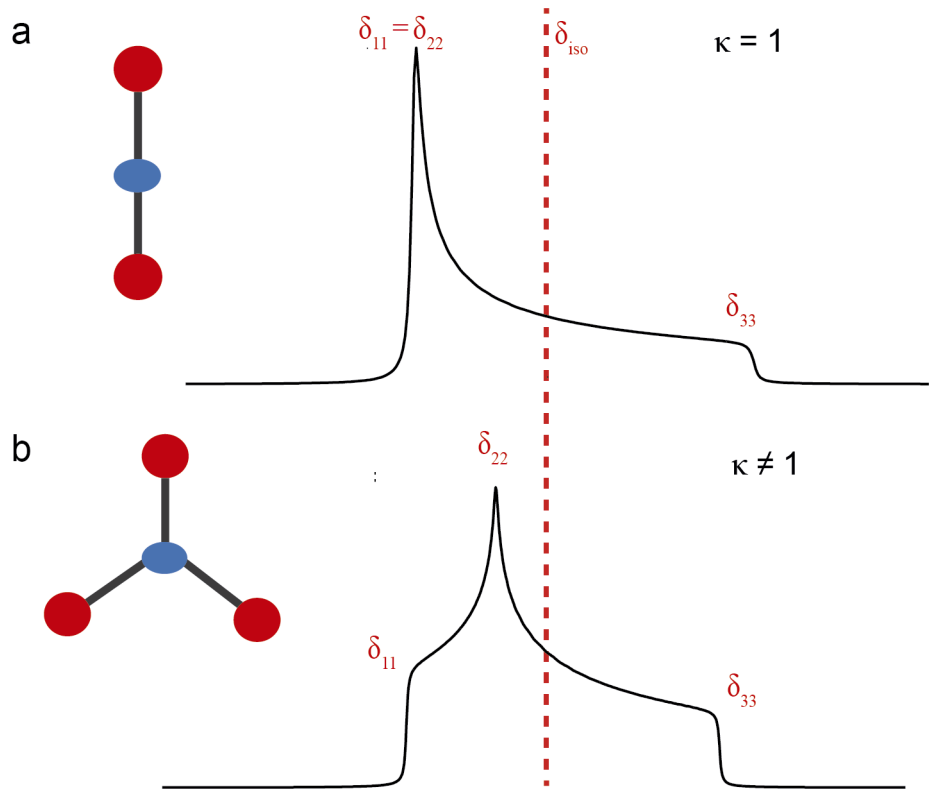

Figure 2.6. Schematic static CSA lineshapes observed for a spin I = 1/2 nucleus with (a) axially symmetry and (b) axially asymmetric shielding tensors, with parameters defined by the Herzfeld-Berger convention

The powder lineshape observed depends on the symmetry of the shielding produced and so different lineshapes can be observed for spherical, axially symmetric or axially asymmetric environments, as shown in Figure 2.6. Measurement and analysis of the CSA to establish a relationship with crystal structure has been undertaken over a number of years and several examples are known in literature.[10]

2.1.6.2 Dipolar coupling

In addition to the CSA, there are other interactions that can affect the spins. Dipolar coupling results from the interaction of one spin with the magnetic field generated by a second. This interaction is anisotropic, has no isotropic component, and takes place through space. In liquids, the dipolar coupling is removed because of the rapid tumbling of molecules. However, in solids, it is a major source of broadening of the resonances. The magnitude of this interaction depends on the gyromagnetic ratios of the spins involved (γ_I and γ_S), the distance between them (r_{IS}) and the molecular/crystal orientation respect to the magnetic field (θ_{IS}), with the dipolar coupling given by:

$$\omega_D = \omega_D^{PAS} \frac{1}{2}(3 \cos^2 \theta_{IS} - 1) \quad , \qquad [2.26]$$

where

$$\omega_D^{PAS} = -\frac{\mu_0 \gamma_I \gamma_S \hbar}{4\pi r_{IS}^2} \quad . \qquad [2.27]$$

Dipolar coupling can be homo- or heteronuclear and inter- or intramolecular but is always through space.

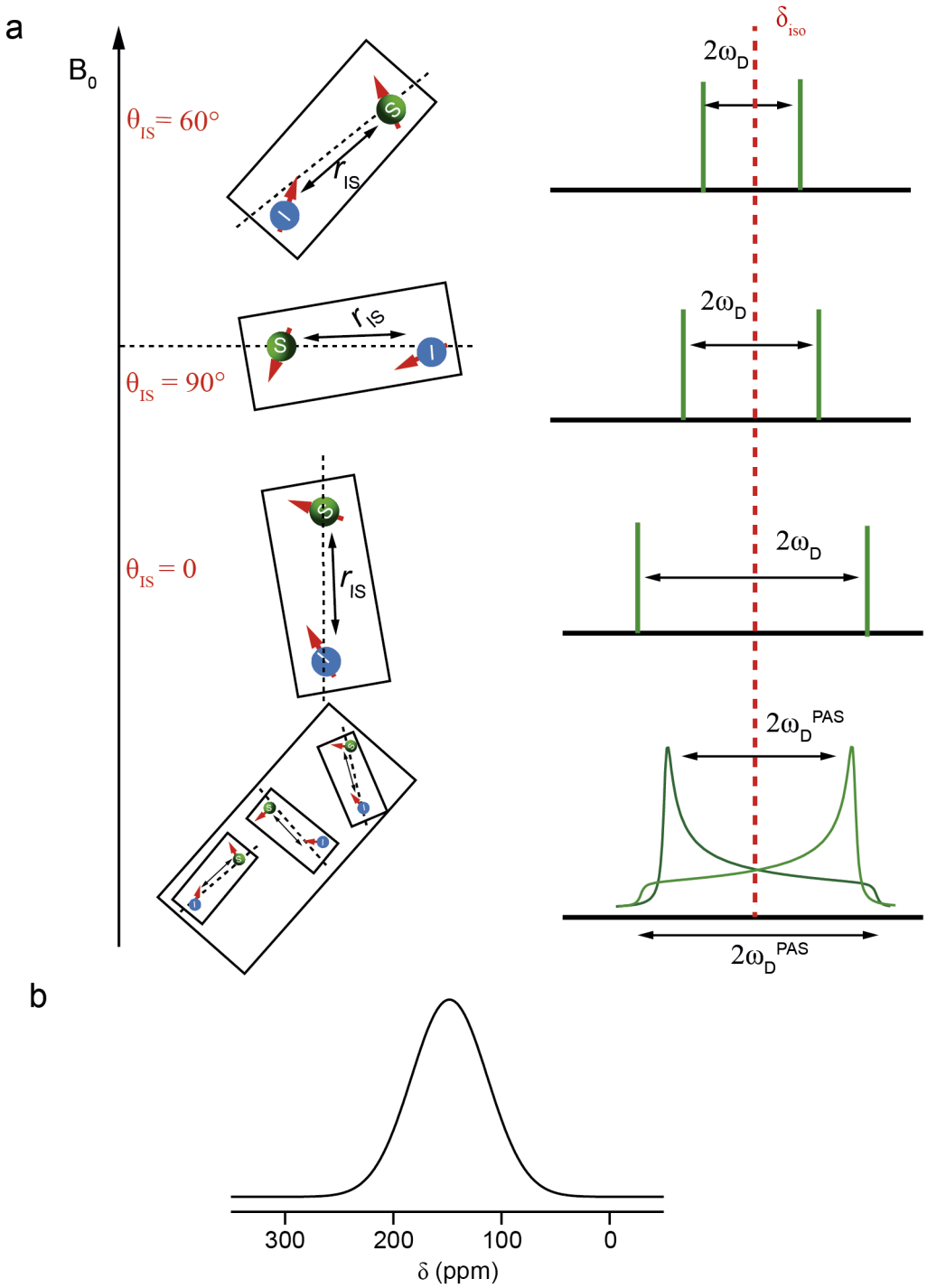

Figure 2.7. Schematic NMR spectra for (a) an isolated spin pair (with I = S = 1/2) in a single crystallite as a function of orientation and in a powdered sample. (b) Gaussian-like broadened spectrum observed for many solids with many spin pairs dipolar interactions (simulated using the Bruker program, Topspin).

The result of this interaction in a single crystallite containing an isolated heteronuclear spin pair (I = S = 1/2), is a doublet separated by $2\omega_D$, as shown in Figure 2.7a. Considering the orientation dependence of the dipolar interaction, for an isolated spin pair in a powder sample, the result is a "Pake doublet"[11] lineshape, which is composed of two superimposed powdered lineshapes with a maximum width of $2\,\omega_D{}^{PAS}$ for the heteronuclear dipolar interaction or $3\omega_D{}^{PAS}$ for the homonuclear dipolar interaction. Pake doublets are rarely observed in real solids owing to the presence of many dipolar couplings between different spin pairs, typically resulting in a Gaussian-like broadened lineshape, as shown in Figure 2.7b.

2.1.6.3 J coupling

The indirect nuclear spin-spin coupling is an electron-mediated interaction that therefore depends on the electron density between the coupled nuclei, and so is sensitive to the molecular geometry. Unlike the chemical shift, the J coupling is independent of the applied magnetic field. The isotropic part of this interaction does depend on the gyromagnetic ratios of the nuclei involved with:

$$J_{KL} = \frac{h\gamma_K\gamma_L}{4\pi^2} k_{KL} \quad , \qquad [2.28]$$

where the indirect spin-spin J coupling is expressed in terms of a reduced constant, k_{KL}, which is the derivative of the total electronic energy of the system:

$$k_{KL} = \frac{\partial^2 E}{\partial\mu_K \partial\mu_L} \quad . \qquad [2.29]$$

The indirect nuclear spin-spin coupling was believed to happen only between covalently bonded atoms. It is in fact described in literature as a "through-bond" interaction, and it was only discovered in 1960 that it can also occur between non-bonded atoms that are very close in space.[12] This non-covalent J coupling is often called a "through-space" coupling and this term will be used in this thesis for the interactions happening between formally non-bonded atoms. However, a through-space J coupling must be distinguished from a dipolar coupling, which also occurs through space, as the former is still mediated by electrons. Moreover, the J coupling has an isotropic component, whereas the dipolar coupling is purely anisotropic.

In solution-state NMR, indirect spin-spin J couplings are widely used to obtain information about nuclear connectivities and to understand bonding or weak interactions present in the molecules studied. However, in solids, these couplings are rarely resolved as they are typically much smaller than the other interactions present and often smaller than the inherent spectral linewidth.

In the simplest case, in solution-state NMR and with no relativistic effects considered, the indirect spin-spin J coupling between nuclei N and M separated by n bonds can be expressed as:

$$J^{n}_{NM} = J^{FC}_{NM} + J^{SD}_{NM} + J^{PSO}_{NM} + J^{DSO}_{NM} \quad , \qquad [2.30]$$

where the four contributions are, Fermi contact (FC), spin-dipolar (SD), paramagnetic spin-orbit (PSO) and diamagnetic spin-orbit (DSO). The spin-dipolar, paramagnetic and diamagnetic spin-orbit terms are also known as "non-contact" terms. The FC is often the dominant contribution governing the scalar J coupling and is highly sensitive to molecular

geometry, while the other terms have a weaker dependence.[13] The FC contribution is based on the spin polarization mechanism. If a nucleus A has a spin α_{nuc} (see Figure 2.8a), the spin polarization leads to a slight excess of β_{elec} spins in its vicinity. Correspondingly, there is then a build up of α_{elec} spins around the neighbouring nucleus B. If B has spin β_{nuc} it will be stabilized by the contact interaction, while if B has spin α_{nuc}, this arrangement will be destabilized. In this way, information about the spin state of a neighbouring nucleus can be transmitted to the nucleus under study.

For two coupled nuclei A = B with I = 1/2, four spin states are possible as shown in Figure 2.8b, with the four allowed transitions represented by blue arrows. This result in two doublets in the spectrum, each split by J_{AB} as shown in Figure 2.8c.

There are other contributions that affect J coupling that cannot be neglected. The PSO and DSO terms arise from the orbital motion of the valence electrons. The motion of the electrons creates electron currents around each nucleus, which results in a magnetic field, felt by the neighbouring atoms. This mechanism was discussed by Gutowsky *et al*.[14] The SD term arises from the direct interaction of the magnetic dipole of a nucleus with that of the orbital electrons inducing spin density.[15]

The sign of the indirect spin-spin J coupling constant can be either positive or negative, depending on the electronic and molecular structure and the sign of the gyromagnetic ratios of the nuclei involved. In general, if the indirect spin-spin coupling interaction stabilizes the antiparallel arrangement of the nuclear spins, then the J coupling is positive.[16]

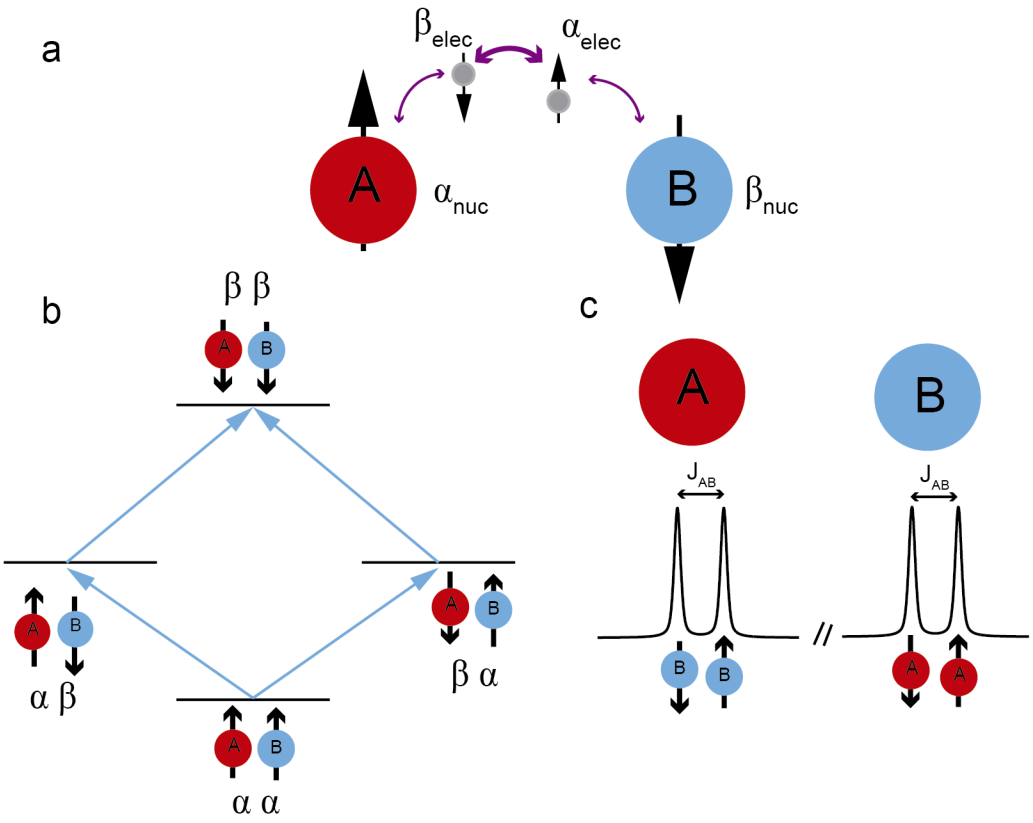

Figure 2.8. Schematic representation of (a) the Fermi contact interaction between two coupled nuclei (A = B = 1/2). (b) The energy levels of a J-coupled heteronuclear AB system, (A = B = 1/2), giving rise to four energy levels. The blue arrows show the allowed transitions. (c) The corresponding spectrum showing two doublets, one for each spin. Each line corresponds to an allowed transition, where the spin state of the passive spin (*i.e.*, the one that is not flipped in the corresponding transition) is represented.

In solution, owing to the rapid tumbling of molecules, only an average, isotropic, J coupling is observed, normally termed as J_{iso}, as mentioned previously, composed of the four different terms as given in Equation 2.30. However, in solids, where the movement is typically more restricted, the J coupling exhibits an orientation dependence, and is

described by a second-rank tensor, **J**, a 3 x 3 matrix, which contains 9 independent components :

$$\mathbf{J}^{lab} = \begin{pmatrix} J_{xx} & J_{xy} & J_{xz} \\ J_{yx} & J_{yy} & J_{yz} \\ J_{zx} & J_{zy} & J_{zz} \end{pmatrix} . \qquad [2.31]$$

As for the CSA, **J** can be defined in the laboratory frame, as shown in Equation 2.31, with the angles (θ_j, Φ_j) describing the orientation of the tensors with respect to B_0, or in its PAS. In the latter system, the diagonal term in $\mathbf{J}^{PAS}$ correspond to the principal components of the tensor (J_{11}, J_{22} and J_{33}), and the Euler angles (α, β, γ) describe the orientation of the PAS with respect to the laboratory frame. The isotropic value, J_{iso}, is given by the average of the three principal components:

$$J_{iso} = \frac{(J_{11} + J_{22} + J_{33})}{3} . \qquad [2.32]$$

The anisotropic part of the J coupling, ΔJ, and the asymmetry parameter, η_J, can be described as:

$$\Delta J = J_{33} - \frac{(J_{11} + J_{22})}{2} , \qquad [2.33]$$

and

$$\eta_J = \frac{(J_{22} - J_{11})}{(J_{33} - J_{iso})} . \qquad [2.34]$$

Unfortunately, the anisotropic part of J coupling is inseparable from the dipolar coupling and so an effective dipolar coupling must be defined as:

$$\omega_D = \omega_D^{PAS} - \frac{\Delta J}{3} . \qquad [2.35]$$

2.2 NMR spectroscopy experiments

As described in section 2.1.6, the NMR spectrum of a solid is determined by a range of interactions that provide useful information, such as connectivity, distances and the number of chemical species present. In solution, only the isotropic components are present but in solids, owing to the absence of motional averaging, the anisotropic components are also present and can provide extra information. These interactions often result in broadening and in order to achieve high-resolution spectra, as for liquids, several routine techniques are used, such as magic angle spinning, decoupling and cross polarization. The remainder of this section describes these three techniques, and also commonly-used techniques to measure interactions in NMR, such as 2D J-resolved spectroscopy.

2.2.1 Magic Angle Spinning (MAS)

The interactions present for spin I = 1/2 nuclei (*e. g.*, chemical shielding, dipolar coupling and J coupling) have an orientational dependence proportional to $(3\cos^2\theta - 1)/2$ (assuming $\eta = 0$), which becomes zero when $\theta = 54.736°$, known as the "magic" angle, shown in Figure 2.9a. If all of the crystallites could be oriented at this angle simultaneously, the anisotropic components of the chemical shift, dipolar and J coupling would vanish. However, this is not possible for a powdered sample, where all possible crystallite orientations are present. In order to achieve the same effect for all crystallites present, the sample is packed in a "rotor" (typically made of ZrO_2) which is oriented along an axis inclined at $\theta_R = 54.736°$, with respect to B_0, as shown in Figure 2.9a. The sample is then rotated rapidly (at a rate faster than the magnitude of the interactions to be removed), to achieve an

average crystallite orientation for all crystallites along the rotor axis (*i.e.,* at the magic angle). If the sample is rotated more slowly than the magnitude of the interaction that is to be removed, the powder-pattern lineshape is broken into a series of "spinning sidebands" (SSBs) that appear separated from the isotropic peak by integer multiples of the spinning rate. The effect of MAS on a lineshape broadened by the CSA can be seen in Figure 2.9b. Fast spinning not only removes the CSA, but also some of the other interactions that broaden the spectrum for spin I = 1/2 nuclei, such as the dipolar coupling and the J anisotropy, yielding a spectrum containing only the average isotropic components of the shielding and the J coupling. The maximum spinning rate that can be achieved using commercial probes is ~110 kHz, however, to achieve faster MAS rates, one must make a compromise in sample volume and, hence, in sensitivity. Available rotor sizes and maximum rotation rates are summarised in Table 2.1.

In fast MAS experiments, the sample temperature must be considered, as this will increase with increasing friction between the rotor and the drive and bearing gas flows required to achieve the MAS. This results in only few degrees change in sample temperature at ~10 kHz MAS, but can be very important at 60 kHz MAS, where the sample temperature typically rises by ~30 °C. This can be extremely important for materials where dynamic processes occur and the study of metastable polymorphs or materials. At slow MAS rates, the sideband manifold mirrors the static lineshape, whereas at intermediate spinning rates the isotropic peak becomes more intense. It is under slow MAS that the anisotropic component of the shielding, the predominant interaction for spin I = 1/2 nuclei, can be measured directly from the intensities of the sideband manifold.

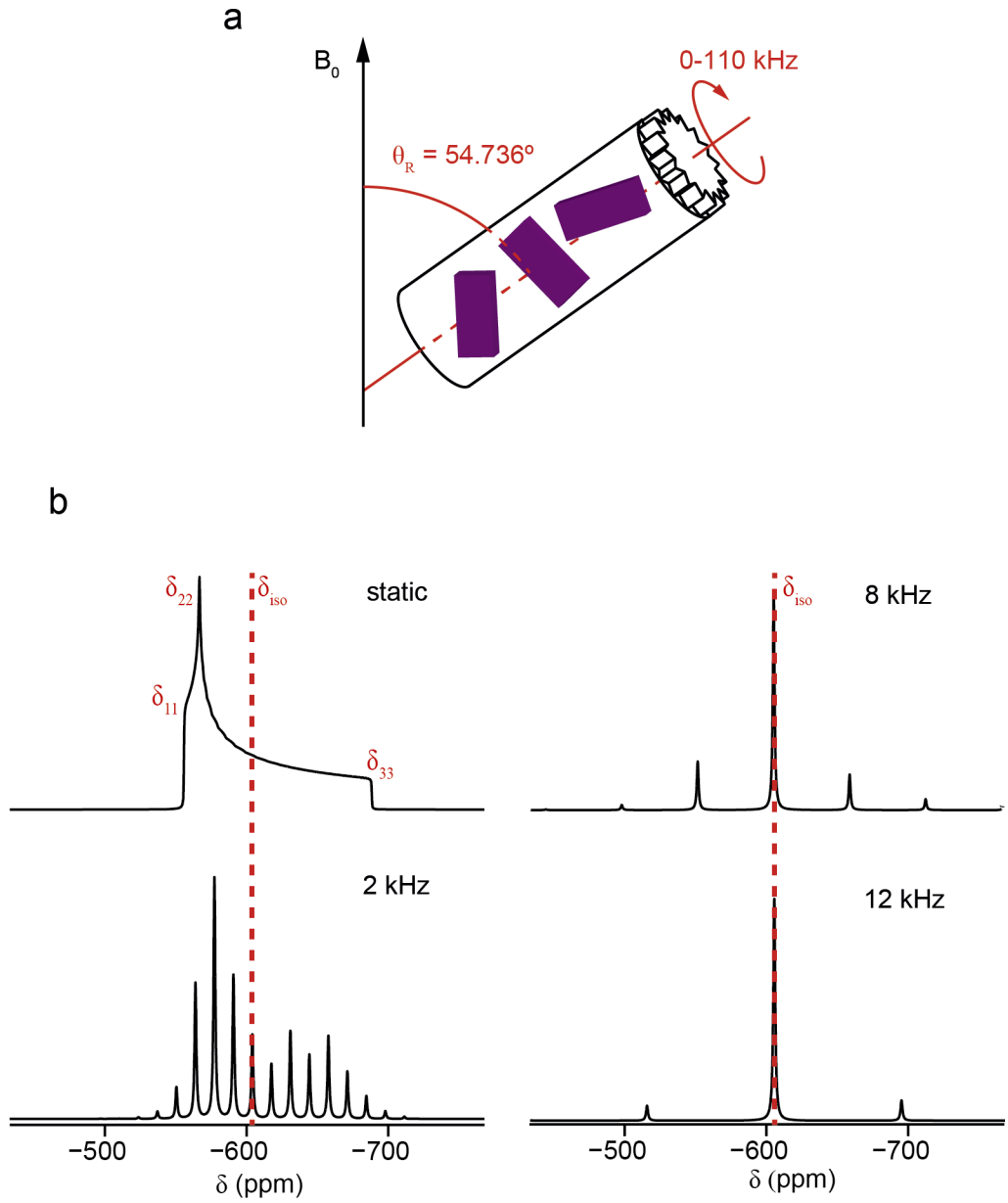

Figure 2.9. (a) Schematic representation of the MAS experiment. (b) The effect of MAS on a simulated I = 1/2 nuclei NMR spectrum, containing a lineshape broadened by the chemical shift anisotropy (CSA). The spectrum was simulated using parameters extracted from experimental ^{119}Sn MAS NMR spectra of SnO_2 (δ_{iso} = –604.3 ppm, Ω = 125 ppm, κ = 1.0 ppm and B_0 = 9.4 T)

Table 2.1. The sample volume and maximum MAS rates accessible for a range of commercially-available rotors.

Rotor diameter / mm	Maximum rotation rate / kHz	Sample volume / μl
7	~7	300–500
4	~14	50–90
3.2	~24	20–40
2.5	~35	14
1.9	~42	10
1.3	~67	1.5
1	~80	0.8
0.75	~110	0.4

Normally, the optimum number of SSBs required to successfully measured the CSA is between six and eight.[17]

2.2.2 Decoupling

Decoupling experiments are routinely used to eliminate any remaining dipolar couplings that are not completely removed by MAS (a significant source of broadening in the spectrum) and any J couplings. The heteronuclear dipolar coupling between two spins, I and S, can be removed by applying continuous rf irradiation at the Larmor frequency of I while recording the FID for spin S. The simplest decoupling sequence is

continuous wave irradiation (CW),[18] where a continuous external radio-frequency (rf) field is applied to the coupled spin, but nowadays there are more sophisticated and more efficient ways of removing dipolar couplings, using multiple-pulse decoupling schemes. One such scheme is two-pulse phase-modulation (TPPM), a decoupling scheme that consists of repeat units of two pulses with duration τ_p (typically slightly less than 180°) and phase +φ and –φ (usually values between 10 – 50°).[19] TPPM often gives the best decoupling results at the higher rf fields, assuming that rotatory-resonance recoupling conditions are avoided, by using a rf-field frequency at least three times that of the spinning speed.[20] This is feasible at slow spinning, however, at fast spinning really high power pulses would be required (*i.e.*, at 100 kHz MAS spinning, a 300 kHz decoupling field would be needed). This limits the applicability of high-power decoupling for sensitive samples that might be affected by sample heating, and for long decoupling times that might cause damage to the probe. Therefore, at fast MAS, alternative decoupling schemes have been explored, such as the use of low-power decoupling.[21] In this case, also a difference of three orders of magnitude is typically desired between the spinning and the rf-field frequency in order to avoid rotatory-resonance recoupling.[22]. However, in this case the rf field strength must be lower than the spinning frequency.

Alternatively, windowed sequences such as RS-HEPT (rotor-synchronized Hahn-echo pulse train), can be used at high MAS.[23] RS-HEPT consists of the application of a π–pulse every two rotor periods in the I channel.[24]

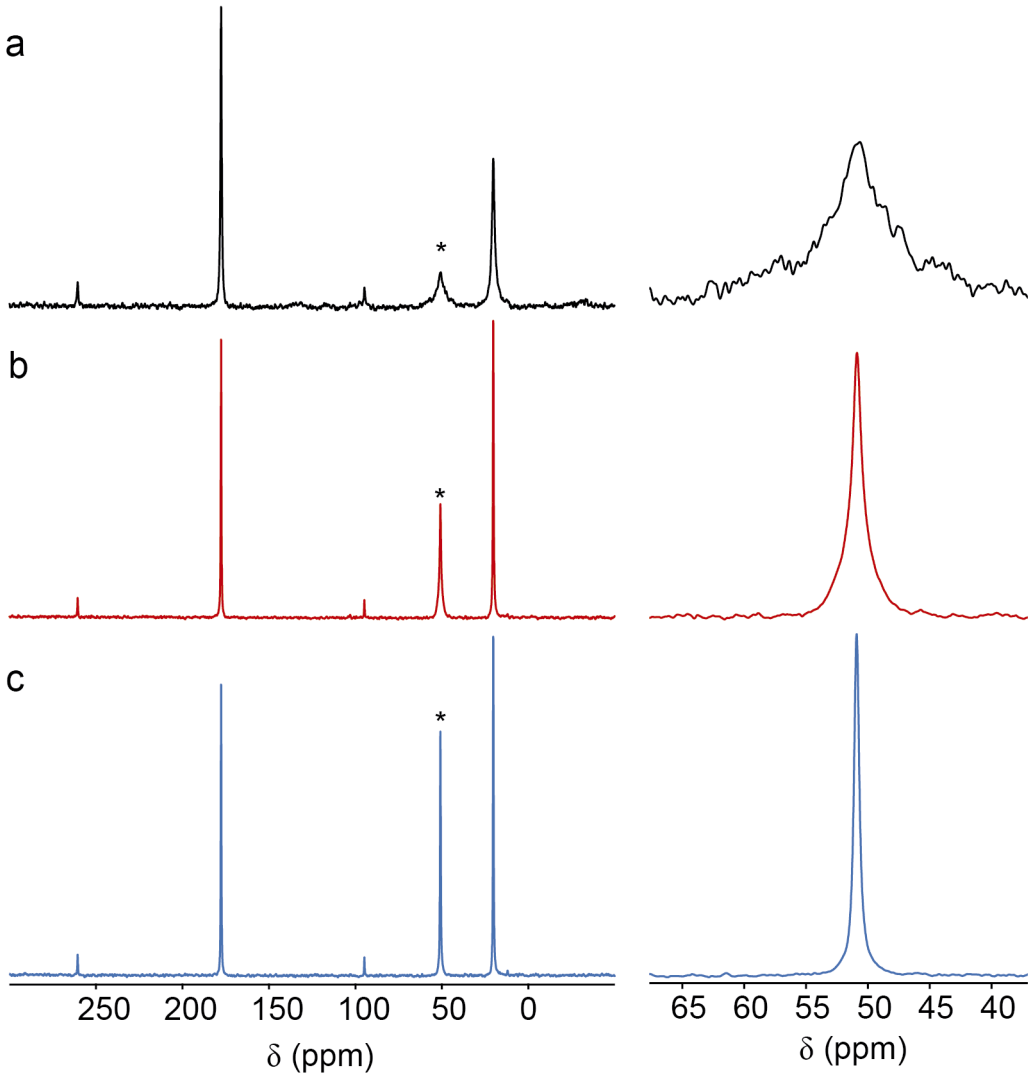

Figure 2.10. ^{13}C (14.1 T, 12.5 kHz) Cross Polarization (CP) MAS NMR spectra of L-alanine with (a) no decoupling, b) CW decoupling (ν_1 = 75 kHz) and (c) TPPM-15 decoupling (ν_1 = 75 kHz, θ = 15°). Insets showing the CH resonances (denoted in the spectra by *) are shown on the right of each spectrum.

In this thesis, CW and TPPM-15 decoupling schemes were routinely used. The effect of both sequences is shown in Figure 2.10.

2.2.3 Cross polarization

Cross polarization (CP)[25] is a routine technique typically used in combination with MAS and decoupling.[26] In contrast to these two techniques, CP enhances the sensitivity of the spectrum by the magnetisation transfer from a high-abundance, high-γ nucleus, such as ^{1}H or ^{31}P, to a "rare spin", *i.e.*, with low-abundance, and low-γ, such as ^{13}C or ^{77}Se. The potential repetition rate of the experiment is often increased for rare nuclei since T_1 relaxation rates for highly abundant nuclei are usually faster. In the most favourable case, assuming relaxation can be neglected, the maximum enhancement factor achieved is γ_I/γ_S (when $N_S \ll N_I$), *i.e.*, for ^{1}H and ^{13}C, the $\gamma_H/\gamma_C = 4$. However, due to relaxation processes and other imperfections, an enhancement factor closer to three is more typically achieved.

CP exploits mutual spin flips that occur between nuclei of different species. These mutual spin flips do not occur spontaneously and are induced by simultaneous irradiation of both nuclei. The pulse sequence for CP is shown in Figure 2.11a and consists of a 90° pulse applied to spin I (high abundance nucleus) to create the maximum transverse magnetisation, followed by a continuous irradiation for both spins to "lock" the magnetisation along the axis, while the magnetisation transfer takes place during a "contact time". Transfer only occurs if the Hartmann–Hann condition,[25] is fulfilled, where:

$$\gamma_I B_{1I} = \gamma_S B_{1S} \quad . \qquad [2.36]$$

Under MAS conditions, Equation 2.36 must be modified to

$$\gamma_I B_{1I} = \gamma_S B_{1S} \pm n\omega_R \quad , \qquad [2.37]$$

where ω_R is the spinning rate and n is an integer (typically 1 or 2).[27]

After the magnetisation transfer takes place during the contact time, the rf is turned off on the S channel in order to record the FID, while some irradiation (*i.e.,* decoupling) normally continues on the channel I to remove the heteronuclear interactions.

The CP transfer efficiency depends on the heteronuclear dipolar coupling network and therefore is distance dependent ($\propto r_{IS}^{-3}$). The magnetisation builds up during the "contact time", which is normally chosen to maximise the transferred signal intensity. This build up of magnetisation depends on the transfer rate (proportional to the dipolar coupling and therefore the distance between the spins), and the relaxation rate of each type of spin during the spin-lock pulses (described by a time constant $T_{1\rho}$). The transfer rate results in faster magnetisation build up for those S spins that are closer in space to I spins, *e.g.*, magnetisation builds up more quickly for CH than quaternary carbons. The relaxation rate can result in a slow decay (long $T_{1\rho}$), or fast decay (shorter $T_{1\rho}$) depending on the sample studied, with longer $T_{1\rho}$ usually enabling greater signal build up. Although, different CP contact time experiment can help in the assignment of the spectrum, by intensity variation to identify chemically-different species, it must be noted that CP is non-quantitative, as a consequence of the dipolar coupling dependence. Therefore, care must be taken when considering the relative intensities of chemically-different species in a CP spectrum. As an example, the ^{1}H-^{13}C CP MAS NMR spectra of naphtho[1,8-cd]1,2-dithiole (structure shown in Figure 2.11b) with different contact times are shown in Figure 2.11c.

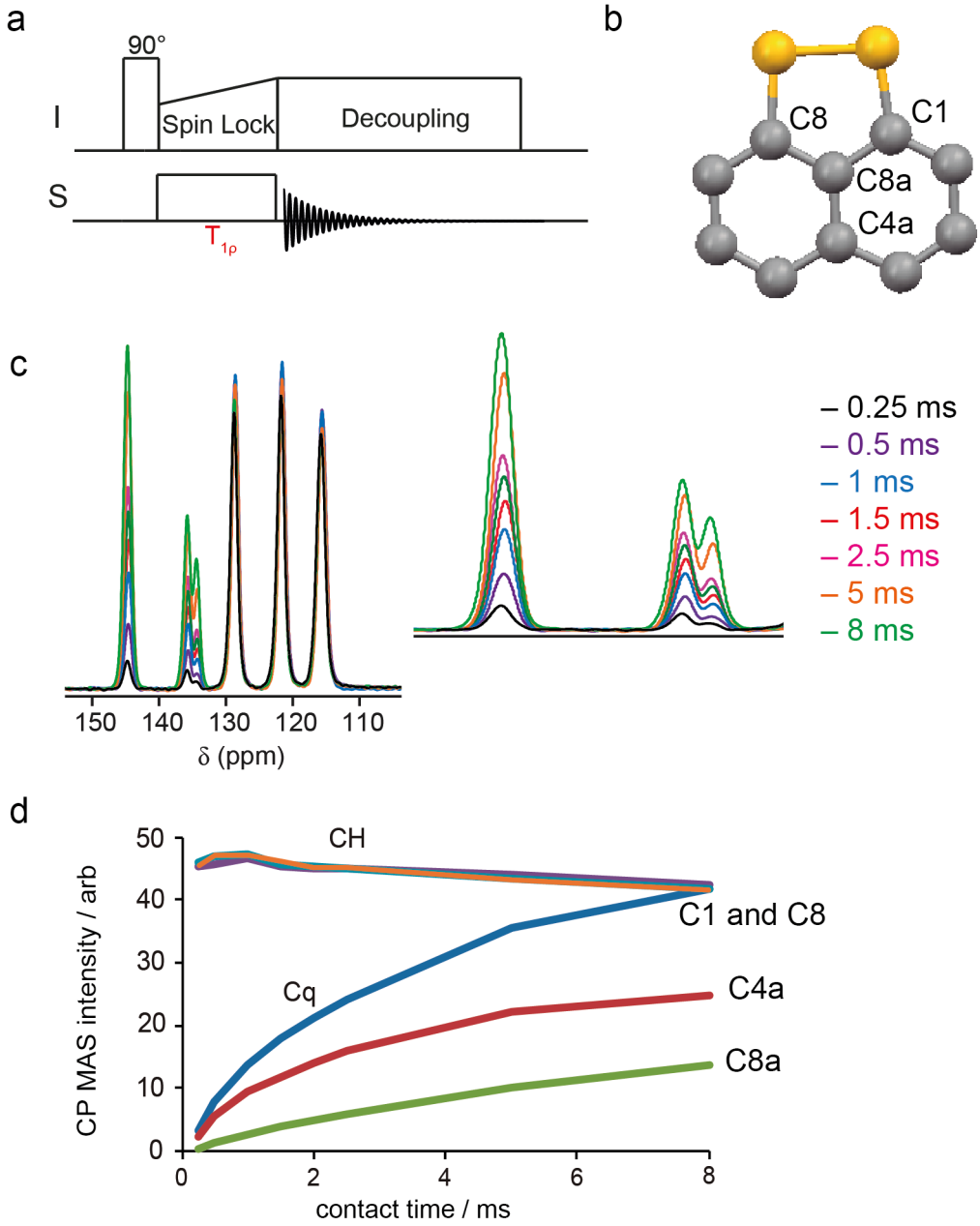

Figure 2.11. (a) A basic CP pulse sequence. (b) The structure of naphtho[1,8-cd]1,2-dithiole with sulfur and carbons atoms represented by yellow and grey spheres, respectively. Hydrogen atoms were omitted for clarity. (c) ^{13}C (14.1 T, 12.5 kHz) CP MAS NMR spectra of naphtho[1,8-cd]1,2-dithiole acquired at different contact times. (d) Plot of integrated peak intensities for each signal in the ^{13}C CP MAS spectra of naphtho[1,8-cd]1,2-dithiole as a function of contact time.

As the contact time increases, the magnetisation slowly builds up for quaternary carbons (Cq), due to the lack of surrounding protons. In contrast, CH species exhibit a maximum of intensity at shorter contact times, around 1 ms, with a subsequent decrease as a consequence of $T_{1\rho}$ relaxation, shown in Figure 2.11d. Furthermore, Cq (blue, red and green lines) can be differentiated in the spectra as shown in Figure 2.10d. The blue line corresponds to the two carbons directly bonded to sulfur, which explains the higher intensity in the spectra in comparison to the other two Cq (red and green lines, where only a single species is present). The signal shown in green line builds up more slowly than that shown in red line, due to the proximity of ^{13}C to ^{1}H. The carbon corresponding to the red line is closer in space to the nearest protons, while the carbon contributing to the green line is further away, which results in less efficient magnetisation transfer at short contact times.

At fast MAS rates the magnetisation transfer becomes more difficult as the dipolar coupling is partially removed by MAS. Several methods are available to improve the cross polarization efficiency at high spinning rates, including the use of amplitude-modulated contact pulses. A "ramped" pulse (*i.e.*, where the I spin rf field strength is varied during the contact time) improves efficiency considerably.[28] This ramped pulse (typically from 90 – 100 % strength) is used routinely for the acquisition of ^{13}C, ^{77}Se and ^{125}Te CP MAS NMR spectra in this thesis.

2.2.4 Spin-echo and relaxation measurements

The spin-echo effect was first discovered by Hahn, with two 90° pulses, separated by a short delay, leading to the detection of an echo signal (*i. e.*, signal at a delayed time in acquisition).[29] A variation of this technique was introduced by Carr and Purcell, who utilised a 180° pulse in place of the second 90° pulse in the sequence. This technique is now commonly known as a spin echo.[30]

The spin-echo pulse sequence is shown in Figure 2.12a. Transverse magnetisation is created by the 90° pulse, followed by an echo delay, denoted $\tau/2$, allowing the spins to precess. Inhomogeneous effects can cause different spins in the same sample to precess at different frequencies. After that, a 180° pulse is applied and the magnetisation is again allowed to evolve for the same echo delay, enabling all the inhomogeneous effects and the offset to be refocussed, before the NMR signal is detected and Fourier transformed to give the NMR spectrum. The evolution under an offset in a spin-echo sequence is illustrated in Figure 2.12b.

The longitudinal relaxation constant, T_1, can be measured using two different techniques, saturation recovery or inversion recovery experiments. Pulse sequences for these techniques are shown in Figures 2.13a and 2.13b, respectively. The inversion recovery experiment consists of a 180° pulse, where the magnetisation is inverted to lie along the –z axis. A delay, τ_{rec}, is then applied, followed by a 90° pulse. For short delay, no relaxation occurs and a signal with negative intensity is observed. As the delay increases the signal intensity passes through zero and eventually becomes positive.

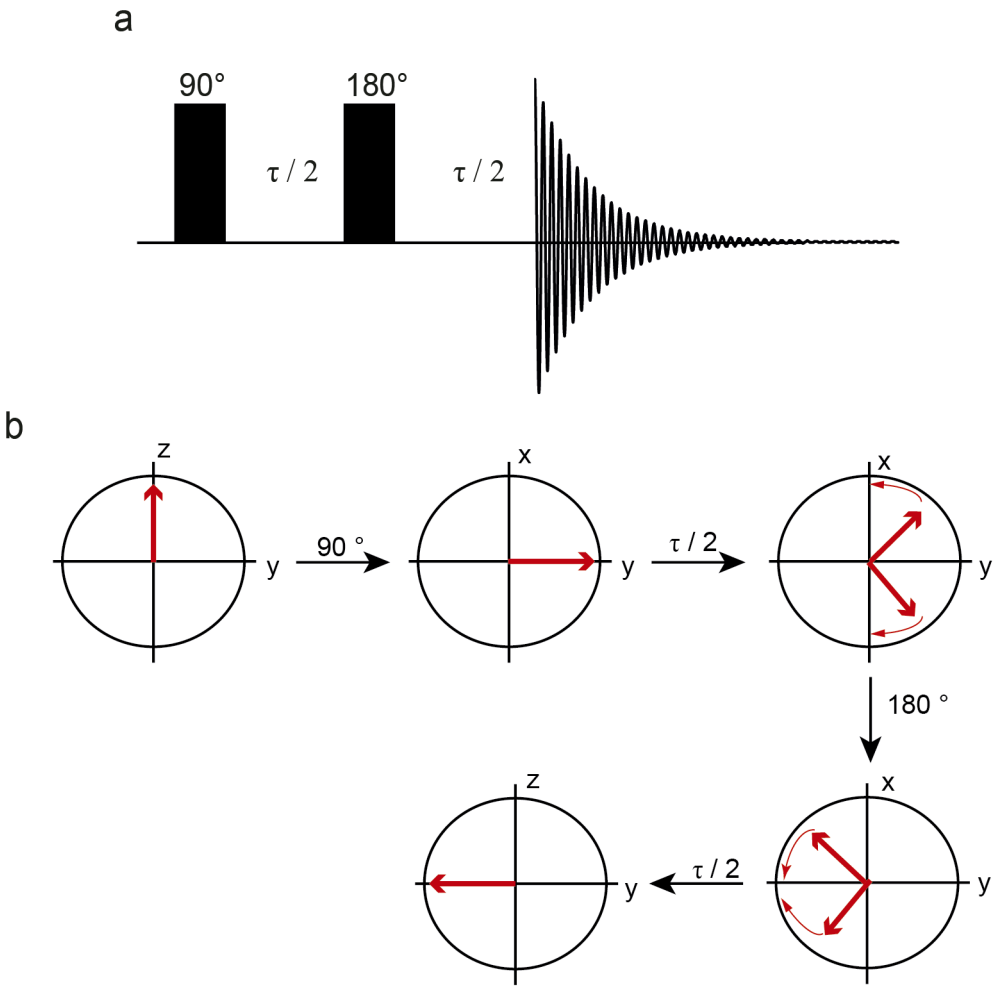

Figure 2.12. (a) Pulse sequences for spin echo. (b) Illustration of the refocussing of the offset using this sequence.

By acquiring signals from $\tau_{rec} = 0$ to suitable values of τ_{rec}, a plot of $M(\tau_{rec})/ M_0$ against τ_{rec}/T_1 can be constructed, and T_1 values can be measured by iterative line fitting, as shown in Figure 2.13c, following Equation 2.38.

$$M(\tau_{rec}) = M_0\left(1-2e^{-\frac{\tau_{rec}}{T_1}}\right) . \qquad [2.38]$$

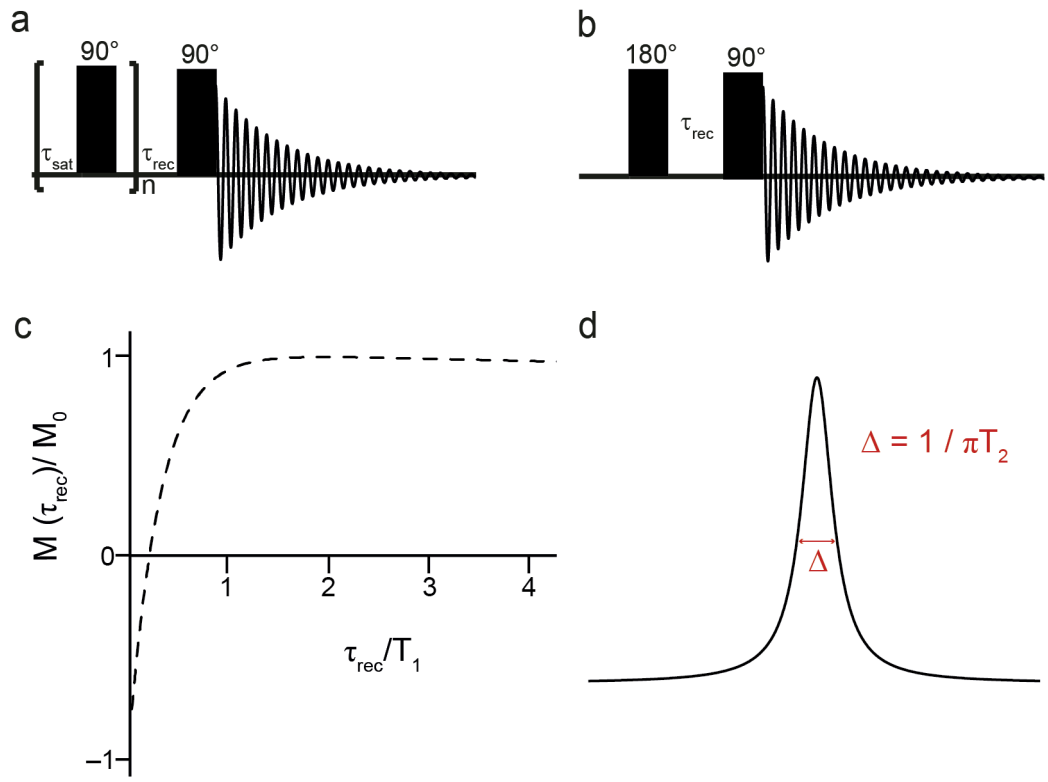

Figure 2.13. Pulse sequences for (a) saturation recovery and (b) inversion recovery experiments. (c) Schematic representation of the signal intensity in an inversion recovery experiment used to measure T_1. Magnetisation recovery ($M(\tau_{rec})/ M_0$) is plotted as a function of the delay, τ_{rec}/T_1 (d) Schematic representation of the relationship between T_2 and the half linewidth Δ for a Lorentzian peak in the liquid state.

Inversion recovery typically provides a more accurate determination of T_1 in comparison to saturation recovery approaches. However, saturation recovery is strongly recommended for compounds with long T_1 times as, in inversion recovery, the magnetisation must be returned to thermal equilibrium ($+M_z$) at the beginning of each transient.

For magnetisation to be restored, there must be an interval equal to the largest τ_{rec} (normally >5 T_1) between transients, making the experiment suitable for samples with short T_1 but very long for samples with longer T_1. In this case, saturation recovery experiment are normally used, which consist of a train of pulses to saturate the magnetisation, followed by a delay that is then varied, allowing relaxation of the system back to thermal equilibrium. A 90° pulse is then applied and transverse magnetisation is created and measured. T_1 can then be determined by plotting the magnetisation recovery as a function of the delay, τ_{rec}, as shown in Equation 2.39.

$$M(\tau_{rec}) = M_0\left(1 - e^{-\frac{\tau_{rec}}{T_1}}\right) . \qquad [2.39]$$

Transverse relaxation, defined by T_2, is the loss of magnetisation in the xy plane. The magnetisation follows a free induction decay in the form of

$$M = M_0\left(e^{-\frac{\tau}{T_2}}\right) . \qquad [2.40]$$

In principle, T_2 can be obtained by direct analysis of the linewidth, Δ, as shown in Figure 2.13d.

$$\Delta = \frac{1}{\pi T_2} . \qquad [2.41]$$

However, in practice, inhomogeneities from either B_0 and/or B_1 can cause the loss of transverse magnetisation and can therefore contribute to apparent T_2 rates, which can complicate the direct analysis of T_2. The

apparent transverse relaxation and half linewidth are defined by Lesage *et al* as T_2* and Δ*, respectively.[31]

An alternative method for measuring T_2 is the CPMG (Carl-Purcell-Meiboom-Gill) experiment,[32] which employs a train of 180° pulses in acquisition. This is a very reliable method, as the spin echoes refocus the effects of inhomogeneities in the B_0 and B_1 magnetic fields. T_2' is now defined as the transverse relaxation that can be measured in a spin echo measurement. In liquids, $T_2 = T_2'$, as all inhomogeneities are refocused. However, in solids, this is not usually possible owing to non-refocusable interactions, such as high-order terms of the heteronuclear dipolar interaction, that contribute to T_2'.[31] This typically results in $T_2 \geq T_2' > T_2$* in solids, making the linewidth a poor indicator of the true T_2.

2.2.5 Two-dimensional correlation experiments

In a two-dimensional NMR experiment, the signal is recorded as a function of two time variables, t_1 and t_2, and the resulting data must be Fourier transformed in both dimensions to yield the spectrum as a function of two frequency variables.[33] 2D NMR pulse sequences involve a first period termed preparation, where the transverse magnetisation is created, often by a 90° pulse or perhaps by CP, followed by a second period, or evolution, where the magnetisation is allowed to evolve during t_1. A mixing period, consisting of further pulses can then be applied before a final detection period where the signal is recorded in t_2.

2.2.5.1 Two dimensional J-resolved spectroscopy

In liquids, the J coupling can be easily extracted from the splitting present in conventional NMR spectra or by using 2D experiments. However, in solids, J couplings are often not resolved owing to the broadening arising from the other interactions present, and it is in those cases, where, 2D "J-resolved" spectroscopy represents a useful approach for the measurement of these interactions. In fact, this technique has been successfully applied to study J couplings in a range of solids including disordered materials,[34] metabolites[35] or inorganic materials.[36] These interactions, studied by J-resolved spectroscopy, can be homonuclear or heteronuclear,[37] and can be between pairs of I = 1/2 nuclei,[38] between a quadrupolar nucleus and a spin half nucleus[39] or even between a pair of quadrupolar nuclei.[40]

J-resolved spectroscopy is based on the spin-echo sequence described in section 2.2.4, but has the advantage of being able to separate the chemical shift from the J coupling information in different dimensions. This allows an improvement in resolution due to the separation of overlapping multiplets that can make spectral analysis difficult and, it can also improve the resolution of multiplets that can not be observed in the conventional spectrum. Moreover, a further gain in resolution in the indirect dimension, F_1, can be achieved using this technique, as the spin-echo suppresses the effects of the B_0 inhomogeneity, giving F_1 linewidths that approach the natural limit of $1/\pi T_2'$.[41]

The pulse sequence for a homonuclear J-resolved experiment is shown in Figure 2.14a and comprises 90° – ($t_1/2$) – 180° – ($t_1/2$) –acquisition. The delay, $t_1/2$, is incremented in order to create an indirect time axis for the second dimension. This delay must be an integer multiple of the sample rotation period, otherwise additional modulation effects are

introduced by the CSA.[42] The pulse sequence for the heteronuclear experiment, the 2D J-resolved experiment, comprises:

S – 180° –

I 90° – (t_1/2) – 180° – (t_1/2) – acquire,

where broadband decoupling is normally used during the FID, to remove the multiplet structure from the direct dimension (F_2). A decoupled spectrum in F_2 is then obtained, while the J coupling information can be observed in the indirect dimension (F_1). In the 2D homonuclear J-resolved experiment, decoupling during the FID is not possible. However, for weakly coupled spin systems, a similar effect to the heteronuclear case can be achieved by tilting the 2D data.[41] As an example, the tilting effect for a homonuclear 2D J-resolved spectrum for a AX-AX_2 spin-system, for which the conventional spectrum for the A spin, is shown in Figure 2.14b, is given in Figure 2.14c.

The J coupling information can also be obtained by monitoring the J-modulated curve as a function of the echo delay. Analysis of the effect of spin echo modulation by homonuclear J couplings under MAS in solids for isolated spin 1/2 pairs, has been investigated in great detail.[41] In this particular case, a complex spin-echo behaviour is expected as a consequence of the dependence of the modulation upon the J coupling, the CSA tensors and the dipolar coupling interactions as well as their mutual orientations. For solids, a "z-filter" (consisting of 90° – τ – 90° sequence) is inserted prior to acquisition in the 2D homonuclear J-resolved experiments in order to obtain a phase-pure lineshapes.[43]

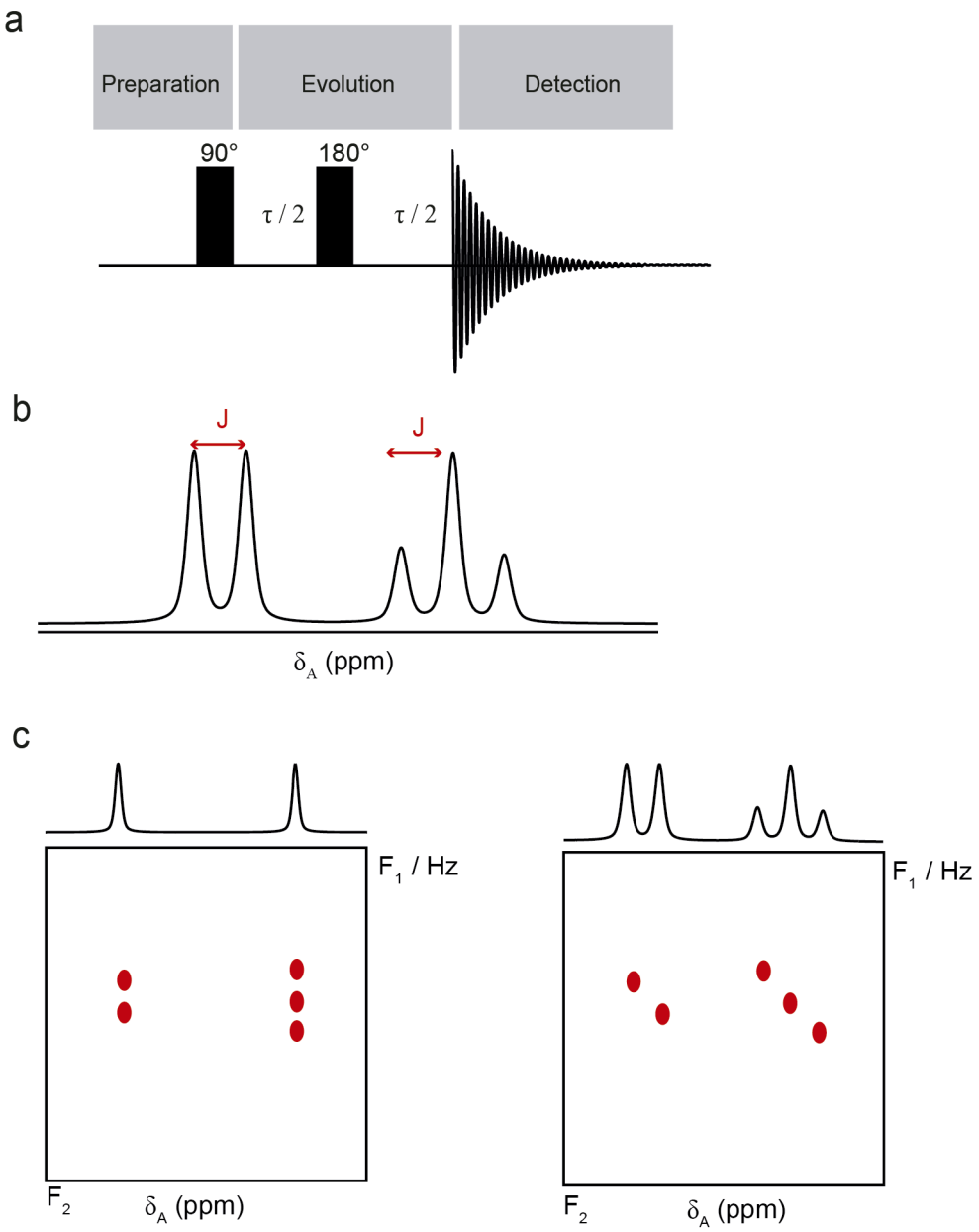

Figure 2.14. (a) Schematic representation of the pulse sequence for a homonuclear 2D J-resolved spin-echo experiment. (b) Schematic NMR spectrum for an AX-AX_2 spin-system and (c) schematic representation of a heteronuclear 2D J-resolved spectrum for an AX-AX_2 spin-system with (left) and without (right) broadband decoupling.

2.3 An introduction to X-ray crystallography

X-ray crystallography is a non-destructive technique widely used for the structure determination of a variety of solids, ranging from inorganic and organic materials to biological macromolecules, proteins and viruses.[44] This technique provides insight into the atomic-scale structure and specific arrangements of the atoms in the crystal, which is typically repeated in building blocks in three-dimensional space. The smallest building block, which contains all of the structural information required to produce a structure, is the asymmetric unit. Symmetry operations on the asymmetric unit yield the unit cell, which can reproduce the whole crystal by translations in three dimensions. The wavelength of the X-ray radiation employed in crystallography is of the same order of magnitude as the inter-atomic distances, which makes it an excellent tool for studying internal structures. Crystallography provides information on bond lengths and angles, torsion angles, non-bonded distances and packing of molecules. This information can be useful in the understanding of weak interactions, but the technique has limitations, and is often used in combination with more localized techniques such as NMR spectroscopy, which can provide useful complementary information on the local structure.

2.3.1 Unit cell and Bravais lattice

The primitive unit cell can be defined as the smallest repeating unit that can reconstruct the whole crystal simply by translation along the three crystallographic axes, a, b and c. There are four types of lattice centering, depending on the position of the lattice points in the cell.

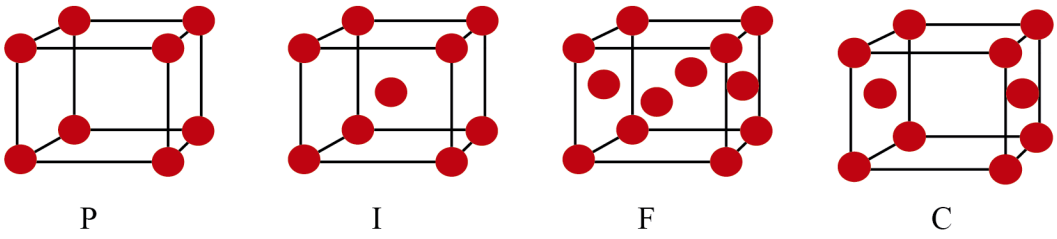

Figure 2.15. The four different lattice types, P (Primitive), I (Body centered), F (Face centered) and centered on a single face (A, B, C). Lattice points are represented by red spheres.

These are: primitive (P), Body centered (I), Face centered (F) and centered on a single face (A, B or C centering), as shown in Figure 2.15. To define the crystal systems, six parameters are used, three defining distances within the three dimensions (a, b and c) and one for each angle (α, β, γ). These angles define the relative orientations of the lattice vectors.

In three-dimensional space, there are 14 Bravais lattice arising from the combination of the seven crystals systems (cubic, tetragonal, orthorhombic, hexagonal, monoclinic, triclinic and trigonal) with the lattice centering. Note that not all types of lattice centering are possible in all of the crystal systems, yielding 14 conventional Bravais lattices rather than 28, as summarised in Table 2.2.

To describe the symmetry operations within a crystal, two types of symmetry elements can be used: point group symmetry and space group symmetry. Point group symmetry defines the elements of symmetry present in the unit cell, such as reflections, rotations and inversions; while space group symmetry takes into account elements that involve lattice translation, such as screw axes and glide planes, in a certain lattice system.

Table 2.2. The seven crystal systems with their conventional lattice types.

Crystal system	Lattice types	Cell lengths	Cell angles
Triclinic	P	$a \neq b \neq c$	$\alpha, \beta, \gamma \neq 90°$
Monoclinic	P C	$a \neq b \neq c$	$\beta \neq 90°$ and $\alpha,\gamma = 90°$
Orthorhombic	P I C F	$a \neq b \neq c$	$\alpha = \beta = \gamma = 90°$
Hexagonal	P	$a = b \neq c$	$\alpha = \beta = 90°$ and $\gamma = 120°$
Trigonal	R[a]	$a = b = c$	$\alpha = \beta = \gamma \neq 90°$
Tetragonal	P I	$a = b \neq c$	$\alpha = \beta = \gamma = 90°$
Cubic	P I F	$a = b = c$	$\alpha = \beta = \gamma = 90°$

[a] R (Rhombohedral)

There are 230 space groups that arise from the combination of 32 crystallographic point groups with the 14 Bravais lattices.[45]

2.3.2 Bragg´s law

In any unit cell, there are lattice planes, which are parallel planes in the three dimensions that are separated by a distance d. These planes are known as Miller planes. In order to identify each lattice plane, a set of integers are used, known as Miller indices (h, k and l).

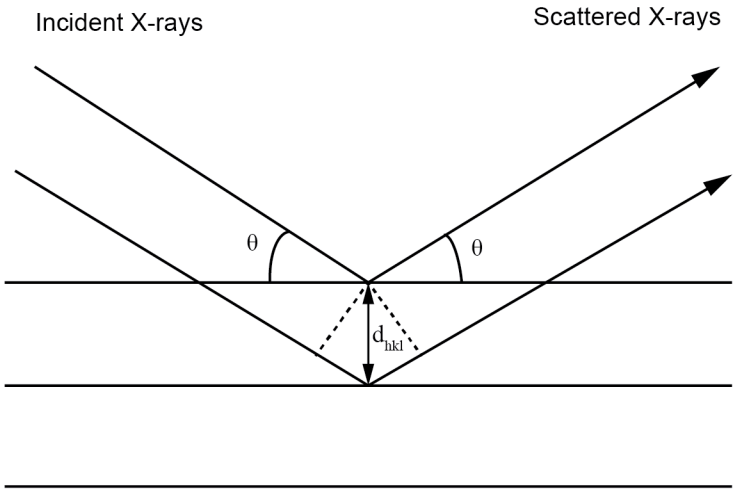

Figure 2.16. Schematic representation of radiation reflected by adjacent Miller planes, which are represented by black horizontal lines.

X-rays have a wavelength (λ) on the order of an angstrom (~1 Å), which, as previously mentioned, is similar to the inter-atomic distances in crystalline materials. When parallel X-rays hit the lattice planes at an incident angle, θ, some of the radiation is reflected with the same angle, and some radiation passes through the first plane. This radiation that passes through is then reflected by the next plane with the same angle θ.

$$2d_{hkl}\sin\theta = n\lambda \quad . \qquad [2.42]$$

The separation between both planes is d_{hkl}. If Equation 2.42 is satisfied, then the radiation is in phase and constructive interference is produced leading to a reflection following the Bragg condition, as shown in Figure 2.16.[46] This theory states the conditions for constructive interference to occur in order to obtain a diffraction pattern.

2.3.3 The reciprocal lattice

In order to understand diffraction, it is essential to understand the concept of reciprocal space. Diffraction patterns do not display the real-space reflections of a crystal, instead Fourier transformation of the real space yields the reciprocal lattice. The reciprocal lattice is a vector perpendicular to the Miller planes and the lattice parameters can be calculated from those of the crystal lattice in real space by $1/d_{hkl}$, where h, k and l represent the Miller indices.

2.3.4 Single-crystal *vs* powder X-ray diffraction

X-ray diffraction techniques can be classified into two groups, depending on the type of sample to be analyzed, *i.e,* single-crystal X-ray diffraction or powder X-ray diffraction, where the latter contains many small crystallites with all possible orientations.

In a single crystal, a general distribution of scattered density ρ(xyz) is obtained. Each reflection, represented by spots in the diffraction pattern, as shown schematically in Figure 2.17a, is associated with a scattering intensity and a phase. Normally, only the intensity can be measured. This is well known as the crystallographic *phase problem,*[47] that required different approach for the determination of the phases in order to construct the electron density map.

In the case of powder diffraction, as mentioned above, the sample is composed of a large number of small crystallites randomly oriented with respect to each other. As a consequence, only certain crystallites that fulfil the Bragg condition will diffract. The corresponding construction of reciprocal space for a powder consists of a set of nested spherical shells

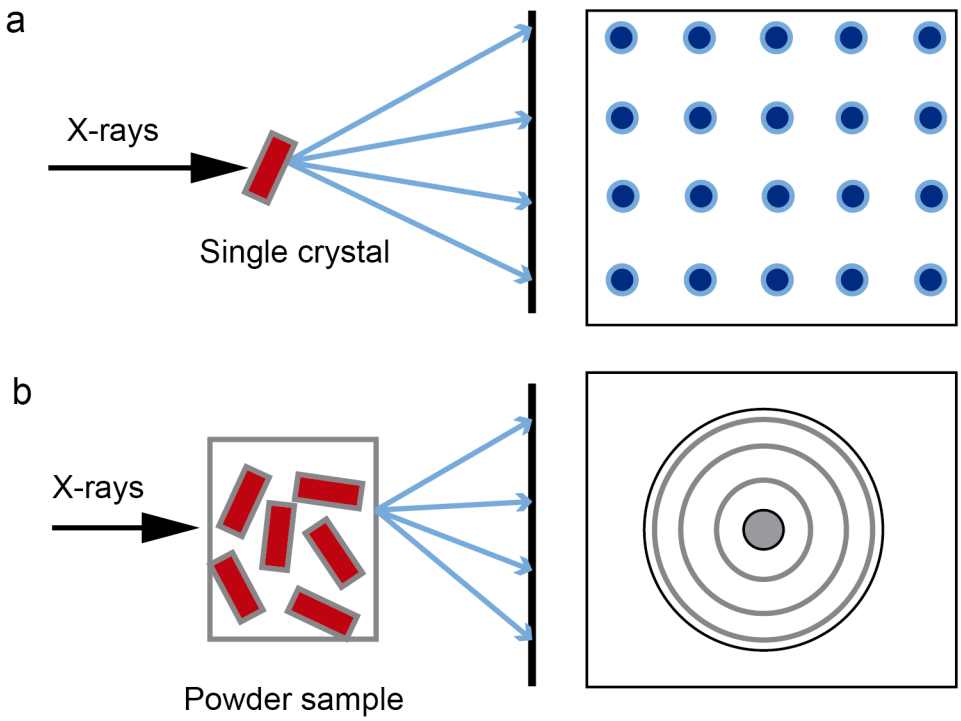

Figure 2.17. Schematic representation of the difference in (a) single-crystal X-ray diffraction and (b) powder X-ray diffraction technique.

with uniform density, centred at the reciprocal space origin, as shown in Figure 2.17b. Each shell arises from a set of reciprocal lattice planes (hkl) in the crystal, and its intensity can be measured.

Nowadays, structures can be determined using both techniques. However, the reliability is still better for single crystal diffraction than for powder diffraction, even with the advantages of the Rietveld method[48] that allows structure assignment by refining a previous or theoretical model structure. This is mostly a result of the information lost when three dimensional reciprocal lattice points are projected onto one dimensional powder diffraction pattern. Nevertheless, with the improvements in instrumentation and algorithm developments, increasingly complex structures are being solved from powder diffraction data alone.[49]

2.3.5 Types of powder X-ray diffraction diffractometers

The most common geometries that can be used for powder diffraction experiments are the reflection mode or Bragg-Bretano technique, and the transmission mode or Debye-Scherrer technique. In the reflection mode a larger amount of sample is required since the sample is packed onto a flat plate, while, in transmission mode, the sample is packed in a rotating glass capillary, and a smaller amount of sample is required. The transmission mode is, therefore, better if only a small amount of sample is available and, moreover, the problem of preferred orientation is generally avoided by using this mode. Preferred orientation or the *texture* problem occurs because certain crystallites prefer to be oriented in a certain way on a flat surface, producing a suppression of the intensities of certain reflections. Reflection mode is suitable for strongly absorbing materials while transmission mode is highly recommended for samples containing light atoms.[49]

2.3.6 Polymorphism

Polymorphism comes from the greek words *Polus*, (meaning many) and *morph*, (meaning shape), and is described as the ability of a substance to exist in different crystalline forms with a different spatial arrangement of the atoms forming the crystal lattice. Polymorphic forms can exhibit different physical properties such as colour, solubility, melting point, vapour pressure, stability, density and reactivity, amongst others, and these properties can be directly connected to the final use of the substance.

Polymorphism has a real impact in those areas where the final application of the materials will depend directly on their properties, as is the case in the pharmaceutical, pigment, agrochemical, explosive and fine

chemical industries.[50] This is the case for active pharmaceutical ingredients (APIs), which is the active part of a certain drug. The efficiency of these drugs is determined by their bioavailability, which is a measure of the quantity of drug that achieves systemic circulation. This bioavailability depends on the solubility and stability of the drug, and is often related to the polymorphic form of the drug. If the drug has low solubility, poor efficiency will be expected for that drug; in contrast, if the drug has higher solubility than intended, side effects may appear.[51] Therefore, it is crucial to study and understand all the possible polymorphic forms that a substance can form in order to be able to control the formation of a specific polymorph.

As well as crystalline forms, amorphous phases can also exist, which are defined by the lack of long range order present in the material, as shown in Figure 2.18. Characterisation of amorphous phases, by X-ray diffraction, is rather challenging since none or few of the crystallites might exhibit the conditions required for diffraction. Solid-state NMR has been widely used, especially in combination with density functional theory (DFT) to study these materials.[52] In some cases, a model structure can be obtained by combination of these two techniques for samples where no crystal structure is available. In some cases, solvent molecules can co-crystallise with the crystal, forming a solvate, as shown in Figure 2.18. This is a pseudo-polymorph since the solvent molecules can adopt regular positions in the crystal structure.

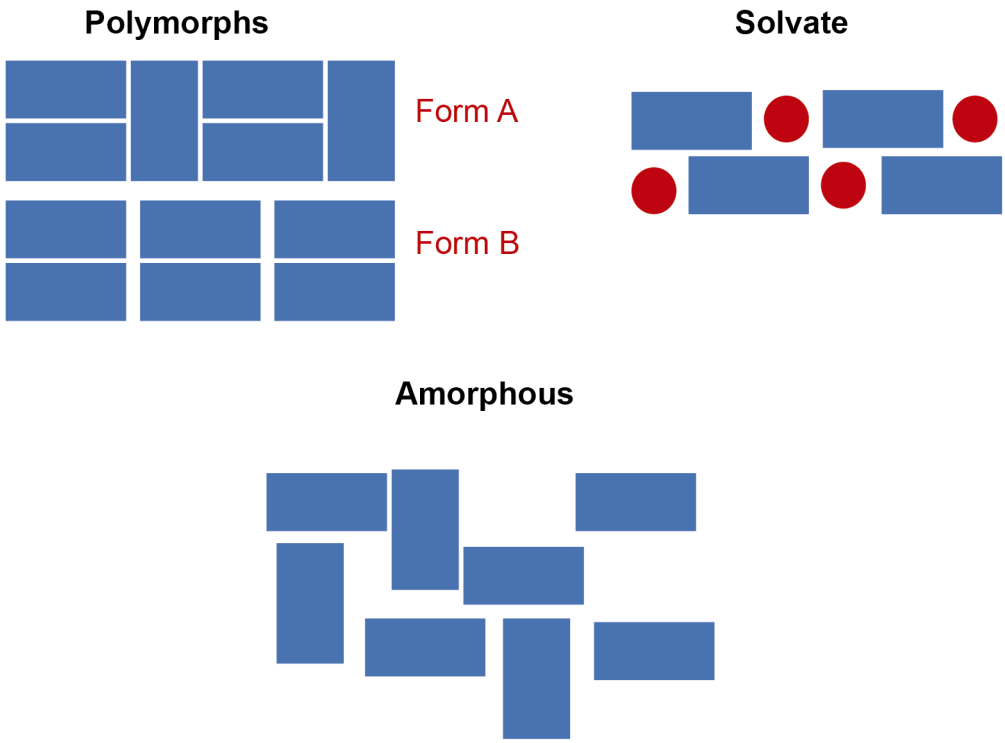

Figure 2.18. Schematic showing of different types of solid compound in nature presenting different molecular arrangements. The blue rectangles represent the molecules and the red spheres solvent molecules.

All polymorphic forms have, in principle, different energy due to the different molecular arrangements. Normally, a single thermodynamically stable polymorph is formed and the rest of the polymorphic forms are metastable. Over time, the metastable phase can transform into the thermodynamically stable one, unless the energy barrier is too high, allowing in such cases, the coexistence of several metastable phases.

Two types of polymorphism are known, a monotropic system, where one polymorphic form is always more stable, independent of the temperature, and an enantiotropic system, where one polymorph is more stable until a certain temperature and then the stability is inverted. The controlled formation of a specific polymorph remains challenging, as knowledge is required not only of all the possible polymorphic phases of a substance, but also their thermodynamic stability and the possible phase transitions between metastable phases.

Computational techniques, such as crystal structure prediction[53], can be an advantage in this area, as they can predict possible polymorphs that can exist, based on possible packing arrangements in reasonable space groups. However, this normally leads to many predicted crystal structures that are not observed experimentally. These methods are also restricted to rigid molecules and to properly account for kinetics is still a challenge. Nevertheless, this molecular modelling method represents a complementary technique for the understanding of polymorphism and could lead to the discovery, or identification of new polymorphs not yet known experimentally.

2.4 Calculation of NMR parameters

First-principles calculations have been used over the past 15 years[54] to help understand the nature and origin of NMR parameters in solids.[55] These computational methods can provide help in assigning spectra where more than one site is present due to crystal packing. They can also be useful to predict NMR parameters in order to guide NMR experiments, for example, the chemical shift range, magnitude of the J coupling or the quadrupolar interaction. In some cases, first-principles calculations can confirm the nature of an experimental observation, for example, a J coupling that could not be explained in the first instance,[56] and in some cases it can even go further and predict parameters not observable with routine techniques. Furthermore, first-principles calculations can be used to test structural models by including disorder or substitution and monitor changes in NMR parameters in order to guide the synthetic scope.[57] In molecular materials they can provide information about the dependence of NMR parameters on the local structure and can hint at the possible presence of dynamics if there are significant differences between experimental and calculated parameters.

In this thesis, a DFT approach was adopted in two different computational codes. The CASTEP code[58] was most predominantly used, as it employs periodic boundary conditions, allowing the study of extended solids. The second code employed was the Amsterdam Density Functional (ADF) code[59] used in this thesis for investigating the effects of various relativistic corrections detailed below. Some of the methodologies relevant to the calculation of NMR parameters[60] will be briefly discussed

in the following sections. For a full description of DFT and computational calculations, which is beyond the scope of this thesis, see reference 1b.

2.4.1 First-principles calculations

In principle, the energy of the system can be determined in terms of the wavefunction of a system as a solution to the Schrödinger equation shown in Equation 2.43:

$$\hat{H}\,\Psi(R, r) = E(R, r)\Psi(R, r)\ , \qquad [2.43]$$

where $\hat{H}$ is the Hamiltonian operator, Ψ is the ground-state wavefunction, R denotes the positions of the nuclei and r the positions of the electrons. In a system composed of electrons and atoms, the Hamiltonian can be expressed as:

$$\hat{H} = -T_e - T_n - V_{ne} + V_{ee} + V_{nn}\ , \qquad [2.44]$$

where T represents the kinetic energy of the electrons (T_e) and nuclei (T_n) and V represents the potential associated with interactions between nuclei and electrons (V_{ne}), between electrons (V_{ee}) and between nuclei (V_{nn}). However, solutions to this time-dependent form of the Schrödinger equation are only feasible for few atoms.

If the difference in masses between the nuclei and the electrons are considered, then the nuclei can be thought of as static during any electron motion due to the lighter mass of the latter (2000 times even in the case of a hydrogen atom). This is known as the Born-Oppenheimer approximation[61] and simplifies the Schrödinger equation to a time-independent expression, as now the kinetic energy of the nuclei is zero

and the potential energy of the nucleus-nucleus interaction is a simple constant. The Hamiltonian given in Equation 2.44, can then be reduced to the so-called electronic Hamiltonian:

$$\hat{H}_{elec} = -T_e - V_{ne} + V_{ee} \quad . \qquad [2.45]$$

One approximation to the Schrödinger equation is Hartree Fock (HF) theory.[62] However, for solid-state systems, the many-electron Hamiltonian becomes very complicated to solve by HF theory and required high computational cost (in terms of processor power and time required) precludes the use of this theory for larger systems. Therefore, the principles of this theory will not be longer discussed in this thesis due to the size of the systems studied.

Alternatively, DFT can be used to study the ground state electronic structure of molecules and solid-state systems with a practical balance between accuracy and computational expenses. This theory was elaborated by Hohenberg and Kohn[63] and states that the ground state electron density can be used to uniquely determined the Hamiltonian operator and thus all the properties of the system. The authors proposed a functional dependency of the ground state energy on the electron density ($\rho(\vec{r})$) in the presence of an external potential V_{ext}, given by:

$$E[\rho(\vec{r})] = \int \rho(\vec{r}) V_{ext} d\vec{r} + F_{HK}[\rho(\vec{r})] \quad , \qquad [2.46]$$

where F_{HK} is the functional of the electron density defined by Hohenberg and Kohn. However, this functional is remained unknown and Kohn and Sham[64] defined instead the functional for non-interacting electrons as:

$$F[\rho(\vec{r})] = \int T_S[\rho(\vec{r})] + J[\rho(\vec{r})] + E_{XC}\ [\rho(\vec{r})]\ , \qquad [2.47]$$

where, $T_S[\rho(\vec{r})]$ represents the kinetic energy, $J[\rho(\vec{r})]$ describes the classical Coulomb interaction and $E_{XC}[\rho(\vec{r})]$ is the exchange-correlation energy, a functional that contains everything that is unknown.

The Local Density Approximation (LDA),[65] used to approximate the exchange-correlation functional, is based on the uniform electron gas. This simply means that the electron density is considered constant over a discreet volume of space, as given by:

$$E_{XC}^{LDA}[\rho] = \int \rho(\vec{r}) E_{XC} d\vec{r}\left(\rho(\vec{r})\right)\ , \qquad [2.48]$$

where E_{XC} is the exchange-correlation energy per particle of a uniform electron gas of density $\rho(\vec{r})$. As a result, LDA works well for regions where the electron density changes relatively little over space, but can not provide, for instance, an accurate description of the electronic structure near the nucleus. Better results can be obtained by using the Generalized Gradient Approximation (GGA),[66] which takes into account the gradient of the charge density, in order to account for the non-homogeneity of the true electron density. The exchange-correlation functional is now given by:

$$E_{XC}^{GGA}[\rho] = \int E_{XC}(\rho, \nabla\rho)\ \rho(r) dr^3\ , \qquad [2.49]$$

where $\nabla\rho$ represents the gradient of the charge density.

Many examples of GGA functionals are available. One functional that is widely used for solids and is routinely used in this thesis is PBE (Perdew-Burke-Ernzerhof).[67]

2.4.2 Basis sets and planewave basis set

The charge density $\rho(\vec{r})$ and the wavefunction of a system can be constructed by a set of functions used to represent the electronic orbitals. Ideally, each function represents a localized atom-centered orbital. A linear combination of atomic orbitals (LCAO) can be used to construct the wavefunction. The atomic orbitals (AO) are typically represented by Gaussian-type orbitals (GTO) or slater-type orbitals (STO). Owing to the variational principle, the more basis functions used, the more accurate is the resulting wavefunction.

For solid-state systems, where periodic boundary conditions are needed, the use of planewave basis sets is recommended as a mathematically simple basis that already incorporates periodicity. For a planewave calculation, a minimum number of planewaves is required to represent the wave function. The number of planewaves is defined by the cutoff energy, E_{cut}, which is the maximum kinetic energy of the planewave used.[54] This value is established by performing a convergence test, which entails increasing E_{cut} until there is not a significance improvement in the results.

2.4.3 Frozen-core and pseudopotential approximations

To account for the core electrons, two possible approximations are used to reduce computational cost. The frozen core approximation used in both

ADF and CASTEP calculations in this thesis and, the pseudopotential approximation used in CASTEP calculations. The frozen core approximation, assumes that the core electrons do not participate in chemical bonding and can be therefore separated from valence electrons and represented by a fixed columbic potential. The pseudopotential approximation, smooths the wavefunction of the valence electrons by neglecting the oscillations of this close to the nucleus. As a result, a lower E_{cut} can be used and therefore computational cost is reduced.

The pseudopotential approach is valid for properties that are not influenced by the core electrons, however, NMR properties are sensitive to the electronic structure around the nucleus. In order to overcome that, the projector augmented wave (PAW) introduced by Blöchl[68] is used to reconstruct the electrons of the core. This approach was adapted by Pickard and Mauri to give the gauge-included PAW (GIPAW)[53] used to calculate NMR parameters of a nucleus within a magnetic field.

2.4.4 Geometry optimization

The DFT CASTEP code[69] was used to optimise the geometry of structural models previously obtained by single-crystal diffraction, typically using the PBE (GGA) functional, ultrasoft pseudopotentials and periodic boundary conditions. The latter is used in solids to reduce the number of atoms to be computed by considering a small unit cell that will reproduce the three-dimensional structure.

Crystal structure parameters, such as unit cell dimensions and atomic coordinates were obtained in this thesis from single-crystal X-ray diffraction data. Typically the unit cell dimensions and positions of the

atoms were allowed to vary, so as to minimize the stresses and forces acting on the system, thus obtaining the ground-state structure. This was seen to provide better agreement between NMR experiments and calculation[70] and was of particular importance where disorder was present in the crystal structure.

In order to obtain accurate calculations two parameters must be considered, the cut-off energy (E_{cut}) and the *k*-point spacing. Each of these must be tested for convergence. This convergence is achieved when further increasing the E_{cut} or the number of *k*-points gives no significant improvement in the results. However, in some cases even when using the most accurate parameters, there are still differences between calculated and experimental values. This could arise from the approximations made in the calculations such as the functional used, the treatment of relativistic effects and the static nature of the calculations. The latter, could explain differences between calculated and experimental NMR parameters due to dynamics not taken into account in calculations as they are carried out on a frozen structure (0 K).[54]

2.4.5 The supercell approximation

The application of periodic boundary conditions forces periodicity upon the system studied. However, this periodicity is disrupted, in cases such as disordered materials, defects, impurities or the interaction of molecules and surfaces. In order to account for these phenomena, the so-called supercell approximation is used. This simply means that the region of interest is enclosed in either bulk material (for a defect) or vacuum (for a molecule) and the resulting model is then periodically repeated throughout space. This can be clearly visualized in Figure 2.19.

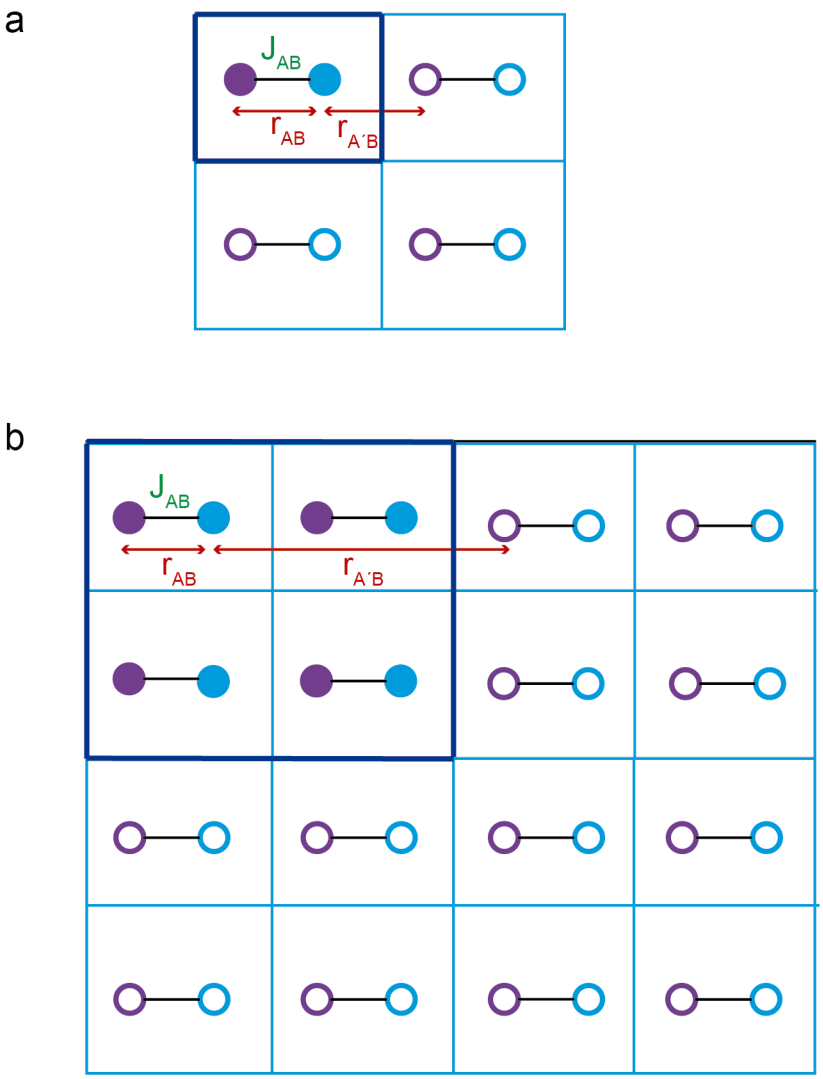

Figure 2.19. Schematic representation of (a) a unit cell where two spins A (purple ball) and B (blue ball) are coupled together by a J_{AB} and separated by a distance r_{AB}. The periodic repeated image of A, appears at a distance $r_{A'B}$ that is similar to r_{AB}. (b) A 2 × 2 supercell, where the periodic repeated image of A now appears at a much larger distance (*i.e.*, $r_{AB} << r_{A'B}$).

2.4.6 Calculation of NMR parameters

NMR calculations using the GIPAW approach implemented in the CASTEP code[53] calculate the absolute shielding tensor, **σ**, which allows the determination of the σ_{iso} as well as the principal components of the tensor, σ_{11}, σ_{22} and σ_{33}, and the anisotropy, typically expressed using the Haeberlen convention.[9]

In order to transform the absolute shielding into chemical shift, a reference shielding is needed:

$$\delta_{iso} = \sigma_{ref} - \sigma_{iso} \text{ , (assuming } \sigma_{ref} << 1) \text{ ,} \qquad [2.50]$$

where δ_{iso} is the isotropic chemical shift, σ_{ref} is the reference shielding and σ_{iso} is the isotropic shielding. δ_{iso} must be obtained experimentally for the appropriate reference material chosen for each system, and σ_{iso} is calculated by CASTEP, allowing the determination of σ_{ref} using Equation 2.50, which can then be used for other materials. Alternatively, σ_{ref} can be determined by plotting the calculated σ_{iso} *vs* the experimental δ_{iso} obtained for a series of compounds, by a simple linear regression.

In addition to the chemical shielding, CASTEP calculates the J coupling as a sum of a number of components, given by:

$$J_{Total} = J^{FC} + J^{SD} + J^{PSO} + J^{DSO} \quad . \qquad [2.51]$$

In the case of J coupling calculations, where a single "perturbing" atom has a magnetic field placed upon it, Yates *et al*[71] showed that, to avoid interaction between the perturbing atom and its periodic image, the use of a supercell approximation may be required. As such, the atom of interest is effectively modelled as a defect.

A further development that was required in the implementation of J coupling calculations was the use of Zeroth Order Regular Approximation (ZORA) relativistic treatment, described in the next section.

2.4.7 Accounting for Relativity

The study of systems that contain heavy atoms, such as selenium and tellurium, typically requires the treatment of the effect of relativity, due to the higher kinetic energy in the vicinity of the nucleus that will affect the valence and the core states. The motion of the electrons in these states begins to approach the speed of light and so the energies are affected by relativity.

ZORA is used in DFT to account for this phenomenon, which is particular important in heavy atoms. Autschbach and Ziegler developed the inclusion of scalar[72] and spin-orbit[73] ZORA treatment of relativistic effects in the Amsterdam density functional (ADF) program. Such calculations have been widely applied for solution-state NMR of molecular systems. However, the application of ZORA in solid materials must be adapted to account for a planewave-pseudopotential framework.[71]

It was not until 2014, when Yates and Green[74] incorporated the ZORA scalar-relativistic approach within the planewave pseudopotential DFT framework. This was implemented in CASTEP 8, where it is now available throughout the code and is a prerequisite for J coupling calculation. Fully relativistic effects (with the spin-orbit term) have since

been implemented in CASTEP 16.1 (released October 2015) in a limited form, but have not been implemented in GIPAW calculations.

To give some insight into the effect of spin-orbit relativity in some NMR parameters for molecules containing selenium and tellurium in closed proximity, DFT calculations were carried out using the Amsterdam Density Functional (ADF) program package.[59] The calculations were performed on an isolated molecule extracted from the optimized crystal structure. Calculations adopted the PBE exchange-correlation functional and all-electron TZ2P (triple zeta doubly polarised) basis sets for all atoms. Relativistic corrections were based on the implementation of the ZORA formalism, including scalar and spin-orbit effects.

2.5 References

1. a) D. E. Sands, *Introduction to Crystallography*, Dover Publications Inc, New York, **1969**. b) W. Koch and M. C. Holthausen, *A Chemist's Guide to Density Functional Theory. Second edition*, Wiley-VCH Verlag, Weinheim, Germany, **2001.**

2.F. Bloch, *Phys. Rev*., **1946**, 70, 460-474.

3. W. A. Anderson, "Fourier Transform Spectroscopy", *eMagRes*, John Wiley & Sons Ltd, USA, **2007**. DOI: 10.1002/9780470034590.emrstm0177.

4. S. E. Ashbrook, D. M. Dawson and J. M. Griffin, *Local Structural Characterisation*, John Wiley & Sons Ltd, Chichester, UK, **2013**, 1-88.

5. J. Herzfeld and X. Chen, "Sideband Analysis in Magic Angle Spinning NMR of Solids", *eMagRes*, John Wiley & Sons Ltd, USA, **2007**. DOI: 10.1002/9780470034590.emrstm0503.

6. R. K. Harris and A. C. Olivieri, "Spinning Sideband Analysis for Spin-1/2 Nuclei", *eMagRes*, John Wiley & Sons Ltd, UK, **2007**. DOI: 10.1002/9780470034590.emrstm0528.

7. G. Wilkinson, *Pure. Appl. Chem*., **1972**, 29, 627-636.

8. J. Herzfeld and A. E. Berger, *J. Chem. Phys.*, **1980**, 73, 6021-6030.

9. U. Haeberlen, *High Resolution NMR in Solids*, Academic Press, New York, **1976**.

10. J. K. Harper, "Chemical Shift Anisotropy and Asymmetry: Relationships to Crystal Structure", *eMagRes*, John Wiley & Sons Ltd, USA, **2007**. DOI: 10.1002/9780470034590.emrstm1013.

11. G. E. Pake, *J. Chem. Phys.*, **1948**, 16, 327-336.

12. J.-C. Hierso, D. Armspach and D. Matt, *C. R. Chim*., **2009**, 12, 1002-1013.

13. J. M. García de la Vega and J. San Fabián, *High Resolution NMR Spectroscopy Understanding Molecules and their Electronic Structures, Vol. 3*, 1st edn., Elsevier Science, Oxford, UK, **2013**, 161-207.

14. H. S. Gutowsky, D. W. McCall and C. P. Slichter, *J. Chem. Phys*., **1953**, 21, 279-292.

15. J. R. Yates, *Magn. Reson. Chem.*, **2010**, 48, 23-31.

16. R. E. Wasylishen, "Indirect Nuclear Spin-Spin Coupling Tensors", *eMagRes*, John Wiley & Sons Ltd, Canada, **2007**. DOI: 10.1002/9780470034590.emrstm0237.

17. P. Hodgkinson and L. Emsley, *J. Chem. Phys.*, **1997**, 107, 4808-4816.

18. P. Hodgkinson, *Prog. Nucl. Magn. Reson. Spectrosc.*, **2005**, 46, 197-222.

19. I. Scholz, P. Hodgkinson, B. H. Meier and M. Ernst, *J. Chem. Phys.,* **2009**, 130, 114510-114517.

20. M. Ernst, A. Samoson and B. H. Meier, *Chem. Phys. Lett.,* **2001**, 348, 293-302.

21. M. Ernst, *J. Magn. Reson.,* **2003**, 162, 1-34.

22. M. Ernst, A. Samoson and B. H. Meier, *J. Magn. Reson.,* **2003**, 163, 332-339.

23. X. Filip, C. Tripon and C. Filip, *J. Magn. Reson.,* **2005**, 176, 239-243.

24. J. M. Griffin, C. Tripon, A. Samoson, C. Filip and S. P. Brown, *Magn. Reson. Chem.,* **2007**, 45, 198-208.

25. S. R. Hartmann and E. L. Hahn, *Phys. Rev.*, **1962**, 128, 2042-2053.

26. S. Sternhell, *Org. Magn. Reson.,* **1983**, 21, 711-770.

27. B. H. Meier, *Chem. Phys. Lett.*, **1992**, 188, 201-207.

28. D. P. Burum, "Cross Polarization in Solids", *eMagRes*, John Wiley & Sons Ltd, USA, **2007**. DOI: 10.1002/9780470034590.emrstm0103.

29. E. L. Hahn, *Phys. Rev.,* **1950**, 80, 580-594.

30. H. Y. Carr and E. M. Purcell, *Phys. Rev.*, **1954**, 94, 630-638.

31. A. Lesage, M. Bardet and L. Emsley, *J. Am. Chem. Soc.,* **1999**, 121, 10987-10993.

32. S. Meiboom, D. Gill, *Rev. Sci. Instrum.,* **1958**, 29, 688-691.

33. J. Keeler, *Understanding NMR Spectroscopy*, John Wiley & Sons Ltd, 2nd edn, Chichester, UK, **2010**, 1-501.

34. P. Florian, F. Fayon and D. Massiot, *J. Phys. Chem. C,* **2009**, 113, 2562-2572.

35. C. Ludwig and M. R. Viant, *Phytochem, Anal.,* **2010**, 21, 22-32.

36. P. Thureau, G. Mollica, F. Ziarelli and S. Viel, *J. Magn. Reson.,* **2013**, 231, 90-94.

37. I. Hung, A.-C. Uldry, J. Becker-Baldus, A. L. Webber, A. Wong, M. E. Smith, S. A. Joyce, J. R. Yates, C. J. Pickard, R. Dupree and S. P. Brown, *J. Am. Chem. Soc.,* **2009**, 131, 1820-1834.

38. G. Wu and R. E. Wasylishen, *Inorg. Chem.,* **1996**, 35, 3113-3116.

39. T. Wiegand, H. Eckert, O. Ekkert, R. Fröhlich, G. Kehr, G. Erker and S. Grimme, *J. Am. Chem. Soc.,* **2012**, 134, 4236-4249.

40. F. A. Perras and D. L. Bryce, *J. Am. Chem. Soc.,* **2013**, 135, 12596-12599.

41. G. A. Morris, "Two-Dimensional J-Resolved Spectroscopy", *eMagRes*, John Wiley & Sons Ltd, UK, **2007**. DOI: 10.1002/9780470034590. emrstm0579.

42. L. Duma, W. C. Lai, M. Carravetta, L. Emsley, S. P. Brown and M. H. Levitt, *ChemPhysChem.,* **2004**, 5, 815-833.

43. S. P. Brown, M. Perez-Torralba, D. Sanz, R. M. Claramunt and L. Emsley, *Chem. Commun.,* **2002**, 17, 1852-1853.

44. C. F. Campana, *Analytical application note*. BRUKER AXS Inc., **2000**.

45. *International Tables for Crystallography,* 4th edn., **1995**.

46. W. L. Bragg, *Nature,* **1912**, 90, 410.

47. E. E. Lattman and P. J. Loll, *Protein Crystallography*, The Johns Hopkins University Press, Baltimore, Maryland, **2008**,1-152.

48. H. M. Rietveld, J. *Appl. Cryst*., **1969**, 2, 65-71.

49. W. I. F. David and K. Shankland, *Structure Determination from Powder Diffraction Data, Vol.* 64., Oxford University Press, UK, New York, **2008,** 1-331.

50. S. L. Morissette, Ö. Almarsson, M. L. Peterson, J. F. Remenar, M. J. Read, A. V. Lemmo, S. Ellis, M. J. Cima and C. R. Gardner, *Adv. Dru. Deliv. Rev.,* **2004**, 56, 275-300.

51. D. Mangin, F. Puel and S. Veesler, *Org. Process. Res. Dev.,* **2009**, 13, 1241-1253.

52. S. E. Ashbrook, D. McKay, *Chem. Commun.,* **2016**, *in press*. DOI: 10.1039/c6cc02542k

53. S. Price and L. Price, *Intermolecular Forces and Clusters I, Vol. 115*, Springer-Verlag, Berlin, **2005**, 81-123.

54. C. J. Pickard and F. Mauri, *Phys. Rev. B,* **2001**, 63, 245101.

55. C. Bonhomme, C. Gervais, F. Babonneau, C. Coelho, F. Pourpoint, T. Azaïs, S. E. Ashbrook, J. M. Griffin, J. R. Yates, F. Mauri and C. J. Pickard, *Chem. Rev.,* **2012**, 112, 5733-5779.

56. P. Sanz Camacho, K. S. Athukorala Arachchige, A. M. Z. Slawin, T. F. G. Green, J. R. Yates, D. M. Dawson, J. D. Woollins and S. E. Ashbrook, *J. Am. Chem. Soc.,* **2015**, 137, 6172-6175.

57. S. E. Ashbrook, D. M. Dawson, *Acc. Chem. Res.,* **2013**, 46, 1964-1974.

58. M. D. Segall, P. J. D. Lindan, M. J. Probert, C. J. Pickard, P. J. Hasnip, S. J. Clark and M. C. Payne, *J. Phys. : Condens. Matter.,* **2002**, 14, 2717-2744.

59. G. te Velde, F. M. Bickelhaupt, E. J. Baerends, C. Fonseca Guerra, S. J. A. van Gisbergen, J. G. Snijders and T. Ziegler, *J. Comput. Chem.,* **2001**, 22, 931-967.

60. J. R. Yates and C. J. Pickard, "Computations of Magnetic Resonance Parameters for Crystalline Systems: Principles", *eMagRes*, John Wiley & Sons, Ltd, UK, **2007**. DOI: 10.1002/9780470034590.emrstm1009.

61. M. Born and R. Oppenheimer, *Annalen der Physik*, **1927**, 389, 457-484.

62. a) D. R. Hartree and W. Hartree, *Proc. Roy. Soc.*, **1935**, 150, 9-33; b) J. C. Slater, *Phys. Rev.*, **1930**, 35, 210-211.

63. P. Hohenberg and W. Kohn, *Phys. Rev.,* **1964**, 136, 864-871.

64. W. Kohn and L. J. Sham, *Phys. Rev.,* **1965**, 140, 1133-1138.

65. D. M. Ceperley and B. J. Alder, *Phys. Rev. Lett.*, **1980**, 45, 566-569.

66. Y. M. Juan and E. Kaxiras, *Phys. Rev. B*, **1993**, 48, 14944-14952.

67. J. P. Perdew, K. Burke and M. Ernzerhof, *Phys. Rev. Lett.,* **1996**, 77, 3865-3868.

68. P. E. Blöchl, *Phys. Rev. B,* **1994**, 50, 17953-17979.

69. a) J. R. Yates, C. J. Pickard and F. Mauri, *Phys. Rev. B,* **2007**, 76, 024401; b) S. J. Clark, M. D. Segall, C. J. Pickard, P. J. Hasnip, M. I. J. Probert, K. Refson and M. C. Payne, *Z. Kristallogr.,* **2005**, 220, 567-570.

70. T. Charpentier, *Solid State Nucl. Magn. Reson.,* **2011**, 40, 1-20.

71. S. A. Joyce, J. R. Yates, C. J. Pickard and F. Mauri, *J. Chem. Phys.,* **2007**, 127, 204107.

72. J. Autschbach and T. Ziegler, *J. Chem. Phys.,* **2000**, 113, 936-947.

73. J. Autschbach and T. Ziegler, *J. Chem. Phys.,* **2000**, 113, 9410-9418.

74. T. F. G. Green and J. R. Yates, *J. Chem. Phys.,* **2014**, 140, 234106-16.

This page intentionally left blank.

Chapter 3: ^{77}Se and ^{125}Te solid-state NMR studies of *peri*-substituted acenaphthene systems

3.1 Chapter overview

In this chapter, solid-state ^{77}Se and ^{125}Te CP MAS NMR spectroscopy are used to probe the local environment of the chalcogen atoms (and the interactions they experience) in a series of nine mixed *peri*-substituted acenaphthenes. These materials have been characterised previously using single-crystal X-ray diffraction, solution-state NMR spectroscopy and DFT by Woollins and co-workers[1] in order to understand the effect of the Te-based substituent upon the molecular geometry and the inter-chalcogen interactions. In the previous study it was shown that a weakly attractive interaction was present between the *peri*-atoms by using a combination of DFT calculations performed in gas phase, single-crystal X-ray diffraction and solution-state NMR spectroscopy. Furthermore, periodic first-principles calculations, using the CASTEP code, were performed for all compounds and the agreement between experimental and calculated NMR parameters from geometry-optimized crystal structures will be discussed in order to understand whether good estimation of NMR parameters can be acquired using periodic DFT.

3.2. Acknowledgements

Work reported here would have been impossible without Dr Fergus Knight (postdoctoral research fellow, St Andrews) and Martin Stanford (summer project student), who produced the samples studied in this

Chapter. Dr Kasun Arachchige and Junyi Du were essential for the assistance provided in the robot-based analysis of many single crystals. Dr David B. Cordes and Prof. Alexandra M. Z. Slawin are thanked for the single-crystal structure determinations. Prof. Michael Bühl is thanked for his advice and patience in providing assistance for the ADF calculations, and NSCCS are thanked for access to additional computational resources.

3.3 Introduction and objectives

^{77}Se solution-state NMR spectroscopy has been widely used as a characterisation technique for selenium-containing materials as the considerable chemical shift range (over 3000 ppm), and the presence of typically large J couplings, provides a sensitive potential method for the detection of small changes in local structure. An extensive review has been done by Duddeck for ^{77}Se solution-state NMR in organic, inorganic compounds and even metal complexes.[2] In contrast, less attention has been given to the heavier congener of the chalcogen group, Te. The larger chemical shift range (over 5800 ppm) makes Te a potentially useful probe to study tellurium-containing materials, but this considerably un-explored area of chemistry is responsible for its label as a rare element.[3] This is been fortunately addressed in a recent review by Nordheider *et al*, summarizing all the ^{125}Te solution-state NMR studies performed until now on organotellurium compounds.[4]

The theoretical study of heavier elements, such as Te and Se, are also known to present challenges due to relativistic effects, which become more relevant in studies of these heavy atoms containing materials.[5, 6] Although the need to account for these effects have been known for decades,[7] it is still a challenge for theorists to implement such effects in

periodic-DFT programs and their effects in materials containing heavy atoms is still a hot topic.[8, 9, 10, 11, 12.]

Selenium has only one NMR-active nucleus, with spin quantum number I = 1/2, a natural abundance of 7.58% and receptivity (relative to ^{13}C) of 3.15. While reasonably straightforward for solution-state NMR spectroscopy, the significant CSA and long relaxation times results in more challenging and time consuming acquisition of ^{77}Se NMR spectra of solids, although a number of applications have appeared in the literature.[13, 14, 15, 16] In contrast, solid-state Te NMR spectroscopy, and its solution-state analogue, is generally less widely applied, with only a handful of studies in binary glasses,[17, 18] some trimethyltellurium salts[19, 22, 21] and transition-metal ditellurites.[22] However, studies of ^{125}Te have increased over recent years.[23, 24] Te has two NMR-active isotopes (^{123}Te and ^{125}Te), both of which have spin quantum number I = 1/2, with natural abundances of 0.9 and 7.1%, respectively. The receptivities (relative to ^{13}C) are 0.96 and 13.4, respectively and so ^{125}Te NMR is typically the species of choice for experimental study. The extremely large shift range (and correspondingly large CSA values), and long relaxation times result in long acquisition times, and have perhaps limited wider study. However, for the organoselenium and organotellurium compounds studied here, the use of CP,[25] *i.e.*, transfer of magnetisation from nearby ^{1}H, is possible, and is able to overcome, at least to some extent, the slower relaxation and low sensitivity for both Se and Te NMR. It should be noted, however, that owing to the low natural abundance of both ^{77}Se and ^{125}Te, only a small number of molecules will exhibit a J coupling (*i.e.*, have both NMR-active Se and Te nuclei) and the doublets produced by any through-space interaction will be of low intensity when compared with the (unaffected) centreband. Nonetheless, it is anticipated that measurement of the ^{77}Se and

^{125}Te isotropic chemical shifts, CSAs and (where possible) the heteronuclear J coupling, and comparison to corresponding parameters calculated using DFT, could provide considerable insight into the changes in the local chemical environment and any interaction between the *peri* substituents in these materials.

3.4 Experimental details

3.4.1 General synthesis

Compounds **3.1** – **3.9** were prepared as shown in Scheme 3.1. The starting material, 5-bromo-6-(phenylselenyl) acenaphthene, prepared as reported in literature,[5b] was treated with a single equivalent of n-butyllithium in diethyl ether to afford the precursor 5-(lithio)-6-(phenylselanyl) acenaphthene. This was then reacted with the corresponding diaryl ditelluride (R-Te-Te-R): diphenyl ditelluride (PhTeTePh), bis(4-fluorophenyl) ditelluride (FpTeTeFp), bis(1-naphthyl) ditelluride (NapTeTeNap), bis(2,4,6-triisopropanylphenyl) ditelluride (TipTeTeTip), bis(4-methoxyphenyl) ditelluride (Ani-pTeTeAni-p), bis(2-methoxyphenyl) ditelluride (Ani-oTeTeAni-o), bis(4-*tert*butylphenyl) ditelluride (TpTeTeTp), bis(4-methylphenyl) ditelluride (TolTeTeTol) or bis(2,4,6-trimethylphenyl) ditelluride (MesTeTeMes), to afford **3.1** – **3.9** in moderate to good yields.[1]

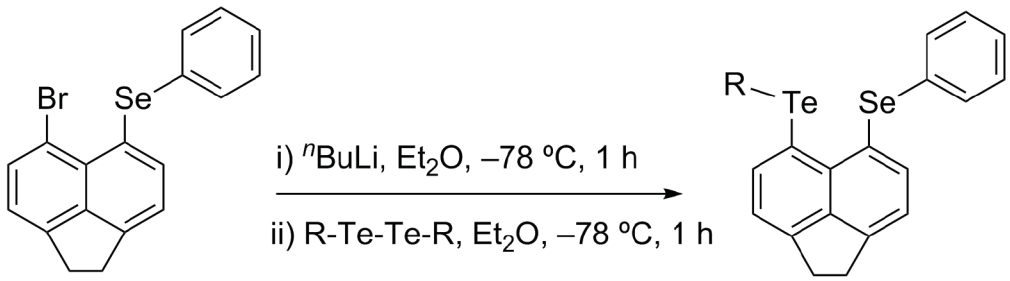

Scheme 3.1. *The preparation of **3.1** – **3.9** from 5-bromo-6-(phenylselenyl) acenaphthene.*

Table 3.1. Compounds studied in this chapter.

Compound	R group	Compound	R group
3.1	Ph	**3.6**	Ani-o
3.2	Fp	**3.7**	Tp
3.3	Nap	**3.8**	Tol
3.4	Tip	**3.9**	Mes
3.5	Ani-p		

3.4.2 Solid-state NMR spectroscopy

^{77}Se and ^{125}Te solid-state NMR were performed using a Bruker Avance III spectrometer operating at magnetic field strength of 9.4 and 14.1 T, corresponding to Larmor frequencies of 76.3 or 114.4 (^{77}Se) and 126.2 or 189.3 (^{125}Te) MHz at 9.4 and 14.1 T, respectively. Experiments were carried out using conventional 4- and 1.9-mm MAS probes, with MAS rates of 5, 20 and 40 kHz. Chemical shifts are referenced relative to $(CH_3)_2Se$ at 0 ppm using the isotropic resonance of solid H_2SeO_3 at 1288.1 ppm as a secondary reference, and to $(CH_3)_2Te$ at 0 ppm using the isotropic resonance of solid $Te(OH)_6$ (site 1) at 692.2 ppm as a secondary reference. For all compounds transverse magnetisation was obtained by CP from ^{1}H using optimised contact pulses durations of 8–20 ms, and TPPM ^{1}H decoupling during acquisition. Spectra were acquired with between 500 and 8000 transients separated by recycle intervals of between 3 and 90 s, depending on the longitudinal relaxation time of the individual samples. For all spectra, the positions of isotropic resonances within the spinning sideband patterns were unambiguously determined by recording a second spectrum at a higher MAS rate. Experimental ^{77}Se and ^{125}Te NMR

parameters were determined by lineshape analysis using the Bruker Topspin software package, SOLA.

Owing to the large chemical shift range of Se and Te, and the low CP match normally used, it is necessary to record the spectra on resonance, otherwise no signal will be acquired. Moreover, measurement of T_1, and $T_{1\rho}$, are advisable for each sample.

3.4.3 First-principles calculations

NMR parameters were calculated using the CASTEP DFT code version 7,[26] employing the gauge including projector augmented wave (GIPAW) algorithm,[27] which allows the reconstruction of all-electron wave function in the presence of a magnetic field. The generalized gradient approximation (GGA) PBE functional[28] was employed and core and valence interactions were described by ultrasoft pseudopotentials.[29] All calculations were performed with the G06 dispersion correction scheme,[30] a planewave energy cutoff of 50 Ry (816 eV) and a *k*-point spacing of 0.04 2π Å^{-1}. For all calculations, the initial atomic positions and unit cell parameters were taken from existing single-crystal X-ray diffraction structures.[1] Therefore, prior to the calculation of NMR parameters, geometry optimisations were performed for each structure (using cutoff energies of 50 Ry and k-points spacing of 0.04 2π Å^{-1}). All internal atomic coordinates and lattice parameters were allowed to vary. Calculations were performed using the EaStCHEM Research Computing Facility, which consists of 136 AMD Opteron 280 dual-core processors running at 2.4 GHz, partly connected by Infinipath high speed interconnects. Calculations wallclock times ranged from 1 to 24 h using 4 cores.

Calculations of ^{125}Te and ^{77}Se NMR magnetic shielding tensors were also carried out using the Amsterdam Density Functional (ADF) program

package. Calculations were performed on single isolated molecules using atomic coordinates extracted from a CASTEP-optimized crystal structure. Relativistic corrections to the magnetic shielding tensors were based on the implementation of the ZORA formalism GGA PBE exchange-correlation functional and all-electron TZ2P basis sets were used for all atoms.

3.4.4 X-ray crystallography

All crystal structures were determined at –148 (1) °C using a Rigaku MM007 high-brilliance RA generator (Mo-K_α radiation, confocal optic) and Saturn CCD system. The new polymorphs (**3.1b**, **3.1c** and **3.7b**) described in this chapter were acquired either on a Rigaku XtaLAB P200 diffractometer using multi-layer mirror monochromated Mo-K_α radiation or on a Rigaku SCX mini diffractometer using graphite monochromated Mo-K_α radiation.

The high-throughput "robot-based" crystallography of a large number of crystals was performed on a STANDARD System (St Andrews Robotic Diffractometer) consisting of a Mo sealed tube X-ray system with SHINE optic, Saturn CCD and ACTOR robotic sample changer and XStream LT accessory.

Unless otherwise stated, powder X-ray diffraction (XRD) data presented and discussed in this Chapter have been acquired at room temperature and with a PANalytical Empyrean instrument operated in reflection, Bragg Brentano, θ-2θ mode and equipped with a Cu X-ray tube, a primary beam monochromator ($CuK_{\alpha1}$) and X'celerator RTMS detector. Typically, a 5-50° 2θ range was investigated in one hour.

3.5 Results and discussion

The series of nine mixed selenium-tellurium substituted acenaphthenes shown in Figure 3.1, were previously synthesised and characterised by solution-state NMR amongst other analytical techniques in order to determine their purity. The ^{77}Se and ^{125}Te solution-state NMR spectra for all nine compounds exhibit a single resonance with satellites attributed to ^{125}Te–^{77}Se coupling.[1] The chemical shift and J coupling values for all compounds are summarised in Table 3.2. The large J values (~687 Hz to ~749 Hz) indicate a potential weak, attractive, though-space interaction between the two *peri*-atoms. In order to gain insight into the large J values, DFT calculations (using ADF program packed on isolated molecules) were performed and the results are also summarised in Table 3.2. However, the computed J values predicted for the series of compounds are significantly underestimated compared to the solution-state NMR values.

DFT calculations also provided an insight into the mechanism of the interaction in the systems studied, which occurs between a p-type lone pair on Se and a σ* (Te-C) antibonding orbital,[1] confirming the onset of 3c-4e (three-centres, four-electrons)[31] type bonding.

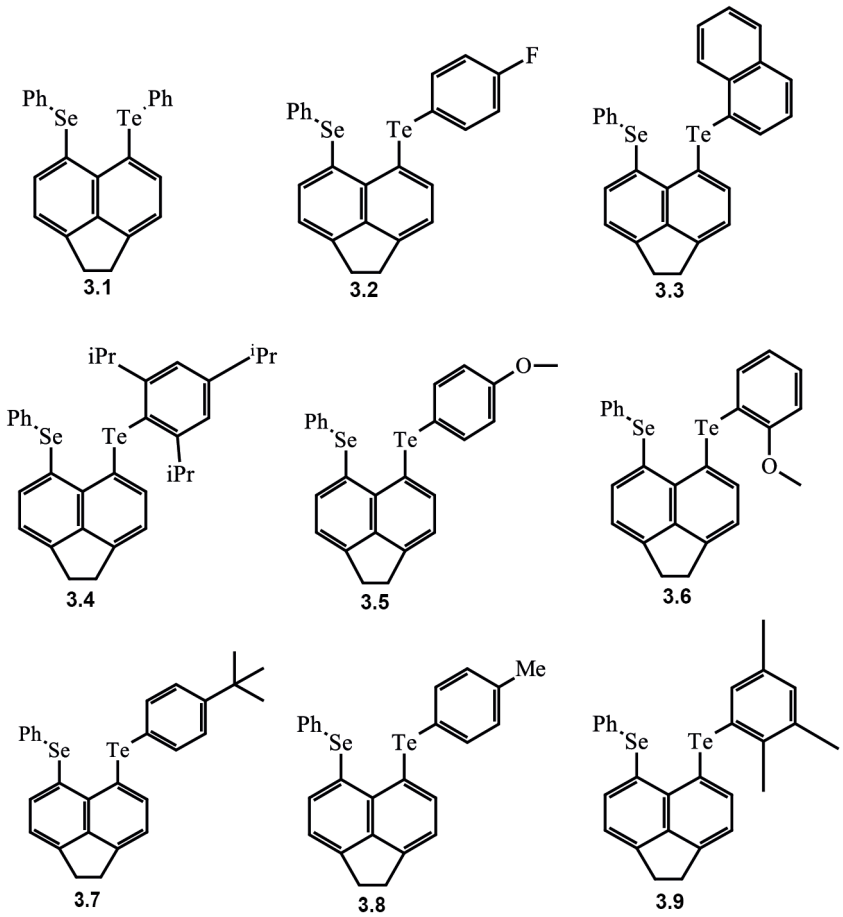

Figure 3.1. The nine acenaphthenes compounds studied.

3.5.1 Solid-state NMR study

The ^{77}Se solid-state NMR spectra of **3.1** – **3.9** were recorded at 298 K, without temperature control, at 5 kHz MAS in a 4- mm rotor (see Table A1 of Appendix A for experimental details). The crystal structures for each (determined in previous work[1]) contain a single crystallographically-distinct molecule, with the exception of **3.6** and **3.8**, where two molecules are found in the asymmetric unit. From this, a single resonance is expected in each ^{77}Se and ^{125}Te spectrum, arising from the single environment present in the structure, with two resonances expected for **3.6** and **3.8**. ^{77}Se CP MAS NMR spectra of all compounds are shown in Figure 3.2. A single

isotropic resonance is observed for all except **3.8**, shown in Figure 3.2h, where two resonances are seen, with a significant sideband manifold in each case as a result of the CSA. The presence of one resonance in the ^{77}Se CP MAS NMR spectrum of **3.6** was unexpected, and so experiments were performed at multiple fields in order to attempt to resolve the two resonances expected. However, possibly owing to a small difference in the ^{77}Se environments, resolution was not obtained, and the two sites may appear as an overlapped and broadened resonance.

The J(^{77}Se–^{125}Te) coupling previously mentioned for solution-state NMR, could only be resolved in some cases (*e.g.*, **3.2**, **3.4, 3.5** and **3.9**) as seen in Figure 3.3, which shows the doublets (appearing as "satellites" due to the ^{125}Te natural abundance of 7.1 %). Note that the J values were taken from the centreband and for the spectra recorded at 20 kHz. In all cases, the J values summarised in Table 3.2 are in agreement with the solution-state NMR data except for **3.9**, where the J value is closer to that predicted by DFT calculations.

Table 3.2. Chemical shift and J coupling extracted from ^{77}Se and ^{125}Te NMR spectra

Compound	**3.1**	**3.2**	**3.3**	**3.4**	**3.5**	**3.6**	**3.7**	**3.8**	**3.9**
R group	Ph	Fp	Nap	Tip	Ani-p	Ani-o	Tp	Tol	Mes
$\delta_{iso}^{solution}(^{77}Se)$	341	340	400	345	342	347	343	342	345
$\delta_{iso}^{solid}(^{77}Se)$	338	344	357	316	331	336	339	308 311	368
$\delta_{iso}^{solution}(^{125}Te)$	663	653	552	376	639	544	643	649	428
$\delta_{iso}^{solid}(^{125}Te)$	663	634	606	362	632	503	607	572 585	478
$J^{solution}(^{125}Te–^{77}Se)$	716	726	724	688	722	748	723	723	711
$J^{comp}(^{125}Te–^{77}Se)$[a]	–526	–484	–460	–469	–537	–585	–468	–471	–519
$J^{solid}(^{125}Te–^{77}Se)$	–	700	–	678	732	–	–	–	472

All solution-state NMR spectra run in $CDCl_3$; δ (ppm), *J* (Hz). [a] calculated J values with ADF program package.

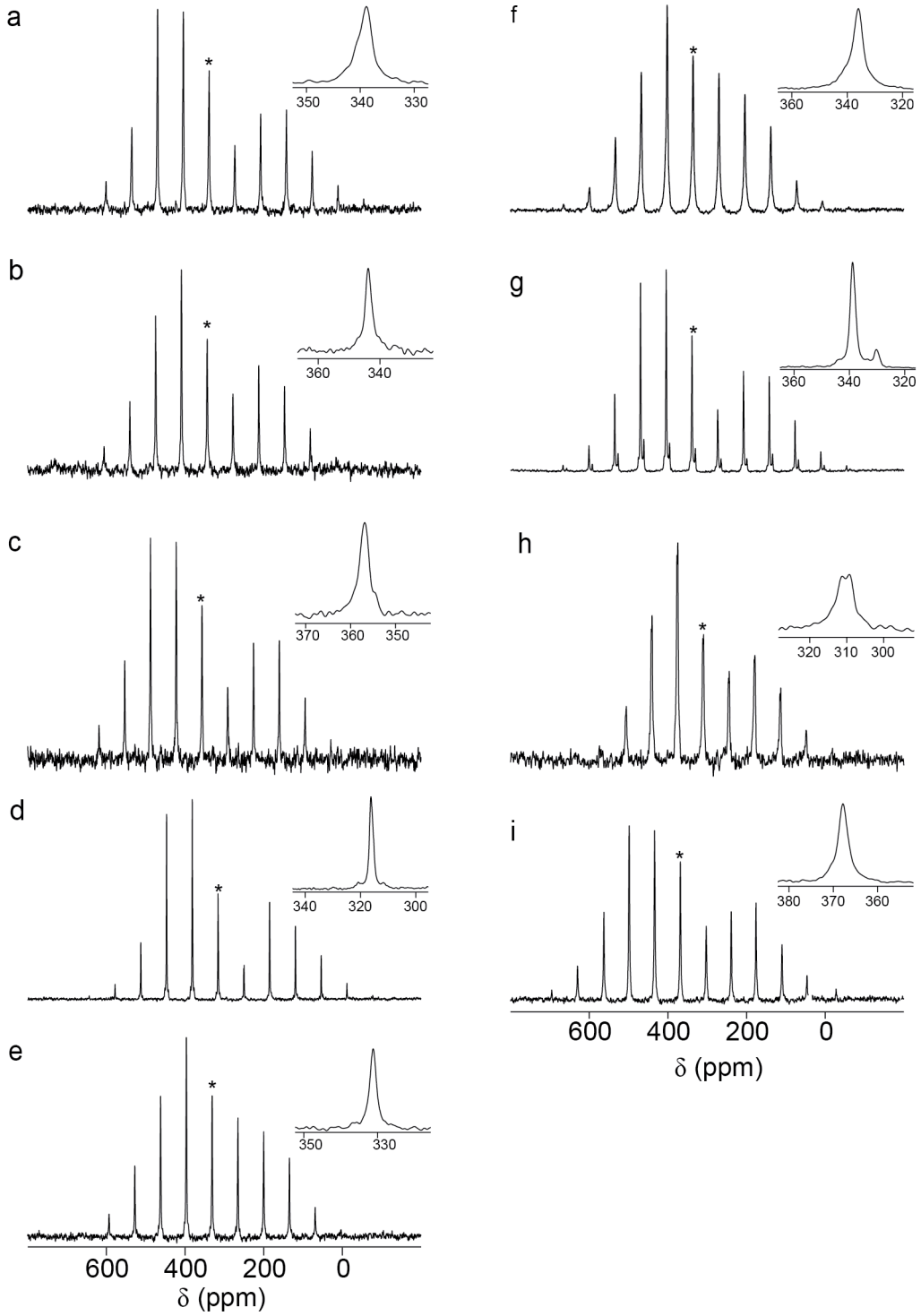

Figure 3.2. ^{77}Se CP (9.4 T, 5 kHz MAS) NMR spectra of compounds (a) **3.1**, (b) **3.2**, (c) **3.3**, (d) **3.4**, (e) **3.5**, (f) **3.6**, (g) **3.7**, (h) **3.8** and (i) **3.9**. Isotropic resonances in each spectrum are indicated by * (also shown expanded).

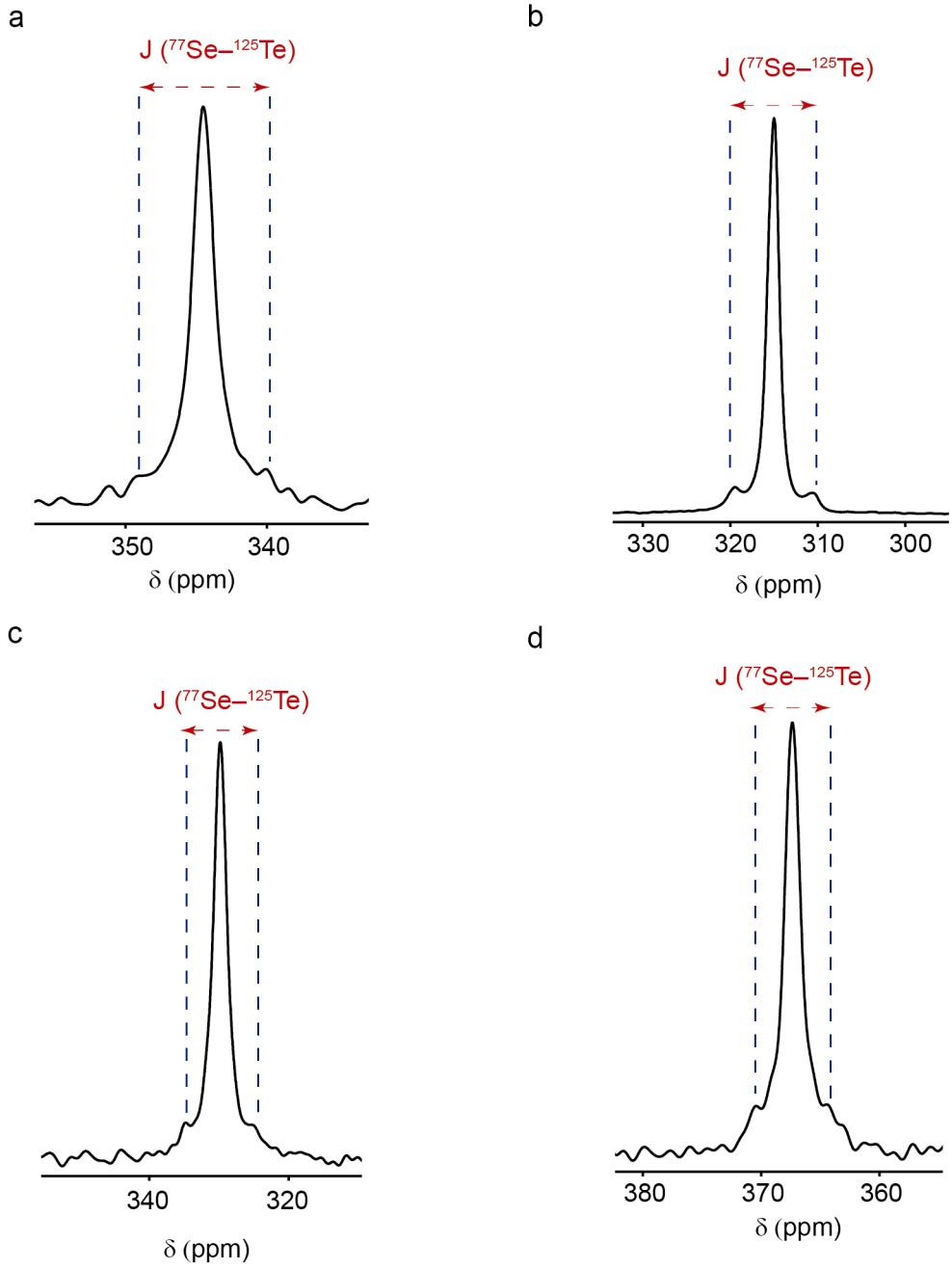

Figure 3.3. ^{77}Se CP (9.4 T, 20 kHz MAS) NMR spectra of (a) **3.2** recorded at 323 K and (b) **3.4**, (c) **3.5**, (d) **3.9** recorded at 278 K. Only the isotropic resonances in each spectrum are shown.

The range of ^{77}Se isotropic chemical shifts seen in solution for **3.1** – **3.8** is small, between 340 – 347 ppm, with a difference of ~7 ppm,

suggesting a chemically similar Se environment in each compound. The change in the Te aryl-group does not appear to significantly affect the ^{77}Se environment. The one exception to this, is **3.3**, which has a chemical shift of 400 ppm. The range of ^{77}Se isotropic chemical shifts in the solid-state NMR spectra is larger than that in solution, ranging from 308 – 368 ppm, giving a difference of ~60 ppm. This suggests that the ^{77}Se chemical shift in solid-state NMR is more sensitive to structural changes.

In order to establish any correlation between the size of the Te aryl-group and the NMR parameters (*i.e.*, isotropic and anisotropic components of the ^{77}Se and ^{125}Te tensors), a cone angle, θ, was calculated from the crystallographic data to provide a quantitative measure of the steric bulk of the aryl group. This angle is a modified version of the Tolman Cone Angle[32], defined as the angle between the hydrogen atoms that occupies the extreme edge of the cone to the tellurium atom located at its vertex and is illustrated in Figure 3.4. This cone angle, θ, is described in this chapter as the steric parameter.

Plots of the ^{77}Se isotropic chemical shift in solution and in the solid state against θ are shown in Figures 3.5a and 3.5b, respectively. In these plots, no correlation is observed for the either solution-state or solid-state measurements, showing that any effect on the selenium environment by modifications to the Te aryl-group is limited. Although the ^{77}Se chemical shift range in the solid state seems more sensitive to small structural changes in the nature of the aryl group, this could maybe arise as a consequence of some other effects that do not affect the solution-state NMR spectra. The ^{77}Se chemical shift difference observed between solution-state and solid-state NMR is given in Table 3.3 for compounds **3.1** to **3.9**.

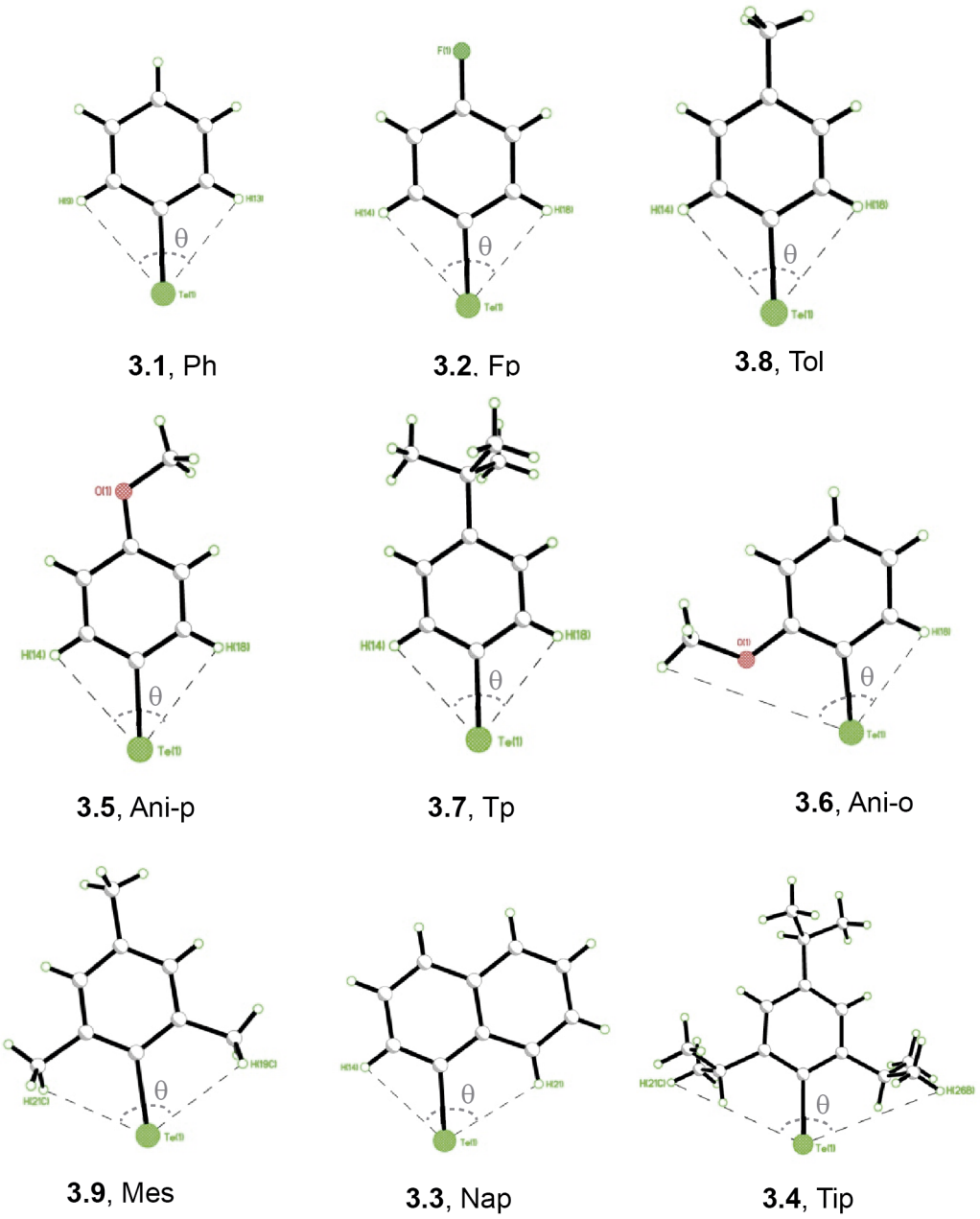

Figure 3.4. Schematic representation of the crystallographic steric parameter θ for the Se-Te compounds, ordered by increasing θ.

The larger difference is encountered for **3.3** (Nap), **3.4** (Tip), **3.8** (Tol) and **3.9** (Mes). With the exception of **3.8** (Tol), these compounds are those with aryl groups with higher steric hindrance, as shown by the θ values in Table 3.3.

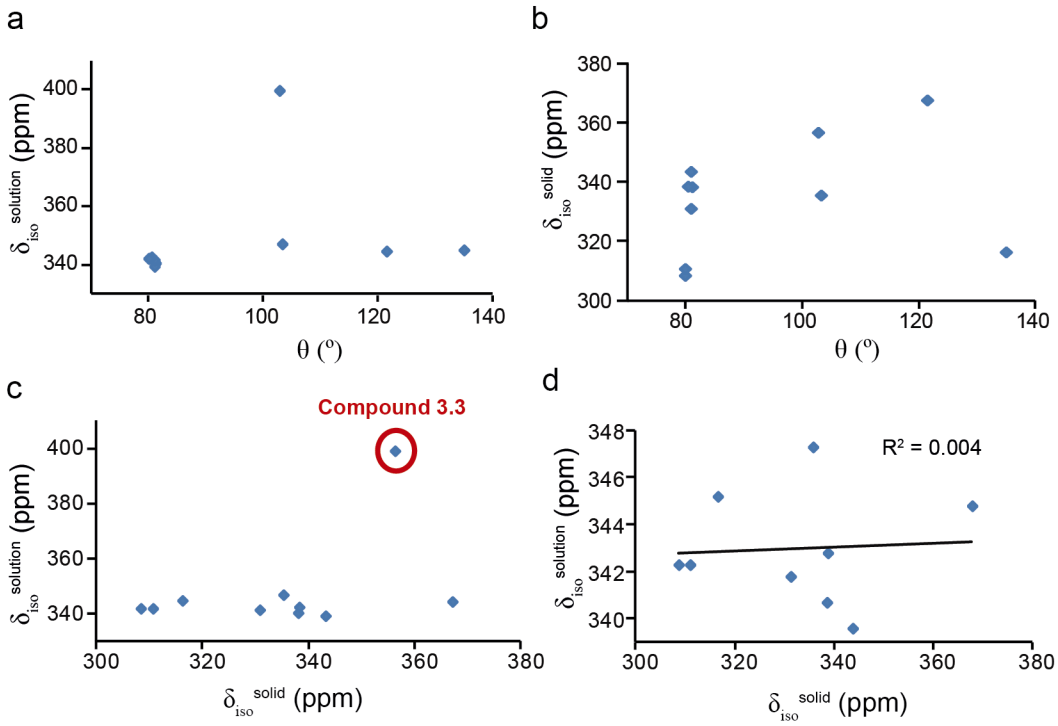

Figure 3.5. Plots of (a) $\delta_{iso}^{solution}$ (^{77}Se) and (b) δ_{iso}^{solid}(^{77}Se) *vs* θ for **3.1 – 3.9**. (c and d) $\delta_{iso}^{solution}$(^{77}Se) *vs* δ_{iso}^{solid}(^{77}Se) for **3.1 – 3.9** and (d) for all compounds except **3.3**.

Table 3.3. ^{77}Se chemical shift difference between solid and solution and crystallographic steric parameter θ for **3.1 – 3.9**.

Compound	R groups	$\Delta\delta_{iso}^{(solution-solid)}$ (ppm)	θ (°)
3.1	Ph	3	81.2
3.2	Fp	4	81.0
3.3	Nap	43	102.8
3.4	Tip	29	135.0
3.5	Ani-p	11	81.0
3.6	Ani-o	11	103.3
3.7	Tp	4	80.5
3.8	Tol	34	80.4
	Tol	31	80.4
3.9	Mes	23	121.5

The differences observed between the ^{77}Se isotropic chemical shift in solution and in the solid are shown in Figures 3.5c and 3.5d, and are often ascribed to effects resulting from crystal packing. The packing arrangement is often influenced by the presence of weaker intermolecular interactions. In solution-state NMR rapid tumbling is present and so the intermolecular interactions that affect the solid will be averaged, resulting in limited effects in solution-state NMR. However, the dependence of the chemical shift on the solvent is well-known. The solvent effect is caused by the interactions of the solvent molecules with the solute, *e.g.,* through hydrogen bonds, van der Waals forces, or other non-bonding interactions. In this case, different solvents can favor a specific conformation which will result in differences in the chemical shift value.[33] These differences are normally small between solvents and, as mentioned above, depend on the possibility of the solvent forming some interaction with the solute.

In this study, ^{77}Se solution-state NMR spectra for **3.1 – 3.9**, were recorded in $CDCl_3$, so solvents effects can, in principle, be neglected as a low-polar solvent has been used. However, in the solid state, crystal packing effects must be considered, especially for those compounds containing a sterically bulky group attached to Te, as those compounds may arrange very differently, giving the higher differences between the chemical shift in solution and in the solid, $\Delta\delta_{iso}^{(solution\text{-}solid)}$.

The $\Delta\delta_{iso}^{(solution\text{-}solid)}$ for **3.1 – 3.9**, plotted against θ, is shown in Figure 3.6a. A relatively good correlation is observed, except for compounds **3.3** (Nap) and **3.8** (Tol) that appear to have a very significant difference. Figure 3.6b shows that there is a good correlation ($R^2 = 0.91$) for the rest of the compounds in the series. This suggests that as the steric parameter increases, larger differences between the ^{77}Se chemical shift in solution and in the solid are found as a consequence of the increase of crystal-packing.

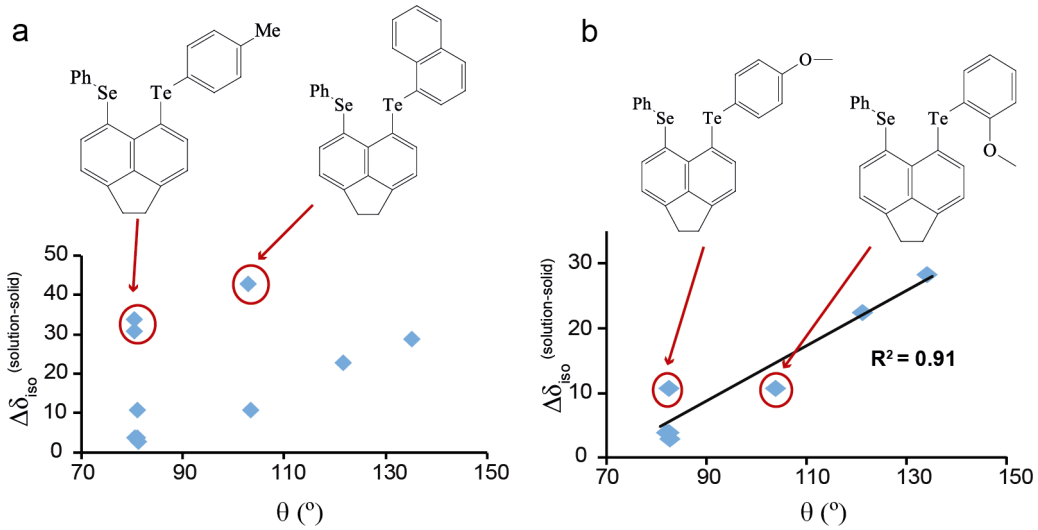

Figure 3.6. Plot of $\Delta\delta_{iso}(^{77}Se)^{(solution\text{-}solid)}$ *vs* θ for (a) **3.1** – **3.9** and (b) all compounds except **3.3** (Nap) and **3.8** (Tol).

Although **3.5** (Ani-p) and **3.6** (Ani-o), differ only in the position of a OMe group, the "size" of the aryl group is different, as can be observed from the steric parameter, θ = 81° and 103.3°, respectively. However, the $\Delta\delta_{iso}^{(solution\text{-}solid)}$ is the same for both cases, suggesting similar packing in the solid state and a limited effect on the electronic differences encountered in these two compounds.

In the solid state, the CSA can also be explored to obtain additional information on the local structure. This anisotropy can be extracted experimentally using an analytical fitting algorithm implemented in the Bruker Topspin program. Using the Herzfeld-Berger convention, the CSA is described using the span (Ω) and the skew (κ), as described in Chapter 2. These parameters where extracted from the experimental spectra recorded at 5 kHz MAS shown in Figure 3.2 for **3.1** – **3.9** and are summarised in Table 3.4.

Table 3.4. Experimental ^{77}Se NMR anisotropic parameters.

Compounds	**3.1a**	**3.2**	**3.3**	**3.4**	**3.5**	**3.6**	**3.7**	**3.8**	**3.9**
R group	Ph	Fp	Nap	Tip	Ani-p	Ani-o	Tp	Tol	Mes
Ω	573	532	580	528	525	491	564	414 533	602
κ	0.47	0.40	0.44	0.7	0.22	0.14	0.45	0.37 0.45	0.36
δ_{11}	580	575	604	519	501	570	579	490 536	633
δ_{22}	429	414	441	439	414	359	422	359 391	440
δ_{33}	7	42	24	–9	77	79	15	76 3	31

All Ω (ppm) and δ_{11}, δ_{22}, δ_{33} (ppm).

The small range of ^{77}Se Ω, and the principal components of the tensor δ_{11} , δ_{22} and δ_{33} , reveals some similarity in the anisotropy throughout the series, with Ω varying between 491 – 580 ppm, with the exception of **3.8** and **3.9**, which Ω values of 414 and 602ppm, respectively, are out of the range, as observed in Table 3.4. A plot of the span and the principal components (δ_{ii}) against θ, shown in Figure 3.7, confirms that the substitution of the aryl group does not significantly affect the local environment of selenium, as observed also for the isotropic chemical shift.

All ^{125}Te solid-state NMR spectra of **3.1** – **3.9** were recorded at 298 K and with 10.5 kHz MAS in a 4- mm rotor and are shown in Figure 3.8 (see Table A2 of Appendix A for experimental details). ^{13}C CP NMR of all compounds were also recorded at 14.1 T and 12.5 kHz MAS (see details of the experimental parameters in Table A3, and the spectra is shown for all compounds in Figure A1 of the
Appendix A).

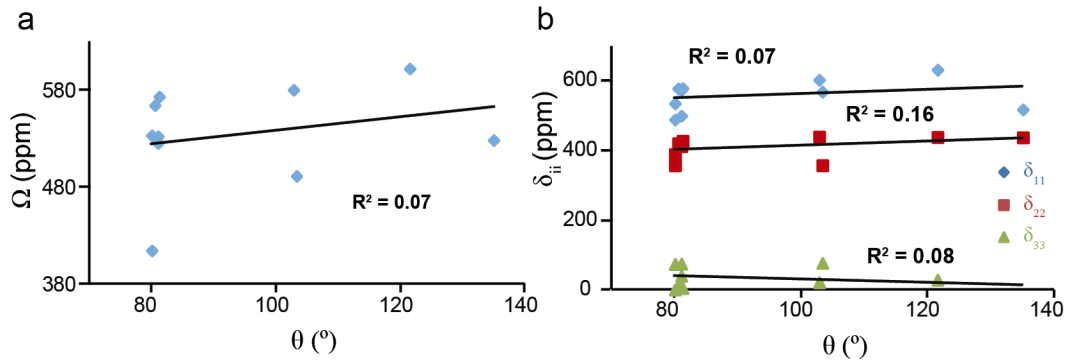

Figure 3.7. Plots of ^{77}Se (a) Ω and (b) δ_{ii} *vs* θ for **3.1 – 3.9.** The blue, red and green points denotes δ_{11}, δ_{22} and δ_{33} respectively, for **3.1 – 3.9**

All compounds, with the exception of **3.8**, exhibit a single resonance, as observed for ^{77}Se. Compound **3.6** was also expected to exhibit two resonances, but, as seen in the ^{77}Se spectrum of **3.6**, a single resonance is observed. The chemical shifts in solution and in solid-state NMR spectra for each compound are summarised in Table 3.2. It was not possible to resolve the J(^{77}Se–^{125}Te) coupling for any compound from the spectra recorded at 10.5 kHz MAS, with the exception of **3.4**, where the J-coupling value is in good agreement with that determined from the ^{77}Se solution-state NMR spectrum. In solution, the aryl group substitution has a greater influence on the ^{125}Te chemical shift than on the ^{77}Se chemical shifts. This can be seen in the larger ^{125}Te chemical shifts range observed in solution (*i.e.*, varying from 663 to 362 ppm), showing a difference of 287 ppm within the series. A similar effect is observed for the ^{125}Te chemical shift in the solid state, with even larger differences across the series, of up to 301 ppm. The ^{125}Te chemical shifts in solution for **3.1 – 3.9** plotted against θ, show a good correlation (R^2 = 0.99); as θ, increases, a shielding effect is observed, as shown in Figure 3.9a.

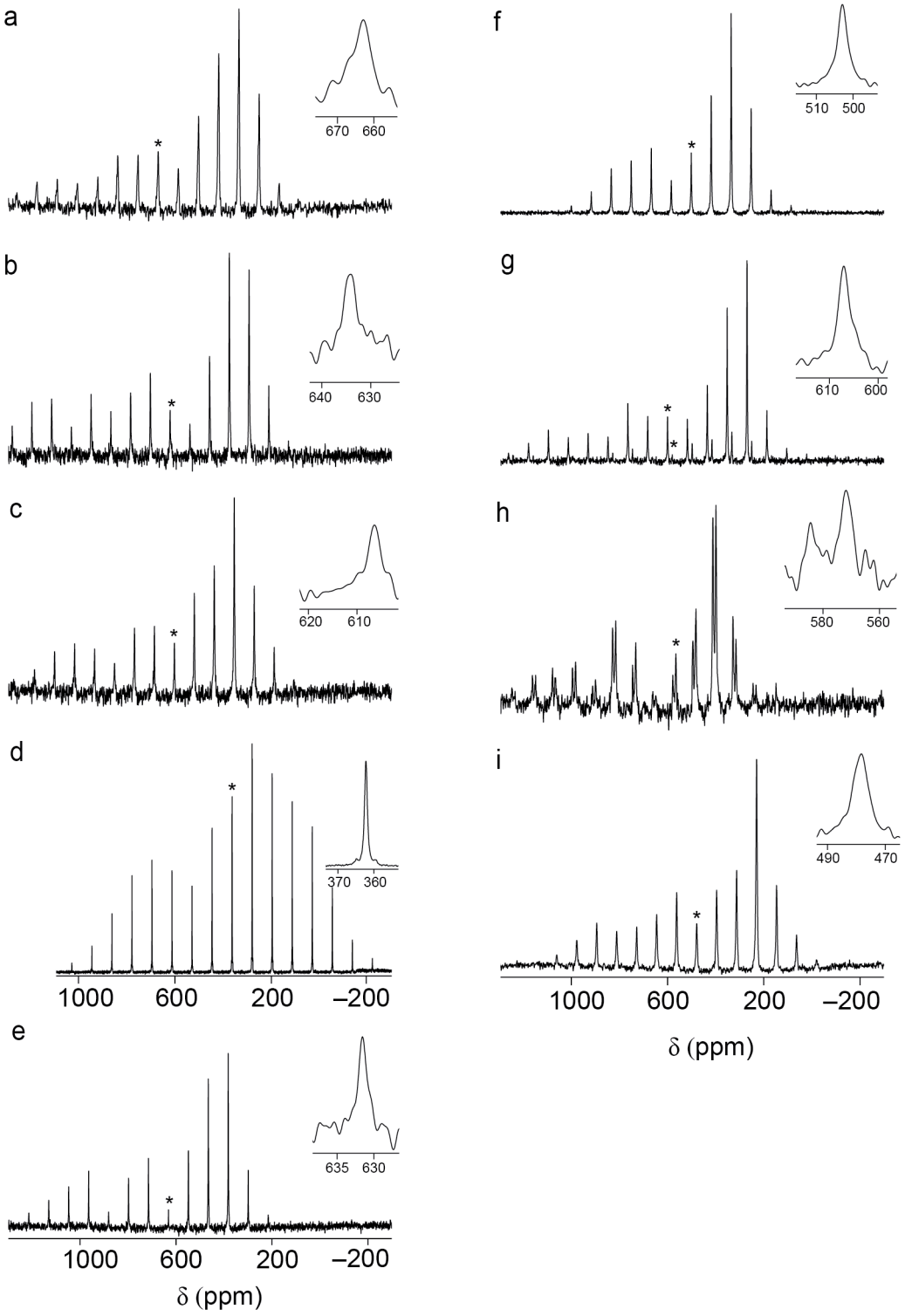

Figure 3.8. ^{125}Te CP MAS (9.4 T) NMR spectra of (a) **3.1**, (b) **3.2**, (c) **3.3**, (d) **3.4**, (e) **3.5**,(f) **3.6**, (g) **3.7**, (h) **3.8** and (i) **3.9**. Isotropic resonances in each spectrum are indicated by * (also shown expanded).

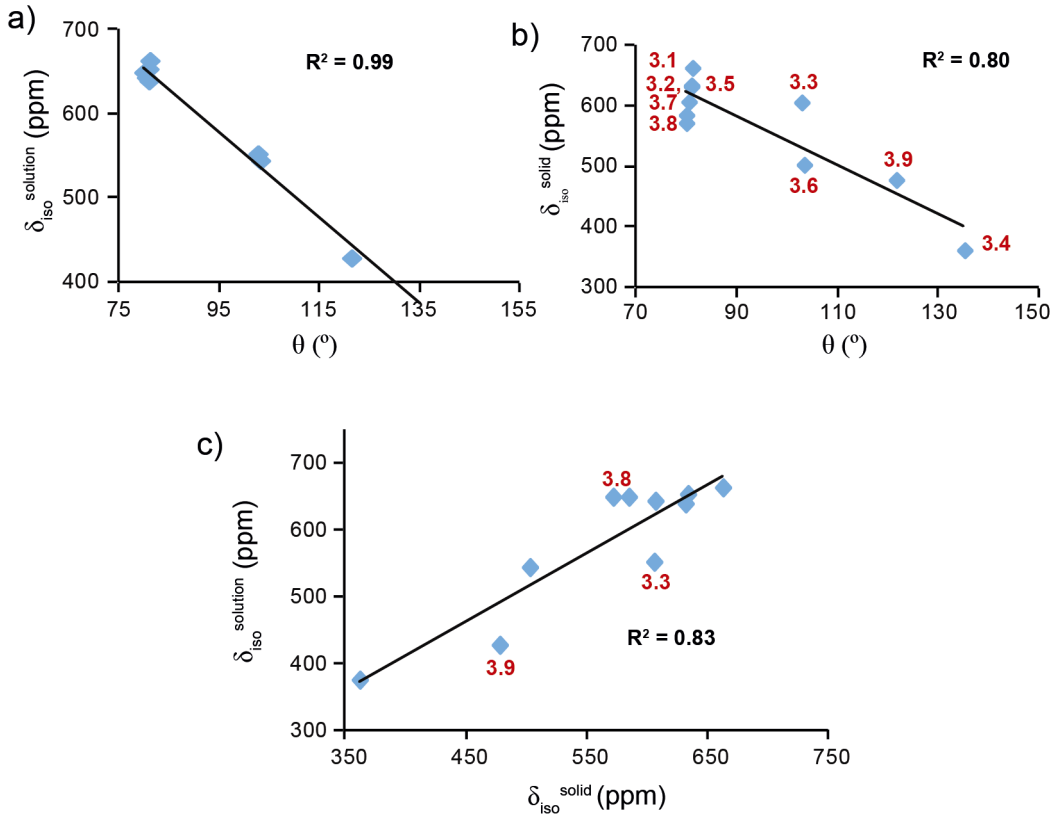

Figure 3.9. Plot of (a) $\delta_{iso}^{solution}(^{125}Te)$ and (b) $\delta_{iso}^{solid}(^{125}Te)$ *vs* θ for **3.1** – **3.9** and (c) $\delta_{iso}^{solution}$ (^{125}Te) *vs* δ_{iso}^{solid} (^{125}Te), for **3.1** – **3.9**.

The same effect is observed for the solid-state ^{125}Te chemical shift, as shown in Figure 3.9b, with a less good correlation (R^2 = 0.80), possibly because of the presence of other effects in the solid state that may contribute to the ^{125}Te chemical shift, such as crystal packing. A plot of $\delta_{iso}^{solution}$ (^{125}Te) against δ_{iso}^{solid} (^{125}Te) is shown in Figure 3.9c. Although, a reasonable correlation is observed, the scatter observed suggests that the differences between the two could arise from crystal packing in the solid. The biggest difference observed between the ^{125}Te chemical shift in solution and in the solid state is for **3.8** (Tol) and **3.3** (Nap), followed by **3.9** (Mes). These differences are perhaps not surprising, as for bulkier compounds such as, **3.3** and **3.9** that have θ values of 102.8° and 121.5°

Table 3.5. ^{125}Te chemical shift difference between solid- and solution-NMR spectra and steric parameter θ for **3.1 – 3.9**.

Compound	R groups	$\Delta\delta_{iso}^{(solution-solid)}$ (ppm)	θ (°)
3.1	Ph	0	81.2
3.2	Fp	19	81.0
3.3	Nap	54	102.8
3.4	Tip	14	135.0
3.5	Ani-p	7	81.0
3.6	Ani-o	41	103.3
3.7	Tp	36	80.5
3.8	Tol	77	80.4
	Tol	64	
3.9	Mes	50	121.5

respectively, may packed very differently. However, this is quite surprising for **3.8** that possess the least bulky group with a θ of 80.4°. These differences are summarised in Table 3.5 together with the steric parameter.

A plot of $\Delta\delta_{iso}^{(solution-solid)}$ for **3.1 – 3.9** against θ is shown in Figure 3.10a. At first, no apparent correlation between the two is observed. However, two regions can be distinguished, one for the compounds where θ is between 80.4° and 81.2° and another region for the bulkier compounds where θ is bigger than 81.2°. If the two regions are separated, as observed in Figure 3.10b and in Figure 3.10c, for the small range of θ, and for the bulkier compounds, respectively, a good correlation ($R^2 = 0.96$) is observed for the former and a relatively poor correlation ($R^2 = 0.57$) for the latter.

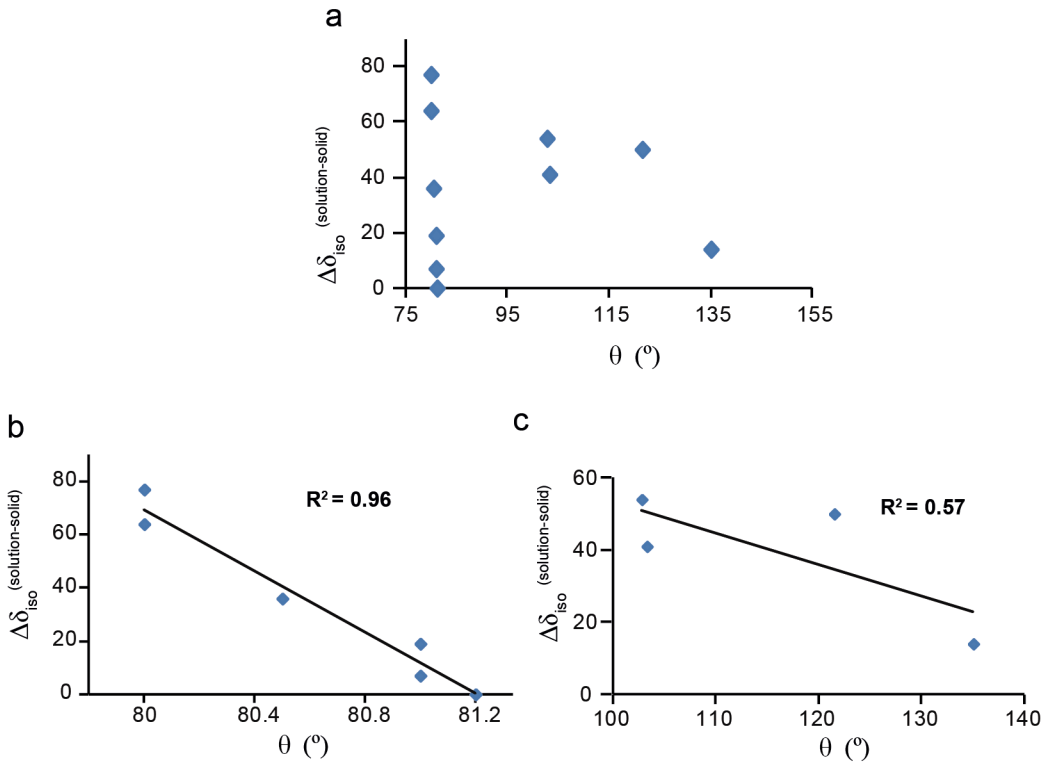

Figure 3.10. (a) Plot of $\Delta\delta_{iso}(^{125}Te)^{(solution\text{-}solid)}$ *vs* θ for **3.1** – **3.9**, (b) same plot but for compounds with θ from 80.0° to 81.2° and (c) same plot but for compounds with θ from 100° to 140°.

In both regions, as θ increases, a smaller chemical shift difference is observed between solution- and solid-state NMR for ^{125}Te. This effect is the opposite to that observed in ^{77}Se NMR.

The ^{125}Te CSA parameters for **3.1** – **3.9** were extracted (using Topspin) from the experimental spectra recorded at 10.5 kHz MAS shown in Figure 3.8, and are given (using Herzfeld-Berger convention) in Table 3.6. The larger variation observed in the span, Ω, for ^{125}Te confirms the greater sensitivity to the changes in the aryl group throughout the series, as was observed with the isotropic chemical shift.

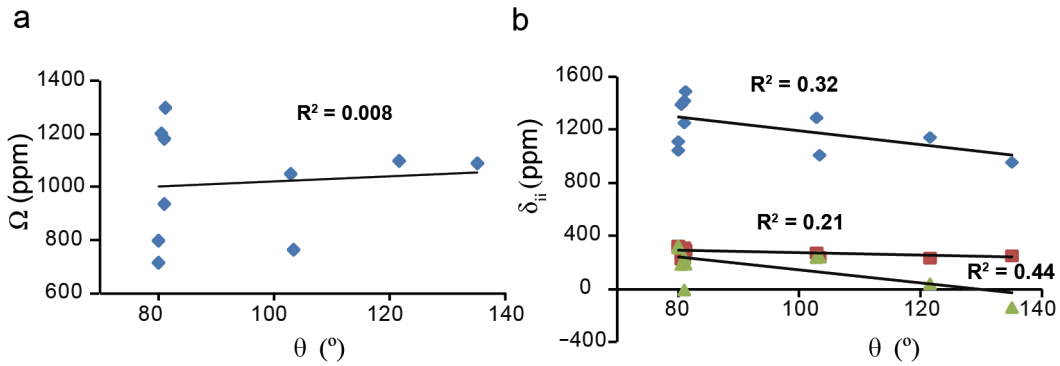

Figure 3.11. Plots of ^{125}Te (a) Ω and (b) δ_{ii} *vs* θ for **3.1** – **3.9**. The blue, red and green points denotes δ_{11}, δ_{22} and δ_{33} respectively.

Table 3.6. Experimental ^{125}Te NMR anisotropic parameters.

	3.1	**3.2**	**3.3**	**3.4**	**3.5**	**3.6**	**3.7**	**3.8**	**3.9**
R group	Ph	Fp	Nap	Tip	Ani-p	Ani-o	Tp	Tol	Mes
Ω	1302	1185	1053	1087	940	768	1207	719 802	1102
κ	–0.84	–1.0	–0.93	–0.28	–1.0	–1.0	–0.93	–1.0 –1.0	–0.65
δ_{11}	1496	1424	1297	961	1258	1015	1396	1051 1118	1149
δ_{22}	300	239	279	257	318	247	233	332 318	240
δ_{33}	194	239	243	–132	318	247	191	332 316	47

All Ω (ppm) and δ_{11}, δ_{22}, δ_{33} (ppm).

In this case, the span varies from 1302 to 719 ppm, with the latter, the value for **3.8,** the one that exhibits the smallest θ. However, this may be a coincidence, as a plot of Ω and δ_{ii} against θ, shown in Figure 3.11a and 3.11b, confirms that the steric parameter, θ, does not show any significant correlation with the ^{125}Te shielding anisotropy.

3.5.2 Discovery of polymorphism

In addition to the resonances expected for each compound from the number of distinct species determined in the crystal structure, **3.1** and **3.7** exhibit additional peaks in the ^{77}Se and ^{125}Te NMR spectra as shown in Figure 3.12.

The ^{77}Se NMR spectrum of **3.1**, shown in Figure 3.12a, exhibits a main signal at 338.5 ppm and a shoulder at ~340.3 ppm (also observed in each of the spinning sidebands), suggesting a second type of selenium environment is present. This is unexpected as the crystal structure for **3.1** determined in previous work[34] contains only one crystallographically-distinct molecule (and therefore only one distinct ^{77}Se species). Furthermore, the spectrum obtained does not match that shown for this material in previous work,[34] where a shift of 350 ppm was reported experimentally. In order to gain insight into the differences between the samples, a second measurement of the ^{77}Se CP MAS NMR of the sample reported in previous work was obtained. The ^{77}Se NMR spectrum confirmed the presence of a main resonance at 350 ppm, as previously reported, but the additional presence of a resonance with lower intensity at ~340.3 ppm, overlooked previously. This signal coincides with the shoulder observed in the new spectrum of **3.1**, as shown in Figure 3.13. In this figure, the spectrum for the sample studied previously is shown by the blue line and the new spectrum by the black line. In both cases, there is a main resonance (labelled A for the blue spectrum and C for the black spectrum) while signal B is present in both samples.

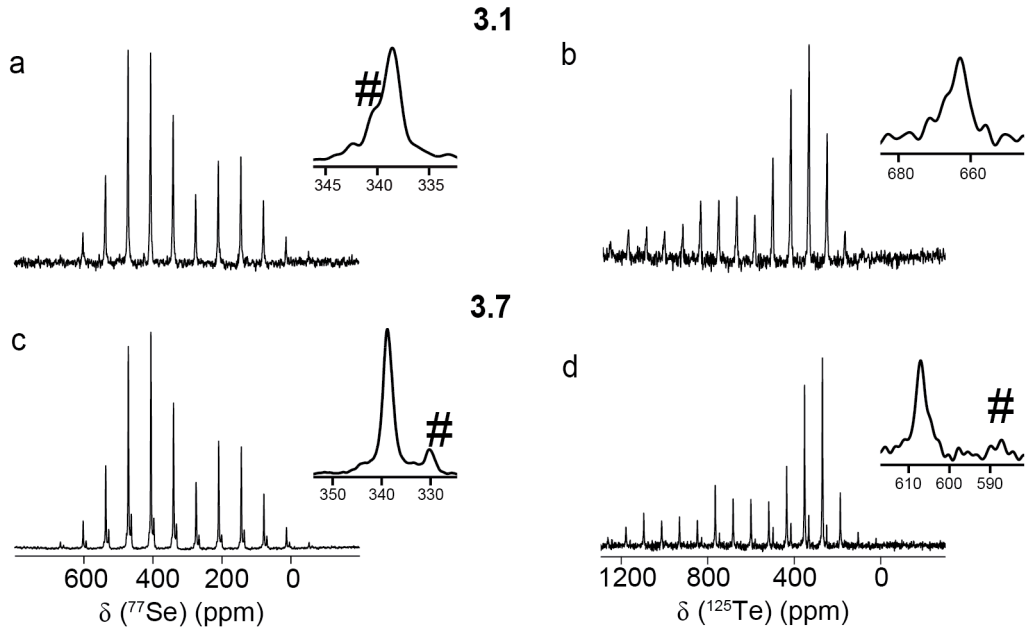

Figure 3.12. ^{77}Se CP (9.4 T, 5 kHz MAS) NMR spectra of (a) **3.1** and (c) **3.7** and ^{125}Te CP (9.4 T, 10 kHz MAS) NMR spectra of (b) **3.1** and (d) **3.7**. Isotropic resonances in each spectrum are shown expanded. The # indicates additional resonances found in the spectra.

Not only do the three resonances have different chemical shifts (*i.e.*, a difference of 11.5 ppm between the main resonances A and C is found), they also have different shielding anisotropies. This difference is, however, not very large as shown in Table 3.7, with a difference in the span of ~14.8 ppm and very similar values of κ. The principal components of the tensors are also quite similar, except δ_{33}, which shows a difference of ~27 ppm. This suggests that Se in both samples has slightly different environments.

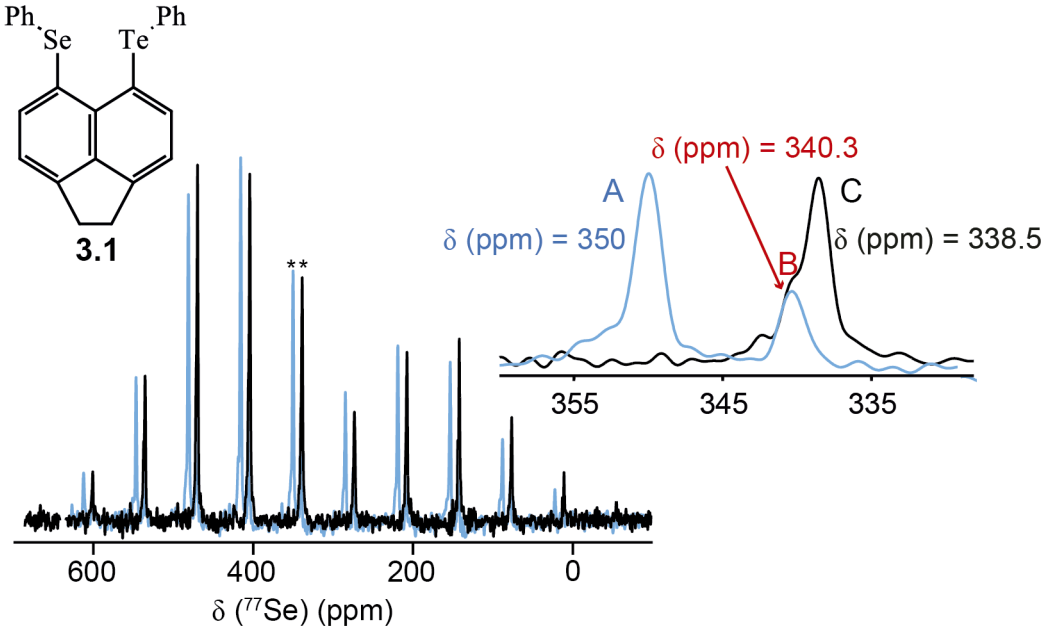

Figure 3.13. ^{77}Se CP (9.4 T, 5 kHz MAS) NMR spectra of two different samples of **3.1**. The sample reported previously is shown by the blue line and the spectrum of the sample studied in this work by the black line. The isotropic resonances for both spectra are expanded in the inset and labelled by A (older sample) and C (newer sample), while resonance B is present in both spectra. Isotropic resonances in each spectrum are shown expanded and are indicated with a *.

Table 3.7. Experimental ^{77}Se and ^{125}Te NMR parameters

Resonance	R group	δ_{iso}	Ω	κ	δ_{11}	δ_{22}	δ_{33}
^{77}Se NMR, recorded at 9.4 T and 5 kHz MAS							
A[a]	Ph	350.1	558.1	0.39	592.5	423.4	34.4
C[a]	Ph	338.5	572.9	0.47	580.1	429.4	7.21
^{125}Te NMR, recorded at 14.1 T and 20 kHz MAS							
A[a]	Ph	682.2	1387.0	–0.86	1575.2	283.4	188.1
B[a]	Ph	665.2	1106.9	–0.88	1381.1	340.4	274.2
C[a]	Ph	662.1	1135.0	–0.91	1401.6	318.2	266.6

[a] A, B and C denote the resonances shown in Figure 3.13. All Ω (ppm), δ_{iso}(ppm) and δ_{11}, δ_{22}, δ_{33} (ppm). Experimental ^{77}Se CSA parameters of resonance B, were not able to be determined owing the low intense manifold.

The ^{125}Te CP MAS NMR spectra recorded at 14.1 T and 20 kHz MAS of **3.1** were also analyzed for both samples. As shown in Figures 3.14a and 3.14b, some differences are observed between the samples, as previously shown for ^{77}Se. The sample studied previously shows two main resonances in the spectrum at 682.2 and 665.2 ppm (though the sensitivity of the centreband is poor) while only one resonance appears to be seen for the new sample, centred at 662.1 ppm. In order to improve resolution, the ^{125}Te CP MAS spectra of both samples were recorded at lower field (9.4 T) and higher spinning speed (40 kHz) to reduce the anisotropic broadening and increase the sensitivity of the isotropic peak, at least in principle. For the previous sample two clear resonances are observed (Figure 3.14c). Note that the low intensity of the peaks is probably due to inefficient CP at faster MAS as almost no sideband manifold can be seen. In contrast, Figure 3.14d now shows the presence of a main resonance at 662.1 and a shoulder at ~669.8 ppm represented by **#** in the spectrum for the sample studied in this work.

The shielding parameters for the three resonances, (A and B at 682.2 and 665.2 ppm, for the previously studied sample and C at 662.1 ppm for the new sample), were extracted experimentally and are summarised in Table 3.7. It must be noted that although, there is a clear shoulder in the ^{125}Te spectrum of the new sample in Figure 3.14d, the anisotropic shielding cannot be extracted due to the poor resolution. From the values in Table 3.7, it can be seen that the resonance centred at 682.2 ppm has a very different CSA compared to the other two resonances, with a difference in Ω of ~281 ppm and very different tensor components, while the anisotropy for the two resonances at 665.2 and 662.1 ppm is much more similar.

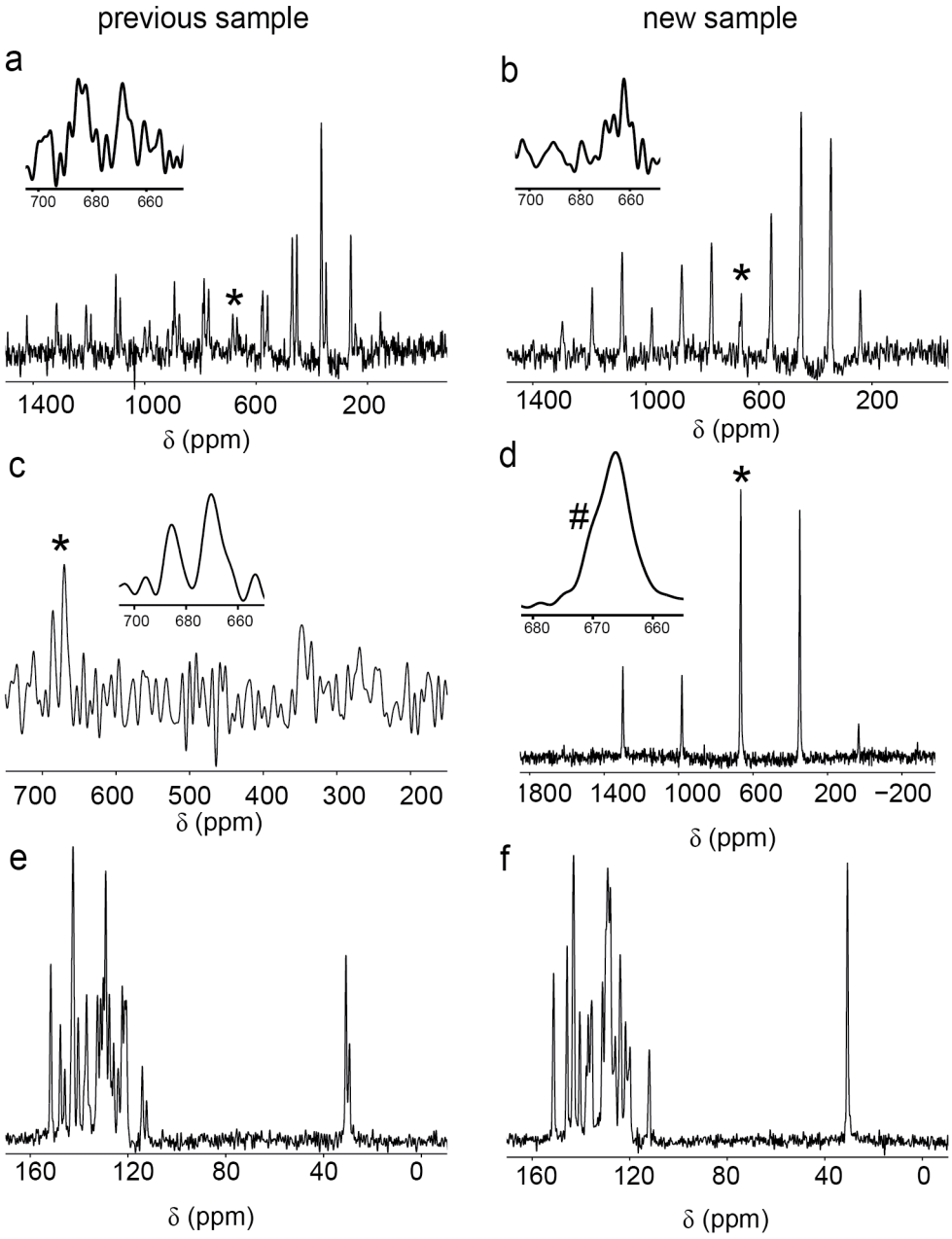

Figure 3.14. ^{125}Te CP (14.1 T, 20 kHz MAS) NMR spectra of two samples of **3.1** for (a) studied previously and (b) prepared in this work. ^{125}Te CP (9.4 T, 40 kHz MAS) NMR spectra of two samples of **3.1** for (c) studied previously and (d) prepared in this work. ^{13}C CP (9.4 T, 20 kHz MAS) NMR spectra of two samples of **3.1** for (e) studied previously and (f) prepared in this work. Isotropic resonances in each spectrum are shown expanded and indicated by a *. The # indicates additional resonances.

The ^{13}C CP MAS NMR spectra recorded at 9.4 T and 20 kHz MAS for the two samples are shown in Figures 3.14e and 3.14f respectively. Some differences are observed, however owing to the overlap of signals in the aromatic regions, it is very difficult to obtain any useful information from this region. In contrast, the aliphatic region shows one resonance for the new sample and two clear resonances for the sample studied previously. This is consistent with the two distinct resonances found in the ^{125}Te and ^{77}Se spectra for the older sample. However, the known crystal structure published in previous work,[34] only contains one molecule in the asymmetric unit, suggesting these additional resonances arise from a different polymorph present in the sample. It must be noted that no impurities are found by solution-state NMR for either sample. In addition, the inconsistent data obtained between the two samples that in principle are both **3.1**, as confirmed by other analytical techniques (solution-state NMR, IR, EA and mass spectrometry), suggest different major polymorphs are present in each sample, explaining the different chemical shifts and anisotropy observed.

In order to clarify this problem, both samples were re-crystallised from hexane/DCM, the solvent mixture used in a previous study, and studied using single-crystal X-ray diffraction.[34] The result was, surprisingly, that two new crystal structures were found (one in each sample) confirming polymorphism. The three crystal structures termed **3.1a** (structure from previous literature[34]), **3.1b** (new crystal structure from the crystallisation of the previous sample) and **3.1c** (new crystal structure from the crystallisation of the newer sample) are all compared in the Table A4 of Appendix A, where the bond lengths and angles for each are also summarised. Structures of the three polymorphs (both asymmetric unit and with crystal packing motifs) are shown in Figure 3.15, and all three

structures have just one distinct molecule within the asymmetric unit. It can be seen that the crystal structures **3.1a** and **3.1b** are more similar, while **3.1c** differs more significantly. This difference is not only the conformational differences of the molecules, which is illustrated in Figure 3.16, but also the differences in packing motifs. Structure **3.1c** has only two molecules within the unit cell, forming a tightly packed dimer, while **3.1a** and **3.1b** both have four molecules, although the extended packing is different between the two. In **3.1a**, the stacks of molecules form extended chains lying parallel to each other along the b axis, while in **3.1b** the chains of molecule stack perpendicular to each other along the a axis.

The strain of the three polymorphs was studied by analyzing the splay angles, torsion angles and out-of-plane displacement for each of them that are summarised in the Table A4 of Appendix A. The splay angle seems very similar between the polymorphs (17.1°, 17.6° and 16.4° for **3.1a**, **3.1b** and **3.1c**, respectively). In all cases, a positive value was found, indicating a repulsive force between *peri* atoms. The out-of-plane displacement varied through the series, in **3.1a**, Se is almost in plane with the acenaphthene, while, Te is further away (*i.e.,* the out-of-plane displacements were 0.032 Å for Se and 0.403 Å for Te). In contrast, in **3.1b** and **3.1c**, both atoms are almost the same distance apart from the acenaphthene ring, being **3.1c** the further of the two, (*i.e.,* with out-of-plane displacement of 0.195 Å and 0.137 Å for Se and Te in **3.1b**, and 0.335 Å and 0.361 Å for Se and Te in **3.1c**). This is clearly observed in Figure 3.16. The distortion of the backbone is studied with the torsion angles, which vary from 170° to 177° between the three, the smaller value being found in **3.1c**.

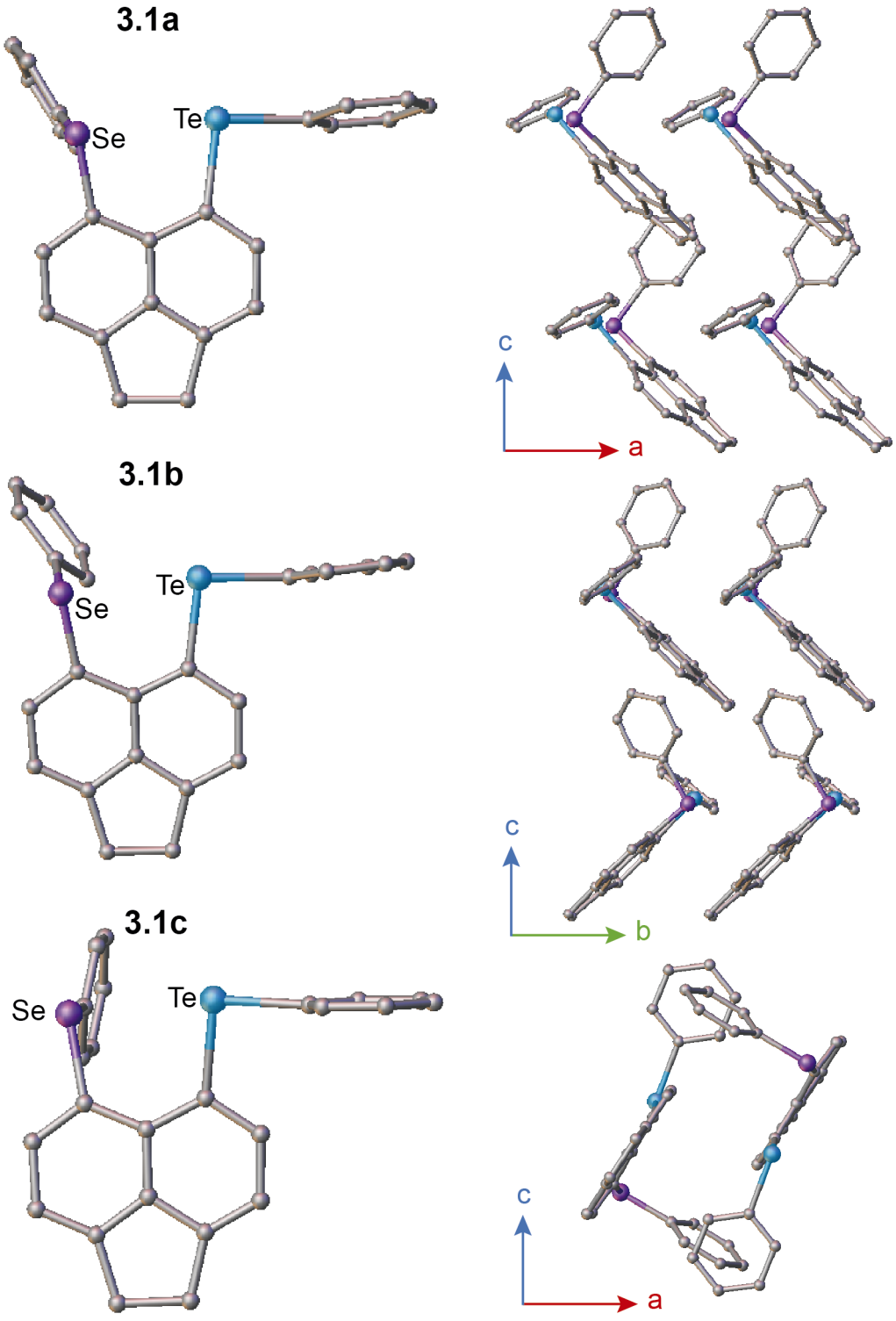

Figure 3.15. Isolated molecules in the asymmetric unit and extended crystal packing motifs showing the unit cell for the three crystal structures of **3.1**, where **3.1a** and **3.1c** are viewed along the b axis and **3.1b** is viewed along the a axis. Hydrogen atoms are omitted for clarity.

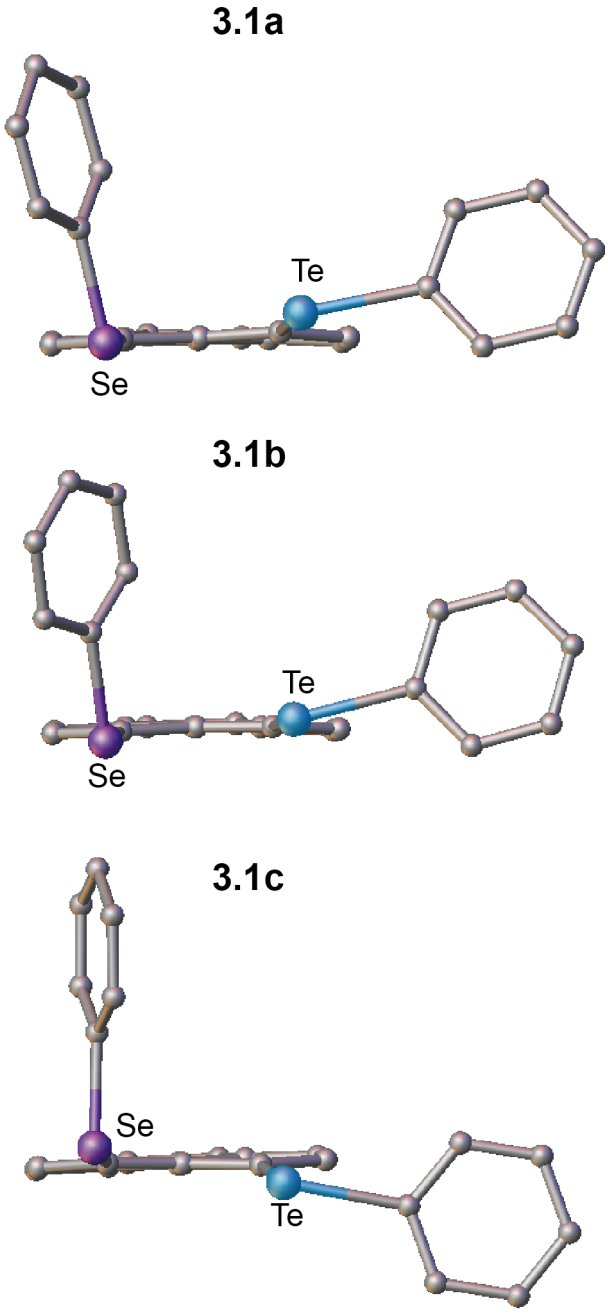

Figure 3.16. Illustration of the conformational differences between the three crystal structures **3.1a**, **3.1b** and **3.1c**. The purple and blue atoms show Se and Te, respectively. Hydrogen atoms are omitted for clarity.

A significant difference was also found for the Te1-C1···C9-Se1 torsion angle between the three polymorphs (*i.e.*, with values from 7.85°, 9.10° and

16° for **3.1b**, **3.1a** and **3.1c**, respectively). This is clearly shown in Figure 3.16, where a bigger distortion of the backbone is found for **3.1c** while, relatively planar backbones are observed in **3.1a** and **3.1b**.

The observation of two resonances in the ^{77}Se, ^{125}Te and ^{13}C aliphatic region NMR spectra in Figure 3.13, 3.14c and 3.14e could be explained by the presence of two polymorphs, **3.1a** and **3.1b**. However, for the newer sample, only one crystal structure could be solved from the re-crystallised sample (**3.1c**), which may explain the main resonances found in ^{77}Se and ^{125}Te NMR spectra, but does not explain the minority phase found as shoulder in both ^{77}Se and ^{125}Te NMR spectra. It must also be noted that the shoulder on the resonance in the ^{77}Se spectrum of the newer sample, is coincident with the second resonance found in the ^{77}Se spectrum of the old sample as shown in Figure 3.17. This suggests that the second resonance in the older sample (B) is one of the polymorphs (**3.1a** and **3.1b**) identified in this sample.

In order to identify which polymorph corresponds to which resonance, DFT calculations of the three crystal structures (**3.1a**, **3.1b** and **3.1c**) were performed using the CASTEP DFT code version 7, described previously in the experimental section. The results are summarised in Table 3.8, and confirm that the **3.1a** is expected to exhibit the smallest isotropic shielding σ_{iso} (^{77}Se), yielding a higher chemical shift, and that **3.1c** would have the highest isotropic shielding σ_{iso} (^{77}Se), giving a lower chemical shift. This suggests that the resonance A in the ^{77}Se spectra of the sample studied previously corresponds to **3.1a**, and the resonance C to **3.1c** as shown in Figure 3.17. Similar results are also found for σ_{iso} (^{125}Te) for **3.1a** and **3.1c**, confirming the experimental results observed in Figure 3.17.

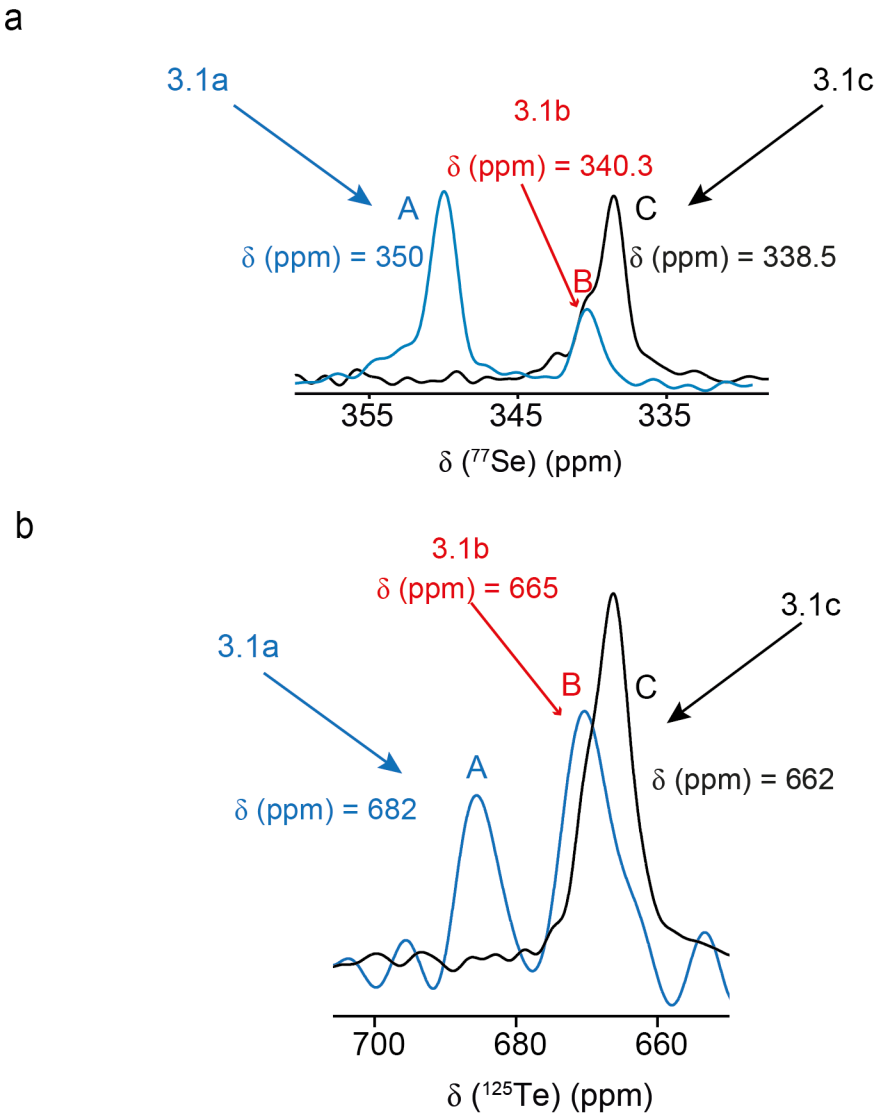

Figure 3.17. ^{77}Se CP (9.4 T, 5 kHz MAS) NMR spectra of two samples of **3.1** for two different samples. An old sample previously reported in the literature represented by the blue spectrum and the newer sample is represented by the black spectrum.

Table 3.8. Calculated ^{77}Se and ^{125}Te isotropic shieldings.

	3.1a	**3.1b**	**3.1c**
σ_{iso} (^{77}Se)	1337.3	1338.6	1366.1
σ_{iso} (^{125}Te)	2016.7	2003.8	2068.9

All σ_{iso}(ppm).

The crystal structure **3.1b** determined from the sample previously studied is thought to result in the shoulders (denotes B in Figure 3.17) at 340.3 and at 665 ppm in the ^{77}Se and ^{125}Te spectra respectively, and is coincident in both samples. In order to investigate this further, a high-throughput "robot-based" crystallography approach was undertaken, studying several crystals from the new sample to see if crystals with structure **3.1b** could also be obtained. This structure was obtained from some of the crystals, suggesting it is present in this sample. However, DFT calculations for **3.1b**, predict σ_{iso} to be closer to that of A (**3.1a**) while, experimentally it appears closer to B. Furthermore, **3.1b** also is predicted to exhibit the smallest isotropic shielding σ_{iso} (^{125}Te), contradicting what is observed experimentally. The differences observed are relatively small compared to the Se and Te shift ranges, and may result from small inaccuracies in the DFT calculations.

The ^{77}Se and ^{125}Te NMR spectra of **3.7,** shown in Figure 3.18a and 3.18b, respectively, also reveal the presence of additional peaks, suggesting a second type of Se and Te is present. However, the crystal structure of **3.7**, determined previously,[1] only contains one molecule in the asymmetric unit. It seems, therefore, that additional peaks must be caused by the presence of another polymorph, as no impurity was found by solution-state NMR, EA, IR and mass spectrometry. The ^{77}Se spectrum shown in Figure 3.18a for **3.7** exhibits two resonances A and B centred at 338.5 and 330.2 ppm, respectively. The shielding anisotropy was also measured experimentally, and shows the span differs by ~61 ppm between the two. The principal components of the CSA tensor are also different, as shown in Table 3.9. The ^{125}Te spectrum of **3.7** shown in Figure 3.18b, also exhibits two resonances, A and B, centred at 607 and 587.3 ppm, respectively.

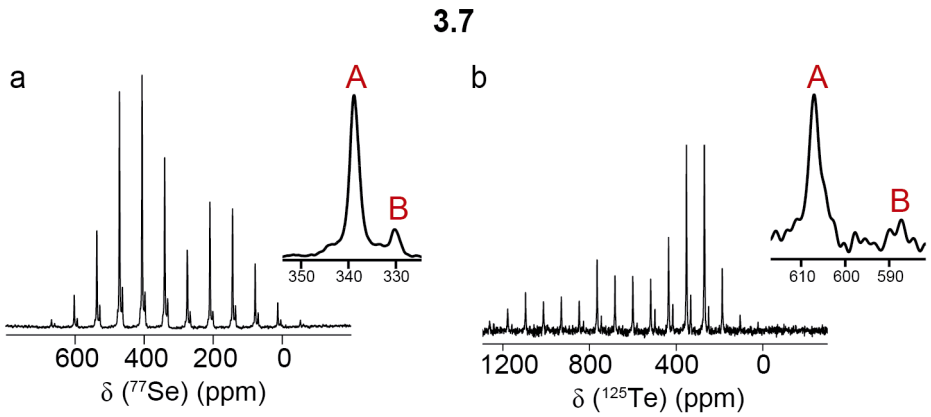

Figure 3.18. (a) ^{77}Se CP (9.4 T, 5 kHz MAS) NMR spectrum of **3.7** and (b) ^{125}Te CP (9.4 T, 10 kHz MAS) NMR spectrum of **3.7**. Isotropic resonances in each spectrum are shown expanded. A and B indicate the different resonances for each polymorph.

Table 3.9. Experimental ^{77}Se and ^{125}Te CSA parameters for compounds **3.7**.

Resonance	δ_{iso}	Ω	κ	δ_{11}	δ_{22}	δ_{33}
^{77}Se NMR, recorded at 9.4 T and 5 kHz MAS						
A[a]	338.5	564.0	0.45	578.8	422.46	14.77
B[a]	330.2	625.4	0.44	597.5	420.9	–27.9
^{125}Te NMR, recorded at 14.1 T and 20 kHz MAS						
A[a]	607.0	1207.8	–0.9	1383.4	261.9	175.7
B[a]	587.3	1093.7	–0.6	1248.0	359.5	154.3

[a] A and B resonances shown in Figure 3.18. All Ω (ppm), δ_{iso}(ppm) δ_{ii}(ppm).

The span extracted for the two differs by ~114 ppm. The principal components of the shielding tensor summarised in Table 3.9 are also very different for the two resonances. This suggests that both polymorphs have different local structure and/or packing. In order to investigate further, **3.7** was crystallised using the same solvent (hexane/DCM mixture) as previously used.[8] Subsequent analysis using single-crystal XRD yielded a second crystal structure. The two crystal structures denoted **3.7a** and **3.7b**

are compared in detail in the Table A5 of Appendix A, where the bond lengths, torsion angles, out-of-plane displacements, *etc.*, are summarised. Structures of the two polymorphs (both as isolated molecules and with crystal packing) are shown in Figure 3.19, with both seen to have just a distinct molecule within the asymmetric unit. From Figure 3.19, it can be seen that the two structures differ significantly, both in terms of their conformations as illustrated in Figure 3.20, and also from the different packing motifs. Structure **3.7a** has only two molecules within the unit cell, forming a tightly packed dimer, whilst **3.7b** has four molecules that stack antiparallel along the c axis.

The strain in both compounds is also different, as shown from the the splay angles, torsion angles and out-of-plane displacement for both of them summarised in the Table A5 of Appendix A. The splay angles vary from 16.43° to 17.98° for **3.7a** and **3.7b**, respectively. The distance between *peri* atoms also vary a little (*i.e.*, from 3.233 Å to 3.247 Å for **3.7a** and **3.7b**, respectively). In Figure 3.20 it can be seen that both Te and Se atom, are far away in opposite directions from the naphthalene plane, the out-of-plane displacement were estimate to be 0.332 Å and 0.929 Å for Te and Se in **3.7a** and 0.244 Å and 0.304 Å for Te and Se in **3.7b**. The distortion of the backbone is studied with the torsion angles, which vary from 170° to 174° between the two. A reasonable difference was also found for the Te1-C1-C9-Se1 torsion angle between the both (*i.e.*, with values of 15° and 13° for **3.7a** and **3.7b**, respectively) This is clearly shown in Figure 3.20, where a bigger distortion of the backbone is found for **3.7a** while, more planar backbone is observed in **3.7b**.

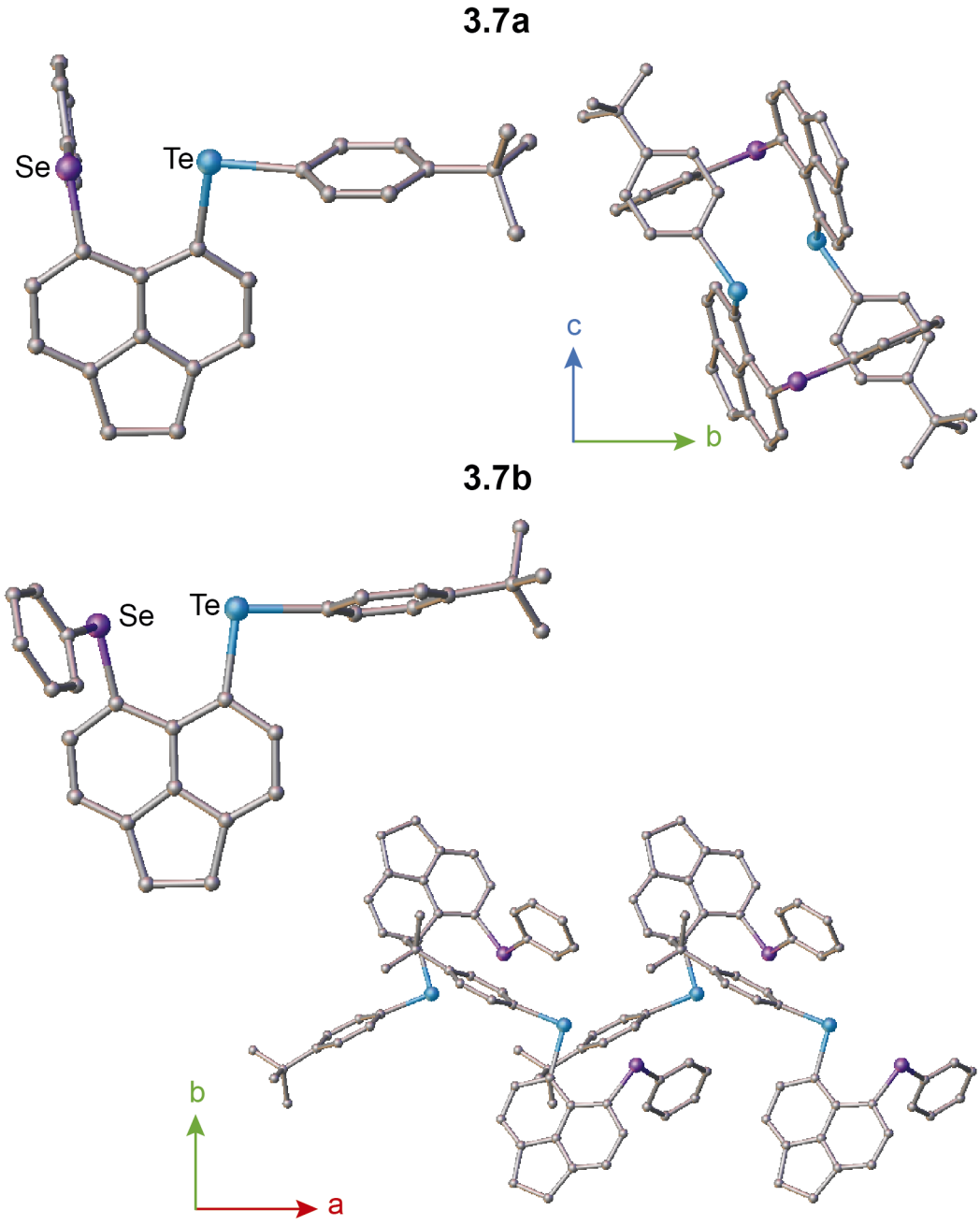

Figure 3.19. Isolated molecules in the asymmetric unit and extended crystal packing motifs showing the unit cell for the **3.7a** and **3.7b**. Structure **3.7a** is viewed along the a axis and **3.7b** is viewed along the c axis. Hydrogen atoms were omitted for clarity.

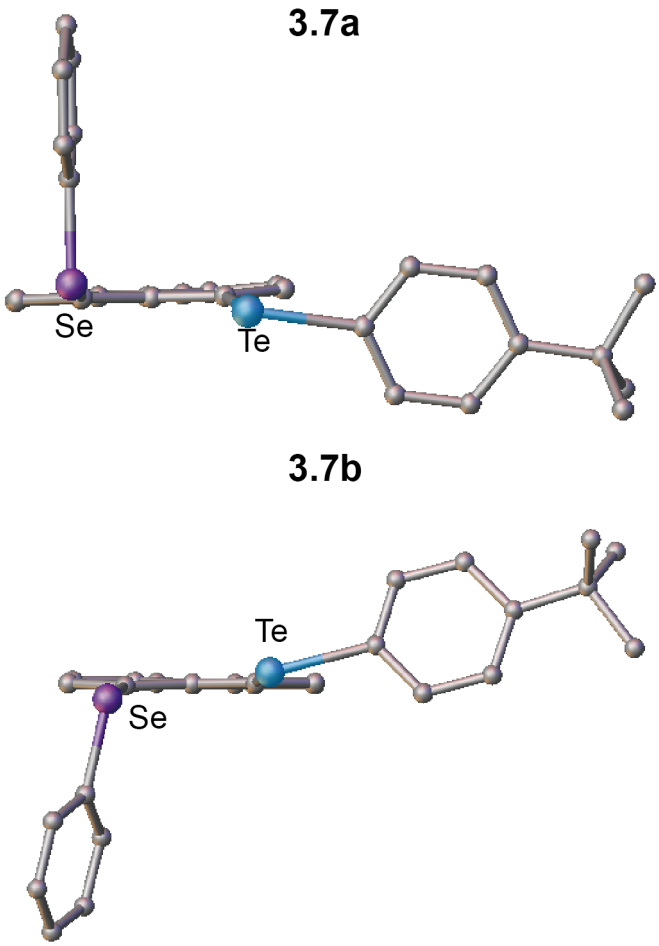

Figure 3.20. Structures showing the conformational differences between **3.7a** and **3.7b**.Hydrogen atoms were omitted for clarity.

As before, DFT calculations were used to help in the spectra assignment of polymorphs **3.7a** and **3.7b** using the CASTEP DFT code version 7. The results are summarised in Table 3.10, and show that **3.7a** exhibits the highest isotropic shielding σ_{iso} (^{77}Se), giving the lowest ^{77}Se chemical shift, and the lowest shielding σ_{iso} (^{125}Te), resulting in the highest ^{125}Te chemical shift. The calculated NMR parameters for **3.7a** and **3.7b** are, however, inconsistent with the experimental data observed in Figure 3.18.

Table 3.10. Calculated ^{77}Se and ^{125}Te NMR parameters for compound **3.7**.

	3.7a	**3.7b**
$\sigma_{iso}(^{77}Se)$	1358.5	1344.2
$\sigma_{iso}(^{125}Te)$	2063.7	2131.6

All σ_{iso}(ppm).

As can be seen in Figure 3.18, the majority of the sample corresponds to the phase labeled A that appears at higher chemical shift in both ^{77}Se and ^{125}Te NMR spectra, and there is a minor phase B that appears at lower chemical shift in both ^{77}Se and ^{125}Te NMR spectra. Therefore, the spectra cannot be assigned just using the calculated parameters, as it is not clear which phase (A or B) corresponds to structures **3.7a** and **3.7b**.

The comparison of the simulated powder XRD pattern from each crystal structure (**3.7a** and **3.7b**) with the experimental powder XRD pattern for the bulk sample could, in principle, help to assign which resonance results from which phase in the ^{77}Se and ^{125}Te spectra. As can be seen in Figure 3.21c, the peaks between 5° and 10° in the experimental powder pattern have lower intensities than predicted as a result of preferential orientation of the molecules. This results from the packing of the sample in a disc and can generally be avoided by performing a powder XRD experiment using a capillary. However, due to the loss of the small amount remaining of the sample in the packing and unpacking processes, this experiment was not performed. Although the intensities of the peaks that appear in the powder XRD pattern cannot be compared to the simulated data, it is still possible to consider relative positions to determine which polymorph forms the majority of the bulk sample.

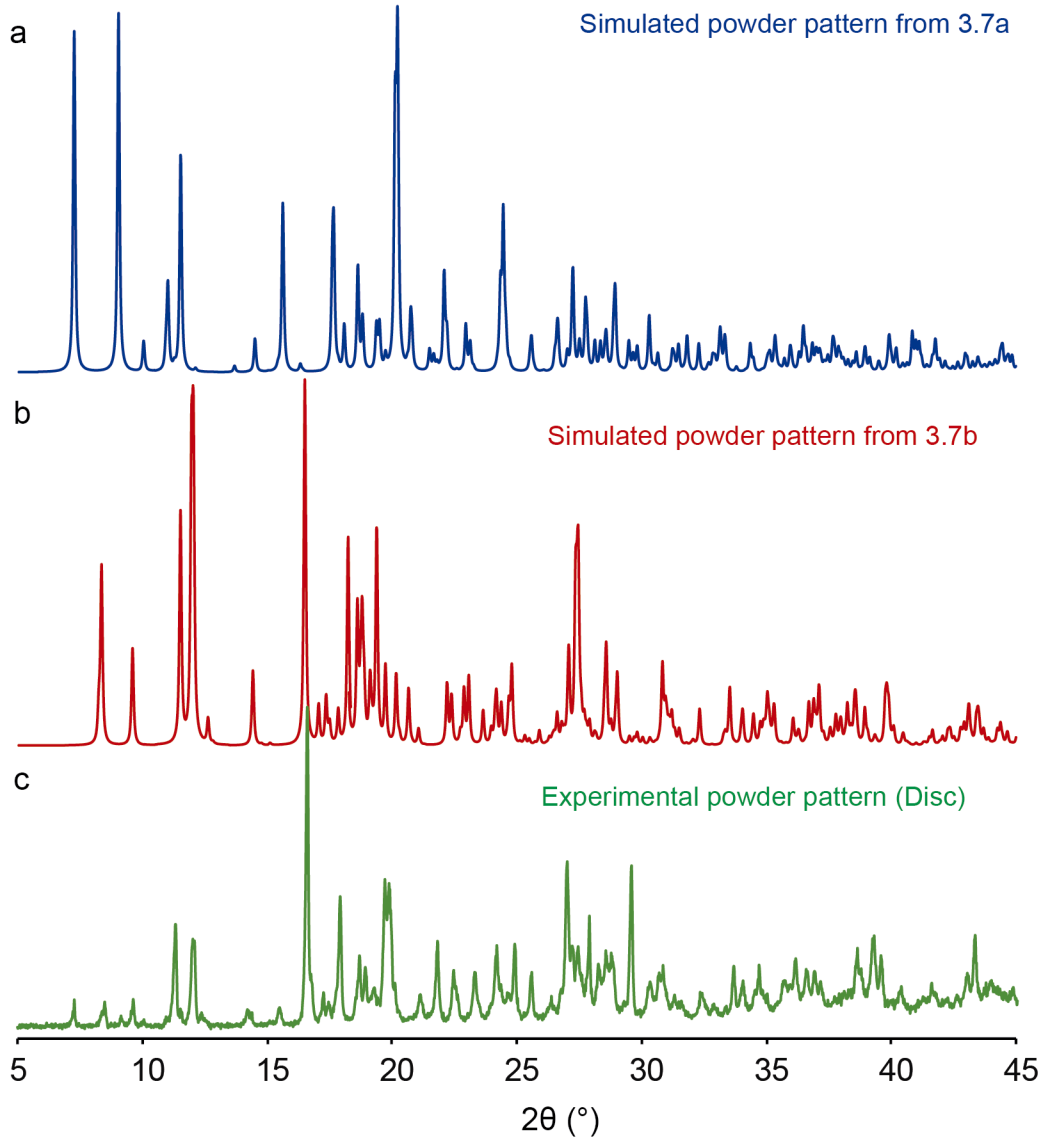

Figure 3.21. Simulated powder XRD patterns for (a) **3.7a** and (b) **3.7b.** (c) Experimental powder XRD pattern from bulk sample of **3.7**.

It can be seen from Figure 3.21 that the experimental powder XRD pattern is more similar to the simulated XRD pattern from **3.7b**, suggesting this corresponds to the majority of the sample, and the lineshape labeled phase A in the spectra in Figure 3.18. Therefore, **3.7a** results in lineshape B and forms the minority of the sample. This demonstrates the need to utilize more than one technique when characterizing these materials.

3.5.3 Calculation of NMR parameters

To gain insight into the structural origins of the ^{77}Se and ^{125}Te magnetic shielding tensors, first-principles GIPAW calculations were performed on full (geometry-optimized) crystal structures obtained from single-crystal X-ray diffraction for each compound. The ^{77}Se magnetic shielding tensors for **3.1 – 3.9** were calculated using CASTEP code version 7, and the values obtained are given in Table 3.11.

As discussed in Chapter 2, in order to transform the absolute shielding into a chemical shift, a reference, σ_{ref} is needed. This reference can be determined by plotting calculated σ_{iso} against the experimental δ_{iso} obtained for a range of compounds, using a simple linear regression approach. Normally, this plot should yield with a gradient of 1, and the value of the σ_{ref} is taken when the y-intercept is zero. However, this ideal situation seldom occurs, and the scaling factor is usually considered to determine σ_{ref}. As seen in Figure 3.22a, σ_{ref} was determined to be 1959.4 ppm for ^{77}Se. A plot of δ_{iso}^{exp} *vs* δ_{iso}^{calc} is shown in Figure 3.22b. In this plot, good agreement ($R^2 = 0.82$) between experimental and calculated values is observed between the two. A plot of experimental against calculated Ω for ^{77}Se shown in Figure 3.22c, shows the points scattered around the line of perfect agreement (shown as a dashed line), confirming that there is a overall tendency of calculations to under- or overestimate Ω, depending on the compound, while all of the δ_{ii}^{calc} principal components were generally overestimated in comparison to the experimental values, as shown in Figure 3.22d.

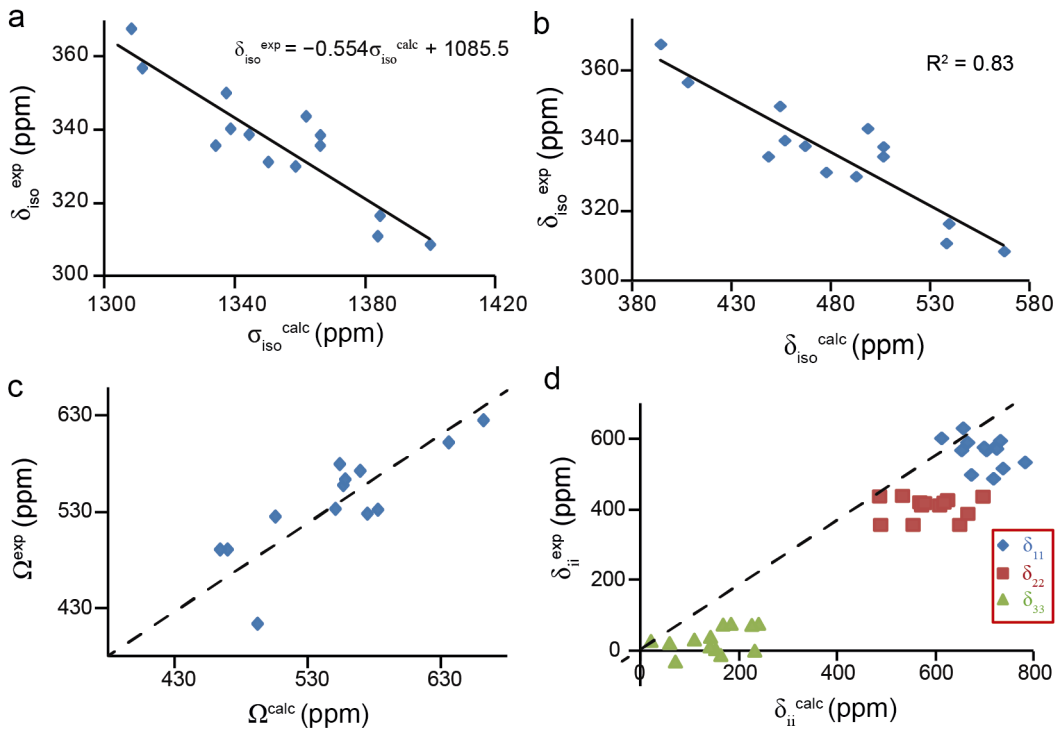

Figure 3.22. Plots of ^{77}Se (a) δ_{iso}^{exp} *vs* σ_{iso}^{calc}, (b) δ_{iso}^{exp} *vs* δ_{iso}^{calc}, (c) Ω^{exp} *vs* Ω^{calc} and (d) δ_{ii}^{exp} *vs* δ_{ii}^{calc}, for **3.1** – **3.9**. Dashed lines represent perfect agreement between calculated and experimental results.

Table 3.11. Calculated ^{77}Se anisotropic shielding parameters.

	3.1a	**3.1c**	**3.2**	**3.3**	**3.4**	**3.5**	**3.6**	**3.7a**	**3.7b**	**3.8**	**3.9**
R group	Ph	Ph	Fp	Nap	Tip	Ani-p	Ani-o	Tp	Tp	Tol	Mes
Ω	556.7	569.4	582.7	554.1	575.8	505.7	469.7 464.2	662.0	558.2	492.3 550.8	635.9
κ	0.6	0.6	0.6	0.7	0.8	0.5	0.3 0.3	0.7	0.5	0.7 0.5	0.5
δ_{11}	665.5	721.5	724.5	612.5	737.5	673.1	653.3 703.9	732.2	699.0	718.1 782.6	656.4
δ_{22}	567.9	624.4	608.2	532.6	696.6	571.5	488.1 554.2	577.7	617.2	649.1 665.7	485.8
δ_{33}	108.8	152.1	141.7	58.4	162.7	167.3	183.5 239.7	70.1	140.8	225.8 231.7	20.4

All Ω (ppm), δ_{iso}(ppm) δ_{ii}(ppm).

The ^{125}Te magnetic shielding tensors for **3.1 – 3.9** were also predicted using CASTEP 7, and the parameters are summarised in Table 3.12. A value of σ_{ref} was also determined, as described previously, using linear regression from a plot of δ_{iso}^{exp} *vs* σ_{iso}^{calc}, shown in Figure 3.23a and by also using scaling factor. The value σ_{ref} was determined to be 2827.9 ppm. Figure 3.23b shows a plot of δ_{iso}^{exp} against δ_{iso}^{calc}, which reveals a poorer correlation ($R^2 = 0.77$) than seen for ^{77}Se data. A plot of Ω^{exp} vs Ω^{calc} for ^{125}Te shown in Figure 3.23c, shows the points scattered around the line of perfect agreement (shown as a dashed line), confirming that there is a overall tendency of calculations to underestimate the Ω, with a maximum difference between calculated and experimental values of 344 ppm. This also occurs for δ_{ii}^{calc} that were generally underestimated in comparison to the experimental ones as shown in Figure 3.23d.

It is well known in the literature that the theoretical study of heavy atoms, such as Se and Te, represents a challenge for computation as relativistic effects may need to be accounted for in order to properly describe the NMR parameters, as discussed in Chapter 2. Demko *et al*[11] studied the effect of different relativistic levels of theory on calculated magnetic shielding tensors, and compared these to the experimental values, for a series of organic, organometallics and inorganic selenium-containing materials. The levels of theory considered were non-relativistic, scalar-relativistic and spin-orbit relativistic. The results showed that although the isotropic chemical shifts could be calculated approximately equally well by all methods, relativistic contributions to the magnetic shielding tensor were found to be significant for cases where selenium was directly bonded to an another heavy atom, and of less importance for compounds in which selenium was the only heavy atom.

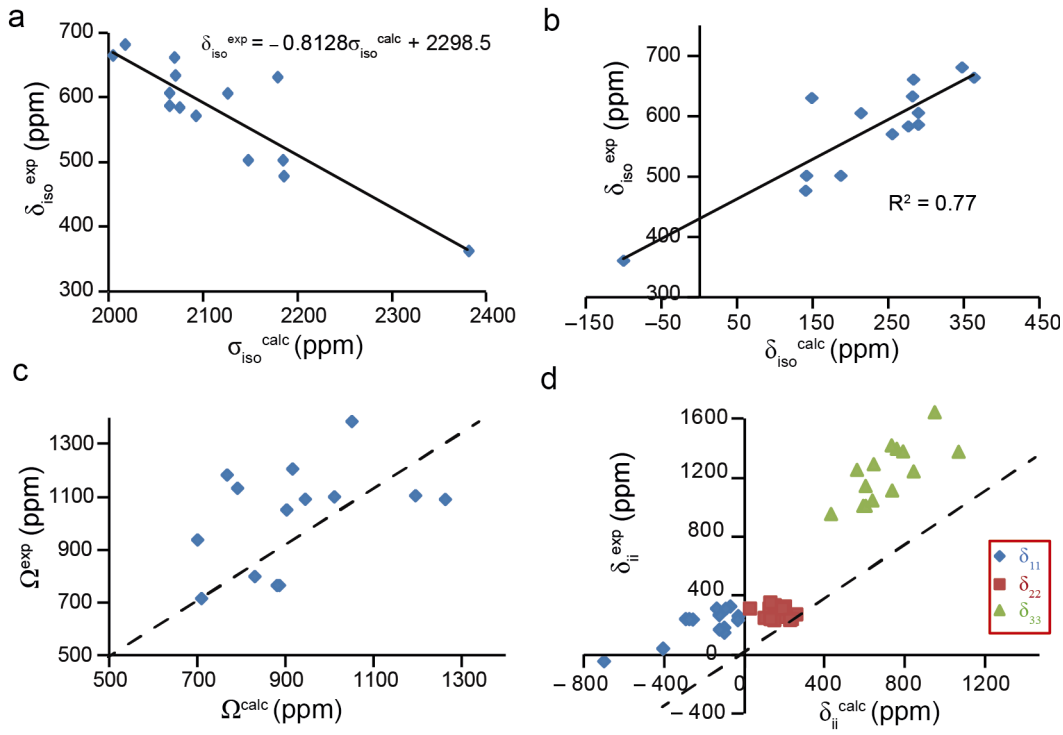

Figure 3.23. Plots of ^{125}Te (a) δ_{iso}^{exp} *vs* σ_{iso}^{calc}, (b) δ_{iso}^{exp} *vs* δ_{iso}^{calc}, (c) Ω^{exp} *vs* Ω^{calc} and (d) δ_{ii}^{exp} *vs* δ_{ii}^{calc}, for **3.1** – **3.9**. Dashed lines represent perfect agreement between calculated and experimental results.

Table 3.12. Calculated ^{125}Te anisotropic shielding parameters.

	3.1a	**3.1b**	**3.1c**	**3.2**	**3.3**	**3.4**	**3.5**	**3.6**	**3.7a**	**3.7b**	**3.8**	**3.9**
R group	Ph	Ph	Ph	Fp	Nap	Tip	Ani-p	Ani-o	Tp	Tp	Tol	Mes
Ω	1050	1194	791	767	902	1262	700	886 881	944	915	709 830	1010
κ	–0.4	–0.5	– 0.6	– 0.5	0.1	0.5	–0.5	–0.0 0.1	–0.5	–0.3	– 0.2 – 0.3	0.2
δ_{11}	947	1066	758	732	643	430	559	590 603	842	789	636 735	602
δ_{22}	196	149	122	146	256	99	25	127 234	127	204	200 187	225
δ_{33}	–103	–128	–33	–35	– 260	–832	–141	–295 –278	– 102	– 126	–73 –95	–408

All Ω (ppm), δ_{iso}(ppm) δ_{ii}(ppm).

In the series of compounds studied by Demko *et al*,[11] δ_{33} was generally underestimated and δ_{11} was overestimated, typically resulting in an overestimation of the calculated Ω by all relativistic levels of theory. However, for the cases where selenium was bonded to another heavy atom, the Ω^{calc}, using a non-relativistic level of theory, was considerably underestimated in comparison to the rest of compounds, suggesting that in this case, non-relativistic calculations cannot reproduce accurately the principal components of the magnetic shielding tensor.

In this chapter, although Se and Te atoms are not directly bonded, they are very close in space and a weak interaction is expected to be present between them, as evidenced by the large J couplings, which may suggest that accounting for relativistic effects could allow more accurate calculation of the shielding tensors.

3.5.4 Accounting for relativistic effects

The GIPAW calculations used previously were carried out with version 7 of the CASTEP code, which approximates scalar relativistic effects and does not account for spin-orbit relativistic effects. Therefore, in order to evaluate the effect of these different approximations to relativistic effects (spin-orbit ZORA and scalar ZORA) on the isotropic and anisotropic components of the ^{77}Se and ^{125}Te shielding for all compounds, calculations were carried out using the Amsterdam Density Functional (ADF) program package on a molecule isolated from the previously-optimized crystal structure.

Plots of σ_{iso}^{calc} for ^{77}Se and ^{125}Te comparing full relativistic effects (*i.e.,* including spin-orbit effects) *vs* scalar (ZORA) relativistic effects for the acenaphthene series are shown in Figure 3.24a and 3.24b respectively. These plots show a clear correlation for both nuclei, with R^2 = 0.99,

indicating that there is no effect on the isotropic magnetic shielding and consequently on the chemical shift, as previously shown by Demko *et al*.[11] However, as shown in Figures 3.24c and 3.24d, computing the span (Ω) with different levels of relativistic treatment has a significant effect for ^{125}Te (Figure 3.24d), and a much smaller effect for ^{77}Se (Figure 3.24c).

Figure 3.24d shows a very poor agreement between scalar and full relativistic effects, where the scalar values are underestimated in comparison to the full relativistic values by 245 – 369 ppm. A dashed line indicating the perfect agreement between the two shows that all the values are underneath the line, except for **3.4**, which presents the smallest difference between both relativistic levels (~17.9 ppm). The compounds with relatively large θ, such as **3.3**, **3.4**, **3.6** and **3.9**, do not exhibit larger differences with respect to level of relativity, which indicates that the disagreement found is not related to crystal packing effects. Accounting for spin-orbit relativity could decrease the difference between calculated and experimental span for ^{125}Te, for which values were underestimated, possibly as an approximation to scalar relativity was used in the CASTEP calculations. Unfortunately, this could not be addressed yet by including full relativistic in the periodic CASTEP calculations, as this has not yet been implemented.

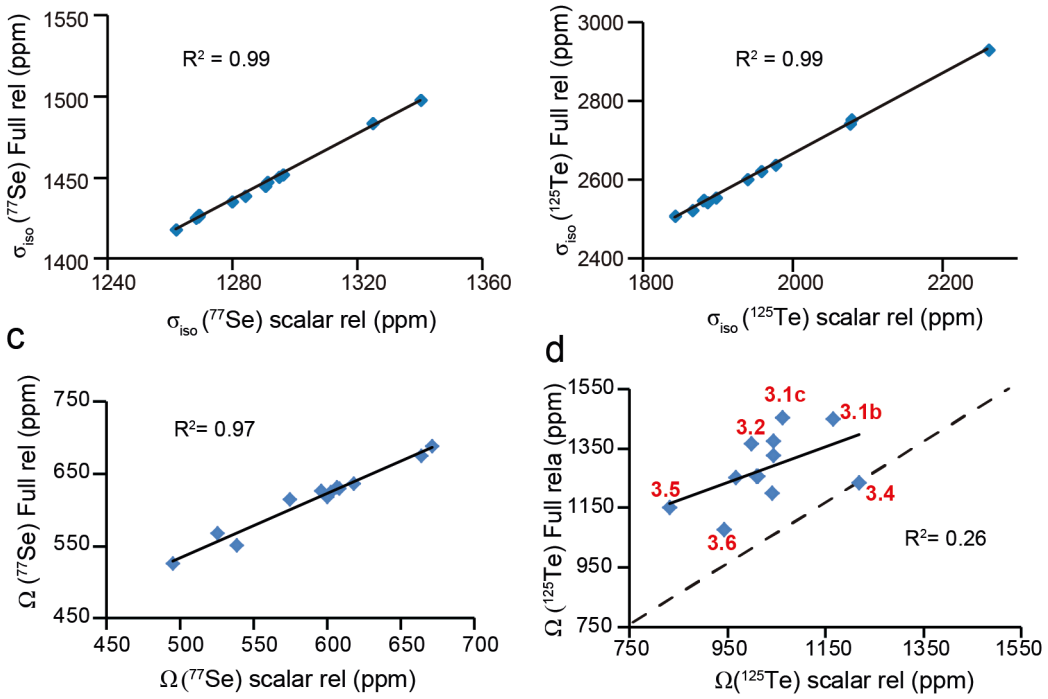

Figure 3.24. Plots of calculated (a, b) $\sigma_{iso}^{Full\ rel}$ *vs* $\sigma_{iso}^{Scalar\ rel}$ of ^{77}Se and ^{125}Te, respectively for **3.1** – **3.9** and (c, d) $\Omega_{iso}^{Full\ rel}$ *vs* $\Omega_{iso}^{Scalar\ rel}$ of ^{77}Se and ^{125}Te, respectively for **3.1** – **3.9**. Calculations were carried using ADF and molecules extracted from a previously optimized structure. Dashed lines represent perfect agreement between calculated and experimental results.

3.5.5 Dynamics

DFT calculations are carried out at 0 K. Therefore, any variation of the NMR parameters with temperature will not be taken into account. This, in principle, could explain some or all of the disagreement between the calculated isotropic chemical shift and experimental values. Therefore, ^{77}Se CP MAS NMR spectra for all compounds except **3.3** and **3.6** (which were unavailable due to decomposition) were measured at three different temperatures, 278, 298 and 323 K, in order to investigate any temperature dependence of the isotropic chemical shift that could, in part, explain the disagreement between δ_{iso}^{calc} and δ_{iso}^{exp} found for ^{77}Se and ^{125}Te.

As shown in Figure 3.25, the isotropic chemical shift for all compounds undergoes a downfield shift with increasing temperature of the order of ~1 to 3 ppm (depending on the sample) over the temperature range studied. Furthermore, variation in the spectral intensities is observed, between the 278 K spectra (blue), which generally appear more intense than the 298 K (red) and the 323 K (black), with the exception of **3.2** and **3.7**, where the spectra at 298 K are most intense. The remaining CSA that is not averaged at 20 kHz MAS, appears approximately equal at all three temperatures, meaning that the intensity change cannot be attributed to a re-distribution of signal intensity among the spinning sidebands, as shown in Figure 3.26, for **3.4**. It must be noted, that all three experiments were carried out after optimization and tuning at 298 K. Regardless, under normal circumstances the tuning would not be expected to vary significantly over the time taken to record the three spectra (*i.e.,* as the spectra were recorded with automatic temperature change), the detuning of the spectra could, in principle, explain the intensity reduction. In order to ensure that this was not the case, some of the experiments were repeated with retuning at each temperature. The results show that the same decrease in signal intensity is observed. Another explanation for that effect must lie in relaxation processes. It is well known that T_1 typically increases with temperature, which can only result in an increase in intensity, this is in contrast to what is observed experimentally (*i.e.,* a reduction in intensity is observed as the temperature increases). Therefore, in order to investigate this further, the T_1 time constant was measured for **3.5** at three different temperatures (273, 298 and 323 K).

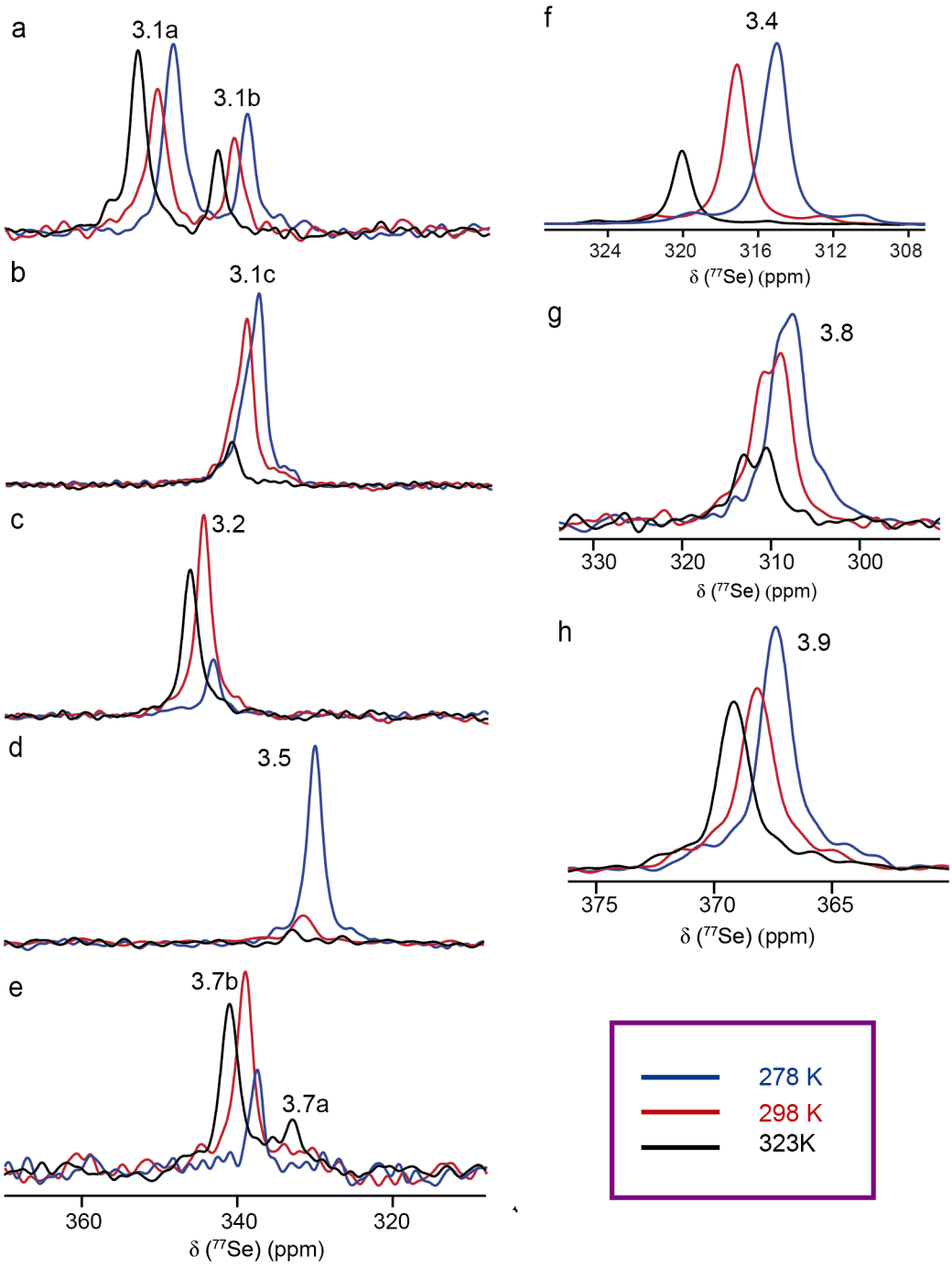

Figure 3.25. ^{77}Se CP (recorded at 9.4 T, 20 kHz MAS) NMR spectra of (a) **3.1a** and **3.1b**, (b) **3.1c**, (c) **3.2**, (d) **3.5**, (e) **3.7**, (f) **3.4**, (g) **3.8** and (h) **3.9**. Only isotropic resonances are shown in each spectrum for clarity. The blue spectra were recorded at 278 K, the red at 298 K and the black one at 323 K.

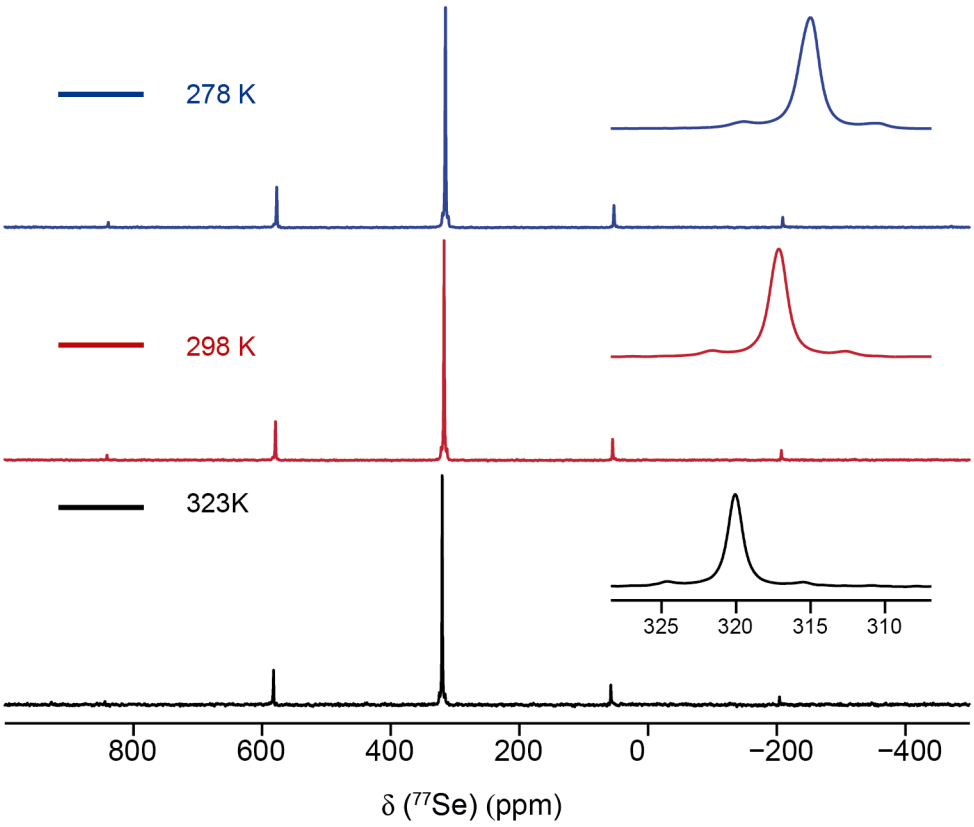

Figure 3.26. ^{77}Se CP (recorded at 9.4 T, 20 kHz MAS) NMR spectra of **3.4** were recorded at 278 K (blue), 298 K (red) and at 323 K (black). The sideband manifold is observed in each spectrum and the isotropic resonances are shown in the insets.

The results show that there is an increase in T_1 as the temperature increased, as expected, suggesting that T_1 relaxation is not responsible for the intensity change. Another possibility might be a poor CP efficiency, as a result of faster $T_{1\rho}$ relaxation during the spin-lock pulses.

It is clear from Figure 3.25, that even different polymorphs of the same compound (such as **3.1a**, **3.1b** and **3.1c)** exhibit different dynamic behavior suggesting different relaxation rates and, therefore, different mobility depending on the packing motifs. Polymorphs **3.1a** and **3.1b** seems to display similar reduction in intensity, while **3.1c** exhibits a

dramatic change in intensity between 298 and 323 K. This similar behavior between **3.1a** and **3.1b** can be linked to their more similar packing motifs, while a different packing is observed in **3.1c**, as shown previously in Figure 3.15.

3.6 Conclusions

In this chapter, a series of nine mixed *peri*-substituted acenaphthenes have been successfully characterised by natural abundance ^{77}Se and ^{125}Te solid-state NMR. It is clear from the beginning of this chapter that these are both challenging nuclei and time consuming experiments (see Table A1 and A2 of Appendix A for experimental details). However, the spectra are very sensitive to changes in molecular structure and, therefore, represent good tools for studying these chalcogen-containing organocompounds.

The Se and Te spectra of all compounds exhibit a single resonance except for **3.8**, where two resonances are observed**,** in agreement with structures from single-crystal X-ray diffraction. An exception is **3.6**, which presents two molecules in the asymmetric unit but only one resonance is resolved in the ^{77}Se and ^{125}Te spectra. The J(^{77}Se–^{125}Te) couplings were determined for some compounds despite the time-consuming experiments (see Table A1 and A2 of Appendix A) required to resolve the J coupling that appears as satellites in the spectra. For **3.2**, **3.4** and **3.5**, the J coupling is in good agreement with the solution-state NMR value, while for **3.9**, the experimental value appears closer to that predicted by molecular DFT calculations in previous work.[1] Compound **3.9** has a very bulky aryl group attached to Te with $\theta = 121.55°$, but this is also the case for **3.4** ($\theta = 134.98°$), for which little difference in J coupling was found between solution- and solid-state measurements, suggesting that the steric hindrance is not the

principal reason for the J value of **3.9** being closer to that from DFT. No polymorphs have been found for this compound by NMR and no additional peaks are present in the ^{77}Se and ^{125}Te for **3.9** confirming the presence of only one environment and suggesting the crystal structure determined by diffraction is relevant to the bulk material. The difference in chemical shift found between solution and solid for **3.9** is 23 and 50 ppm for ^{77}Se and ^{125}Te, respectively. This could suggest a change in conformation imposed by the crystal packing, while a smaller difference is found for **3.4**. If there is a change in the conformation in the solid state, it could be that the distance between Se and Te is modified, resulting in a change of the J value. Unfortunately, it was not possible to measure the J(^{77}Se–^{125}Te) coupling for all compounds, as some of them decomposed after a while (*e.g.,* **3.3**) and some of them exhibit broadened resonances, sometimes owing to the presence of two molecules in the unit cell that have very similar environments (*e.g.,* **3.6**, **3.8**) or owing to the presence of polymorphs (*e.g.,* **3.7**, **3.1**). In any case, as the J(^{77}Se–^{125}Te) coupling is observed as satellites due to the abundance of ^{125}Te (7.1%), the determination of J(^{77}Se–^{125}Te) contains an error (between 0 – 50 Hz), unless very long experiments with very high sensitivity were recorded, which sometimes were not possible as that would involve weeks of spectral acquisition.

For the compounds studied here, the environment around Se remains relatively unchanged while that of Te involves the substitution by different aryl-groups. In order to quantify the steric differences introduced by different R groups, a steric parameter, θ, was defined. The poor correlation of isotropic chemical shift in solution or solid *vs* θ for Se confirms the limited effect that the Te substitution has though the series. This aryl-substitution could, in principle, vary the distances between Se

and Te affecting in that way the J coupling. However no correlation between the J coupling in solution and θ was found in the previous study.[1] In contrast, the Te environment is shown to be affected between solution and the solid state, as the chemical shift undergoes a upfield shift with increasing θ.

The chemical shift differences found in the series between solid- and solution-state NMR spectra for both nuclei, and the poor correlation of anisotropic shielding parameters with θ, suggest that the behavior in solids is more complex than in solution, and that θ is not the only parameter affecting the nuclear environments. The other effects not present in solution include; unaveraged dynamics, the presence of different polymorphs and the effects of crystal packing in solids. It was found in this work that all these effects may in fact contribute to the NMR parameters observed in the solid state.

Solid-state NMR spectroscopy was shown to be an excellent tool for the study and discovery of polymorphism, as it probes the bulk material, but the combination of other techniques, such as X-ray diffraction and DFT calculations, can be very helpful in identifying and assigning the spectra. In this work, resonances in the spectra of polymorphs of **3.1** and **3.7** were assigned using a range of techniques. In both cases, DFT calculations showed some disagreement and inconsistency with the experiments, probably as a result of dynamics and relativistic effects, as discussed in this chapter.

The NMR parameters for all compounds were calculated using the periodic CASTEP code, and a reasonable correlation between calculated isotropic chemical shifts for ^{77}Se and ^{125}Te with experiment was found. However, this work demonstrates that full and accurate treatment of relativistic effects is necessary for calculations of the anisotropic

components of the magnetic shielding tensor for Te. The poor correlation observed between experimental and calculated Ω for ^{125}Te was thus explained. In contrast, little apparent effect is observed for ^{77}Se with the different treatments of relativity. It is noted that other phenomena, such as thermal motion, which is not accounted for in calculations, could be responsible for discrepancies between computed and experimental NMR parameters. The performance of ^{77}Se CP MAS NMR experiments carried out at three different temperatures demonstrated that thermal motion is present in these systems with relaxation differences and variable isotropic shifts observed, even if some restriction due to the crystal packing must be also present.

This work contributes to the un-explored area of ^{125}Te NMR and probes that as its lighter congener, ^{125}Te is highly sensitive to change in the conformation in the solid state. However, further work is needed in the area of computational studies of those systems in order to get a better representation of the NMR parameters in organotelluride-compounds.

3.7 Future work

Periodic GIPAW calculations including spin-orbit relativistic corrections could, in principle, give better agreement with the experiments, especially for ^{125}Te shielding anisotropy. This can provide more insight into the variation of local structure around the nucleus, but at present cannot be performed. The variation of the conformation can also be studied and even the crystal packing effects by performing calculations in isolated molecules.

Despite the time-consuming nature and cost of the calculations, molecular dynamics could reduce the errors that result from comparing data calculated at 0 K with experiments performed at ~298 K.

3.8 References

1. M. W. Stanford, F. R. Knight, K. S. Athukorala Arachchige, P. Sanz Camacho, S. E. Ashbrook, M. Bühl, A. M. Z. Slawin and J, D. Woollins, *Dalton Trans.*,**2014**, 43, 6548-6560.

2. H. Duddeck, *Prog. Nucl. Magn. Res. Spectrosc*., **1995**, 27, 1-323

3. T. Chivers and R. S. Laitinen, *Chem. Soc. Rev*., **2015**, 44, 1725-1739.

4. A. Nordheider, J. D. Woollins and T. Chivers, *Chem. Rev*., **2015**, 115, 10378-10406.

5. S. Hayashi, K. Matsuiwa and W. Nakanishi, *RSC Adv*., **2014**, 4, 44795-44810.

6. J. Autschbach, "Calculating NMR Chemical Shifts and J-Couplings for Heavy Elements Compounds", *Encyclopedia of Analytical Chemistry*, John Wiley & Sons, Ltd, **2006**.

7. P. Pyykkö, *Annu. Rev. Phys. Chem*., **2012**, 63, 45-64.

8. I. L. Rusakova, Y. Y. Rusakov, L. B. Krivdin, *Magn. Reson. Chem*., **2014**, 52, 500-510.

9. Y. Y. Rusakov, I. L. Rusakova, L. B. Krivdin, *Magn. Reson. Chem*., **2014**, 52, 214-221.

10. Y. Y. Rusakov, L. B. Krivdin, *Magn. Reson. Chem.,* **2015**, 53, 93-98.

11. B. A. Demko, K. Eichele and R. E. Wasylishen, *J. Phys. Chem. A,* **2006**, 110, 13537-13550.

12. C. A. Bayse, *Inorg. Chem.,* **2004**, 43, 1208-1210.

13. B. A. Demko and R. E. Wasylishen, *Prog. Nucl. Magn. Res. Spectrosc.*, **2009**, 54, 208-238.

14. M. Deschamps, C. Roiland, B. Bureau, G. Yang, L. Le Pollès and D. Massiot, *Solid State Nucl. Magn. Reson.*, **2011**, 40, 72-77.

15. K. Sykina, G. Yang, C. Roiland, L. Le Polles, E. Le Fur, C. J. Pickard, B. Bureau and E. Furet, *Phys.Chem. Chem. Phys.*, **2013**, 15, 6284-6292.

16. J. Struppe, Y. Zhang and S. Rozovsky, *J. Phys. Chem. B*, **2015**, 119, 3643-365.

17. B. Bureau, C. Boussard-Plédel, M. Lefloch, J. Troles, F. Smektala and J. Lucas, *J. Phys. Chem. B*, **2005**, 109, 6130-6135.

18. D. Holland, J. Bailey, G. Ward, B. Turner, P. Tierney, R. Dupree, *Solid State Nucl. Magn. Reson.*, **2005**, 27, 16-27.

19. M. J. Collins and J. A. Ripmeester, *J. Am. Chem. Soc.*, **1987**, 109, 4113-4115.

20. M. J. Collins, J. A. Ripmeester and J. F. Sawyer, *J. Am. Chem. Soc.*, **1988**, 110, 8583-8590.

21. R. J. Batchelor, F. W. B. Einstein, I. D. Gay, C. H. W. Jones and R. D. Sharma, *Inorg. Chem.*, **1993**, 32, 4378-4383.

22. I. Orion, J. Rocha, S. Jobic, V. Abadie, R. Brec, C. Fernandez and J.-P. Amoureux, *J. Chem. Soc., Dalton Trans.*, **1997**, 3741-3748.

23. T. G. Edwards, E. L. Gjersing, S. Sen, S. C. Currie, B. G. Aitken, *J. Non-Cryst. Solids.*, **2011**, 357, 3036-3041.

24. F. R. Knight, R. A. M. Randall, K. S. Athukorala Arachchige, L. Wakefield, J. M. Griffin, S. E. Ashbrook, M. Bühl, A. M. Z. Slawin and J. D. Woollins, *Inorg. Chem.*, **2012**, 51, 11087-11097.

25. S. Sternhell, *Org. Magn. Reson.*, **1983**, 21, 770-770.

26. a) M. D. Segall, P. J. D. Lindan, M. J. Probert, C. J. Pickard, P. J. Hasnip, S. J. Clark and M. C. Payne, *J. Phys. Condens. Matter.*, **2002**, 14, 2717-2744; b)

M. D. Segall, S. J. Clark, C. J. Pickard, P. J. Hasnip, M. I. J. Probert, K. Refson and. M. C. Payne, *Z. Kristallogr.,* **2005**, 220, 567-570.

27. C. J. Pickard and F. Mauri, *Phys. Rev. B,* **2001**, 63, 1-12.

28. J. P. Perdew, K. Burke and M. Ernzerhof, *Phys. Rev. Lett.,* **1996**, 77, 3865-3868.

29. J. R. Yates, C. J. Pickard and F. Mauri, *Phys. Rev. B,* **2007**, 76, 1-12.

30. S. Grimme, *J. Comput. Chem*., **2006**, 27, 1787-1799.

31. a) R. J. Hatch and R. E. Rundle, *J. Am. Chem. Soc.,* **1951**, 73, 4321–4324; b) R. E. Rundle, *J. Am. Chem. Soc.,* **1963**, 85, 112–113; c) R. E. Rundle, *J. Am. Chem. Soc.,* **1947**, 69, 1327–1331.

32. a) C. A. Tolman, *J. Am. Chem. Soc*., **1970**, 92, 2953-2956; b) C. A. Tolman, *J. Am. Chem. Soc*., **1970**, 92, 2956-2965; c) C. A. Tolman, *Chem. Rev*., **1977**, 77, 313-348.

33. M. Dračínský, M. Buděšínský, B. Warżajtis, U. Rychlewska, *J. Phys. Chem. A,* **2012**, 116, 680-688.

33. J. M. Griffin, F. R. Knight, G. Hua, J. S. Ferrara, S. W. L. Hogan, J. D. Woollins and S. E. Ashbrook, *J. Phys. Chem. C,* **2011**, 115, 10859-10872.

This page intentionally left blank.

Chapter 4: Studying interactions in chalcogen-phosphorus heterocycles

4.1 Chapter overview

Chalcogen-containing materials often support weak interactions, owing to the large polarizable atoms present in these systems, which lead to unusual magnetic and electronic properties desirable for many applications.[1] The study of these weak interactions is a fundamental aspect of understanding the stability, reactivity and other properties of these systems and in enabling the design of new materials.

In this chapter, the synthesis of a series of novel chalcogen-phosphorus heterocycles is discussed in terms of the stability and reactivity through the series. The incorporation of chalcogens of different sizes and the use of different R groups attached to the phosphorus atoms is studied and with the help of crystallographic data, the strain of the systems in the series is considered. The different environments and behaviour found in solution- and solid-state NMR spectra for these novel heterocycles is discussed. Furthermore, ^{77}Se and ^{31}P solid-state NMR spectroscopy together with DFT calculations is used to understand the spectra of these chalcogen-containing materials, where unexpected signals were present for some of them.

4.2 Acknowledgements

Dr. Jonathan R. Yates, Dr Tim F. G. Green and Dr David McKay are thanked for performing the first-principles J-coupling calculations and

generated the CDD plots presented in this chapter, and the transition-state calculation for **4.5**.
Dr Kasun S. A. Arachchige, Dr David B. Cordes and Prof. Alexandra M. Z. Slawin were essential for the single-crystal structure determinations.
Ms Christin Kirst (a visiting masters student in the Woollins group) is thanked for the synthesis of Nap(S)Ph and Nap(Se)Ph.

4.3 Introduction

Indirect spin-spin J couplings have been used for over 60 years[2] in NMR spectroscopy to obtain structural information on atomic connectivity and bonding.[3] As discussed in previous chapters, this electron-mediated interaction was considered to occur only between formally bonded atoms until 1960, when it was discovered also to exist between atoms that are not formally bonded but are held very close in space, termed "through-space" J-coupling.[4] Typical examples of through-space J coupling involve atoms such as P, F, Se and Te that are forced into close proximity together by rigid molecular backbones, such as *peri*-substituted naphthalenes or acenaphthenes.[5] In solids, fewer examples of through-space J couplings have been reported owing to the limitation in resolving this interaction (*i.e.,* the large inherent linewidths present).[6] Moreover, in all these examples, the through-space interaction is intramolecular, *i.e.,* within the same molecule, and, to date, no interactions between molecules, *i.e., intermolecular*, have been reported (to our knowledge).

In solution, it is well known that the indirect spin-spin coupling cannot be determined between two nuclei that have identical chemical shifts and the same J-coupling interactions to all other nuclei external to the coupled pair.[7] This state is defined in solution as "*magnetically*

equivalent" and the J coupling between the coupled pair is not observable directly in the NMR spectra. However, in solids, the definition of magnetically-equivalent species must be modified as anisotropic interactions (such as dipolar coupling, CSAs and quadrupolar coupling) could be present. Therefore, in solids, the two nuclei must also share the same NMR interaction tensor orientations in order to be considered as magnetically equivalent.[8] This suggests that a pair of nuclei that, in solution, are considered magnetically equivalent, may in fact be, magnetically inequivalent in a solid, for example, if the orientation of the CSA tensor is different.[9] It must be noted that, if the orientation of the CSA tensor is different, at high spinning rates, as the system approaches the "liquid-motion" regime, the spins can behave as A_2 spin system, whereas at lower or intermediate MAS rates, a AB-type behaviour is observed.[10] For two nuclei to share the same tensor orientations and, therefore, be magnetically equivalent in solid, they must be related by a translation and/or inversion elements.[8] In order to study J-couplings in solids, 2D J-resolved spectroscopy is often the technique of choice to yield an accurate measurement of the J coupling owing to the broadened lines observed in the NMR spectrum. J-resolved spectroscopy has the advantages over direct methods, that the inhomogeneities are refocused, as previously discussed, and that it separates the J coupling from the chemical shift.[11]

4.4 Experimental details

4.4.1 X-ray crystallography

Unless otherwise stated, powder X-ray diffraction data presented and discussed in this chapter were acquired at room temperature with a STOE STADIP instrument operated in capillary Debye-Scherrer mode equipped

with a Cu X-ray tube, a primary beam monochromator ($CuK_{\alpha 1}$) and a scintillation position-sensitive linear detector. Typically, 5-50° or 5-40° 2θ ranges were investigated in an overnight experiment.

All crystal structures in this chapter were determined at –100 (1), –148 (1), or –180(1)° using a Rigaku XtaLAB P200 diffractometer with multi-layer mirror monochromated Mo-K_α radiation or Rigaku Saturn70 diffractometer using graphite monochromated Mo-K_α radiation

4.4.2 Solid-state NMR

Solid-state NMR measurements were performed using Bruker Avance III spectrometers, operating at magnetic field strengths of 9.4, 14.1 and 20.0 T. Experiments were carried out using conventional 4- or 2.5-mm MAS probes, with MAS rates between 5 and 12.5 kHz

For ^{31}P, spectra were acquired either directly or using cross polarisation (CP) from ^{1}H with a contact pulse (ramped for ^{1}H) of 1 ms. ^{31}P experiments were carried out at 9.4 and 14.1 T. Chemical shifts are shown referenced relative to 85% H_3PO_4 (aq), using BPO_4 ($\delta(^{31}P)$ = –29.6 ppm) as a secondary reference.

For ^{77}Se, CP MAS experiments (using ramped contact pulse durations of 5-8 ms and ^{1}H TPPM decoupling) were carried out at 9.4, 14.1 and 20.0 T. Chemical shifts are referenced relative to $(CH_3)_2Se$, using the isotropic resonance of solid H_2SeO_3 ($\delta(^{77}Se)$ = 1288.1 ppm) as a secondary reference. The position of the isotropic resonances within the spinning sideband patterns were unambiguously determined by recording a second spectrum at a different MAS rate. In some cases, spectra were also acquired with additional ^{31}P continuous wave (CW) decoupling.

Experimental ^{77}Se NMR parameters were determined by lineshape analysis using Bruker TopSpin software.

Two-dimensional ^{31}P homonuclear J-resolved spectra were acquired at 9.4 T, 14.1 T and 20.0 T with MAS rates between 5 and 12.5 kHz. Owing to long ^{31}P longitudinal relaxation times for **4.3** and **4.6**, CP from ^{1}H was used with a 1 ms contact pulse (ramped for ^{1}H). For the other compounds, transverse magnetization was created directly. In each case, between 32 and 64 transients were averaged for each of 256-320 t_1 increments of 800 μs. In each case, ^{1}H decoupling (CW, $\gamma B_1/2\pi$ ~ 100 kHz) was applied in both t_1 and t_2. For **4.2**, a J-resolved spectrum was also acquired at 14.1 T using rotor-synchronised Hahn-echo pulse train (RS-HEPT)[12] decoupling of ^{77}Se ($\gamma B_1/2\pi$ ~ 62.5 kHz) decoupling during t_1 and ^{1}H decoupling (CW, $\gamma B_1/2\pi$ ~100 kHz) was applied in both t_1 and t_2. 64 transients were averaged for each of 256 t_1 increments of 800 μs. Two-dimensional ^{77}Se heteronuclear J-resolved spectra for **4.4** and **4.5** were acquired at 14.1 T with a MAS rate of 12.5 kHz. In each case, CP from ^{1}H was used with a 5 ms contact pulse (ramped for ^{1}H) and between 96 and 160 transients were averaged for each 300 t_1 increments of 800 μs. ^{1}H decoupling (CW, $\gamma B_1/2\pi$ ~ 100 kHz) was applied in both t_1 and t_2. The heteronuclear J coupling was introduced either by a simultaneous 180° pulse on each coupled spin channel (^{77}Se and ^{31}P) or by decoupling of ^{31}P (CW, $\gamma B_1/2\pi$ ~19 kHz) during the first t_1 evolution period. For controlled-temperature experiments recorded at 9.4 T and 14.1 T, the sample temperature was maintained at 0, 25 or 50 °C using a Bruker BCU-II chiller and Bruker BVT/BVTB-3000 temperature controller and heater booster. The sample temperature (including frictional heating effects arising from sample spinning) was calibrated using the isotropic ^{87}Rb shift of solid RbCl.[13]

4.4.3 First-principles calculations

NMR parameters were calculated using the CASTEP DFT code version 7,[14, 15] employing the gauge-including projector-augmented wave (GIPAW) algorithm,[16] which allows the reconstruction of the all-electron wave function in the presence of a magnetic field. The generalized gradient approximation (GGA) PBE functional[17] was employed and core–valence interactions were described by ultrasoft pseudopotentials.[18] All calculations were performed with the G06 dispersion correction scheme,[19] a planewave energy cutoff of 50 Ry (816 eV) and a k-point spacing of 0.04 2π Å^{-1}. For all calculations, the initial atomic positions and unit cell parameters were taken from the single-crystal X-ray diffraction structures determined in this work. Therefore, prior to the calculation of NMR parameters, geometry optimizations were performed for each structure (using cutoff energies of 50 Ry and k-point spacing of 0.04 2π Å^{-1}). All internal atomic coordinates and lattice parameters were allowed to vary. Calculations were performed using the EaStCHEM Research Computing Facility, which consists of 136 AMD Opteron 280 dual-core processors running at 2.4 GHz, partly connected by Infinipath high-speed interconnects. Calculation wallclock times ranged from 1 to 24 h using 4 nodes (48 cores).

The calculations of the J coupling were performed using ultrasoft pseudopotentials and PAW[18] as implemented in CASTEP 8.0[15] using the PBE[18] functional to describe electronic exchange-correlation, and the G06 dispersion correction scheme,[19] a planewave cut-off energy of 50 Ry and a k-point spacing of 0.04 2π Å^{-1}. The crystal structure was first optimized, without constraints, and then a $2 \times 1 \times 1$ supercell constructed from the optimized geometry. J-coupling calculations were then performed on the

supercell to allow reasonable isolation of the perturbing nucleus. The default on-the-fly pseudopotential set was used, with both a Schrödinger (non-relativistic) and a ZORA (scalar-relativistic)[20] atomic solver used to generate the isolated atomic solutions. The latter calculations include the effects of special relativity at the scalar-relativistic level of theory. Calculations were performed using the EaStCHEM Research Computing Facility, which consists of 136 AMD Opteron 280 dual-core processors running at 2.4 GHz, partly connected by Infinipath high speed interconnects and with the ARCHER UK National Supercomputing Service used for larger supercells, *e.g.,* for **4.3**.

4.5 Objectives

The main objective of this chapter is the synthesis of a series of novel P-S and P-Se heterocycles that are constrained by a rigid organic backbone such as naphthalene. The second objective is the characterisation of these materials using a combination of different techniques (*e.g.,* diffraction techniques, solution- and solid-state NMR and DFT calculations) to try to understand the stability and reactivity of the materials. This means a full understanding of the structures is required, not only at the long-range order but also at the specific local environments in order to fully understand the weak interactions that may or may not occur in these systems.

4.6 Results and discussion

4.6.1. Synthesis approach

Compounds **4.1 – 4.6** were prepared as shown in Scheme 4.1. The starting point is the commercially-available naphthalene, used to obtain naphtho[1,8-cd]1,2-dithiole and naphtho[1,8-cd]1,2-diselenole (described in this thesis as, $NapS_2$ or $NapSe_2$, respectively) prepared as previously reported in literature.[21]

The cleavage of the E–E bond, (E = S, Se or Te) in *peri*-substituted naphthalene compounds, followed by metal incorporation such as platinum, when reacted with *e.g.*, $Pt((P(OPh)_3)_2Cl_2$, creates six-membered ring heterocycles as has been illustrated by Fuller *et al*.[21] Based on this previous synthesis, in this chapter a novel synthetic pathway has been developed to incorporate organophosphorus moieties into the E–E bond. The reaction of $NapS_2$ or $NapSe_2$ with two equivalents of a 1 M solution of lithium triethylborohydride (superhydride) in THF affords the lithiated intermediate that was subsequently reacted with the corresponding ^{i}Pr, ^{t}Bu or Ph dichlorophosphine to afford **4.1** to **4.6** in moderate yields, as shown in Table 4.1.

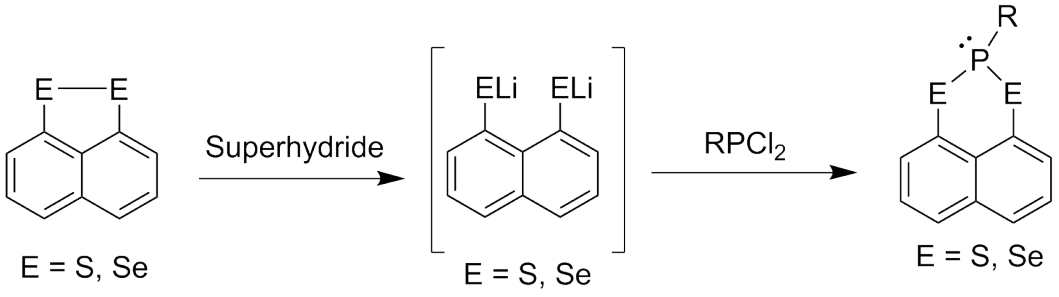

Scheme 4.1*. The preparation of* ***4.1 – 4.6*** *from the starting material naphtho[1,8-cd]1,2-dithiole or naphtho[1,8-cd]1,2-diselenole.*

Table 4.1. Compounds synthesised in this chapter and yields obtained.

Compound	E and R groups	Yield / %
4.1	S, ^{i}Pr	66
4.2	S, ^{t}Bu	72
4.3	S, Ph	73
4.4	Se, ^{i}Pr	45
4.5	Se, ^{t}Bu	48
4.6	Se, Ph	28

The ^{i}Pr and ^{t}Bu sulfur and selenium analogues are stable even in solution or upon exposure to air. In solution, the compounds are stable for up to ~1 week, with subsequent decomposition into the $NapE_2$ precursor favored, rather than an oxidation (to P=O), suggesting that the insertion of a phosphorus atom leads to a more strained system, where tension is relieved *via* elimination of the PR-moiety. However, in the solid state, the compounds are stable upon exposure to air for at least 12 months. In contrast, the stability of the sulfur and selenium Ph analogues is much lower and fast decomposition and oxidation processes were usually observed both by ^{31}P solution- and solid-state NMR spectroscopy. This was extremely important for $NapSe_2PPh$ (**4.6**) and may explain the low yield (28%) obtained for this compound. Due to the instability of **4.6**, it was difficult to obtain all charaterisation data, as the sample decomposed after few weeks even if packed in the rotor inside the glovebox.

As can be seen from Table 4.1, the yields obtained for the sulfur derivatives are higher than their selenium analogues. The reason for this could be the size of the chalcogen. As the size increases, from S to Se, the strain in the system to accommodate that atom, also increases, leading to a

more unfavorable heterocycle. The stability may also be related to bond strength, as the P-Se bond is very fragile and easy to break in comparison to the P-S bond. However, as mentioned previously, both the sulfur and selenium ^{i}Pr and ^{t}Bu compounds are stable in air and all characterisation data were able to be recorded.

All compounds were characterised to check their purity by solution-state NMR, IR, mass spectrometry and microanalysis. This information can be seen in Chapter 6, in great detail for all compounds. ^{13}C CP MAS of all compounds (except **4.2**) were also recorded to check their purity and is shown in Figure B5 of the Appendix B.

4.6.2. Crystal structure analysis

For all compounds only one polymorph was determined for each structure, with the exception of **4.1**, which exhibits three different polymorphs. The asymmetric units and crystal packing motifs showing the unit cell for these polymorphs determined by single-crystal XRD, are shown in Figure 4.1. Suitable crystals were obtained for **4.1a**, **4.2**, **4.4** and **4.5** from hexane, while **4.1b**, **4.1c**, and **4.6** were crystallised by diffusion of hexane into a saturated solution of the compound in dichloromethane. Compound **4.3** was the only one re-crystallised from toluene. All three polymorphs of **4.1**, differ not only in the asymmetric unit, but also in their packing motif. Structure **4.1b** has four molecules in the asymmetric unit, with molecules more separated from each other and where they stack in an antiparallel arrangement along the c axis, while **4.1a** and **4.1c** each have only two molecules in the asymmetric unit, although the extended packing is different between the two. In **4.1a**, the molecules form triangles that stack along the c axis, but with the molecules slightly shifted,

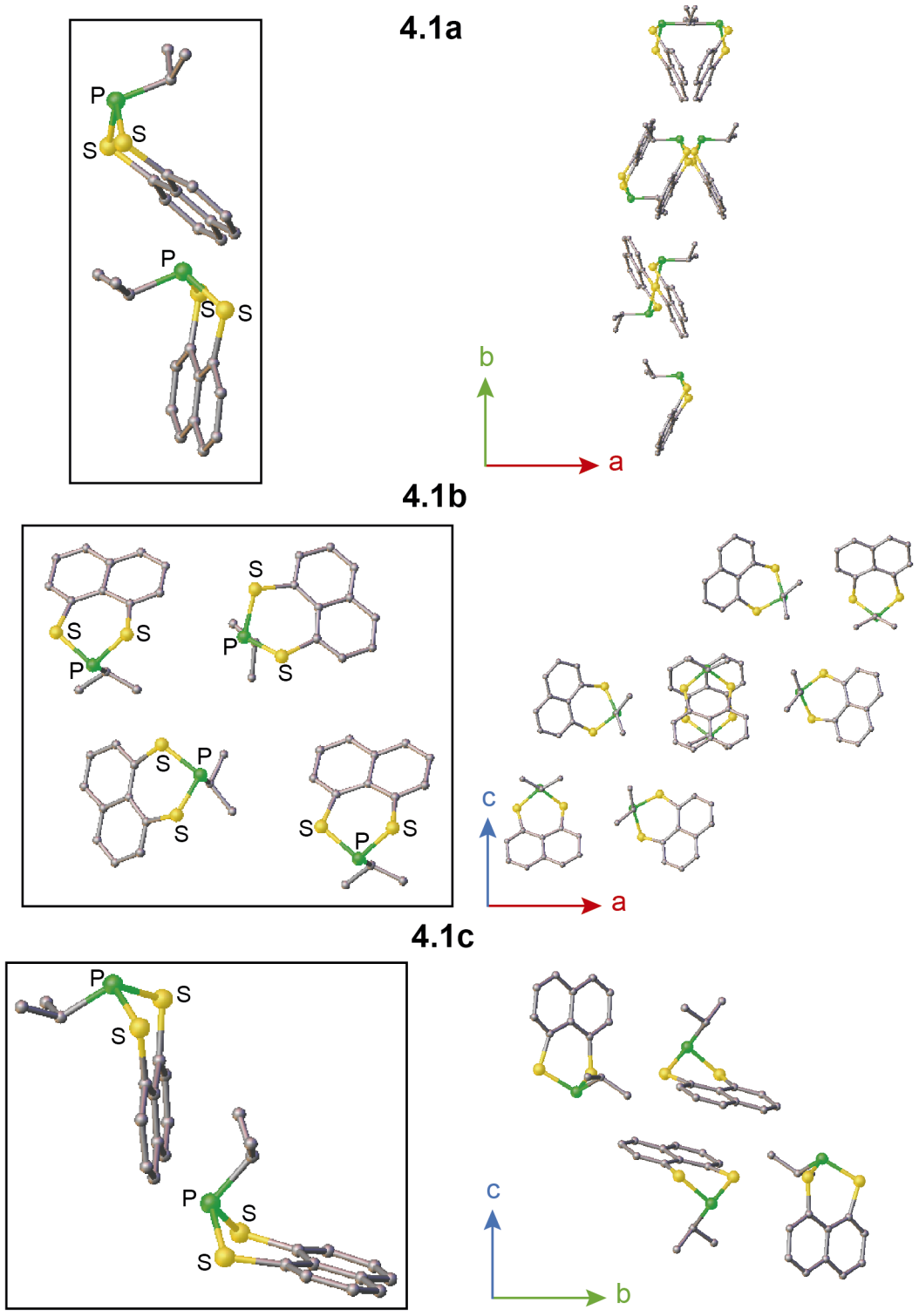

Figure 4.1. Isolated molecules in the asymmetric unit (black box) and crystal packing motifs showing the unit cell for **4.1**, where **4.1a** is viewed along **c, 4.1b** is viewed along the b axis and **4.1c** is view along the a axis. Hydrogen atoms are omitted for clarity.

so that they do not point directly at each other, while in **4.1c** the chains of molecules stack perpendicular to each other along the a axis.

Compounds **4.2** and **4.3** each contain two molecules in the asymmetric unit as shown in Figure 4.2, while all the selenium derivatives (**4.4**, **4.5** and **4.6**) contain an isolated molecule in the asymmetric unit. In **4.2**, the molecules stack in an antiparallel arrangement along a, while in **4.3**, the two molecules form a tightly packed cluster. Compound **4.4** and **4.5** have just two molecules in the unit cell in an antiparallel arrangement. From Figure 4.2, it can be observed that **4.5** and **4.6** exhibit similar packing motifs. The packing for **4.6**, is also very similar to that found for **4.3**.

The strain of the system can be studied by analysing the splay angles, torsion angles of the backbone, and out-of-plane displacements of the *peri* atoms from the X-ray diffraction data,[22] as described in Chapter 1. In order to analyse how the distortion varies through the series of compounds described in this chapter, the crystallographic data for all compounds are summarised in Table B1 – B3 of the Appendix B . The splay angles vary from 18 – 19° for the sulfur compounds, to 23 – 24° for the selenium compounds. This means that the atoms move further apart as the chalcogen size increases, indicating that the selenium compounds have higher steric repulsion. The out-of-plane displacements vary through the series from 0.007 to 0.285 Å, in the sulfur compounds, with an overall increase, as the size of the chalcogen atom increase (*i.e.*, out-of-plane displacements of 0.032 to 0.372 Å for the selenium compounds). The E···E *peri*-distances are less than the respective sum of the van der Waals radii (in all cases between 88 – 89% of the vdW sum), indicating the possibility of weak intramolecular interactions between them.

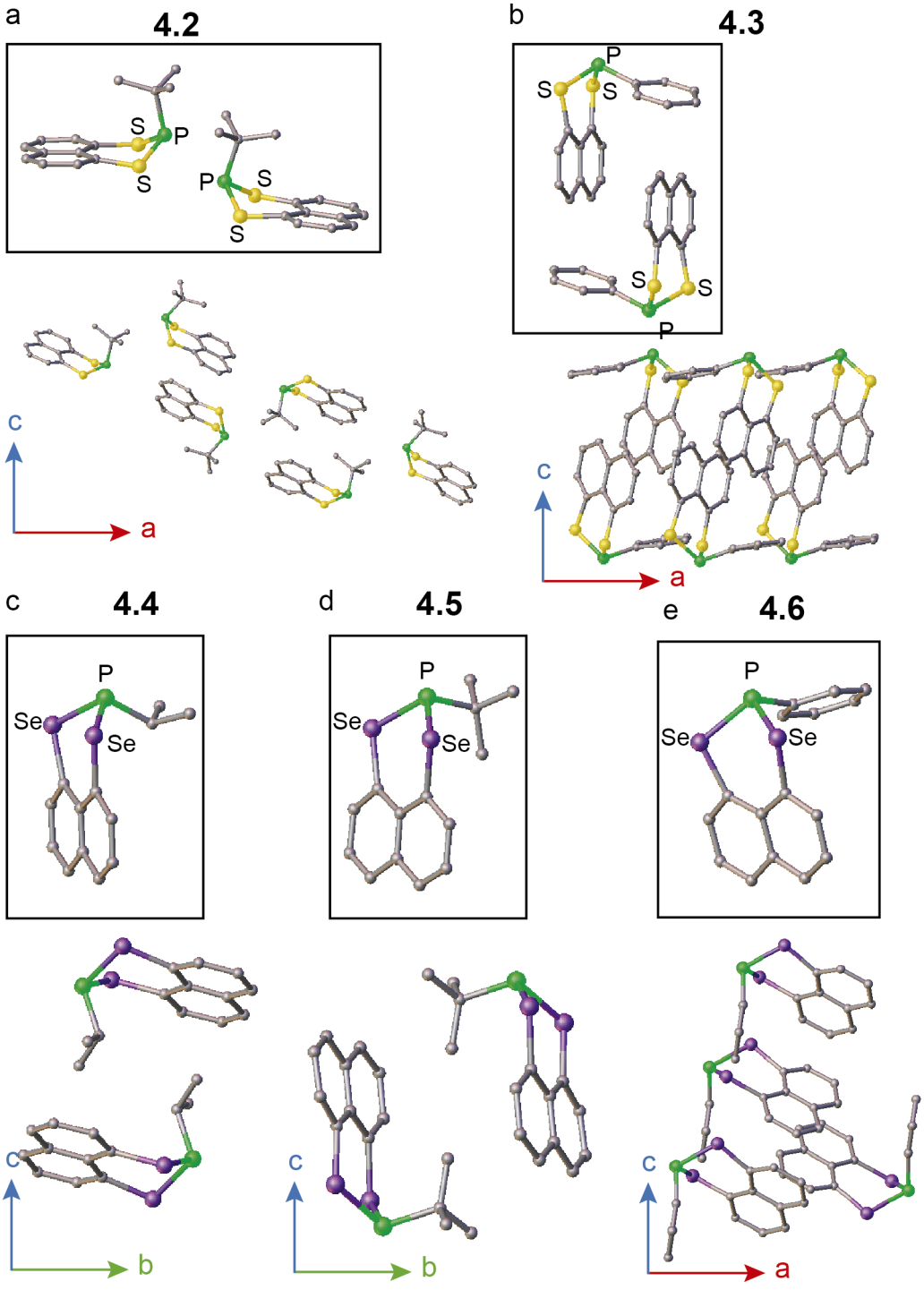

Figure 4.2. Isolated molecules in the asymmetric unit (black box) and crystal packing motifs showing the unit cell for (a) **4.2**, (b) **4.3**, (c) **4.4**, (d) **4.5** and (e) **4.6**, where **4.2**, **4.3** and **4.6** are viewed along the b axis, while **4.4** and **4.5** are viewed along the a axis. Hydrogen atoms have been omitted for clarity.

4.6.3. Solution-state NMR

^{31}P and ^{77}Se NMR data for all compounds is displayed in Table 4.2. The $^{31}P\{^{1}H\}$ NMR spectra recorded in $CDCl_3$ for **4.1** – **4.6** exhibit singlet resonances with satellites due to the $^{1}J(^{31}P\text{-}^{77}Se)$ couplings for **4.4** – **4.6**. Generally, the chemical shift of $^{31}P\{^{1}H\}$ NMR spectra of the sulfur analogues appears deshielded in comparison to the selenium compounds. This is well known in the literature for naphthalene based compounds.[22, 23] Surprisingly, the ^{t}Bu analogues are the most deshielded of the series and appear at a very different chemical shift with respect to the ^{i}Pr compounds, with differences of ~19 and 16 ppm for sulfur and selenium analogues, respectively. This suggests they are chemically very different to each other, while the ^{i}Pr and the Ph analogues seem to have a more similar chemical environment, with a lower difference in chemical shift found between these two (*e.g.*, ~4 and 10 ppm difference for sulfur and selenium analogues, respectively). The trend observed in chemical shift through the series is also unexpected, as normally, the more electron donating a group is, the more shielded the nucleus is expected to be. This would suggest that the expected trend in chemical shift would be Ph < ^{i}Pr < ^{t}Bu, with the Ph analogues the most deshielded and the ^{t}Bu the most shielded. In contrast, the trend observed is the inverse of what might be expected (^{t}Bu analogues appear the most deshielded, followed by ^{i}Pr and then Ph).

The $^{77}Se\{^{1}H\}$ NMR spectra of **4.4** – **4.6** exhibit doublets due to $^{1}J(^{31}P\text{-}^{77}Se)$ couplings. The chemical shifts of ^{77}Se in **4.4**, **4.5** and **4.6** have an inverted trend to that observed for the ^{31}P spectra, with the Ph compound being the most deshielded, then the ^{i}Pr and finally the ^{t}Bu. The $J(^{31}P–^{77}Se)$ coupling decreases ^{t}Bu > Ph > ^{i}Pr as shown in Table 4.2.

Table 4. 2. ^{77}Se and ^{31}P solution-state NMR spectroscopy data

Compound	**4.1**	**4.2**	**4.3**	**4.4**	**4.5**	**4.6**
X,R group	S, ^{i}Pr	S, ^{t}Bu	S, Ph	Se, ^{i}Pr	Se, ^{t}Bu	Se, Ph
δ(^{31}P)NMR	4.7	24.1	1.31	–3.4	12.3	–13.5
δ(^{77}Se) NMR	–	–	–	270.2	210.2	315.4
^{1}J(^{31}P–^{77}Se)	–	–	–	276	302	287

All spectra recorded in $CDCl_3$; δ (ppm), J (Hz).

4.6.4. ^{31}P solid-state NMR characterisation

The ^{31}P MAS NMR spectra of all compounds except **4.2**, which was a sticky solid, were recorded at 14.1 T or 9.4 T and with MAS rates between 5 – 7.5 kHz. The spectra are all shown in Figure 4.3, but, owing to the complexity of some of the spectra, each compound will be described separately.

The ^{31}P MAS NMR spectrum of **4.1** exhibits three main resonances each with a significant sideband manifold as a result of the CSA. The three resonances display integrated intensities of 1 : 1 : 2, suggesting the resonances at lower chemical shift might correspond to two P atoms, with very similar environment. Three polymorphs of **4.1** are known from single-crystal XRD, as described above. In order to determine which polymorphs were present in the bulk sample studied, a powder X- ray diffraction pattern was collected and compared to simulated XRD patterns for each polymorph. This comparison is shown in Figure 4.4, and it can be seen that the relative intensities and position of the reflections from the experimental powder XRD pattern agree best with those simulated for **4.1b**. This crystal structure contains four molecules in the asymmetric unit, in agreement with the integrated intensities of the resonances in the ^{31}P NMR spectrum shown in Figure 4.3a, suggesting that this sample contains just one polymorph.

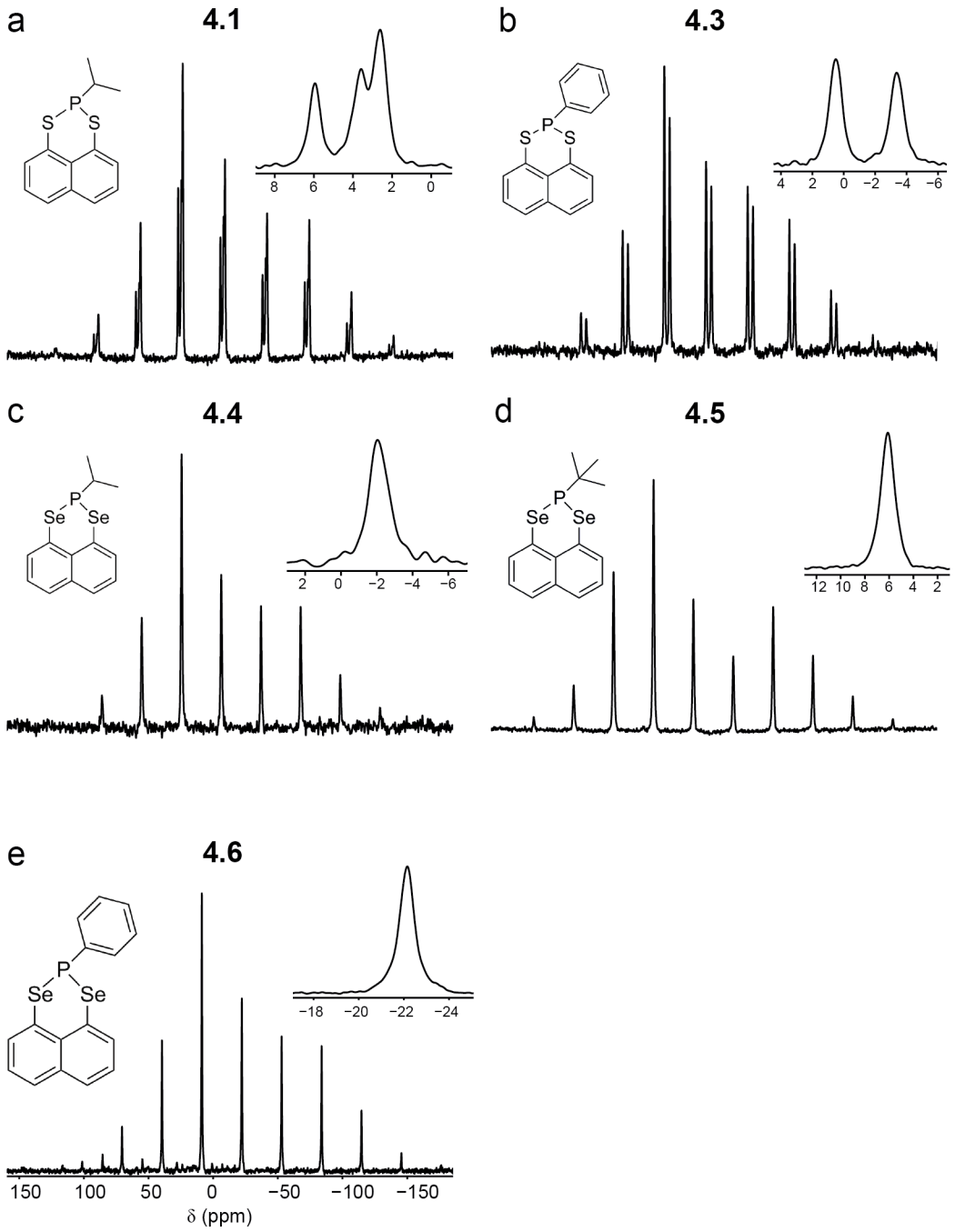

Figure 4.3. ^{31}P (14.1 T, 7.5 kHz) MAS NMR spectra of (a) **4.1**, (c) **4.4**, (d) **4.5**. (b) ^{31}P (14.1 T, 7.5 kHz) CP MAS NMR spectrum of **4.3** and (e) ^{31}P (9.4 T, 5 kHz) CP MAS NMR spectrum of **4.6**. The isotropic resonances in each spectrum are shown expanded in the insets.

The ^{31}P MAS NMR spectrum of **4.3** exhibits two resonances with integrated intensities of 1 : 1, each with a significant sideband manifold as a result of the CSA, in agreement with the presence of two molecules in the asymmetric unit. In contrast, the ^{31}P MAS NMR spectra of **4.4**, **4.5** and **4.6** each exhibit a single resonance, in agreement with the single molecule in each of their asymmetric units. To date, no other polymorphs have been indentified for compounds other than **4.1**. The experimental powder XRD patterns of all samples were measured in capillary mode and compared to the simulated powder XRD pattern from each of the known crystal structures. This comparison can be seen in the Figures B1 – B4 of the Appendix B and, in each case, the patterns are in good agreement, suggesting that the bulk material corresponds to the crystal structure known.

The chemical shifts and the CSA parameters extracted for the experimental ^{31}P MAS NMR spectra shown in Figure 4.3, using TopSpin, are summarised for all compounds in Table 4.3. The CSA parameters will be discussed later in this chapter. The ^{31}P chemical shift range in the solid-state NMR spectra, varies over ~28 ppm, while in solution it varies over ~38 ppm. However, it must be noted that **4.2** could not be measured in the solid state, and this is the most deshielded compound in solution. The ^{31}P chemical shift order across the series appears the same as in solution, *i.e.*, the ^{t}Bu analogue is more deshielded, followed by the ^{i}Pr and Ph for the selenium derivatives. A similar order for the ^{i}Pr and Ph compounds is seen for the S analogues. However the difference in chemical shift between each compound is now different than in solution. In the sulfur compounds, the ^{i}Pr and Ph derivatives exhibit difference of 5 – 10 ppm, while this was 4 ppm in solution.

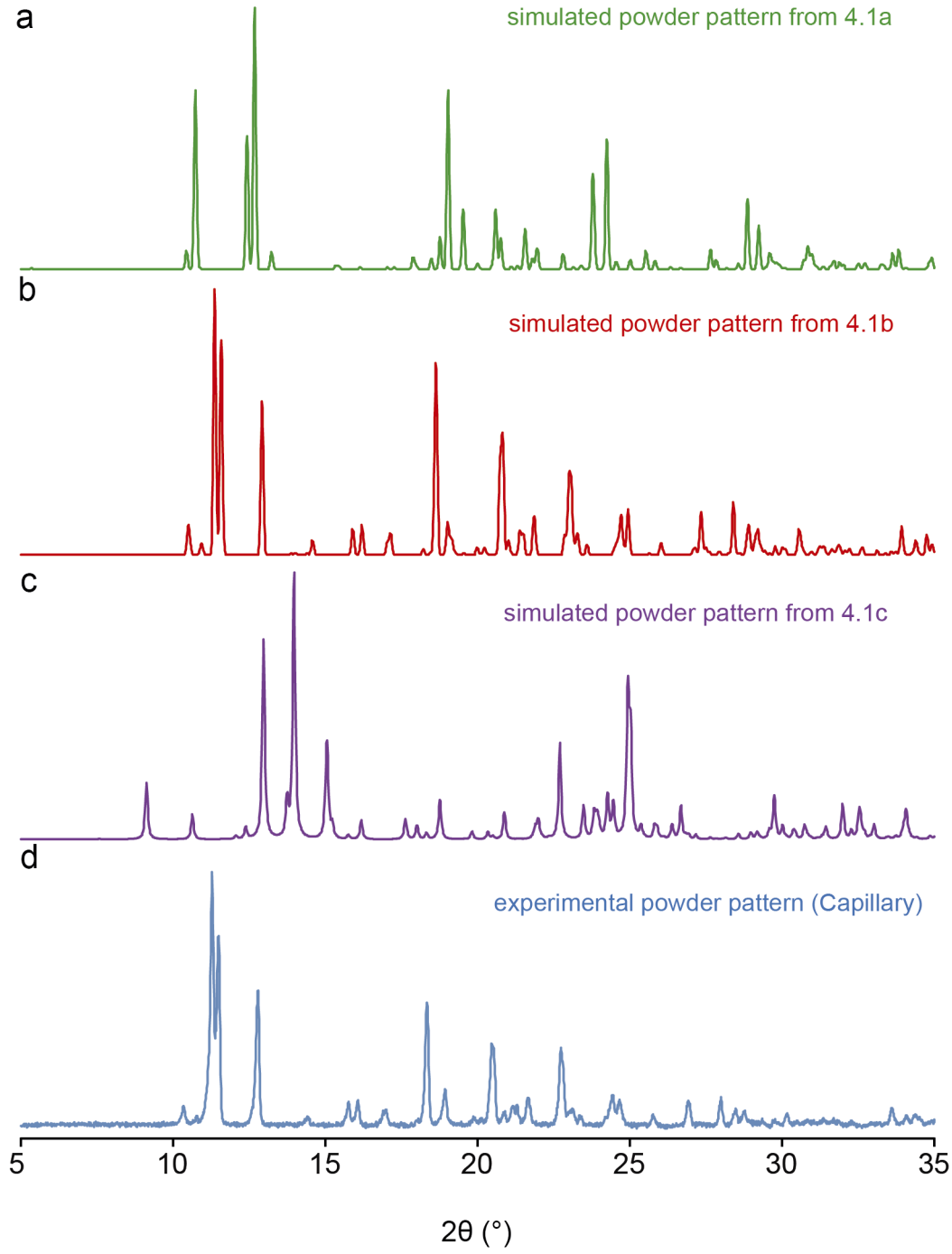

Figure 4.4. Simulated powder XRD patterns from crystal structure (a) **4.1a** (b) **4.1b**, (c) **4.1c** and (d) Experimental powder XRD pattern from bulk sample of **4.1**.

Table 4.3. ^{31}P solid-state NMR spectroscopic parameters.

	4.1	**4.2**	**4.3**	**4.4**	**4.5**	**4.6**
X,R group	S, ^{i}Pr	S, ^{t}Bu	S, Ph	Se, ^{i}Pr	Se, ^{t}Bu	Se, Ph
δ_{iso} (^{31}P)[a]	2.7 3.6 5.9	–	0.5 –3.4	–2.1	6.1	–22.1
(Ω^{exp})[a]	208.6 184.4 169.5	–	197.2 192.9	197.8	231.2	203.4
κ^{exp}	0.3 0.4 0.9	–	0.25 0.23	0.4	0.5	0.3

All δ (ppm), Ω (ppm).

It must be noted that in the solid-state NMR spectra each crystallographically-different environment now result in different chemical shifts, while in solution, only one shift is observed. In the selenium compounds, a smaller difference in chemical shift is found than in solution between ^{t}Bu and ^{i}Pr (*e.g.*, 8.2 ppm difference in the solid state compared to was 16 ppm in solution), which could be an indicative of similar packing of those compounds. However, a larger difference is found between ^{i}Pr and Ph, with 20 ppm difference in the solid state and only 10 ppm in solution. This could indicate more significant packing differences between these compounds.

Figure 4.5a shows a plot of the ^{31}P chemical shift in the solid state *vs* solution. The greatest difference in isotropic chemical shift is found for **4.6** and **4.5**. This difference could be indicative of a more significant crystal packing effect found in these two compounds compared to the rest, which could result from either a steric or electronic effect, or it could be a change in conformation imposed by the packing in the solid state. In order to quantify the steric bulk of the systems as shown in Chapter 3, a steric bulk cone angle θ, calculated from crystallographic data is used to provide a measure of the bulk of the R group introduced (^{i}Pr, ^{t}Bu and Ph).

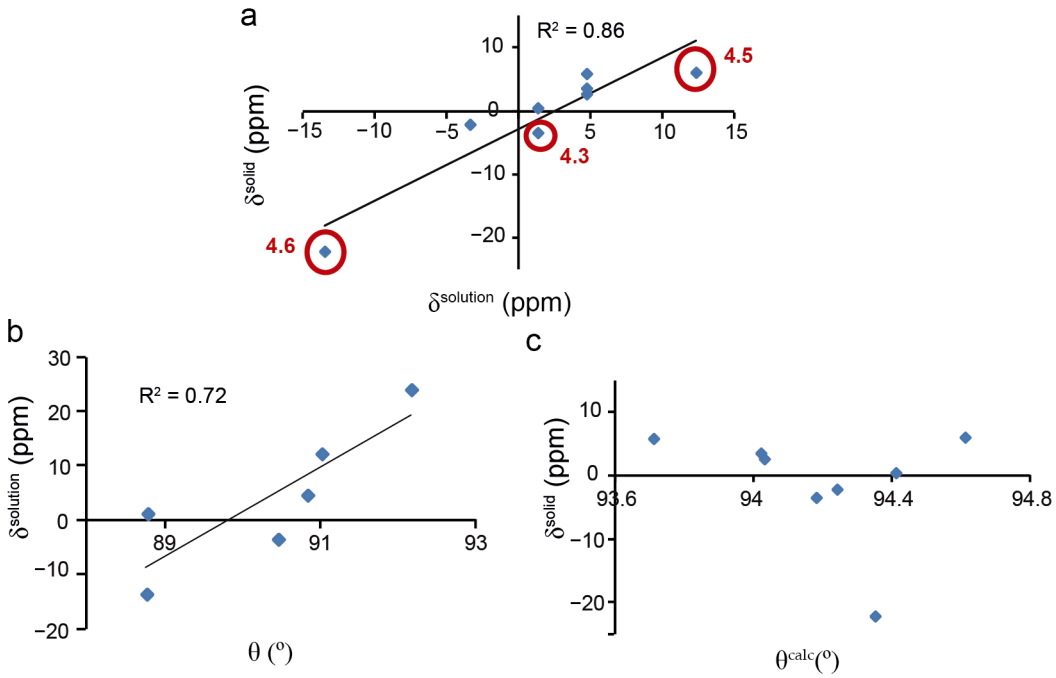

Figure 4.5. Plots of (a) the $\delta_{iso}^{solid}(^{31}P)$ *vs* $\delta_{iso}^{solution}(^{31}P)$, (b) $\delta_{iso}^{solution}$ *vs* θ and (c) δ_{iso}^{solid} *vs* θ^{calc}, for **4.1** – **4.6**, with the exception of **4.2**, which was not measured in the solid state.

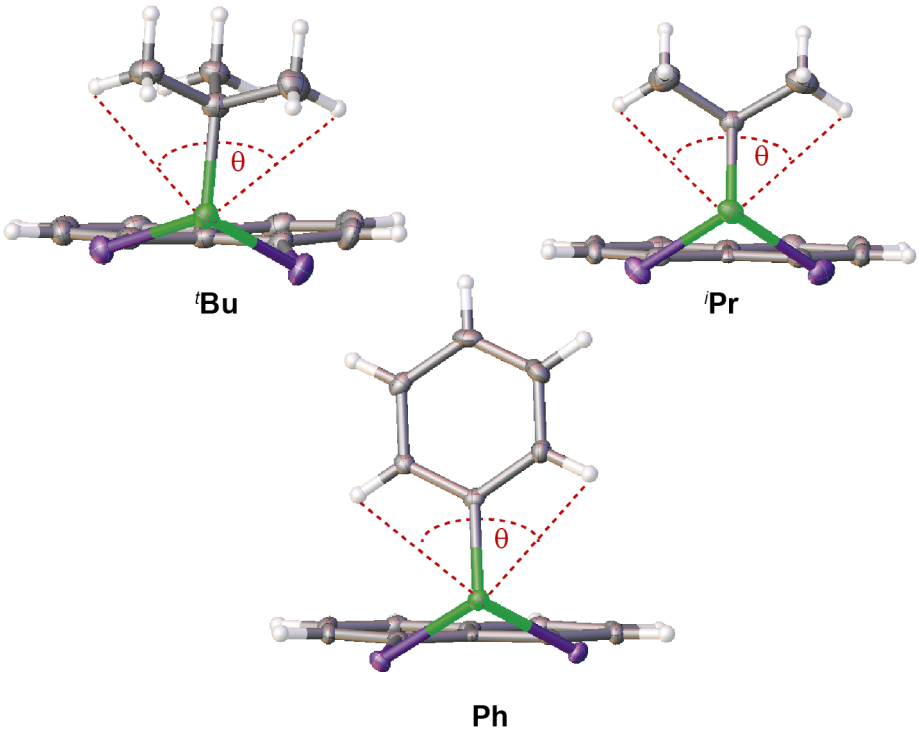

Figure 4.6. Schematic representation of the crystallographic steric parameter θ for the R groups (^{i}Pr, ^{t}Bu and Ph).

This angle is a modified version of the Tolman Cone Angle,[24] defined as the angle between the hydrogen of the R group that occupies the extreme edges of the cone to the phosphorus atom located at its vertex, as illustrated in Figure 4.6. The values of the steric parameter θ, together with the solution- and solid-state NMR chemical shifts and their difference, are summarised in Table 4.4. For **4.1** and **4.3**, where more than one P site is present, an average of the steric parameter was taken. The plot of the chemical shift in solution *vs* steric parameter is shown in Figure 4.5b, and a reasonable linear correlation ($R^2 = 0.72$) is observed. This suggests that, as the steric bulk is increased in the system, (^{t}Bu > ^{i}Pr > Ph), a deshielding effect is observed. This comparison is not possible in the solid state as, for compounds with more than one ^{31}P site , it is not possible to assign which chemical shift corresponds to a given θ. However, DFT calculations can be used to help assign the ^{31}P NMR spectra, allowing the chemical shift associated with a given θ to be determined. Therefore, the solid-state ^{31}P chemical shifts were compared to the calculated θ parameters from a structure previous optimized using the CASTEP code, with the values summarised in Table 4.4. The resonances were assigned taking into account the σ_{iso}^{calc}. However, once optimized, there is little variation in θ and no correlation was observed between δ^{solid} and θ^{calc}, as shown in Figure 4.5c.

In the solid state the CSA parameters may also provide useful information, as has been shown in previous chapters. The CSAs for all compounds (with the exception of **4.2**), were extracted from experimental spectra and the values, described using the Herzfeld-Berger convention are summarised in Table 4.3. The range of span varies over 62 ppm for the series of compounds, with **4.1b** having the smallest span for one of the three resonances observed, and **4.5** having the largest.

Table 4.4. ^{31}P chemical shifts in the solid state, δ_{iso}^{solid}, and in solution, $\delta_{iso}^{solution}$, and the difference between these two, $\Delta\delta_{iso}^{(solution-solid)}$, crystallographic (θ), and computational (θ^{calc}) steric parameters, for **4.1 – 4.6**.

Compound	R groups	$\Delta\delta_{iso}^{(solution-solid)}$	δ_{iso}^{solid}	θ^{calc}	$\delta_{iso}^{solution}$	θ
4.1a	S, ^{i}Pr	2	2.7	94.0	4.7	90.8
4.1b	S, ^{i}Pr	1.1	3.6	94.0		
4.1c	S, ^{i}Pr	1.2	5.9	93.7		
4.2	S, tBu	–	–	–	24.1	92.2
4.3	S, Ph	0.81	0.5	94.4	1.31	88.7
4.3	S, Ph	4.71	–3.4	94.2		
4.4	Se, ^{i}Pr	1.3	–2.1	94.2	–3.4	90.4
4.5	Se, ^{t}Bu	6.2	6.1	94.6	12.3	91.0
4.6	Se, Ph	8.6	–22.1	94.3	–13.5	88.8

All δ (ppm) and θ (°)

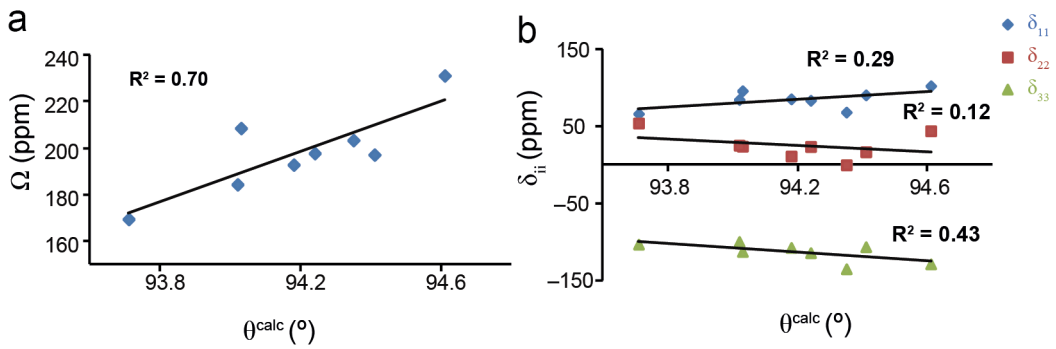

Figure 4.7. Plots of the ^{31}P experimental (a) Ω and (b) δ_{ii}, against $\theta^{calculated}$ from optimized crystal structures, for **4.1 – 4.6** (excluding **4.2**).

Figures 4.7a and 4.7b show plots of Ω and the principal components of the CSA tensor, δ_{ii}, against θ^{calc} from the optimized structures. It seems that a good correlation is found for the span (R^2 = 0.7) but little for the principal components of the tensor. Although there is some scatter, it

could be observed that, generally, the span increases with $\theta^{calc.}$, although the range of θ^{calc} considered is very small.

Most compounds exhibit a small change in the observed isotropic ^{31}P chemical shift, at different spinning speeds (*i.e.,* between 5 and 12.5 kHz). In order to see if there is any evidence for motional behavior in the series of compounds, VT experiments were performed. Figure 4.8 shows the isotropic centrebands of the ^{31}P MAS NMR spectra acquired at 14.1 T for **4.1** and **4.6**, and at 9.4 for **4.3**, **4.4** and **4.5** at three different temperatures. There is a small change in isotropic chemical shift with temperature of ~0.9, 0.7, 1, 0.5 and 0.6 ppm per 25 K for **4.1**, **4.3**, **4.4**, **4.5** and **4.6** respectively, possibly as a result of motion of the R group. However, the CSA remains very similar at the three temperatures for some compounds (**4.1** and **4.5** with differences of ~ Ω = 6 ppm and 1ppm, respectively) but that is more significant for **4.4** and **4.3**, with difference of Ω ~ 26.4 ppm and 38.4 ppm,respectively (details are given in Table B3 in the Appendix B). It must be noted that the CSA was not extracted for **4.6** owing to decomposition of the sample and additional resonances observed in the ^{31}P CP MAS NMR spectrum. It should be noted from the centrebands of ^{31}P (9.4 T) CP MAS NMR spectra of **4.3** at varying temperature, that each resonance is now split into a doublet, suggesting the presence of a possible J coupling, (*i.e.,* it has already been shown that the sample was pure and contained only one polymorph), which will be discussed later in this chapter. In contrast, no further splitting is observed in the rest of spectra, suggesting there is no evidence of J coupling for the rest of compounds.

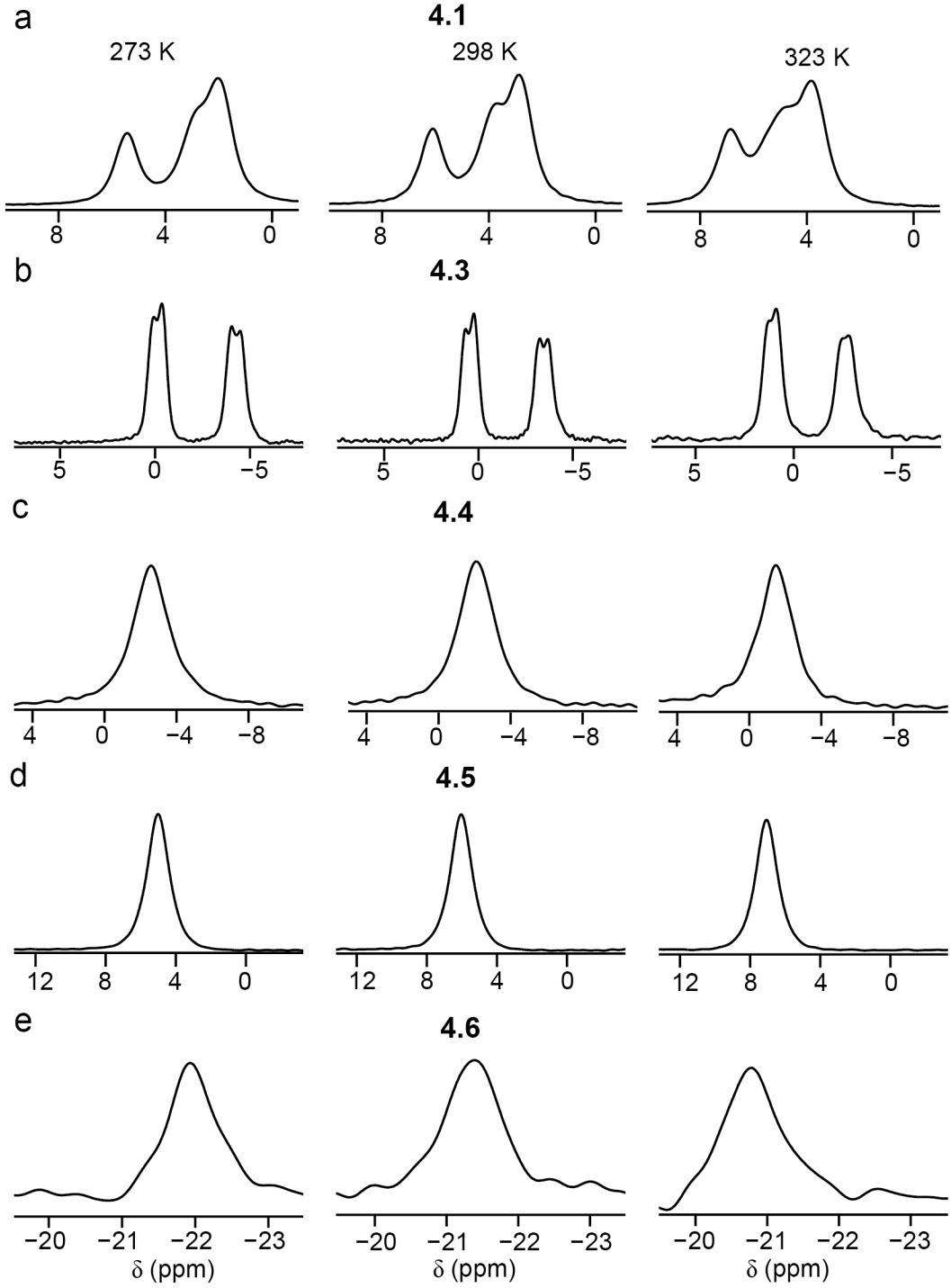

Figure 4.8. Isotropic centrebands of ^{31}P (a) **4.1** (14.1 T, 10 kHz MAS), (b) **4.3** (9.4 T, 7.5 kHz CP MAS), (c and d) **4.4** and **4.5** (9.4 T, 7.5 kHz MAS) and (e) **4.6** (14.1 T, 7.5 kHz CP MAS), NMR spectra recorded at 273, 298 and 323 K.

In the first attempt to perform ^{31}P VT NMR spectra of **4.6**, new peaks at ~20 ppm appeared, as shown in Figure 4.9a. The sample had previously been shown to be pure by ^{31}P solution-state NMR. In order to clarify the origin of the new peak, the ^{31}P solution-state NMR spectrum was again recorded on this sample. The spectrum, shown in Figure 3.9b confirmed the presence of additional P environments, suggesting either oxidation or decomposition of part of the sample, which was packed in contact with air. A fresh batch of **4.6** was again synthesised and was packed into the rotor inside a glovebox in order to avoid oxidation or decomposition. After MAS at 12.5 kHz, the extra peaks were once again observed, as shown in Figure 4.9c, and with an extra peak not observed previously at –10 ppm. The relaxation of the impurity phase and **4.6** is different, (T_1 times for **4.6** is very long, while, T_1 times for the impurity are much shorter), resulting in a relatively poor sensitivity for **4.6** by ^{31}P direct detection. To overcome this problem, CP was used, to improve the relative sensitivity of **4.6**. The ^{31}P CP MAS NMR spectrum of **4.6** acquired at 5 kHz, at 273 K is shown in Figure 4.9d. An isotropic peak at –22.1 ppm is observed with a significant sideband manifold, not observed previously by direct detection. Note that the ^{31}P CP MAS NMR spectrum was recorded at 273 K, to avoid possible further decomposition of **4.6** with temperature. The ^{31}P CP MAS NMR experiment of **4.6** at varying temperature was recorded after few months. Although, the isotropic centreband is shown in Figure 4.8e, the CSA was not extracted as mention before owing to the appearance of additional peaks in the same region that those observed previously (~20 ppm), suggesting that the same had decomposed further.

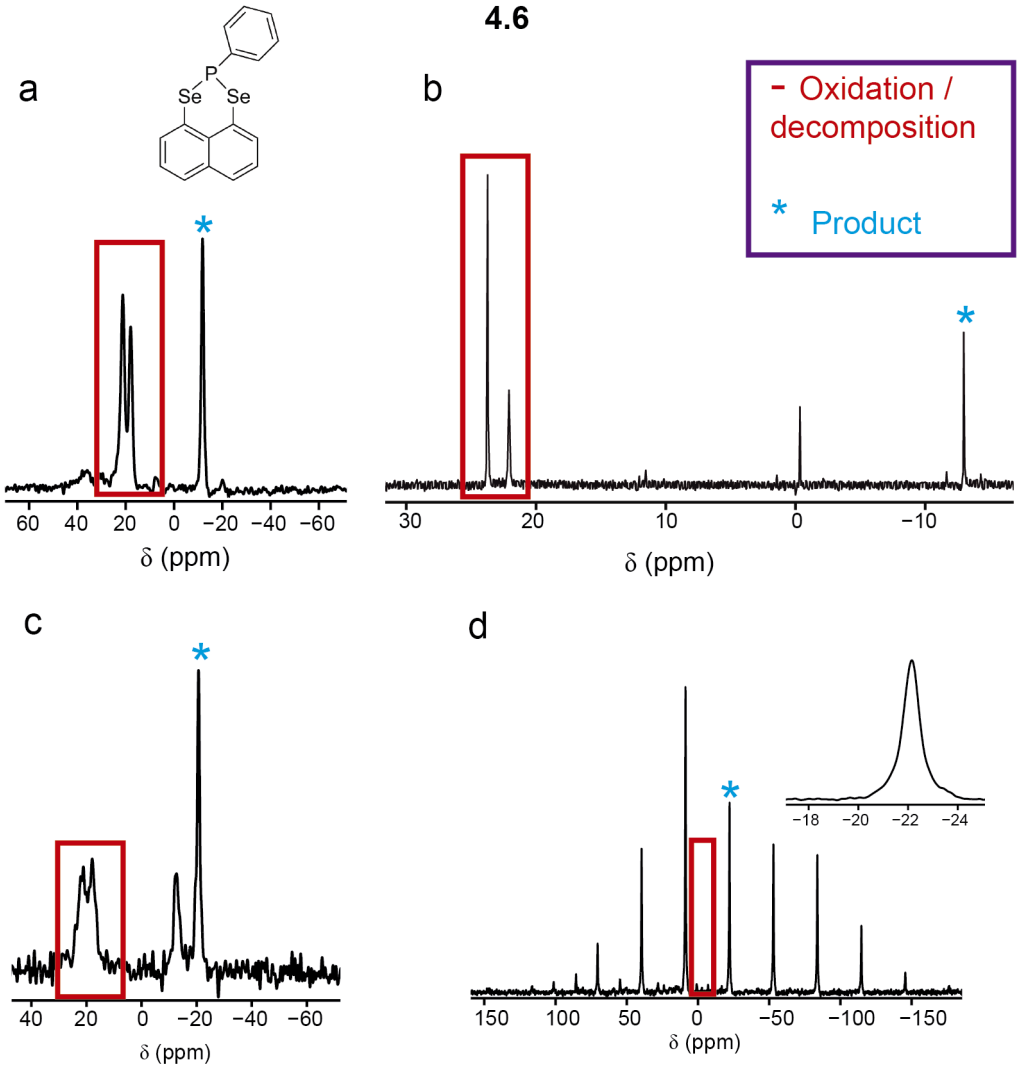

Figure 4.9. ^{31}P NMR spectra of **4.6** (a) at 9.4 T, 14 kHz MAS, (b) at 6.35 T, in $CDCl_3$ recorded after the spectrum in (a), (c) a fresh batch of **4.6**, packed under Argon, at 9.4 T, 12.5 kHz MAS and (d) the sample as in (c) at 9.4 T, 5 kHz CP MAS recorded at 273 K. The red box represent the additional peaks attributed to oxidation/decomposition of the product while, * represent the isotropic peak.

4.6.5. ^{77}Se solid-state NMR characterisation

The ^{77}Se CP MAS NMR spectra of **4.4**, **4.5** and **4.6**, recorded either at 9.4, 14.1 or 20.0 T with MAS rates between 5 and 12.5 kHz are shown in Figure 4.10. Although in solution each spectrum exhibits a doublet, owing to the $^{1}J(^{77}Se–^{31}P)$ and the equivalence of the two selenium atoms, in the solid state, two distinct selenium environments are expected for each compound, as one molecule is present in the asymmetric unit and each molecule has two crystallographically-inequivalent sites. These two inequivalent sites are both expected to couple to ^{31}P with $^{1}J(^{77}Se–^{31}P)$, thus each selenium site should appear as a doublet. However, as shown in the insets in Figure 4.10, this is not observed experimentally for any of the compounds.

At 9.4 T, the isotropic centreband of **4.4** exhibits a complex lineshape, with a significant sideband manifold as a result of CSA. The centreband lineshape changes with B_0 field, indicating the presence of two overlapped selenium signals, (*e.g.,* two ^{77}Se signals with slightly different isotropic shift, both split by a $J(^{77}Se–^{31}P)$ that form an AA′X spin system). The apparent "triplet" observed at higher fields, could lead to an erroneous conclusion as, usually, an AA′X spin system will result in two doublets, whereas an AX_2 system will result in a true triplet. However, these two spin systems can be unambiguously distinguished by consideration of the multiplet linewidth in Hz. For an AA′X spin system, the linewidth is determined by $(J_{AX} + J_{A'X})/2 + \nu_0 (\delta_{iso(A)} - \delta_{iso(A')})$ and will be modified with the field (*i.e.,* is field dependent). However, in an AX_2 system, the linewidth in Hz is $2J_{AX}$ and will not depend on B_0 field. Therefore, the multiple-field experiments were essential for understanding the system studied.

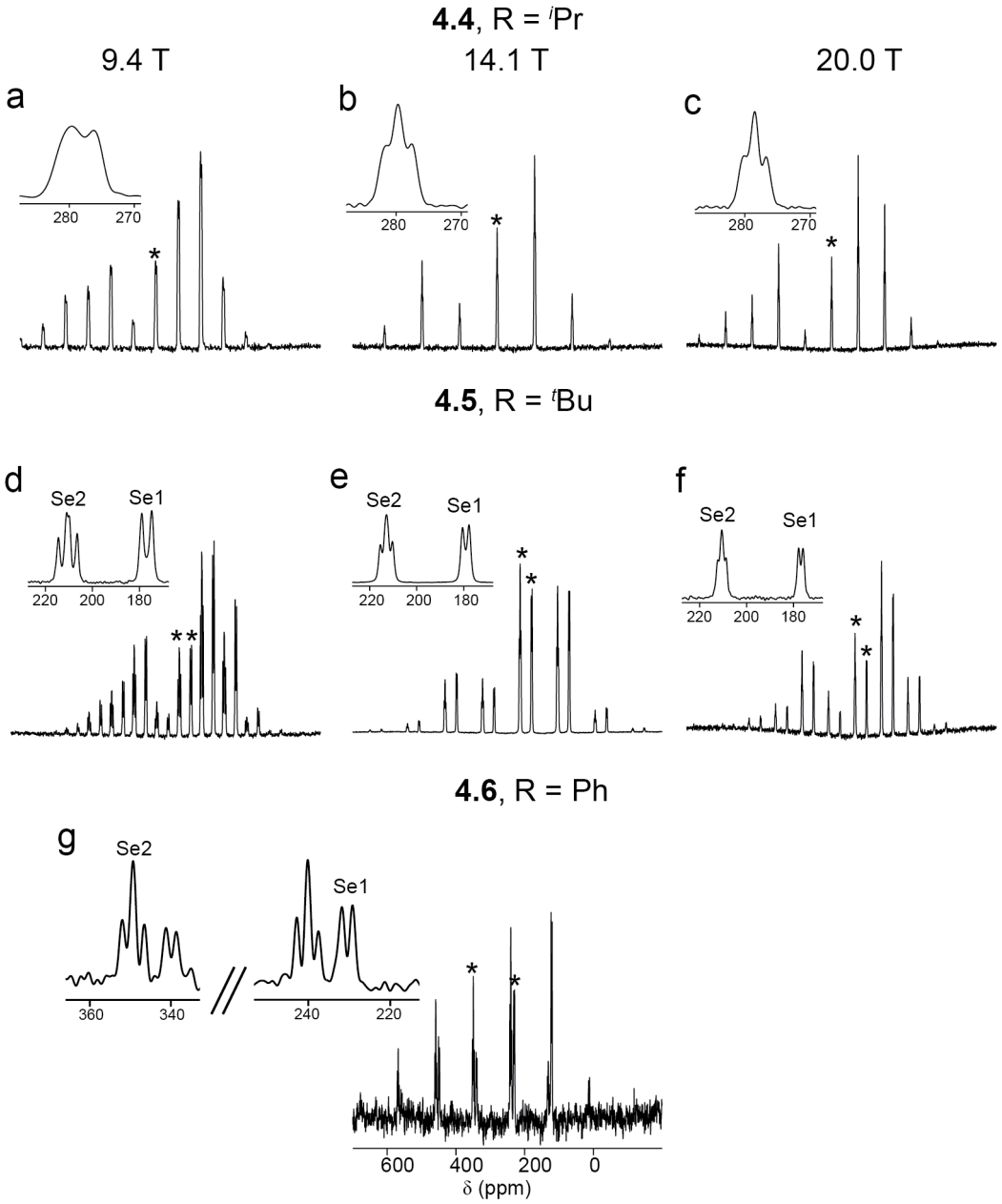

Figure 4.10. ^{77}Se NMR spectra of (a – c) **4.4**, (d – f) **4.5** and (g) **4.6**, at (a, d) 9.4 T, 5 kHz CP MAS, (b, e, g) 14.1 T ,12.5 kHz CP MAS and (c, f) 20.0 T, 12.5 kHz CP MAS. Isotropic resonances in each spectrum are shown expanded and indicated with *.

A plot of the multiplet linewidth in Hz as a function of the Larmor frequency for **4.4**, shown in Figure 4.11a, yields a straight line with a

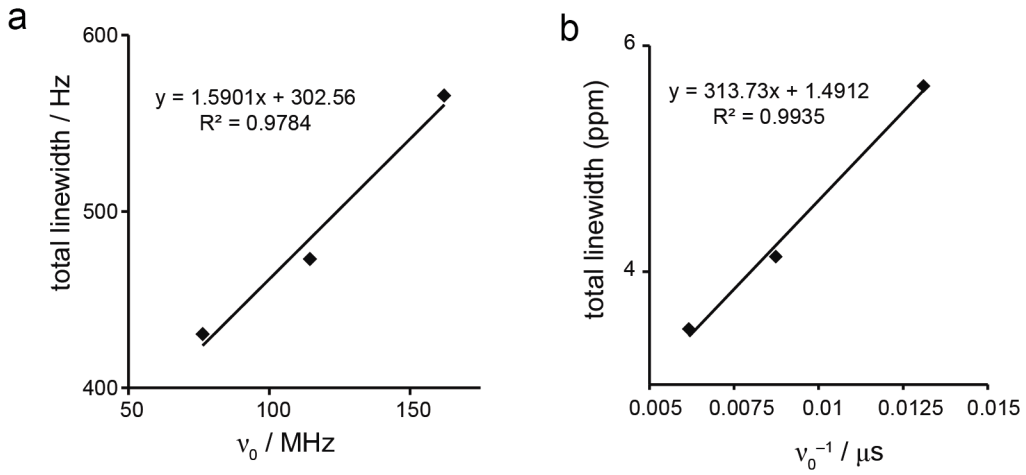

Figure 4.11. Plots of the linewidth of the isotropic ^{77}Se centreband resonance for compound **4.4** in (a) Hz and (b) ppm as a function of (a) ν_0 and (b) $1/\nu_0$. The lines of best fit shown in both parts.

gradient of $(\delta_{iso(A)} - \delta_{iso(A')})$ and a y intercept of $(J_{AX} + J_{A'X})/2$. A plot of the linewidth in ppm *vs* $1/\nu_0$ yields a gradient of $(J_{AX} + J_{A'X})/2$ and a y intercept of $(\delta_{iso(A)} - \delta_{iso(A')})$, as shown in Figure 4.11b. From these two plots, it was determined that $(\delta_{iso(A)} - \delta_{iso(A')})$ = 1.5 (2) ppm and $(J_{AX} + J_{A'X})$ = 615(54) Hz. The majority of the uncertainty in these values comes from the difficulty in determining the width of the idealized "stick diagram" lineshape affected only by isotropic shifts and J couplings (*i.e.,* with no contributions from dipolar couplings and other effects). Although, no distinction of the two Se resonances is observed in the spectra, DFT calculations performed on **4.4**, predicts two very different isotropic shielding for Se(*i.e.,* σ_{iso}^{calc} 1392.8 and 1367.6 ppm).

Compounds **4.5** and **4.6**, both exhibit the expected two resonances, however, the multiplicity observed is not immediately clear. The ^{77}Se CP MAS NMR spectrum of **4.5** at 9.4 T is shown in Figure 4.10d, and contains two isotropic resonances. Although one is a doublet as expected, the other resonance appears to be a doublet of doublets. This multiplicity is difficult

to explain in the spin system expected to be present (an AX_2 spin system), where ^{77}Se (X) can only be coupled to ^{31}P (A) which is 100% abundant giving rise to a doublet for each ^{77}Se (X) site. The presence of a doublet of doublets means that there must be another coupling to an inequivalent nucleus with 100 % abundance. However, in a molecule of **4.5**, there is not another nucleus present with a 100% abundance (as ^{1}H is decoupled during acquisition). Note that Se1 and Se2 are crystallographically-inequivalent and therefore magnetically inequivalent, and could, in principle, couple in the solid-state spectrum. However, owing to the natural abundance of ^{77}Se (7.6 %), such a coupling cannot explain the observed lineshape. DFT calculations could be very helpful in this case, and the two Se sites can be assigned to the structure in terms of their calculated isotropic shielding (*i.e.,* the σ_{iso}^{calc} is 1500.7 and 1508.7 ppm for Se2 and Se1, respectively). In order to clarify whether the observed "coupling" is real or arises from the presence of an additional selenium site, possibly arising for an impurity or undetected polymorph, spectra were recorded at multiple B_0 fields strengths. As can be seen in Figures 4.10e and 4.10f, the lineshape does not change with field, apart from a slight broadening, suggesting that the different multiplicity arises from a J coupling rather than from the presence of an additional Se species, as discussed for **4.4** (now with the opposite conclusion for **4.5**). The sample studied was also analyzed by EA, mass spectrometry, single-crystal and powder X-ray diffraction and solution-state NMR (see also Chapter 6 for more details) confirming that it was pure and that just one polymorph was present.

The ^{77}Se CP MAS NMR spectrum of **4.6** recorded at 14.1 T is shown in Figure 4.10g and can be seen to exhibit a similar multiplicity as for **4.5**. However, in this case, the chemical shift difference between the two

selenium environments is even bigger, (~118.7 ppm) suggesting that the local environments of the two Se sites are more different than in **4.5**. The presence of a doublet for one selenium and a "triplet" for the other in **4.6**, again suggests the presence of another coupling to a highly-abundant nucleus that is not immediately obvious from the molecular structure. DFT calculations again help with the assignment of the two Se sites with the structure (*i.e.,* the σ_{iso}^{calc} is 1304.2 and 1435.1 ppm for Se2 and Se1, respectively). The ^{77}Se CP MAS NMR spectrum of **4.6** acquired at 5 kHz MAS is shown in Figure 4.12a, and a doublet of doublets appears to be distinguished for Se2. This multiplicity changes to a "triplet" as observed in the ^{77}Se CP MAS NMR spectra of **4.6** acquired at 10 and 12.5 kHz MAS (shown in Figures 4.12c and 4.12d, respectively). This difference could arise from a J coupling that change with temperature, as a result of the small temperature variation between each experiment. However, further experiments would be required to confirm this. The ^{77}Se CP MAS NMR spectrum at 7 kHz MAS shown in Figure 4.12b, shows coincidental overlap of sidebands and centrebands for the two sites, as unfortunately, the MAS rate used is a multiple of the chemical shift difference between the two sites. In order to clarify whether any dynamics affect the chemical shifts and also possibly the J couplings, VT experiments were carried out for **4.4** ,**4.5** and **4.6** at 14.1 T and 12.5 kHz CP MAS. Figure 4.13 shows isotropic centrebands of ^{77}Se CP MAS NMR spectra of **4.4**, **4.5** and **4.6**, recorded as a function of temperature. A downfield shift is observed as the temperature increases for the three compounds (~1.8, ~2.5 and 1.5 ppm per 25 K for **4.4**, **4.5** and **4.6**, respectively). A small variation in the J coupling is also observed, but this is much more difficult to measure quantitatively owing to the change in linebroadening as the temperature increases.

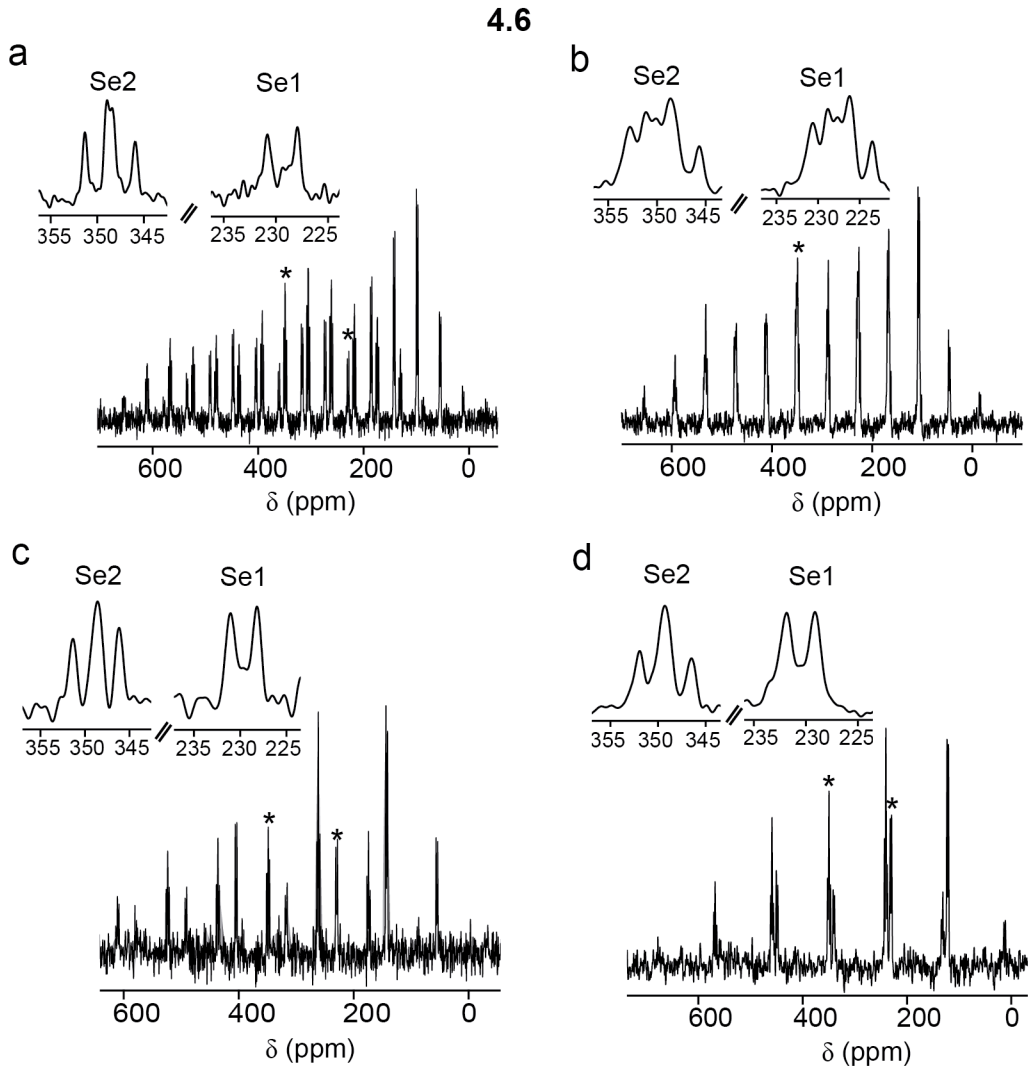

Figure 4.12. ^{77}Se NMR spectra of **4.6** recorded at 14.1 T and (a) 5 kHz, (b) 7 kHz and (c) 10 kHz and (d) 12.5 kHz CP MAS. Isotropic resonances were unambiguously indentified using the spectra in (c) and (d).

The ^{77}Se chemical shift range of the compounds in the solid state is ~171 ppm, while is solution the range is only ~ 91.8 ppm. The order of the ^{77}Se chemical shifts of the compounds also changes between solution- and solid-state NMR, as **4.5** and **4.6** possess two Se environments with very different shifts in the solid state.

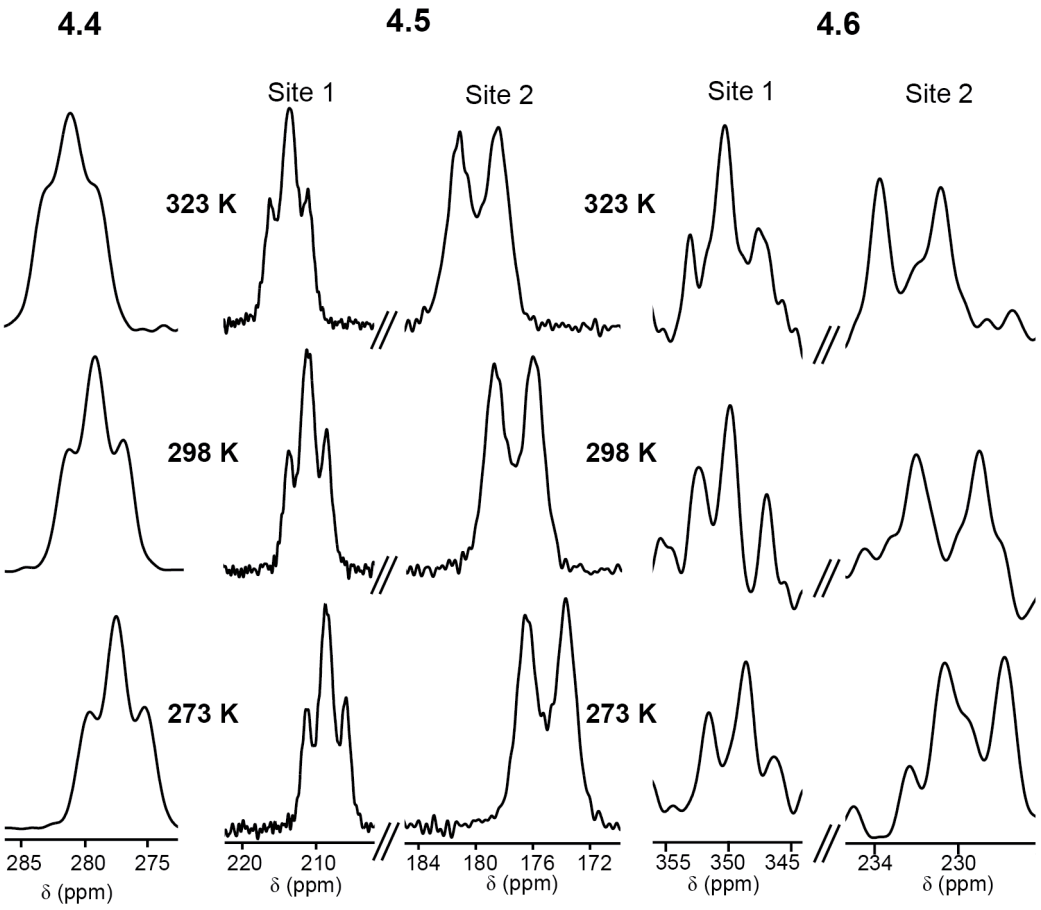

Figure 4.13. ^{77}Se (14.1 T, 12.5 kHz CP MAS) NMR spectra of **4.4**, **4.5** and **4.6** acquired at 273, 298 and 323 K.

The experimental difference in chemical shifts between the two Se environments, increases ^{i}Pr < ^{t}Bu < Ph, being ~1.5 ppm for **4.4**, ~34 ppm for **4.5** and ~119 ppm for **4.6**. Figure 4.14a shows a plot of the isotropic chemical shift in solution against solid, and a poor agreement is observed (R^2 = 0.54). However, it must be noted that there are only a small number of data points (*i.e.*, only three compounds were studied) and so probably more data are need in order to reach a firm conclusion. Figures 4.14b and 4.14c show plots of the ^{77}Se isotropic chemical shift in solution and solid, respectively, against the steric parameter θ and θ^{calc}, respectively.

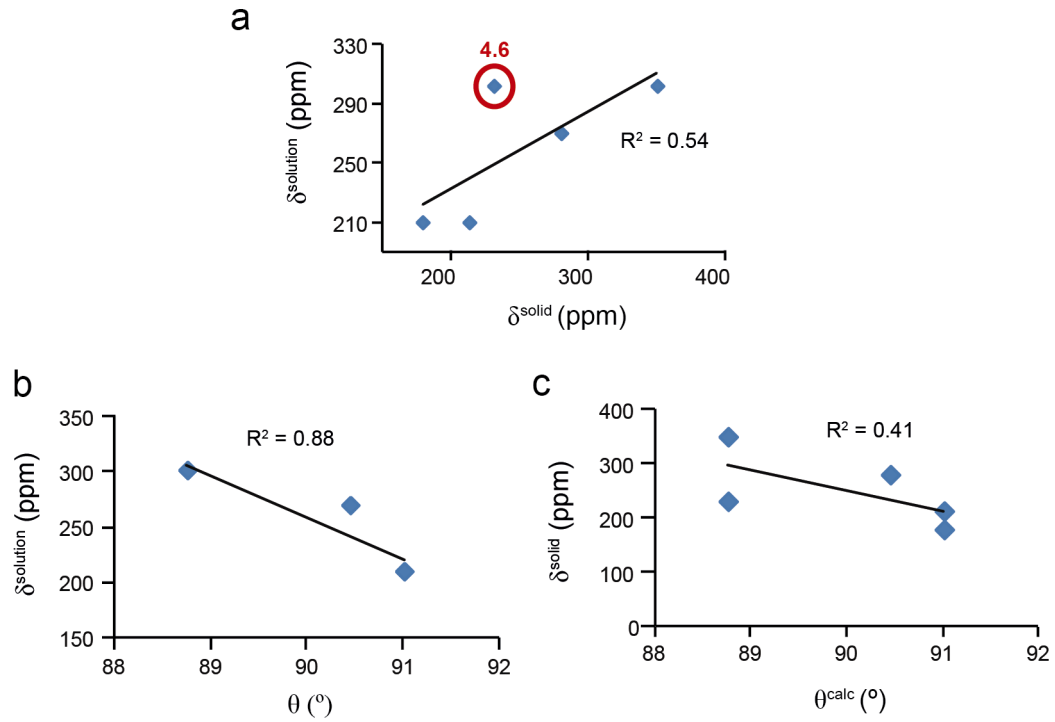

Figure 4.14. Plots of (a) $\delta^{solution}(^{77}Se)$ *vs* $\delta^{solid}(^{77}Se)$, (b) $\delta^{solution}$ *vs* θ and (c) δ^{solid} *vs* θ^{calc} , for **4.4** – **4.6**.

Table 4.5. ^{77}Se solid-state NMR parameters.

Compound	X,R group	δ_{iso}	J(^{77}Se–^{31}P)	Ω^{exp}	κ^{exp}	δ_{11}	δ_{22}	δ_{33}
4.4	^{i}Pr, Se	280	300	589	–1	672	84	83
4.5	^{t}Bu, Se	179 213	319 340/270	470 447	–1 –0.9	492 505	23 77	23 58
4.6	Ph, Se	350 231	335/278 328	593 569	–0.03 –1.0	649.6 610.2	343.0 40.9	56.9 40.9

[a] δ (ppm), J (Hz), Ω (ppm), δ_{ii} (ppm)

Good agreement is found in solution and poorer agreement in the solid, however, it must be noted that, as above, only three compounds have been studied here.

The CSAs for the three selenium compounds were extracted from experimental ^{31}P decoupled ^{77}Se CPMAS NMR spectra recorded at 14.1 T and 12.5 kHz for **4.4** and **4.5** and at 14.1 T and 10 kHz for **4.6**.

The values described in the Herzfeld-Berger convention are summarised in Table 4.5. The range of span varies over 146 ppm for **4.4** – **4.6**, with **4.5** exhibing the smallest span and **4.4** the largest. As observed in Table 4.5, the CSA tensors for the two selenium sites in **4.5** seem very similar, however this is not observed for **4.6**, where the two selenium species have very different κ.

4.6.6 Unusual heteronuclear "through-space" J couplings

The ^{77}Se CP MAS NMR spectra of **4.4**, **4.5** and **4.6** are very different, as discussed above, although the only difference between the compounds is the R group attached to the phosphorus atom. Figure 4.15 shows the ^{77}Se CP MAS NMR spectra of **4.4**, **4.5** and **4.6** acquired with and without ^{31}P decoupling, both recorded at 14.1 T. When all couplings to ^{31}P are removed, a singlet is observed for **4.4**, while two singlets are observed for each of **4.5** and **4.6**. This confirms that all multiplicities observed above, including the unexpected doublet of doublets, must arise from multiple couplings to ^{31}P. From the decoupled spectra it is possible to extract accurate CSA parameters, which are given in Table 4.5.

To understand the origin of the multiple couplings to ^{31}P required for a doublet of doublets, a closer examination of the crystal structures is needed. Figure 4.16 shows the packing motifs for the three compounds, where it can be seen that the different R groups result in different packing of the molecules. For **4.4**, distances of 3.716 and 4.017 Å are observed between each selenium and the phosphorus atom in the adjacent molecule. However, shorter distances of 3.514 Å and 3.522 Å are found between Se2 and a neighboring P1 in **4.5** and **4.6**, respectively, which is within their sum of the van der Waals radii, (3.7 Å).

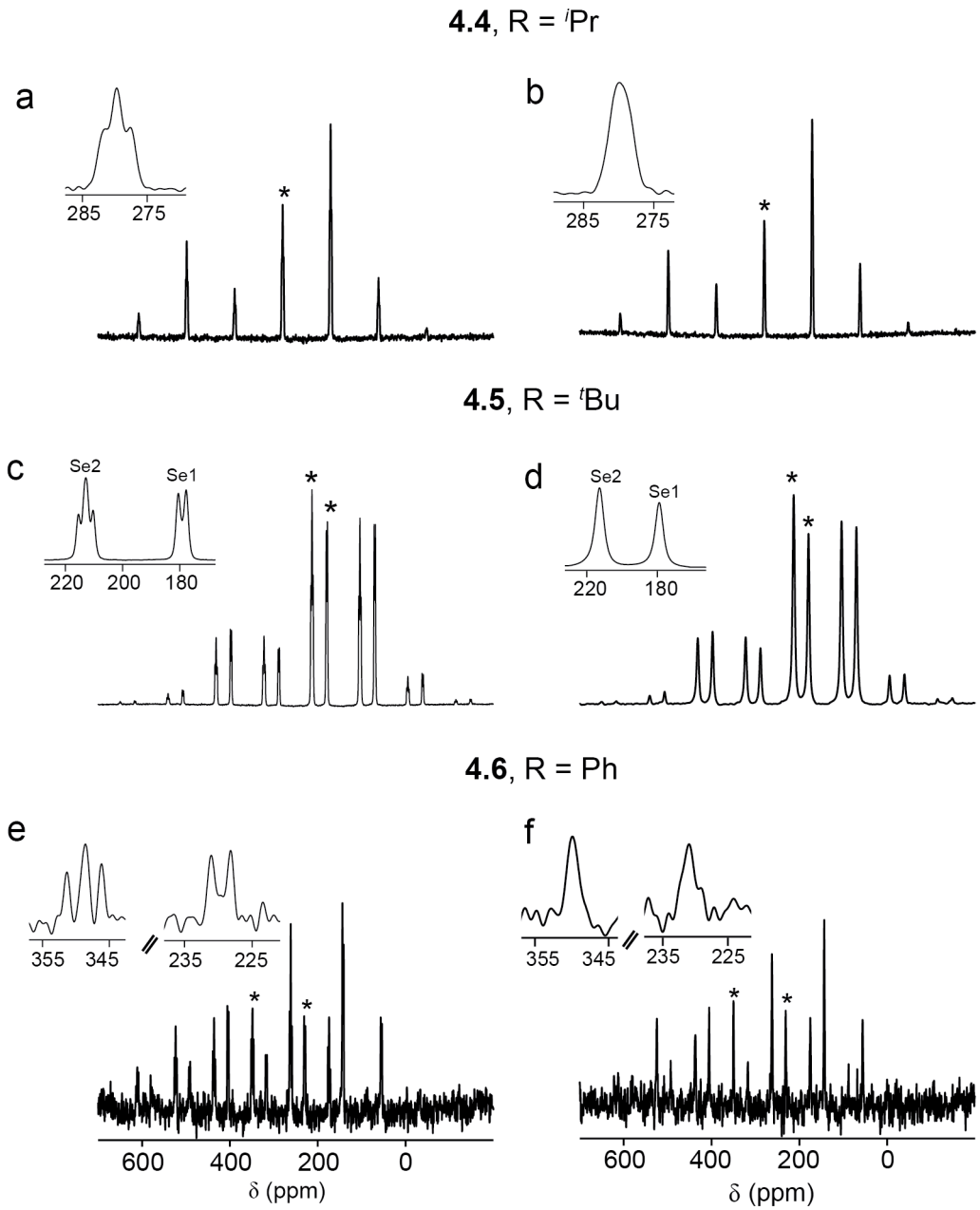

Figure 4.15. ^{77}Se CP MAS NMR spectra of (a, c) **4.4** and **4.5** (14.1 T, 12.5 kHz MAS) and (e) **4.6** (14.1 T, 10 kHz MAS). ^{77}Se CP MAS NMR spectra with ^{31}P decoupling of (b, d) **4.4** and **4.5** (14.1 T, 12.5 kHz MAS) and (f) **4.6** (14.1 T, 10 kHz MAS).

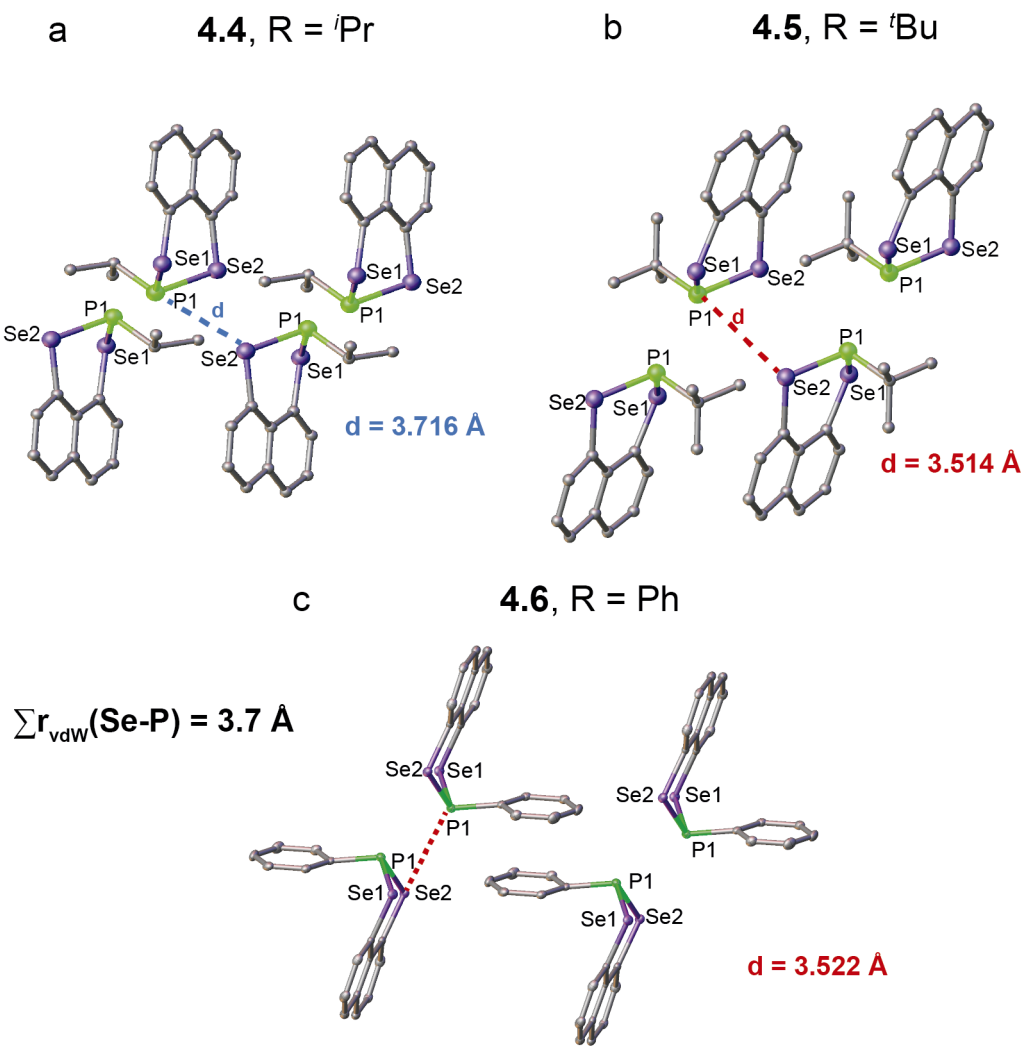

Figure 4.16. Crystal packing motifs for **4.4**, **4.5** and **4.6**, showing the shortest intermolecular Se-P distances.

As observed for *peri*-substituted compounds previously, it is possible that nuclei close in space could exhibit a J coupling that does not proceed *via* conventional covalent bonding. If such a coupling was present between ^{77}Se and ^{31}P in the two different molecules, *i.e.*, an intermolecular coupling, this could explain the unusual multiplet lineshapes observed for both **4.5** and **4.6**.

In order to support the idea that "through-space" J couplings have been observed in the ^{77}Se solid-state NMR spectra of **4.5** and **4.6**, and to

gain insight into the nature and mechanism of the interaction observed, DFT calculations were carried out using CASTEP code, version 8. The J coupling values predicted by DFT for **4.4**, **4.5** and **4.6**, at the scalar relativistic level of theory using the ZORA method[25] are given in Table 4.6.

For **4.4**, Se1-P and Se2-P through-bond couplings were predicted to be –250 and –244 Hz, respectively, in reasonable agreement with the experimental values of ~300 Hz, calculated from the total linewidth. In contrast, the through-space values for Se1-P and Se2-P are much smaller, 69.3 and 111.0 Hz, respectively, which is consistent with the experimental spectra (where no additional J couplings were observed). For **4.5**, two significant Se2-P couplings are predicted, a through-bond coupling of –310.8 Hz and a through-space coupling of 365.2 Hz, which is, surprisingly, of the same order of magnitude as the through-bond coupling. These values are in reasonable agreement with the two experimental couplings of ~340 and 270 Hz, extracted from the experimental ^{77}Se CP MAS NMR spectrum. Only one significant Se1-P (through-bond) coupling was calculated of –280.9 Hz, in reasonable agreement with the experimental value of 319 Hz. For **4.6**, two significant Se2-P couplings are also predicted, a through-bond coupling of –306.8 Hz and a through-space coupling of 335.3 Hz, which are slightly smaller than for **4.5**. These values are in reasonable agreement with the two experimental couplings of ~335 and 278 Hz, extracted from the experimental ^{77}Se CP MAS NMR spectrum. Only one significant Se1-P (through-bond) coupling of –285.0 Hz, was found in reasonable agreement with the experimental value of 328 Hz.

The predicted *peri*- Se-Se couplings were small in all compounds, whereas the predicted Se1-Se1 through-space couplings between molecules are surprisingly large, 112.1 and 107.8 Hz for **4.4** and **4.5**,

respectively, but only 60.8 Hz for **4.6**. However, these couplings are not easy to observe experimentally, owing to the low natural abundance of ^{77}Se.

The dominant J-coupling mechanism in all the intermolecular ^{77}Se-^{31}P couplings was determined from the DFT calculations to be the Fermi contact interaction, indicating that, although formally "through space", there is a significant electronic interaction present. To investigate the through-space coupling pathway, the coupling deformation density (CDD),[26] was calculated (at a non relativistic level), as shown in Figure 4.17 for **4.4** and **4.5** (note that this was not possible for **4.6** as the software was unavailable).The CDD demonstrates that the large Se2-P coupling in **4.5** proceeds by the overlap of the P and Se2 lone pairs, while the P and Se1 lone pairs do not overlap as significantly, resulting in a smaller coupling. In **4.4**, both overlaps are weak, as can seen in the CDD plots in Figure 4.16a, leading to the smaller couplings in both cases.

Table 4.6. J couplings (Hz) (TB = formally through bond, TS = formally through space) for **4.4**, **4.5** and **4.6** predicted by DFT at the scalar-relativistic ZORA level of theory. Quoted values are averaged over J_{A-B} and J_{B-A} calculations, where A and B are the coupled nuclei.

Atoms	Type	**4.4**	**4.5**	**4.6**
Se1-P	TB	–250.0	–280.9	–285.0
Se1-P	TS	69.3	86.4	13.7
Se2-P	TB	–244.0	–310.8	–306.8
Se2-P	TS	111.0	365.2	335.3
Se1-Se2	[a]	32.3	14.3	29.6
Se1-Se2	TS	29.2	25.9	12.5
Se1-Se1	TS	112.1	107.8	60.8
Se2-Se2	TS	7.5	76.9	1.9

[a] *J coupling between the Se atoms in the peri position.*

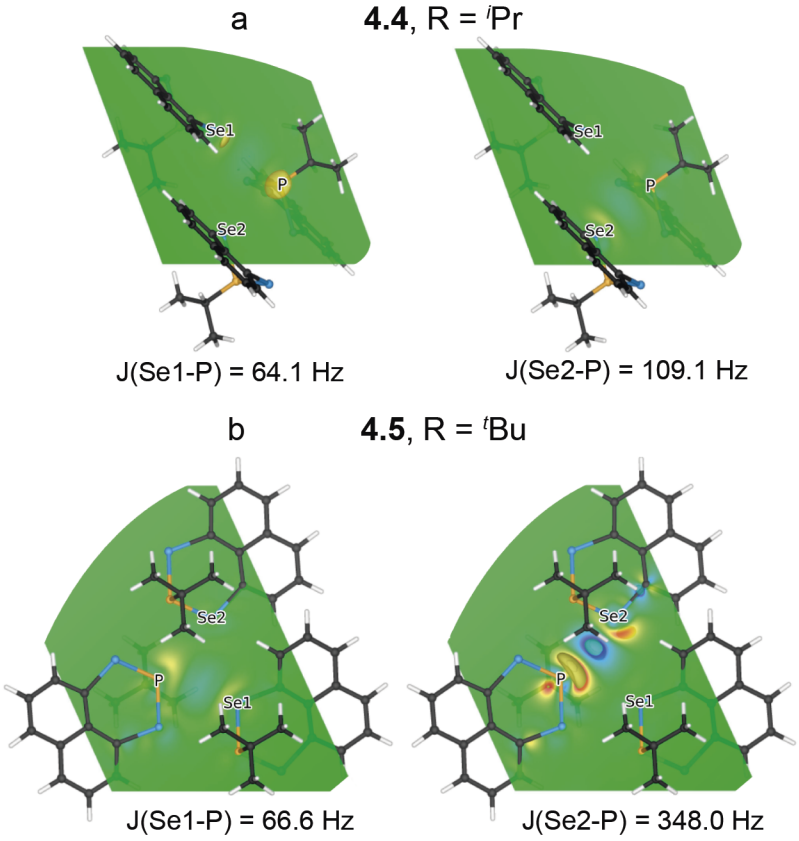

Figure 4.17. Coupling deformation density (CDD) plots (at non-relatitistic level) of the Se1-P and Se2-P through-space J coupling in (a) **4.4** and (b) **4.5**, shown with isosurfaces on the same scale.

4.6.7 Unusual homonuclear "through-space" J couplings

The DFT calculations performed for the heterocyclic systems studied also surprisingly predict ^{31}P-^{31}P through-space couplings in some cases, as shown in Table 4.7. However, these couplings were not observed experimentally in the ^{31}P MAS spectra (as shown in Figure 4.3). Therefore, the P–P distances in the crystal structures for each compound were considered and are summarised in Table 4.7. It can be concluded from Table 4.7 that **4.1a**, **4.1b**, **4.1c**, **4.2** and **4.4,** where the distances are greater than the sum of the van der Waals radii (3.6 Å), are unlikely to exhibit a

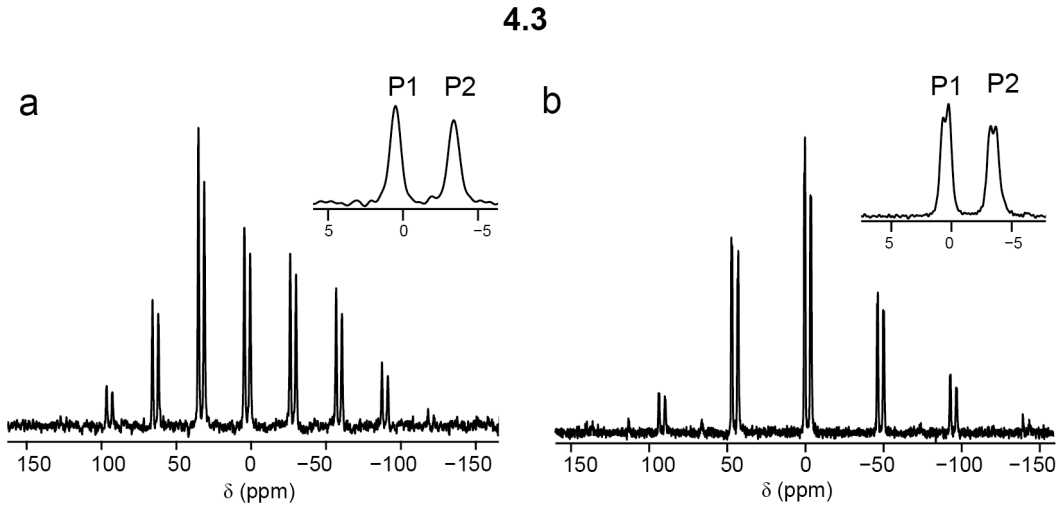

Figure 4.18. ^{31}P CP MAS (7.5 kHz) NMR spectrum of **4.3** at (a) 14.1 T and (b) 9.4 T. Isotropic resonances in each spectrum are shown expanded in the inset.

Table 4.7. Homonuclear through-space ^{31}P–^{31}P J couplings (Hz) predicted by DFT at the scalar-relativistic ZORA level of theory. The P-P^{calc} distance is after geometry optimization and the P-P^{crystal} distance is from the crystal structure.

Compound	J_{PP} / Hz	P-P^{calc} distance / Å	P-P^{crystal} distance / Å
4.1a	–[a]	–[a]	5.494
4.1b	–[a]	–[a]	6.454
4.1c	–[a]	–[a]	4.034
4.2	3.0	4.640	6.349
4.3	150.9	3.578	3.699
4.4	11.2	4.458	4.901
4.5	159.1	3.500	3.586
4.6	145.8	3.642	3.670

[a] *Not calculated due to the system size. Assumed to be < 3.0 Hz (J_{PP} coupling in* ***4.2****) due to larger P–P distances.*

significant through-space coupling. Therefore, owing to computational cost of the calculations (especially for compounds with more than two

molecules in the asymmetric unit *e.g.,* **4.1b**), calculations for **4.1a**, **4.1b** and **4.1c** were not performed.

Compound **4.3,** as previously discussed, has two molecules in the asymmetric unit, giving two ^{31}P resonances in the ^{31}P CP MAS NMR spectrum (recorded at 14.1 T), shown in Figure 4.18a. These two resonances can be assigned to the structure again with the calculated isotropic shielding (*i.e.,* the σ_{iso}^{calc} is 288.5 and 279.7 ppm for P2 and P1, respectively). The spectrum of the same material recorded at 9.4 T, shown in Figure 4.18b, reveals the presence of a splitting for each resonance (~86 Hz) not discussed until now and shown earlier in Figure 4.8. DFT calculations predict a though-space J coupling of 151 Hz between the two crystallographically-inequivalent P atoms, which appears reasonable (*i.e.,* P atoms are separated by 3.699 Å, a distance similar to the van der Waals radii), which could then explain the splitting observed in the spectrum.

In the solid state, owing to the broad inherent linewidths, J couplings are often measured using a spin-echo based experiment, such as, 2D J- resolved spectroscopy, introduced in Chapter 2. This experiment provides more reliable values of J couplings, as the inhomogeneities are refocused and the chemical shift and J coupling are separated into two different dimensions. The isotropic centreband of the homonuclear J-resolved spectrum of **4.3** shown in Figure 4.19a, reveals a clear splitting of 86 Hz, at room temperature in F_1 for both P1 and P2, suggesting the presence of a homonuclear through-space intermolecular J coupling. The same homonuclear J-resolved experiment performed for **4.4**, is shown in Figure 4.19b. In this case, no splitting is observed in the indirect dimension, as predicted by DFT calculations. As shown in Table 4.7, the value of the J coupling predicted is actually very small (~ 11 Hz) confirming the lack of a

splitting observed in the J-resolved experiment.

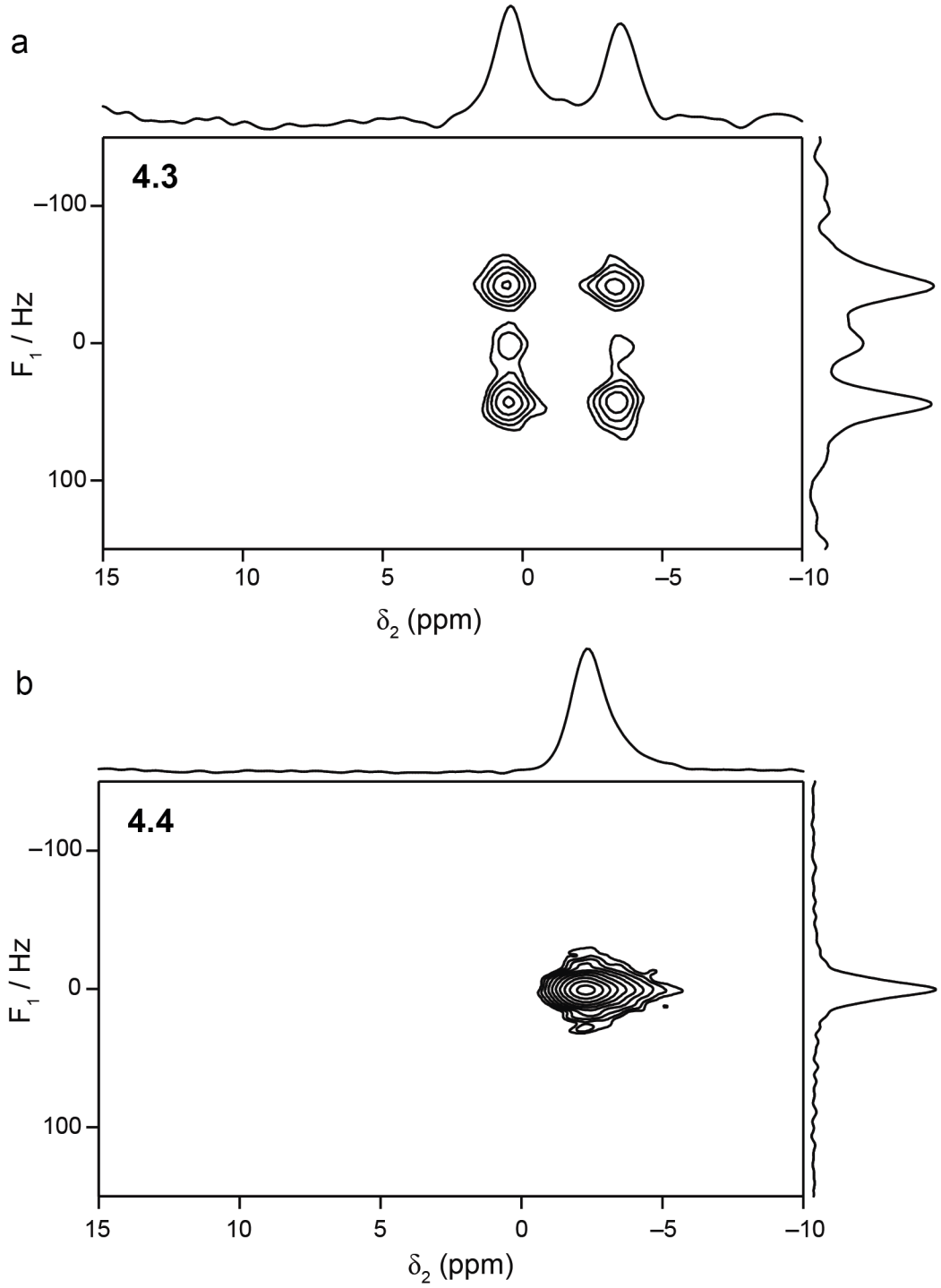

Figure 4.19. Isotropic centrebands of two-dimensional homonuclear ^{31}P J-resolved spectra of (a) **4.3** and (b) **4.4**, acquired at 14.1 T, with a MAS rate of 5 kHz. ^{1}H decoupling (CW) was applied in both t_1.and t_2.

Compounds **4.5** and **4.6** both have, as does **4.4**, a single molecule in the asymmetric unit. Therefore, the through-space, homonuclear J coupling predicted by DFT is between crystallographically-equivalent but magnetically inequivalent sites as will be discussed later on. Figure 4.20a and 4.20b show homonuclear J-resolved spectra for **4.5** and **4.6**, respectively. For **4.5**, a clear splitting of 88 Hz is observed along with an intense central line. However, the presence of a splitting is not very clear for **4.6**, owing the level of noise in the spectrum. Although DFT predicts a J coupling of similar magnitude to that for **4.5** (*i.e.*, 147.6 and 152.6 Hz for **4.5** and **4.6**, respectively), there is not an obvious splitting of a similar magnitude to **4.5** probably as T_2 relaxation problem. The predicted J couplings in Table 4.7, all appeared overestimated in comparison to the experimental values. However, the DFT calculations are performed at 0 K, and the ^{31}P and ^{77}Se NMR parameters (chemical shift and J couplings), display a temperature dependence as described above. Therefore, is possible that the homonuclear ^{31}P J coupling is also temperature dependent. In order to investigate this effect, homonuclear J-resolved spectra were recorded at varying temperatures, and the centreband projections are shown in Figure 4.21, for **4.3** and **4.5** (note that this was not performed for **4.4** and **4.6** as no J coupling was measured in the spectra). Figure 4.21 shows that the J coupling is temperature dependent, with an increase of 2-3 Hz per 25 K temperature decrease for both compounds. If this variation is assumed to be linear over the whole temperature range, the couplings at 0 K would be predicted to be ~110 and ~125 Hz for **4.3** and **4.5**, in better agreement with the calculation.

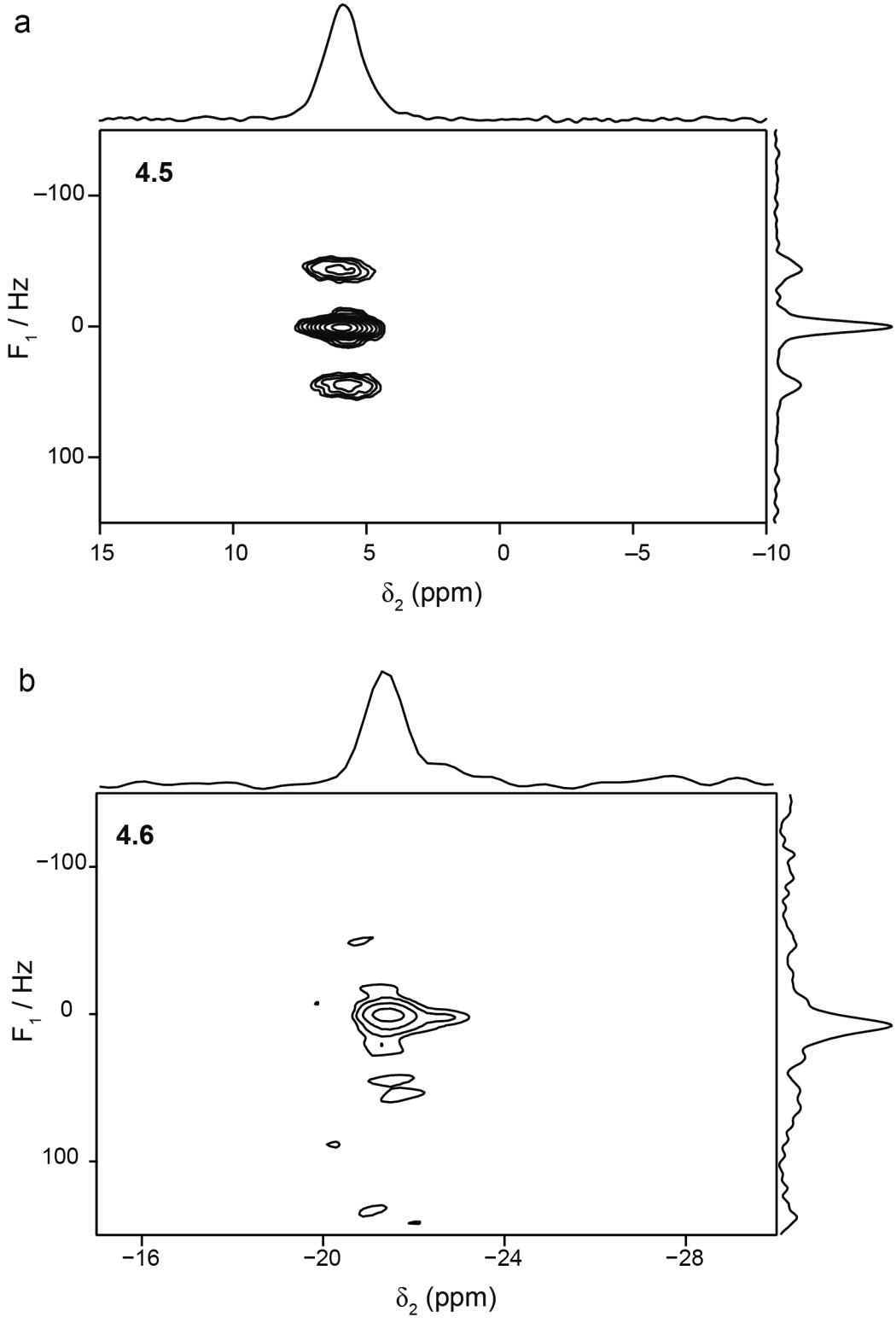

Figure 4.20. Isotropic centrebands of two-dimensional homonuclear ^{31}P J-resolved spectra of (a) **4.5** and (b) **4.6**, acquired at 14.1 T, with a MAS rate of 5 kHz. ^{1}H decoupling (CW) was applied in both t_1.and t_2.

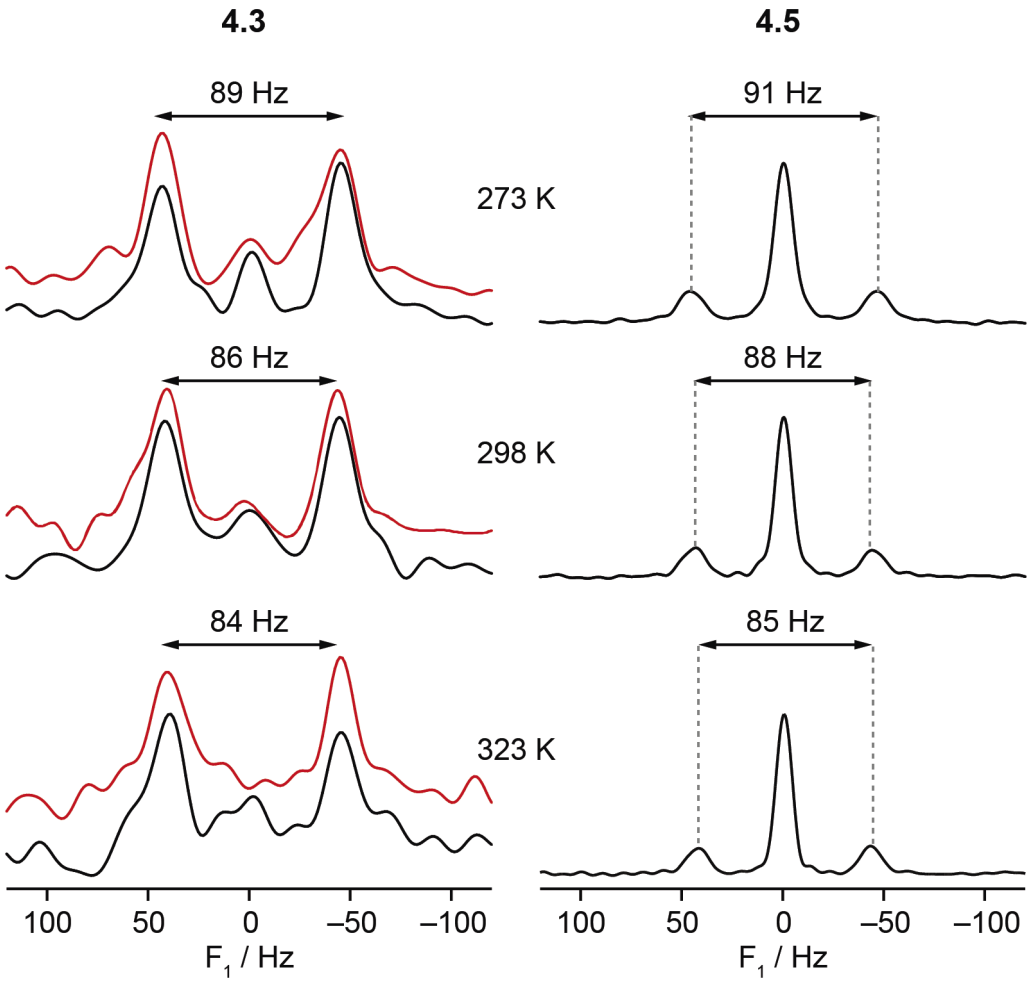

Figure 4.21. F_1 projections of ^{31}P (14.1 T, 5 kHz MAS) homonuclear J-resolved NMR spectra of **4.3** (P1 and P2 are shown in black and red, respectively) and **4.5**, acquired at variable temperature.

The CDD plots for the homonuclear ^{31}P–^{31}P interaction for **4.3** and **4.5** are shown in Figures 4.22a and 4.22b, and demonstrate that the J coupling is mediated *via* the P lone pair electrons in each case, while for **4.4** the CDD plot shown in Figure 4.22c, confirms a very small interaction between the two P atoms.

The presence of a through-space interaction is perhaps not too surprising in **4.3**, as it occurs between crystallographically-inequivalent sites (*i.e.*, two P atoms in the asymmetric unit, that are within the sum of

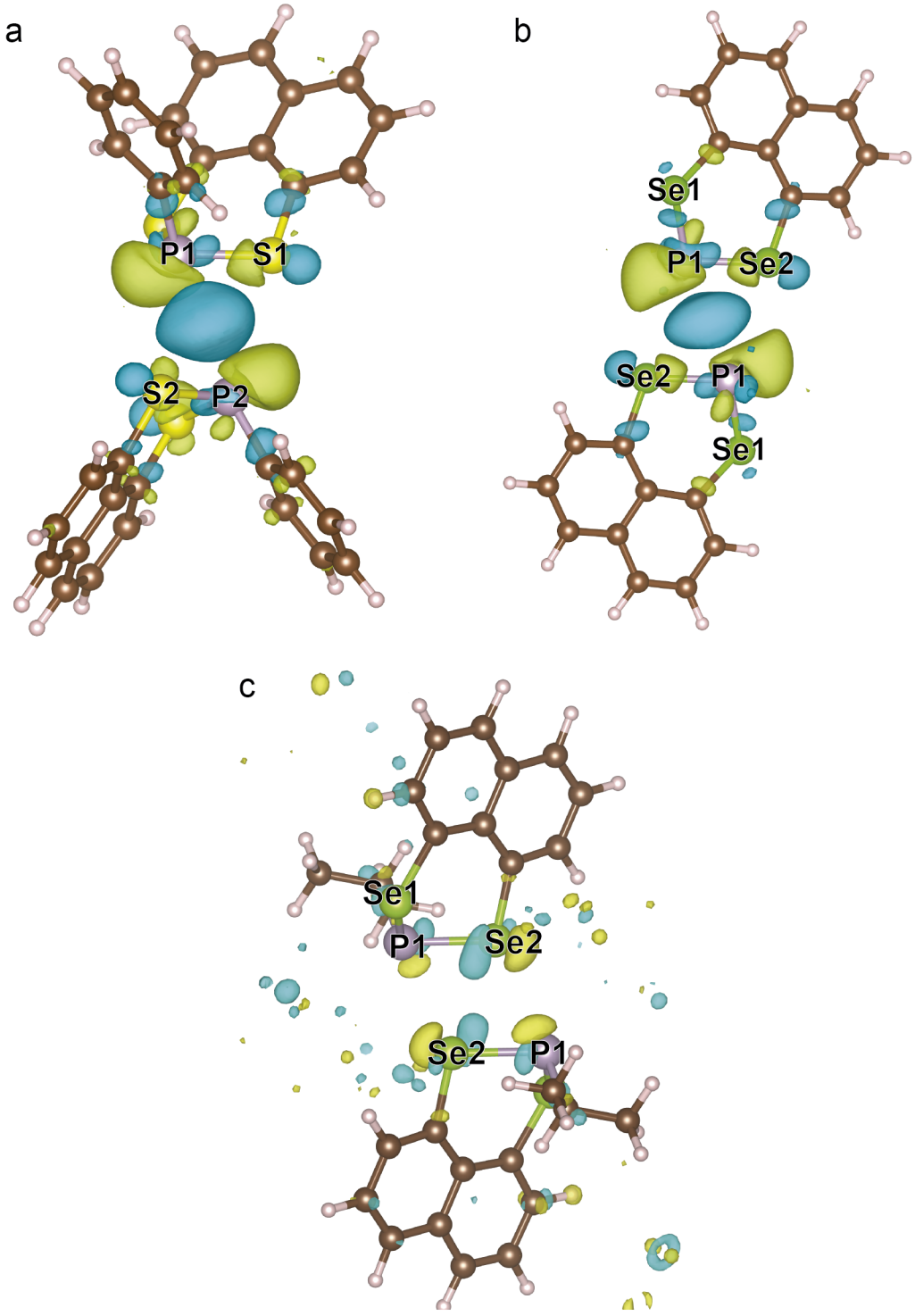

Figure 4.22. CDD plots computed from non-relativistic J-coupling calculations of the ^{31}P-^{31}P through-space J coupling in (a) **4.3**, (b) **4.5** and (c) **4.4**, showing isosurfaces on the same scale. ^{t}Bu groups were omitted for clarity.

their van der Waals radii), although, the intermolecular nature of this interaction is unusual and no examples of this kind of interaction could be found in the literature. In contrast, for **4.5**, the J coupling occurs between crystallographically-equivalent P sites, *i.e.*, that possess the same isotropic chemical shift. It is well known that J couplings between equivalent spins are not observable in solution-state NMR spectra. However, in solids, if the crystallographically-equivalent spins are magnetically inequivalent, it is possible to observe a J coupling between them. Such magnetic inequivalence could occur if, *e.g.*, the CSA tensor of each nucleus has a different orientation with respect to B_0.[9] In this case, the two nuclei will have different anisotropic chemical shifts making them magnetically inequivalent at points during the rotor period. However, if the tensor orientations are identical (or related by an inversion center) the two spins remain magnetically equivalent.[8] Figure 4.23, illustrates schematic NMR spectra for two spin I = 1/2 nuclei in molecules A and B, that are coupled r with coupling constant J_{AB}. Each spin exhibits a different chemical shift each of which is orientation dependent. This magnetic inequivalence, depends on the spinning frequency, as, at high spinning rates, the CSA is averaged and a regime of magnetic equivalence (*i.e.*, an A_2 spin system) is approached. At slow spinning rates, the magnetic inequivalence is enhanced, and the J coupling may be observed, *i.e.*, the AB spin system regime is approached. The strength of the direct homonuclear dipolar coupling between molecules A and B, can also enhance the magnetic inequivalence of the spins.[9a, 27] However, in compound **4.5**, the two molecules (and, therefore, their CSA tensors) are related *via* an inversion centre and so, in principle, this will result in both crystallographic and magnetic equivalence, and does not explain the observation of a J coupling in the homonuclear J-resolved spectrum (Figure 4.20a).

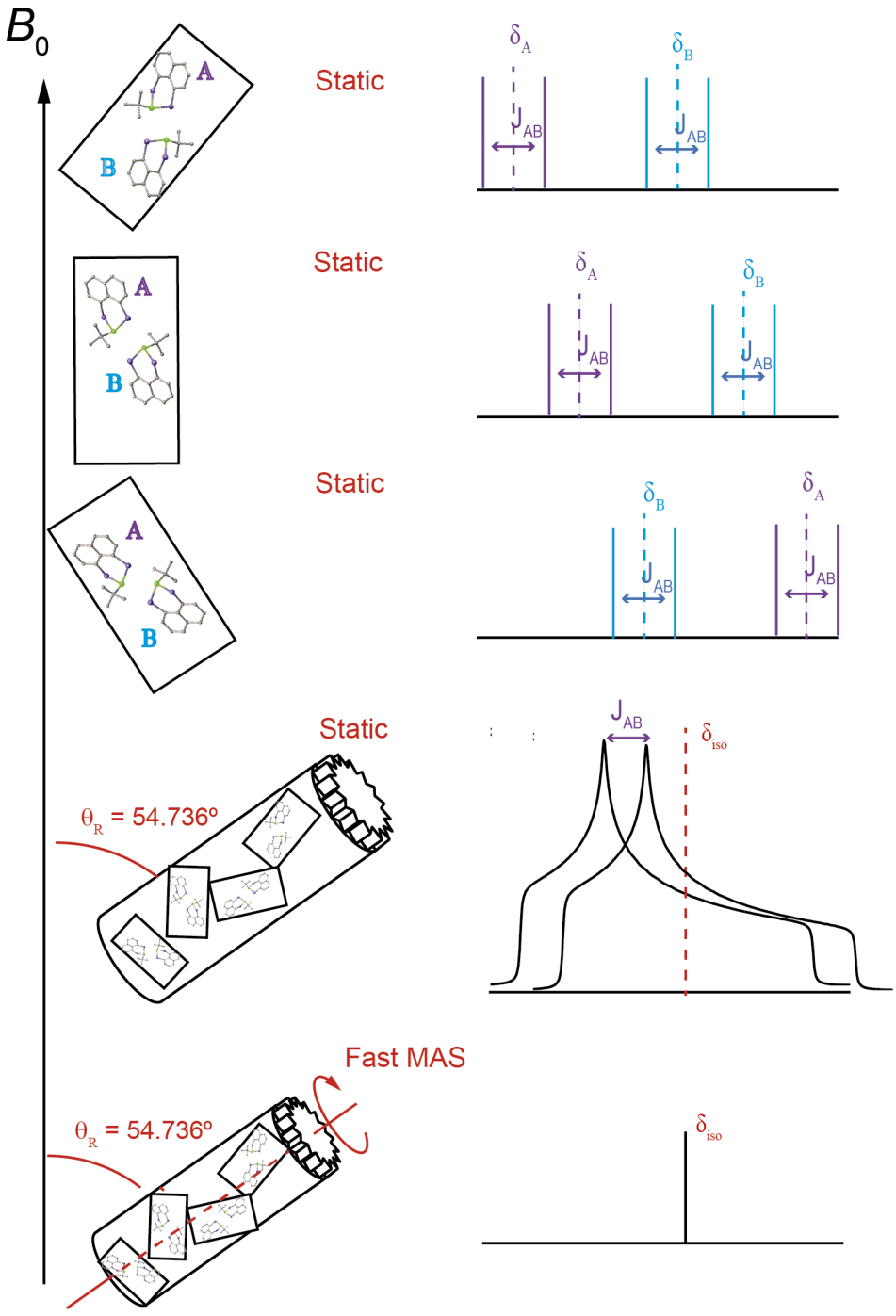

Figure 4.23. Schematic representation of a pair of crystallographically-equivalent spin I = 1/2 nuclei in two molecules, A and B, coupled with coupling constant $\mathbf{J}_{AB}$, where the different orientations of the CSA tensor lead to magnetic inequivalence and a difference in chemical shift as the crystallite orientation with respect to B_0 varies.

The motion of the ^{t}Bu group, could, in principle affect the orientation of the molecules (and the CSA tensors) breaking in this way the inversion centre. In order to investigate this, a calculation was performed to locate the transition state corresponding to rotation of the ^{t}Bu group, thus breaking the inversion centre. This transition state can be visualized in Figure 4.24, where the ^{t}Bu group is shown circled in red. The energy barrier of the transition state is ~55 kJ/mol, which could be overcome at room temperature. The NMR parameters were calculated for this transition state and the CSA tensor on P1 is rotated from its original position ($\alpha = 54.87°$, $\beta = 1.08°$, $\gamma = -62.51°$ {ZYZ convention}). This results in a breaking of the crystallographic inversion centre that could lift the equivalence of the P atoms, in principle, allowing the observation of a homonuclear J coupling. Additionally, a chemical shift difference of ~ 2 ppm is found between its original position and after rotation.

Although, motion could perhaps explain the presence of a homonuclear through-space coupling between crystallographically-equivalent P sites in **4.5**, no significant change in the J-resolved spectrum of **4.5** with varying magnetic field strength, is shown in Figure 4.25, which might be expected if an anisotropic interaction were responsible for lifting magnetic equivalence. Therefore, a more fundamental explanation must be responsible for the magnetic equivalence that could arise from the heteronuclear couplings between ^{31}P and ^{77}Se. To consider the interaction between the two P atoms, a dimer structure needs to be considered, where each P atom is bonded to two Se, leading to four selenium atoms in the dimer in total. However, most Se will be NMR-inactive isotopes, as the natural abundance of the only NMR-active isotope (^{77}Se) is ~ 7.6%. Simple statistics predicts that the probability of the four Se being NMR inactive is ~73%.

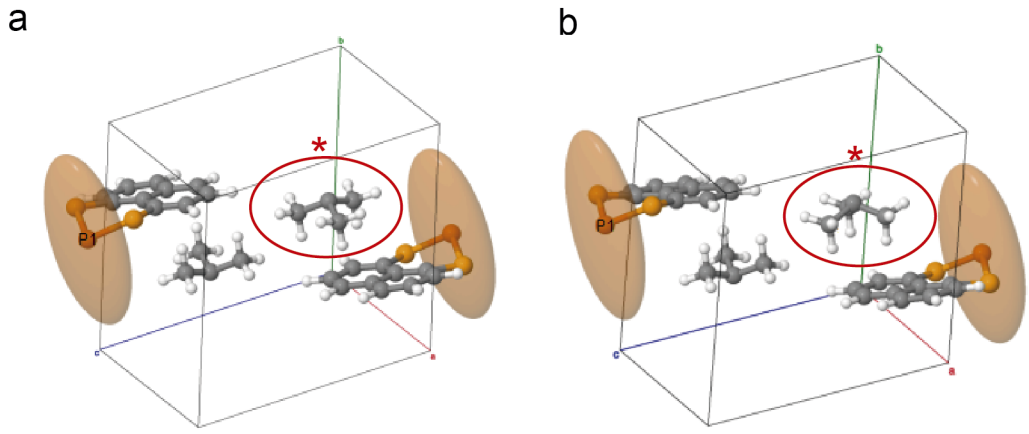

Figure 4.24. (a) Optimized geometry of **4.5** showing the computed CSA tensors for P atoms. In this original position, a centre of inversion is presented (b) Transition-state geometry for rotation of ^{t}Bu substituent of P1 showing computed CSA tensors for P atoms (note change in position of the starred (*). Visualized with magresview.[28]

In this case, both P atoms will be magnetically equivalent, resulting in no splitting observed in a J-resolved spectrum. However, in the case where at least one Se is ^{77}Se, there will be a through-bond ^{77}Se-^{31}P coupling experienced by one ^{31}P (*e.g.*, that highlighted in Figure 4.26) that is not present for the second, resulting in magnetic inequivalence of the P atoms and so the homonuclear J(^{31}P-^{31}P) coupling will then be observed. The probability of this happening in the system considered is ~22%, for one ^{77}Se and ~27% if dimers with more ^{77}Se are included. This will, therefore, result in a combination of signals in the J-resolved spectrum as observed in Figure 4.20a, from 73% of molecules where no coupling is observed (and a central signal is present), and 27% where a splitting is seen. It must be noted that, if ^{77}Se is at site Se2, a significant through-space intermolecular heteronuclear ^{77}Se2-^{31}P1 coupling is also present as described earlier in this chapter in addition to the through-bond

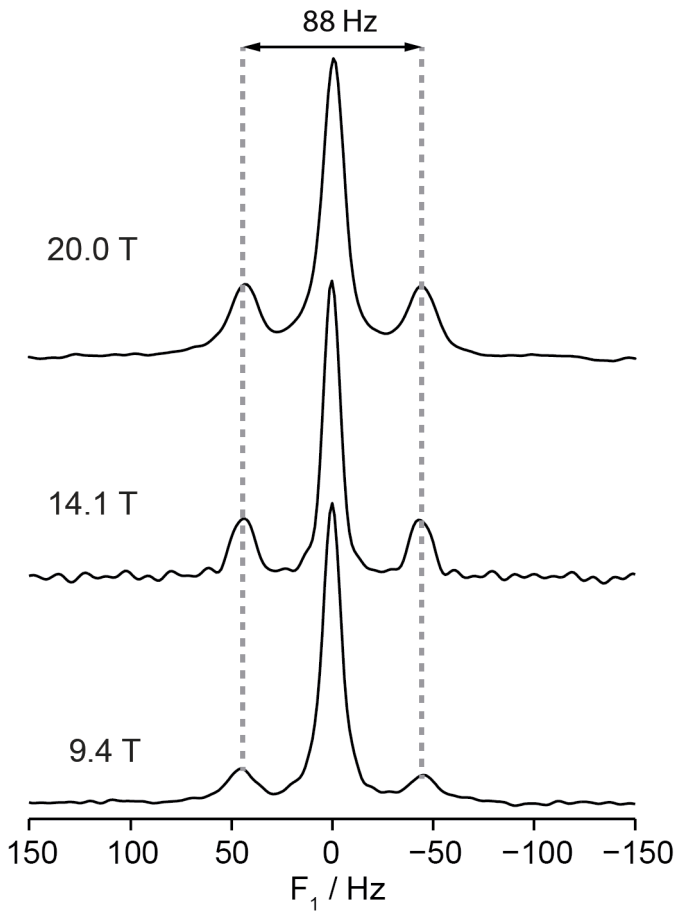

Figure 4.25. F_1 projections of two-dimensional ^{31}P homonuclear J-resolved NMR spectra of **4.5**, acquired at the B_0 field indicated.

heteronuclear $^{77}Se2$-^{31}P coupling, so that, in principle, both P sites may be close to magnetically equivalent once more (if the motional behaviour is neglected). However if the Se1 is occupied by ^{77}Se, there is a much smaller through-space interaction with the ^{31}P in the neighbouring molecule, which will result in greater magnetic inequivalence of the P atoms.

In order to ascertain whether the magnetic inequivalence arises as a consequence of the heteronuclear coupling to ^{77}Se, the homonuclear J-resolved experiment was performed with ^{77}Se decoupling (during t_1) in order to ensure the P atoms are once again magnetically equivalent by

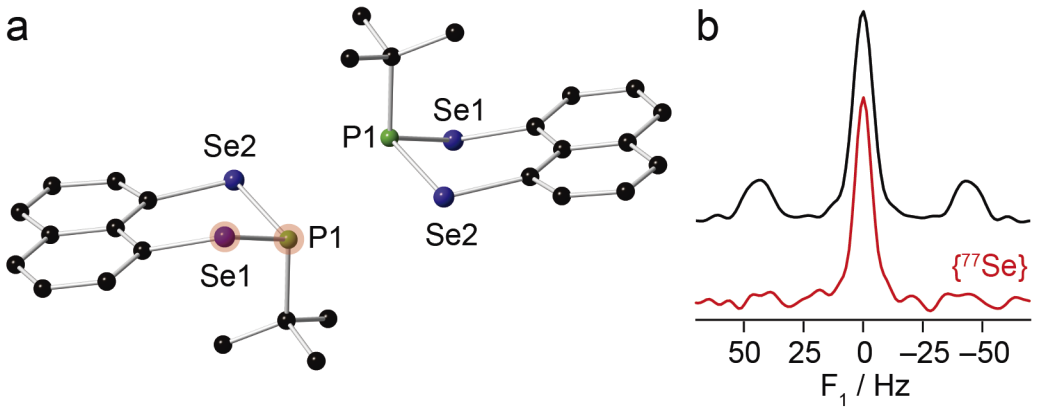

Figure 4.26. (a) Expansion of the structure of **4.5**, showing two molecules, with the atoms involved in a $^{77}Se/^{31}P$ heteronuclear J coupling highlighted. (b) F_1 projections of two-dimensional ^{31}P (14.1 T, 5 kHz MAS) homonuclear J-resolved NMR spectra of **4.5**, acquired with (red) and without (black) ^{77}Se decoupling.

removing all couplings to ^{77}Se. Owing to the large ^{77}Se CSA observed for **4.5**, high-power decoupling is, in principle, required to successfully remove the heteronuclear coupling to ^{77}Se, however due to hardware limitations, it was not possible to use high-power CW decoupling for the long evolution periods required, (~ 100 ms), and so, a pulsed decoupling approach (RS-HEPT)[12] was used instead to limit the impact of the decoupling on the probe. Figure 4.26b shows a comparison of the centreband projections of homonuclear J-resolved MAS NMR spectra of **4.5** acquired with (red spectrum) and without (black spectrum) ^{77}Se decoupling. It can be seen that the homonuclear J(^{31}P-^{31}P) coupling is not observed when the J coupling to ^{77}Se is removed, with only the (unmodulated) central signal present, confirming that it is the heteronuclear J coupling interaction that lifts the magnetic equivalence of ^{31}P.

4.6.8 Heteronuclear J couplings in 4.4 and 4.5

As discussed above, J-resolved experiments provide a easier and more accurate measurement of the J coupling as the offset, dipolar couplings and imperfections of B_0 and B_1 are refocused. For **4.4** it is difficult to determine the J values for the heteronuclear J(^{77}Se-^{31}P) couplings as both selenium sites have very similar δ_{iso} (~1.5 ppm, as shown above), leading to a complex lineshape. However, for **4.5**, a heteronuclear 2D J-resolved experiment can, in principle, provide a better determination of the J couplings than the ^{77}Se CP MAS NMR spectrum, where the CSA, J coupling and dipolar coupling interactions are present at least instantaneously during the rotor period. Such measurements of the J coupling values could be useful in order to determine the accuracy of DFT calculations to predict the J coupling values in these systems. Figure 4.27a shows a heteronuclear 2D ^{77}Se J-resolved spectrum for **4.5** recorded at 14.1 T and 12.5 kHz MAS. The heteronuclear coupling is created by applying simultaneously a 180° pulse to both ^{77}Se and ^{31}P. Figure 4.27b shows the same spectrum, tilted by 45°, in order to extract more easily the J couplings. It can clearly be observed that more peaks appear in the spectrum than expected, as, in principle, for Se2 a doublet of doublets (*i.e.*, four peaks) and a doublet for Se1 (*i.e.*, two peaks) are expected. The extra peaks, shown in green and marked with *, in Figure 4.27b, appear for Se2 and cannot be immediately explained. The signal that appears at $F_1 = 0$ is an unmodulated signal, which can often be observed in the presence of strong coupling effects.[29] One possible explanation for the presence of the extra peaks that appear in the heteronuclear ^{77}Se J-resolved spectrum of both spins. As both P atoms are magnetically inequivalent, the 180° pulse **4.5**, could cause spin mixing between the two coupled ^{31}P, both of which

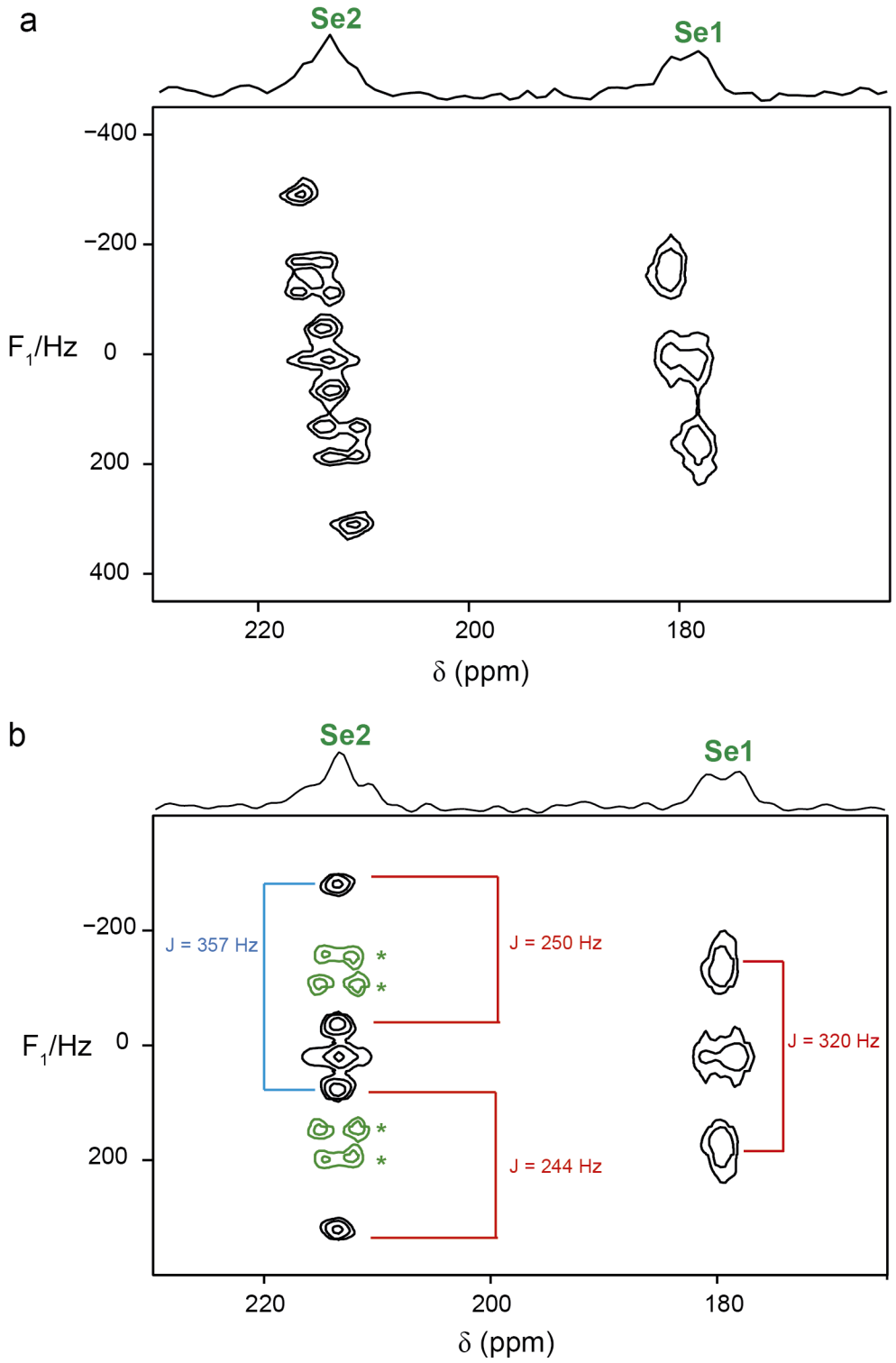

Figure 4.27. (a) Isotropic centrebands of the 2D heteronuclear ^{77}Se J-resolved spectra (14.1 T, 12.5 kHz MAS) of **4.5.** (b) As in (a) but tilted by 45° to allow extraction of J coupling parallel to F_1.

also, couple to Se2. Figure 4.28 shows the heteronuclear 2D ^{77}Se J-resolved experiment for **4.4** recorded at 14.1 T and 12.5 kHz MAS and with simultaneous 180° pulses to both nuclei. In this case a doublet for each selenium site is expected, which could possibly appear as doublet of doublet, as both Se have very similar chemical shifts. Surprisingly, more peaks also appear in this spectrum and their origin is again not immediately obvious. In this case, the multi-spin system should, in principle, be absent, as no homonuclear J(^{31}P–^{31}P) coupling was measureable above (Figure 4.19b).

In order to determine whether the extra peaks appear as a consequence of the 180° pulse, the same experiment was performed, but, instead of a 180° pulse to measure the heteronuclear J(^{77}Se–^{31}P) coupling, CW decoupling was applied during the first $t_1/2$ evolution period. In this case, the observed J coupling will be scaled by a factor of 1/2, as the J coupling only evolves during the second $t_1/2$ period. The spectra recorded for **4.5** and **4.4** using this pulse sequence are shown in Figure 4.29a and 4.29b, respectively. For **4.5**, the comparison of the two experiments (in red when ^{31}P CW decoupling was applied, and in black when the 180° pulse was used) can be seen in Figure 4.29a. The extra peaks observed when a 180° pulse is used appear significantly reduced when using ^{31}P CW decoupling in $t_1/2$, suggesting that their origin is, indeed, spin mixing. This is also confirmed for **4.4**, where comparison of the two methods is shown in Figure 4.29b. The extra peaks also disappear and an isolated doublet with 1/2J is observed. However, for **4.4**, it was not expected the disappearing of the extra peaks as homonuclear J(^{31}P–^{31}P) coupling is negligible.

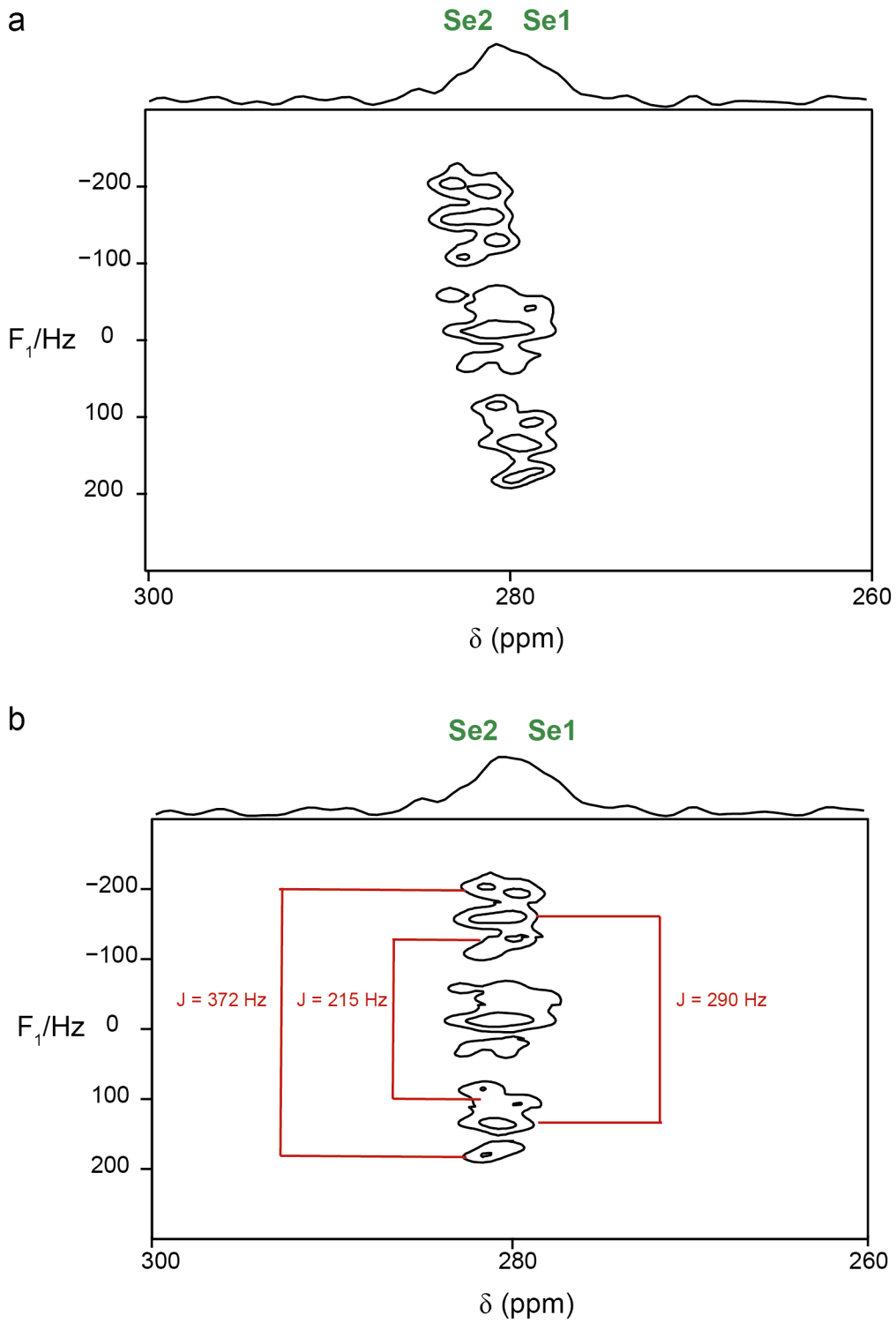

Figure 4.28. (a) Isotropic centrebands of the 2D heteronuclear ^{77}Se J-resolved spectra (14.1 T, 12.5 kHz MAS) of **4.4**. (b) As in (a) but tilted by 45° to allow extraction of J coupling parallel to F_1.

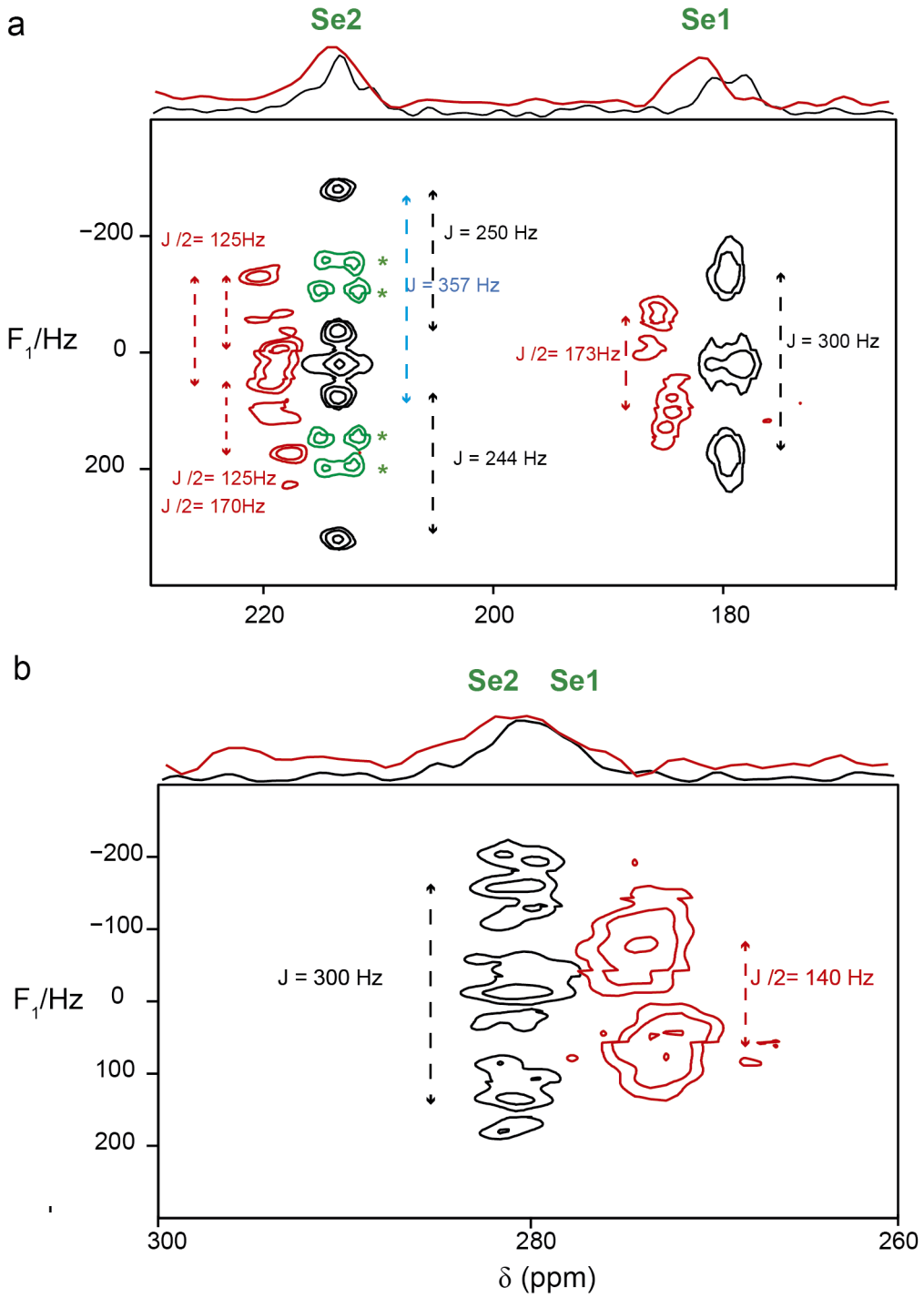

Figure 4.29. Isotropic centrebands of the 2D heteronuclear ^{77}Se J-resolved spectra (14.1 T, 12.5 kHz MAS) tilted by 45° to allow extraction of J coupling parallel to F_1 of (a) **4.5** and (b) **4.4**. In red ^{31}P CW decoupling was applied (and the spectrum is shown with a small frequency shift for clarity), while in black 180° pulse was used.

Table 4.8, summarises the values of the heteronuclear J (^{77}Se–^{31}P) that were measured directly from the ^{77}Se CP MAS NMR spectra, from the 2D heteronuclear J-resolved experiments, or calculated. It can be seen that there is a generally good agreement between the calculated and experimental values.

Table 4.8. Experimental and calculated heteronuclear J (^{77}Se–^{31}P) couplings (Hz), in the first case by direct analysis of ^{77}Se CP MAS NMR spectra or from 2D heteronuclear J-resolved spectra and in the second predicted by DFT at the scalar-relativistic ZORA level of theory.

Compound	J(^{77}Se–^{31}P)	^{77}Se CPMAS /Hz	J-resolved/Hz	J calculated/Hz
4.4	Se1–P	~300	290	–250.0
4.4	Se1–P	~300		–244.0
4.5	Se1–P	312	320	–310.8
4.5	Se2–P	270	250/244	–280.9
4.5	Se2–P	340	357	365.2

4.6.9 Calculation of NMR parameters

To gain insight into the structural origins of the observed ^{77}Se and ^{31}P magnetic shielding tensors, periodic first-principles GIPAW calculations were performed on geometry optimized crystal structures initially obtained by single crystal X-ray diffraction for the series of compounds. The ^{31}P magnetic shielding tensors for **4.1 – 4.6** were calculated using CASTEP 7 and the values are summarised in Table 4.9. Note that only **4.1b** was believed to correspond to the bulk sample of **4.1**, so the calculations for the other two polymoprhs are not included in Table 4.9. The values of σ_{ref} can be determined by linear regression when plotting the δ_{iso}^{exp} against σ_{iso}^{calc} for a series of compounds, as discussed in previous chapters. However, at this point only few compounds have been investigated,

which can lead to errors in the value of σ_{ref} determined. Therefore, σ_{ref} for all compounds discussed in this thesis, will be determined in the following chapter, where more compounds are considered. The relative difference in isotropic shielding between the six molecules is much more significant in the calculation than experimentally (*e.g.,* **4.1** and **4.4** have a experimental δ_{iso} difference of between 8 – 4.8 ppm, while the difference in calculated σ_{iso} is much greater, ~38 ppm). However, this difference decreases for the Ph derivatives (**4.3** and **4.6**), for which the difference in δ_{iso}^{exp} is between 22 – 18 ppm and the σ_{iso}^{calc} difference is between 25 – 17 ppm. Figure 4.30a shows a plot of δ_{iso}^{exp} against σ_{iso}^{calc} for ^{31}P in all compounds. It is clear that there are two sets of points, the ones in the green area corresponding to the sulfur derivatives, and those in the red area corresponding to the selenium derivatives. A plot of Ω^{exp} against Ω^{calc} is shown in Figure 4.30c, demonstrating poor agreement ($R^2 = 0.39$). The calculated values of Ω are generally overestimated for the whole series. The discrepancies observed between sulfur and selenium compounds perhaps suggest a difference in accuracy between the heavy-atom pseudopotentials. While ^{77}Se DFT calculations have been shown to be in good agreement with experiment in similar naphthalene-based systems,[30, 31] there has been little experimental verification of any predicted ^{33}S NMR parameters, owing to the considerable difficulties associated with experimental study of this low-γ, low-abundance quadrupolar nucleus.

The values of σ_{ref} for ^{77}Se will be determined in the next chapter, where more selenium-containing compounds are considered (as only three selenium compounds were considered in this chapter).

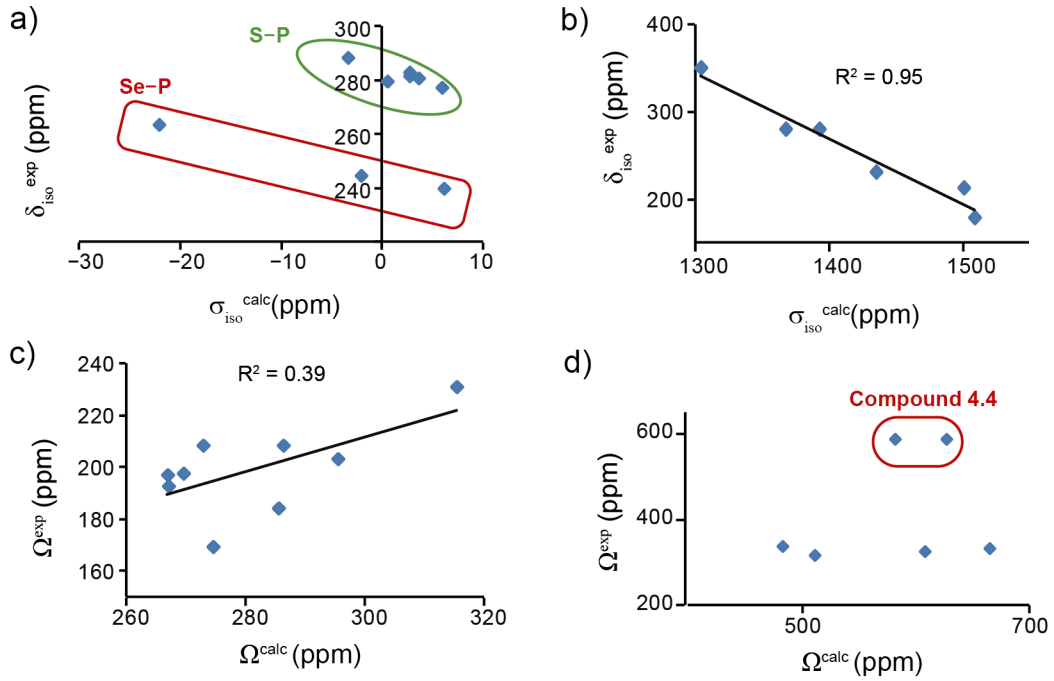

Figure 4.30. Plot of (a) ^{31}P δ_{iso}^{exp} against σ_{iso}^{calc}, (b) ^{77}Se δ_{iso}^{exp} against σ_{iso}^{calc}, (c) ^{31}P Ω^{calc} against Ω^{calc} and (d) ^{77}Se Ω^{calc} against Ω^{calc}, for **4.4 – 4.6**.

Table 4.9. Calculated ^{31}P NMR parameters (isotropic shielding, σ_{iso}^{calc} , span Ω^{calc} and skew κ^{calc} for **4.1b – 4.6**.

	4.1b	**4.2**	**4.3**	**4.4**	**4.5**	**4.6**
E,R group	S, ^{i}Pr	S, ^{t}Bu	S, Ph	Se, ^{i}Pr	Se, ^{t}Bu	Se, Ph
σ_{iso}^{calc}	283.1 281.7 280.9 277.4	282.5 280.9	288.5 279.7	244.7	239.9	263.6
Ω^{calc}	272.9 286.3 285.5 274.5	308.9 308.0	267.1 266.9	269.6	315.4	295.5
κ^{calc}	0.3 0.3 0.3 0.3	0.3 0.2	0.2 0.3	0.2	0.4	0.1

All σ (ppm), Ω(ppm).

It can be observed from Table 4.10 that a similar difference in isotropic shielding is found between calculated and experimental values (*i.e.*, between **4.4** and **4.5**, there is between 101 – 67 ppm difference in the δ_{iso}^{exp}, while 115 – 113 ppm difference is found between σ_{iso}^{calc} for these two compounds). A plot of δ_{iso}^{exp} against σ_{iso}^{calc} for ^{77}Se in **4.4**, **4.5** and **4.6**, shown in Figure 4.30b, and results in a good correlation (R^2 = 0.95), although, it must be noted that only three compounds are considered, while six are studied for ^{31}P. The calculated and experimental spans were also compared and a plot of Ω^{exp} against Ω^{calc} is shown in Figure 4.30d. The values of the calculated span are overestimated by DFT for the three compounds, with the span of **4.6**, being the most different in comparison to the experimental values, with a difference of between 279 – 328 ppm, followed by **4.5** with a difference of between 191 – 141 ppm and then **4.4** which differ only by a few ppm (37 – 8 ppm).

Table 4.10. Calculated ^{77}Se solid-state NMR parameters (isotropic shielding, σ_{iso}^{calc}, span Ω^{calc} and skew κ^{calc} for **4.4** – **4.6**.

	4.4	**4.5**	**4.6**
E,R group	Se, ^{i}Pr	Se, ^{t}Bu	Se, Ph
σ_{iso}^{calc}	1392.8	1508.7	1435.1
	1367.6	1500.7	1304.2
Ω^{calc}	626.1	510.4	607.2
	580.9	482.2	663.9
κ^{calc}	–0.6	–0.6	–0.5
	–0.8	–0.8	–0.02

4.7 Conclusions

In this chapter a series of new six-membered ring P-S and P-Se heterocycles have been successfully synthesised using an adapted route. The compounds were found to be fairly stable upon exposure to air, with the exception of the phenyl versions that decompose quite rapidly.

The strain in the system was analysed for the series of compounds and it was clear from the splay angles, torsion angles of the backbone, and the out-of-plane displacements that more distortion is introduced in the system when the smaller sulfur is substituted by selenium. It is clear from Chapter 3 that the strain can be relieved by distortion of the rigid backbone or by the formation of weak interactions. The systems studied in Chapter 3 were stabilized by *intramolecular* interactions that occur between the *peri* atoms. However, in the systems studied in this chapter, the incorporation of the P into the E–E bond, prevents the formation of *intramolecular* interactions between *peri*-atoms. Therefore, another means to stabilize the systems must be found. This could potentially explain the presence of *intermolecular* interactions observed in some of the compounds studied.

The packing motifs are different between compounds, for example in **4.5** and 4**.6,** the molecules are closer to each other favouring intermolecular contacts, while the molecules in **4.4** are more separated. The different packing in these systems could possibly arise from the different electronic and steric effects introduced by the different R groups or even from the presence of other intermolecular interactions such as π-π stacking. However, the electronic effects are more difficult to quantify, and more examples are needed in order to understand whether there is an effect that drives the packing. The steric parameter θ was calculated from

the crystal structure data for all compounds in order to account for this effect. A plot of ^{31}P chemical shift in solution against θ shows a relatively good agreement (R^2 = 0.72), considering that only a few examples were studied. However for ^{77}Se, as only three compounds were studied, the steric effect cannot be studied in detail. Moreover, θ does not vary significantly through the series (^{i}Pr, ^{t}Bu and Ph), so this parameter may be a poor indicator of the steric bulk of R. In the solid-state NMR spectra a θ parameter calculated from a geometry-optimized structure was considered. As was the case in Chapter 3, this parameter is a poor indicator of the steric bulk, as some other effects are present.

In the three selenium-containing compounds, the difference in isotropic chemical shift between the two selenium environments present in each compound increases along the sequence Ph > ^{t}Bu > ^{i}Pr (*i.e.*, 119 ppm difference in the Ph analogue, 34 ppm difference in the ^{t}Bu and almost no difference (~1.5 ppm) for the ^{i}Pr). This could suggest that the intermolecular interactions increase the chemical shift difference, and, when there is no intermolecular interaction, both selenium sites remains quite similar (^{i}Pr), and when there is a more significant interaction the two selenium environments can be distinguished.

The presence of polymorphism was only found for **4.1**, the sulfur ^{i}Pr analogue. The presence of polymorphism in this case could be related to the lack of *intermolecular* interaction observed for this compound. As a preferential or "strong" interaction in not present in the system, other, weaker interactions, can be present to stabilise it, yielding a number of different ways in which the molecules pack and interact resulting in polymorphism. This will be discussed in more detail in the next chapter, where no possibilities of "though-space" coupling between molecules are found for the systems studied.

DFT calculations were an essential tool to verify the presence of weak interactions in the systems studied, providing insight into the coupling mechanism and pathway of the interactions. The overestimated values obtained for the J couplings could be explained by the through-space nature of the interactions, as the magnitude of these couplings will be crucially dependent upon the exact distance between the nuclear species. The difficulties of accurately reproducing dispersion interactions in periodic DFT calculations may lead to some variation in the exact distances between atoms, and could contribute to the differences between experiment and calculation. Moreover, ^{77}Se and ^{31}P variable temperature experiments confirmed that both shifts and couplings show a small temperature dependency, probably as a result of motion of the R groups, which could also contribute to the difference observed between experiments and calculations.

The presence of a very unusual intermolecular interactions between crystallographic equivalent P species was also demonstrated by J-resolved spectroscopy. It was shown that the magnetic equivalence was lifted by the heteronuclear J coupling to ^{77}Se (7.6 %). This was the first time such an effect has been observed.

The unexpected heteronuclear 2D J-resolved spectrum for **4.5** suggest that strong coupling effects are present in the system studied. In this study, the 180° pulse is believe to be the responsible for the spin mixing resulting in extra peaks observed in the 2D spectrum.

4.7 Future work

In order to have a better understanding of the steric and electronics effects of the R group on the stability and reactivity of these compounds, the

series could be extend to different R groups, such as more electron-deficient and electron-rich aryl groups. This could provide a range of stable heterocycles, which could be studied without the problems of decomposition or oxidation processes occuring, as in **4.6**, and whose properties could easily be explored by modifying the aryl group. The presence of *intermolecular* interactions or polymorphism could be then studied in the proposed series.

In order to have a better understanding of the 2D heteronuclear ^{77}Se J-resolved experiments for compounds **4.4** and **4.5**, it would be desirable to repeat the experiments to improve the signal-to-noise ratio.

4.7 References

1. a) N. A. Semenov, N. A. Pushkarevsky, A. V. Lonchakov, A. S. Bogomyakov, E. A. Pritchina, E. A. Suturina, N. P. Gritsan, S. N. Konchenko, R. Mews, V. I. Ovcharenko and A. V. Zibarev, *Inorg. Chem.*, **2010**, 49, 7558-7564; b) M. Planells, B. C. Schroeder and I. McCulloch, *Macromol*., **2014**, 47, 5889-5894.

2. E. L. Hahn, *Phys. Rev*., **1950**, 80, 580-594.

3. M. Karplus, *J. Chem. Phys.*, **1959**, 30, 11-15

4. A. Saika and H. S. Gutowsky, *J. Am. Chem. Soc.*, **1956**, 78, 4818-4819.

5. J. C. Hierso, *Chem. Rev.*, **2014**, 114, 4838-4867.

6. a) T. Wiegand, H. Eckert, J. Ren, G. Brunklaus, R. Fröhlich, C. G. Daniliuc, G. Lübbe, K. Bussmann, G. Kehr, G. Erker and S. Grimme, *J. Phys. Chem. A*, **2014**, 118, 2316-2331; b) T. Wiegand, H. Eckert, O. Ekkert, R. Fröhlich, G. Kehr, G. Erker and S. Grimme, *J. Am. Chem. Soc.*, **2012**, 134, 4236-4249; c) M. W. Stanford, F. R. Knight, K. S. Athukorala Arachchige, P. Sanz Camacho, S. E. Ashbrook, M. Bühl, A. M. Z. Slawin and J. D.

Woollins, *Dalton Transact*., **2014**, 43, 6548-6560; e) J. M. Griffin, J. R. Yates, A. J. Berry, S. Wimperis and S. E. Ashbrook, *J. Am. Chem. Soc.,* **2010**, 132, 15651-15660.

7. J. I. Musher, *J. Chem. Phys*., **1967**, 47, 5460-5461.

8. U. Haeberlen, *Advances in Magnetic Resonance*, Ed. J. S. Waugh, Academic Press, New York, **1976**.

9. a) G. Wu and R. E. Wasylishen, *J. Chem. Phys*., **1993**, 98, 6138-6149; b) G. Wu and R. E. Wasylishen, *J. Chem. Phys.,* **1994**, 100, 5546-5549; c) G. Wu and R. E. Wasylishen, *Inorg. Chem.,* **1996**, 35, 3113-3116.

10. a) K. Eichele, G. Wu and R. E. Wasylishen, *J. Magn. Reson. A,* **1993**, 101, 157-161; b) F. A. Perras and D. L. Bryce, "Revisiting the Concept of Equivalence in Solid-State NMR" in *eMagRes*, John Wiley & Sons Ltd**,** **2015**, Vol 4: 561–574. DOI 10.1002/9780470034590.emrstm146911.

11. G. Wu and R. E. Wasylishen, O*rganometallics*, **1992**, 11, 3242-3248.

12. J. M. Griffin, C. Tripon, A. Samoson, C. Filip and S. P. Brown, *Magn. Reson. Chem.,* **2007**, S1, 198-208.

13. J. Skibsted and H. J. Jakobsen, *J. Phys. Chem. A*, **1999**, 103, 7958-7971.

14. M. D. Segall, P. J. D. Lindan, M. J. Probert, C. J. Pickard, P. J. Hasnip, S. J. Clark and M. C. Payne, *J. Phys. Condens. Matter.,* **2002**, 14, 2717-2744.

15. M. D. Segall, S. J. Clark, C. J. Pickard, P. J. Hasnip, M. I. J. Probert, K. Refson and. M. C. Payne, *Z. Kristallogr.,* **2005**, 220, 567-570.

16. C. J. Pickard and F. Mauri, *Phys. Rev. B,* **2001**, 63, 1-12.

17. J. P. Perdew, K. Burke and M. Ernzerhof, *Phys. Rev. Lett.,* **1996**, 77, 3865-3868.

18. J. R. Yates, C. J. Pickard and F. Mauri, *Phys. Rev. B,* **2007**, 76, 1-12.

19. S. Grimme, *J. Comput. Chem*., **2006**, 27, 1787-1799.

20. J. Autschbach and T. Ziegler, *J. Chem. Phys.* **2000**, 113, 936-947.

21. A. L. Fuller, F. R. Knight, A. M. Z. Slawin and J. D. Woollins, *Eur. J. Inorg. Chem.*, **2010**, 2010, 4034-4043.

22. F. R. Knight, A. L. Fuller, M. Bühl, A. M. Z. Slawin and J. D. Woollins, *Chem. Eur. J.*, **2010**, 16, 7503-7516.

23. J. Beckmann, T. G. Do, S. Grabowsky, E. Hupf, E. Lork and S. Mebs, *Z. Anorg. Allg. Chem.*, **2013**, 639, 2233-2249.

24. a) C. A. Tolman, *J. Am. Chem. Soc*., **1970**, 92, 2953; b) C. A. Tolman, *J. Am. Chem. Soc*., **1970**, 92, 2956; c) C. A. Tolman, *Chem. Rev*., **1977**, 77, 313.

25. T. F. G. Green and J. R. Yates, *J. Chem. Phys*., **2014**, 140, 1-16.

26. O. L. Malkina and V. G. Malkin, *Angew. Chem., Int. Ed*. **2003**, 42, 4335-4338.

27. L. Duma, W. C. Lai, M. Carravetta, L. Emsley, S. P. Brown and M. H. Levitt, *ChemPhysChem.*, **2004**, 5, 815-833.

28. www. ccpnc.ac.uk/magresview/magresview/magres_view.html.

29. G. Bodenhausen, R. Freeman, G. A. Morris, D. L. Turner, *J. Magn. Reson*., **1987**, 31, 75-95.

30. C. Bonhomme, C. Gervais, F. Babonneau, C. Coelho, F. Pourpoint, T. Azaïs, S. E. Ashbrook, J. M. Griffin, J. R. Yates, F. Mauri, C. J. Pickard, *Chem. Rev*., **2012**, 112, 5733-5779.

31. J. M. Griffin, F. Knight, G. Hua, J. S. Ferrara, S. W. L. Hogan, J. D. Woollins, S. E. Ashbrook, *J. Phys. Chem. C*, **2011**, 115, 10859-10872.

Chapter 5: Synthesis and spectroscopic studies of oxidised S-P and Se-P heterocycles

5.1 Chapter overview

A series of twelve oxidised chalcogen-phosphorus heterocycles were synthesised by reaction of the starting material (the un-oxidised heterocycles described in Chapter 4) with a series of chalcogenides to give the corresponding P^{v} heterocycles ($NapE_2PRX$), where E = S, Se and X = O, S, Se. The new compounds were fully characterised by X-ray crystallography (single-crystal and powder), solution- and solid-state NMR, IR spectroscopy, mass spectrometry and microanalysis. The strain of the system upon oxidation of the P atom with different chalcogenides, was investigated by single-crystal X-ray diffraction and in some cases, examples of polymorphism were found. This was investigated by analysis of the bulk sample by powder X-ray diffraction, and by studying the compounds using ^{77}Se and ^{31}P solid-state NMR spectroscopy, in order to understand which polymorph represented the majority of the sample. The different environments found in solution- and solid-state NMR for these heterocycles are discussed. Furthermore, Periodic DFT calculations were performed and compared experimentally for all compounds included those in Chapter 4, in order to understand whether the NMR parameters can be well reproduced by this method.

5.2 Acknowledgements

Martin Standford is thanked for carrying out some of the synthesis and solid-state NMR characterisation experiments for some samples as part of his undergraduate research project at the University of St Andrews. Dr Kasun Arachchige, Dr David B. Cordes and Prof Alexandra M. Z. Slawin collected data and refined the single-crystal X-ray diffraction structures.

5.3 Introduction

The study of polymorphism has become of great importance in recent years, particularly in areas, where the different properties of a material (*e.g.*, solubility in the case of pharmaceuticals) are essential for its final use and thus commercialization.[1] X-ray crystallography is an essential tool for these studies, as detailed maps of atomic positions in crystallographic unit cells are produced.[2] However, a combination of other techniques are strongly recommended as single-crystal X-ray diffraction has several limitations (*i.e.*, the requirement for crystals of a reasonable size, problems caused by disorder and dynamics, the inaccuracy in the atomic positions of light atoms particularly in the presence of heavy atoms, *etc*,). Powder X-ray diffraction can result in an obvious alternative especially for cases, where single-crystal X-ray diffraction is not available. This technique is now used not only as a fingerprint, but to refine and determine structures itself. However, it is still less powerful than single X-ray diffraction.[3] It is clear that solid-state NMR has a role to play in the study of polymorphism, as it overcomes many of the challenges of diffraction techniques, and acts as a bridge between solution-state NMR and crystallography providing immediate information on the number of distinct species. Disorder, amorphous compounds and dynamics can be

addressed by solid-state NMR, which provides information on the local structure without requiring any long-range order, and is isotope-specific. Moreover, molecular conformations and intermolecular interactions can be studied, as shown in Chapter 4, by solid-state NMR, enabling it to distinguish between polymorphs, as it is very sensitive to changes in the local environment. These advantages, makes solid-state NMR, a useful and powerful technique for the study of pharmaceutical polymorphs.[4] Moreover, solid-state NMR can access more information than in solution, as the anisotropic interactions (*e.g.*, CSA) also contain information on the local structure, and are very sensitive to change in molecular conformation. Wasylishen and co-workers,[5] demonstrated that the ^{77}Se CSA of transition-metal square-planar complexes of $M[N(^{i}Pr_2PX)_2]^-$ (M = Pd, Pt and X = Se, Te) is very sensitive to changes in the conformation around selenium. ^{13}C and ^{15}N CSAs have been used to study conformational polymorphs (*i.e.*, a subclass of polymorphism, where a molecule can adopt different conformations in the solid state through a controlled crystallisation process).[6] The study of polymorphism is often combined with periodic DFT calculations, to help not only in the assignment of solid-state NMR spectra,[7] which could then potentially lead to the identification of polymorphs present in the sample, but also with the prediction of new crystal structures, and their relative energies in order to establish the most favourable structures.[8] An ultimate goal in this area is to control the formation of a specific polymorph, but this can only occur if the thermodynamics and kinetic of the system are known. In order to do this, all possible polymorphs and phase transitions as well as their thermodynamic stability and the kinetics of the phase transition must be known, which requires the use of different techniques to address all of these questions.[9]

In this chapter, a series of chalcogen-phosphorus heterocycles were oxidised with different chalcogens following an adapted synthetic route[10] to afford compounds of the form $NapE_2PRX$, (X = O, S, Se). Oxidation of similar compounds of the form $Nap[P(X)(Ph_2)(ER)]$,(X = O, S, Se), has been previously reported by Woollins and co-workers; solution-state NMR and single-crystal X-ray diffraction were used to investigate the distortion caused by introduction of different chalcogenides in the system and to study the effect on the intramolecular interaction that occurs though space between the atoms in the *peri* positions.[11, 12] In contrast, here, a complete study of the local environment is discussed by investigating the novel compounds produced by solid-state NMR. The compounds studied demonstrate significant polymorphism and the bulk samples were also investigated by using a combination of techniques (diffraction, solid-state NMR and DFT) to understand each material.

5.4 Experimental details

5.4.1 X-ray crystallography

Unless otherwise stated, powder X-ray diffraction data discussed in this chapter have been acquired at room temperature using a STOE STADIP instrument operated in capillary Debye-Scherrer mode equipped with a Cu X-ray tube, a primary beam monochromator ($CuK_{\alpha 1}$) and a scintillation position-sensitive linear detector. Typically, 5-50° or 5-40° 2θ ranges were investigated in an overnight experiment.

All crystal structures in this chapter were acquired at –100 (1), –148 (1) or –180 (1)° using either a Rigaku XtaLAB P200 diffractometer using multi-layer mirror monochromated Mo-K_α radiation, Rigaku Saturn70

diffractometer using graphite monochromated Mo-K_α radiation or Rigaku SCX mini diffractometer using graphite monochromated Mo-K_α radiation.

5.4.2 Solid-state NMR

Solid-state NMR measurements were performed using Bruker Avance III spectrometers, operating at magnetic field strengths of 9.4 and 14.1 T. Experiments were carried out using conventional 4-, 1.3- or 1.9- mm MAS probes, with MAS rates between 5 and 55 kHz. For ^{31}P, MAS NMR spectra were acquired at 298 K at 14.1 T and 7.5 kHz MAS, with ^{1}H decoupling. Chemical shifts are shown referenced relative to 85% H_3PO_4 (aq) at 0 ppm, using BPO_4 at –29.6 ppm as a secondary reference. For ^{77}Se, CP MAS experiments (using ramped contact pulse durations of 5-8 ms and TPPM ^{1}H decoupling) were carried out at 298 K at 9.4 and 14.1 T. Chemical shifts are referenced relative to $(CH_3)_2Se$ at 0 ppm, using the isotropic resonance of solid H_2SeO_3 at 1288.1 ppm as a secondary reference. The position of the isotropic resonances within the spinning sideband patterns were unambiguously determined by recording a second spectrum at a different MAS rate. In some cases, spectra were also acquired with additional ^{31}P continuous wave (CW) decoupling. Experimental ^{77}Se NMR parameters were determined by lineshape analysis using Bruker Topspin software, SOLA.

5.4.3 First-principles DFT calculations

NMR parameters were calculated using the CASTEP DFT code version 7,[13, 14] employing the gauge-including projector-augmented wave (GIPAW) algorithm,[15] which allows the reconstruction of all-electron wave function in the presence of a magnetic field. The generalized gradient

approximation (GGA) PBE functional[16] was employed and core–valence interactions were described by ultrasoft pseudopotentials.[17] All calculations were performed with the G06 dispersion correction scheme,[18] a planewave energy cutoff of 50 Ry (816 eV) and a k-point spacing of 0.04 2π Å^{-1}. For all calculations, the initial atomic positions and unit cell parameters were taken from the single crystal X-ray diffraction structures determined in this work. Therefore, prior to the calculation of NMR parameters, geometry optimizations were performed for each structure (using cutoff energies of 50 Ry and a k-point spacing of 0.04 2π Å^{-1}). All internal atomic coordinates and lattice parameters were allowed to vary.

Calculations for an isolated molecule in different conformations were carried out in a 20 Å box, using the PBE functional, ultrasoft pseudopotentials, the G06 dispersion correction scheme,[18] a planewave energy cutoff of 50 Ry (816 eV) and a k-point spacing of 0.04 2π Å^{-1}. Prior to the calculation of NMR parameters, geometry optimizations were performed for each structure (using cutoff energies of 50 Ry and a k-point spacing of 0.04 2π Å^{-1}), where all internal atomic coordinates and lattice parameters were allowed to vary. All calculations were performed using the EaStCHEM Research Computing Facility, which consists of 136 AMD Opteron 280 dual-core processors running at 2.4 GHz, partly connected by Infinipath high speed interconnects. Calculations wallclock times ranged from 1 to 24 h using 4 nodes (48 cores).

5.5 Objectives

The main objective in this chapter is the synthesis of a series of novel oxidised P-S and P-Se heterocycles in order to fully understand the stability and reactivity of these compounds upon oxidation with different

chalcogenides. The second objective is the characterisation of these materials using a combination of different techniques (*e.g.,* X-ray diffraction techniques, solution- and solid-state NMR spectroscopy and DFT) to obtain all accessible information on the local environment. The final objective is to extend the computational study to further compounds in order to clarify if the isotropic and anisotropic NMR parameters can be accurately reproduced using periodic first-principles calculations in chalcogen-phosphorus systems, and it they provide information about local structure.

5.6 Results and discussion

5.6.1 General synthesis

Compounds **5.1 – 5.12** were prepared as shown in Scheme 5.1, following a procedure previously reported by Karacar *et al.*, where 1,8-bis(diphenylphosphino)naphthalene was monoxidised using stoichiometric amounts of sulfur and selenium.[10, 19] Here, a similar procedure was used to afford the oxidation of **4.1**, **4.2**, **4.4** and **4.5** ($NapS_2P^iPr$, $NapS_2P^tBu$, $NapSe_2P^iPr$ and $NapSe_2P^tBu$, respectively), from a previous chapter, with different chalcogenides, by reaction with a single equivalent of sulfur and an excess of selenium under an oxygen and a moisture-free nitrogen atmosphere and in dry toluene between 80 °C – 110 °C. The corresponding oxygen-derivatives were produced by reaction with excess of H_2O_2 either at room temperature, or at 0 °C and under an air atmosphere. Compounds **5.1 – 5.12** were obtained in moderate yield, as shown in Table 5.1 and characterised by solution- and solid-state NMR spectroscopy, crystallography, IR, mass spectrometry and their purity was confirmed by EA (except for **5.2** and **5.7**). See Chapter 6 for more details.

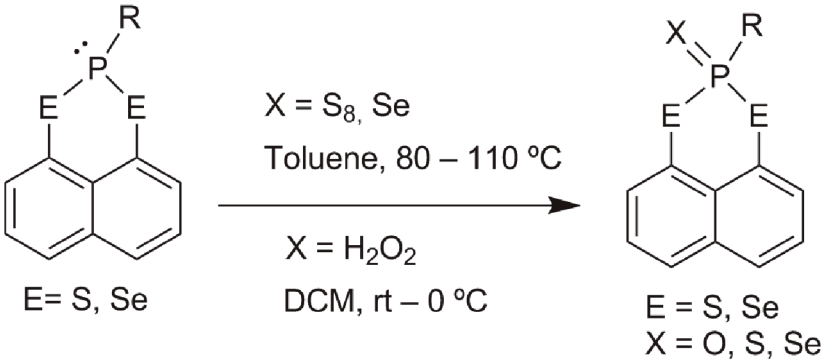

Scheme 5.1. *The preparation of **5.1** – **5.12** from the starting material (**4.1**, **4.2**, **4.4** and **4.5**, $NapS_2P^iPr$, $NapS_2P^tBu$, $NapSe_2P^iPr$ and $NapSe_2P^tBu$, respectively)*

Table 5.1. Compounds studied in this chapter and their yield obtained.

Compound	E, R, X groups	Yield	Compound	E, R, X groups	Yield
5.1	S, ^{i}Pr, O	93	**5.7**	S, ^{t}Bu, O	93
5.2	S, ^{i}Pr, S	56	**5.8**	S, ^{t}Bu, S	43
5.3	S, ^{i}Pr, Se	93	**5.9**	S, ^{t}Bu, Se	97
5.4	Se, ^{i}Pr, O	60	**5.10**	Se, ^{t}Bu, O	88
5.5	Se, ^{i}Pr, S	61	**5.11**	Se, ^{t}Bu, S	69
5.6	Se, ^{i}Pr, Se	77	**5.12**	Se, ^{t}Bu, Se	78

All compounds are stable upon exposure to air in the solid form, however, the decomposition is rapid in solution, where the E–E analogue is favored over the starting material, *i.e.,* the un-oxidised heterocycle, probably as a result of the lower strain in the former. All oxidised versions of $NapSe_2PR$, (*e.g.,* **5.5**, **5.6**, **5.11** and **5.12)**, were treated with almost stoichiometric amount of sulfur (*i.e.,* ~1.03 – 1.07 equivalents) or an excess of selenium (*i.e.,* ~1.2 equivalents) at 80 °C in toluene to afford the target compound. In contrast, the reactions of $NapS_2PR$, were slightly modified, as no reactivity was found for **5.2**, using the same conditions as those described for $NapSe_2PR$. To drive the reaction, the temperature was

increased to reflux, 110 °C and an excess of sulfur flowers (*i.e.*, ~3.4 equivalent) was used to afford **5.2**. Slightly lower temperature and a lesser amount of sulfur were required to synthesise the *tert*butyl analogue, **5.8**, that was produced at 90 °C with a small excess of sulfur (~1.2 equivalent). Compounds **5.3** and **5.9** were also produced using reflux and with an excess of selenium (*i.e.*, ~1.09 equivalents).

The oxygen derivatives were obtained by reactions with excess of H_2O_2 at room temperature in dichloromethane, except for **5.4**, where the temperature was reduced to 0 ° C in order to avoid decomposition and the solvent used was toluene. Several attempts to synthesise **5.1**, were unsuccessful yielding the decomposition product (naphtho[1,8-cd]1,2-dithiole). Compound **5.1** was finally afforded in dichloromethane, but with the presence of an unknown impurity that appears in the ^{31}P solution- and solid-state NMR spectra, while no additional peaks are shown in the ^{13}C and ^{1}H spectra. Note that the microanalysis of this compound was obtained, which, in principle, indicate the purity of the sample, suggesting that the unknown impurity may result from a different phase of the same compound. Attempts to purify **5.1** from the unknown impurity by column chromatography caused complete decomposition of the product to the naphtho[1,8-cd]1,2-dithiole. The *tert*butyl analogues, **5.7** and **5.10**, were more stable and had less tendency to decompose than the *iso*propyl ones. However, further purification by column chromatography of any of the oxidised compounds was not attempted owing to the problems with decomposition on silica.

The yields obtained vary over the series from 43 % to 97 % as shown in Table 5.1, but owing to the different procedures (*i.e.*, different equivalents of chalcogen and different temperatures) used between the $NapS_2PR$ and $NapSe_2PR$ derivatives, they cannot be easily compared.

However, a general observation suggests that the *iso*propyl derivatives have lower yields that the *tert*butyl compounds.

5.6.2 Solution-state NMR

^{31}P and ^{77}Se solution-state NMR data for all compounds is given in Table 5.2. The ^{31}P {^{1}H} NMR spectra of all the compounds exhibit singlets, with satellites due to the ^{1}J(P-Se) and/or ^{1}J(P=Se) couplings, in the case of the selenium analogues. The chemical shifts in ^{31}P {^{1}H} NMR spectra of the sulfur analogues appear the most deshielded of the series, in agreement with previous literature.[11] In addition, all *tert*butyl analogues are surprisingly deshielded in comparison to the *iso*propyl compounds except for **5.7**, as was observed for the un-oxidised series of heterocycles shown in Chapter 4.

The substitution of the P=X (*i.e.*, X = O, S, Se) has an influence on the ^{1}J(P-Se) coupling constants, which increases in the order O ≥ Se > S . The R group attached to the phosphorus atoms, (R = ^{i}Pr and ^{t}Bu) also has an impact on the ^{1}J(P-Se) coupling, with ^{t}Bu > ^{i}Pr. However, the opposite is observed for ^{1}J(P=Se) coupling constant with ^{i}Pr > ^{t}Bu.

The ^{77}Se {^{1}H} NMR spectra of all the selenium analogues exhibit doublets due to ^{1}J(P-Se) and in some cases also a doublet due to the ^{1}J(P=Se) couplings. The chemical shift of ^{77}Se {^{1}H} NMR spectra is affected by the substitution of the oxidised chalcogen in the phosphorus atom, and the δ(^{77}Se) decreases for the *iso*propyl analogues such that Se ≥ S > O, similar behaviour is found for the *tert*butyl analogue, but is this case the S was the most deshielded. In contrast to the chemical shift of ^{31}P {^{1}H} NMR spectra, the δ(^{77}Se) appear as expected, more deshielded for the *iso*propyl analogues.

Table 5.2. ^{77}Se and ^{31}P solution-state NMR data

	5.1	**5.2**	**5.3**	**5.4**	**5.5**	**5.6**
E,R,X group	S, iso,O	S, iso, S	S, iso, Se	Se,iso, O	Se,iso,S	Se,iso,Se
δ(^{31}P) NMR	52.0	67.8	52.3	40.4	43.3	22.0
δ(^{77}Se) NMR	–	–	–310.6	403.8	438.7	439.2 –260.0
^{1}J(^{31}P–^{77}Se)	–	–	–	396.6	385.1	391
^{1}J(^{31}P=^{77}Se)	–	–	797			773
	5.7	**5.8**	**5.9**	**5.10**	**5.11**	**5.12**
E,R,X group	S, tert, O	S, tert, S	S,tert, Se	Se,tert,O	Se, tert, S	Se, tert,Se
δ(^{31}P) NMR	51.1	70.2	53.8	44.08	48.6	27.3
δ(^{77}Se) NMR	–	–	–152.5	392.3	413.2	406.1 –143.7
^{1}J(^{31}P–^{77}Se)	–	–		407	398	407
^{1}J(^{31}P=^{77}Se)	–	–	790			752

[a] All spectra run in $CDCl_3$; δ (ppm), J (Hz).

5.6.3 Solid characterisation

In this section, owing to the complexity of the compounds studied, each of them will be discuss sequentially. All compounds were studied by ^{31}P and^{77}Se solid-state NMR, single-crystal and powder X-ray diffraction data. The comparison of the solution *vs* solid NMR data and the trends observed will be discussed later on in this chapter. ^{13}C CP MAS NMR spectra were also recorded for all compounds and can be seen in the Figure C3 of Appendix C.

Compound **5.1**, was one of the most difficult heterocycles in the whole series to synthesise, as discussed above. A sample of the heterocycle was obtained, with the presence of a minor impurity that is observed by ^{31}P solution- and solid-state NMR spectroscopy. One crystal structure was obtained for **5.1**. The asymmetric unit, containing one isolated molecule, and the crystal packing motif, are shown in Figure 5.1a.

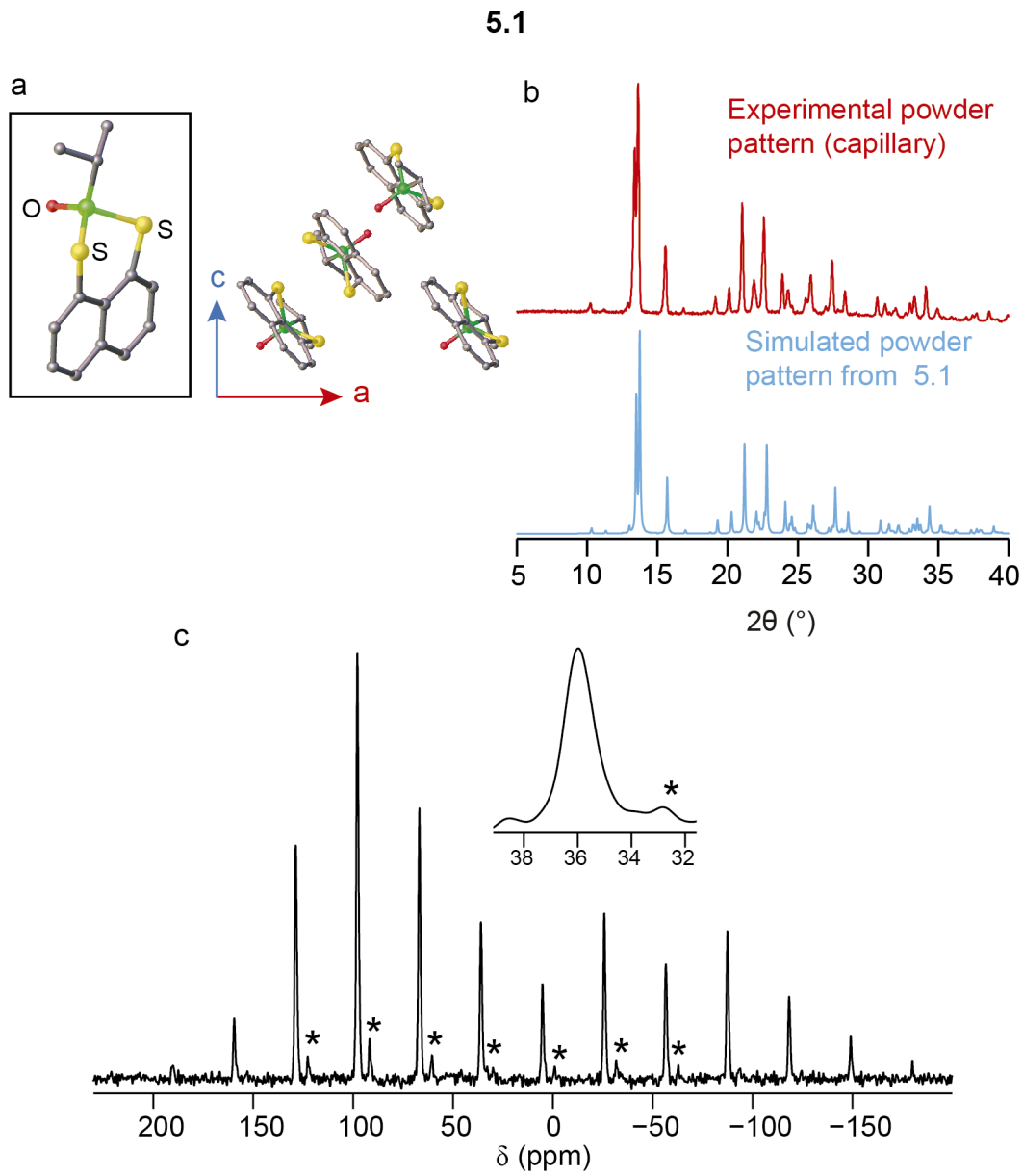

Figure 5.1. (a) Asymmetric unit (black box) and crystal packing motif showing the unit cell for **5.1** along b axis. (b) Comparison of the experimental and calculated powder XRD patterns for **5.1**. (c) ^{31}P MAS NMR spectrum of **5.1** acquired at 14.1 T and 7.5 kHz MAS. The * indicate the presence of an impurity. The isotropic peak is shown in the inset.

Figure 5.1b shows good agreement between the simulated powder XRD pattern from the crystal structure and the experimental powder XRD

pattern from the bulk material, indicating that the bulk corresponds to **5.1**. However, the ^{31}P solid-state NMR spectrum of **5.1** exhibits a main resonance at 35.9 ppm, with an unknown impurity represented by *, as shown in Figure 5.1c. Although, an impurity is present in the sample, the comparison of the powder XRD patterns suggests that this must be a minor component of the bulk.

For **5.2**, three different polymorphs were obtained; **5.2a** and **5.2c** possess two distinct molecules in the asymmetric unit, while only one molecule is found for **5.2b**. The difference in crystal packing motifs between the three is shown in Figure 5.2a. Each polymorph has a very different simulated powder XRD pattern as shown in Figure 5.2b, and comparison with the experimental powder XRD pattern for the bulk sample suggests it is a mixture of the three polymorphs.

Unfortunately, the proportions of each polymorph forming the bulk are not clear from the comparison of the powder XRD patterns. However, solid-state NMR can provide more information. Based on that, the ^{31}P solid-state NMR spectrum of **5.2** was recorded at 14.1 T and 7.5 kHz MAS and exhibit three resonances with relative different intensities, as shown in Figure 5.3a. If the bulk contains the three different polymorphs, five resonances are expected (*i.e.,* **5.2a** and **5.2c** have two molecules in the asymmetric unit while one molecule is found in **5.2b**), if the environment of the P sites are very similar, it could be possible that there is some overlap of the spectral resonances. It is clear, therefore, that must be some similarity in the environments, as only three resonances are observed in the ^{31}P spectrum. It is difficult to identify which resonance corresponds to which polymorph with only the ^{31}P solid-state NMR data.

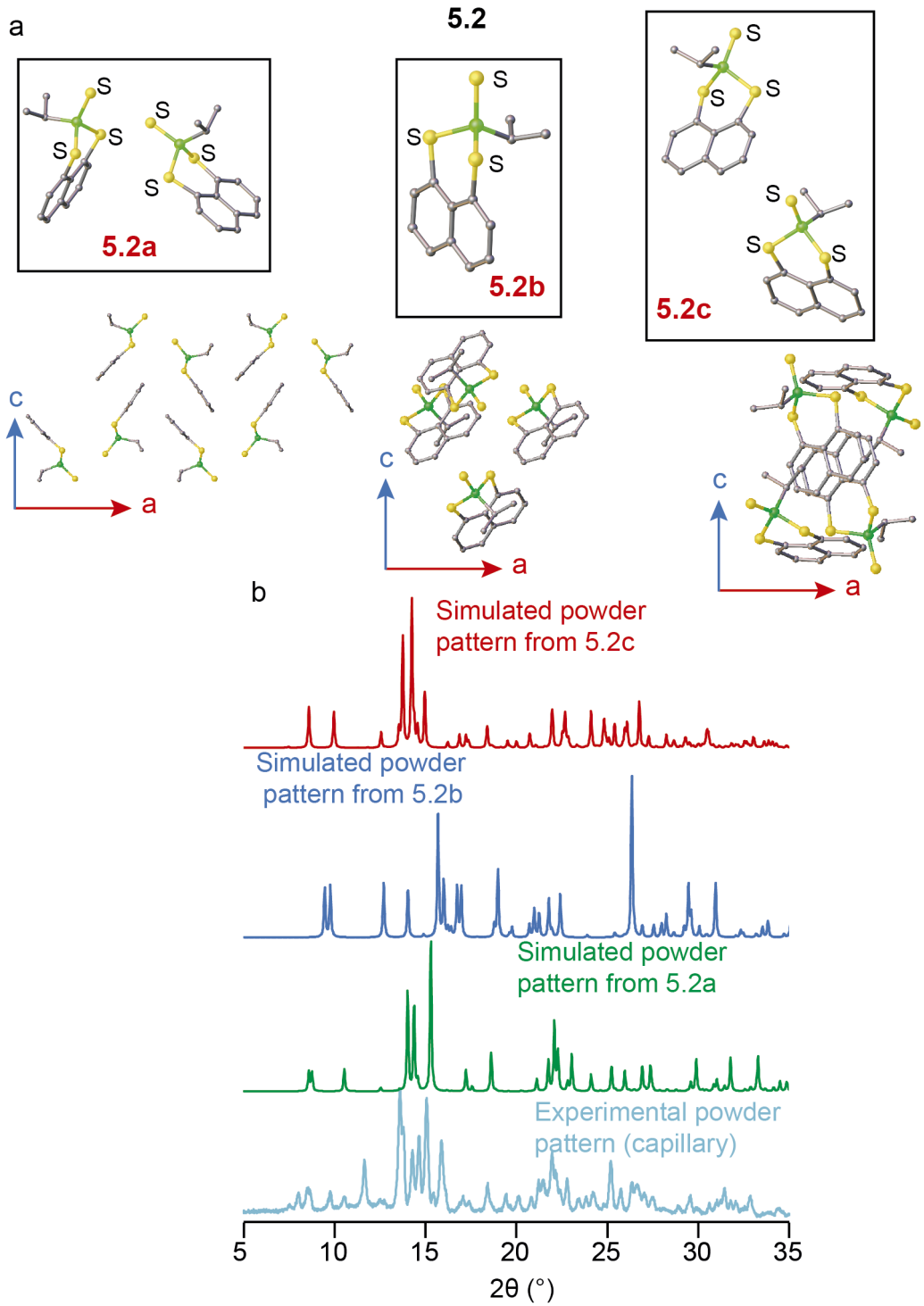

Figure 5.2. (a) Asymmetric unit (black box) and crystal packing motifs showing the unit cell for the three polymorphs, **5.2a**, **5.2b** and **5.2c** along b axis. (b) Simulated and experimental powder XRD patterns for each polymorph and the bulk sample.

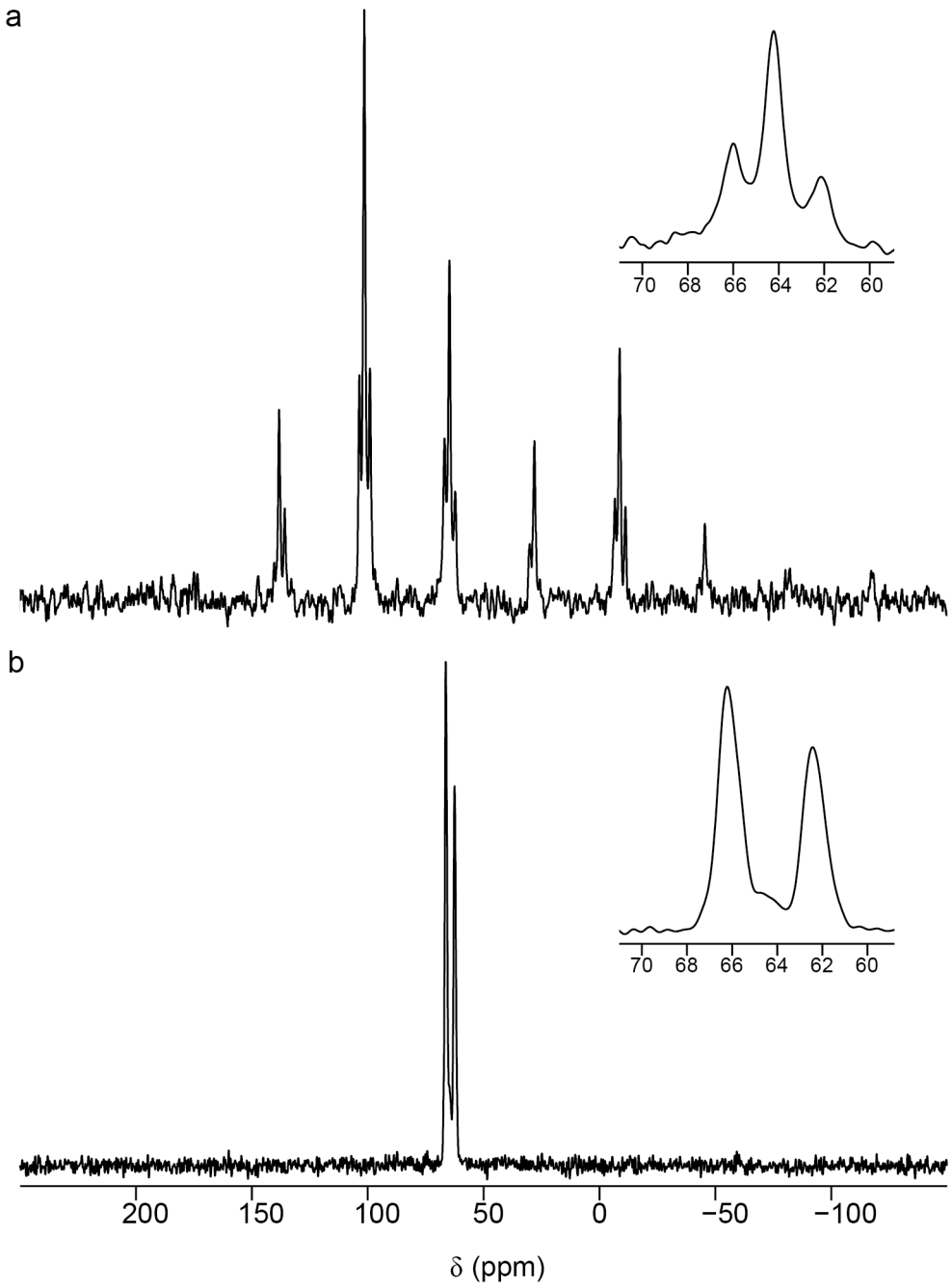

Figure 5.3. ^{31}P solid-state NMR spectrum of **5.2** recorded at (a) 14.1 T and 7.5 kHz MAS and (b) 14.1 T and 55 kHz MAS. Inset shows an expansion of the isotropic region.

As shown in previous Chapters, DFT calculations can be very useful to assign the spectral resonances. Therefore, DFT calculations for each of the three crystal structures (**5.2a**, **5.2b** and **5.2c**) were performed for a previously optimized structure, using the CASTEP 7 code previously described in the experimental section. The results are summarised in Table 5.3.

Table 5.3. Calculated ^{31}P isotropic shielding.

	P sites	**5.2a**	**5.2b**	**5.2c**
σ_{iso} (^{31}P)	P1	211.3	201.4	203.9
σ_{iso} (^{31}P)	P2	202.5		199.9

All σ_{iso} (ppm)

Polymorph **5.2a** and **5.2c** contains two different P sites environments, as shown for the very different σ_{iso} (^{31}P) values, *i.e.*, the two P sites differ by 8.8 and 4 ppm, respectively. A tentative assignment of the three resonances considering the calculated σ_{iso} (^{31}P) values, suggest that the outer peaks correspond to two P sites of different polymorphs (*i.e.*, the resonance at higher chemical shift corresponds to one P site of **5.2c**, which has a σ_{iso} (^{31}P) value of 199.9 ppm, and the other outer resonance at lowest chemical shift correspond to one P site of **5.2a**, which has a σ_{iso} (^{31}P) value of 211.3 ppm) and the central peaks correspond to the resonances left for polymorph **5.2a**, **5.2b** and **5.2c**, that present very similar σ_{iso} (^{31}P) values.

In order to gain insight into the relative intensities of each resonance in the ^{31}P spectrum of **5.1**, and thus the proportions of each polymorph in the bulk material, (*i.e.*, at 7.5 kHz, the CSA is still present and to obtain the real intensity of each peak it is necessary to spin faster to average out the anisotropy), the sample of **5.1** was packed into a 1.3- mm rotor and rotated at 55 kHz MAS. Moreover, it can also be observed in

Figure 5.3a that the intensity of each peak changes throughout the sideband manifold). In the ^{31}P solid-state NMR spectrum at 55 kHz MAS, is shown in Figure 5.3b, and a clear change in intensity is observed, which is not immediately possible to explain, as the central resonance, which was the most intense at 7.5 kHz MAS, has now disappeared almost completely. This could not result from CSA averaging. Therefore, a possible explanation might lie in the fact that different spinning speed and different rotor sizes will result in a variation of the temperature inside the rotor (*i.e.,* from ~20 °C when spinning at 7.5 kHz MAS to 60 °C when spinning at 55 kHz MAS, at 298 K without VT control) arising from frictional heating. The difference in temperature inside the rotor, could perhaps explain changes of the bulk sample as a consequence of a phase transition. In order to study the change in lineshape observed for **5.2**, VT experiments were performed. However, owing to the irreversible change in the sample measured previously, that resulted in the almost complete disappearance of the central resonance, VT experiments were performed for a different batch of the same compound, after proving that the composition of this new sample is similar. This conclusion was tested by different techniques (*i.e.,* single-crystal and powder X-ray diffraction and ^{31}P solid-state NMR and solution-state NMR spectroscopy) and no difference between the samples was found.

Figure 5.4a shows the isotropic region of the ^{31}P solid-state MAS NMR spectrum of **5.2**, at different temperatures (273, 298 and 323 K). To clarify if the spectral change is a reversible or irreversible process, the experiments were performed increasing temperature from 273 to 323 K and then returning to 273 K. It can be observed that the central peak disappears progressively upon heating and that this change is irreversible. Experimental powder XRD pattern was performed before and after the VT

NMR experiment to gain insight into the changes in the sample upon heating. Figure 5.4b shows (in black) the initial powder XRD pattern recorded prior to the VT experiment, and (in green) the powder XRD pattern after heating. It is clear that the powder XRD pattern has changed, and while more peaks are observed initially, possibly owing to the presence of a mixture of three polymorphs, fewer peaks are found in the powder XRD pattern after heating, which indicates a possible phase transformation of one or more polymorphs into one phase. The powder XRD pattern recorded after VT experiment can be compared to the simulated XRD patterns for the three crystal structures, shown in Figure C1 of Appendix C. It is clear from that comparison that the new powder XRD pattern agrees very well with that simulated for **5.2a**. This comparison suggests an alternative assignment of the ^{31}P NMR spectrum of **5.1,** to those provided by DFT calculations. The two outer resonances centred at 66.0 and 62.1 ppm observed after heating, must correspond to the two P sites present in **5.2a**, as the powder XRD pattern after heating corresponds mostly to that phase. The main peak, centred at 64.2 ppm, is a minor component of bulk sample, as observed by the very low intensity of the peak, after the VT experiment was performed, and could result from the other two crystal structures (**5.2b** and **5.2c**), or at least one of them, initially present in the sample. Therefore, before the VT experiment, a greater proportion of these two polymorphs (**5.2b** and **5.2c**) was present in the bulk sample (*i.e.*, as the intensity of the central resonance at 64.2 ppm was more intense).

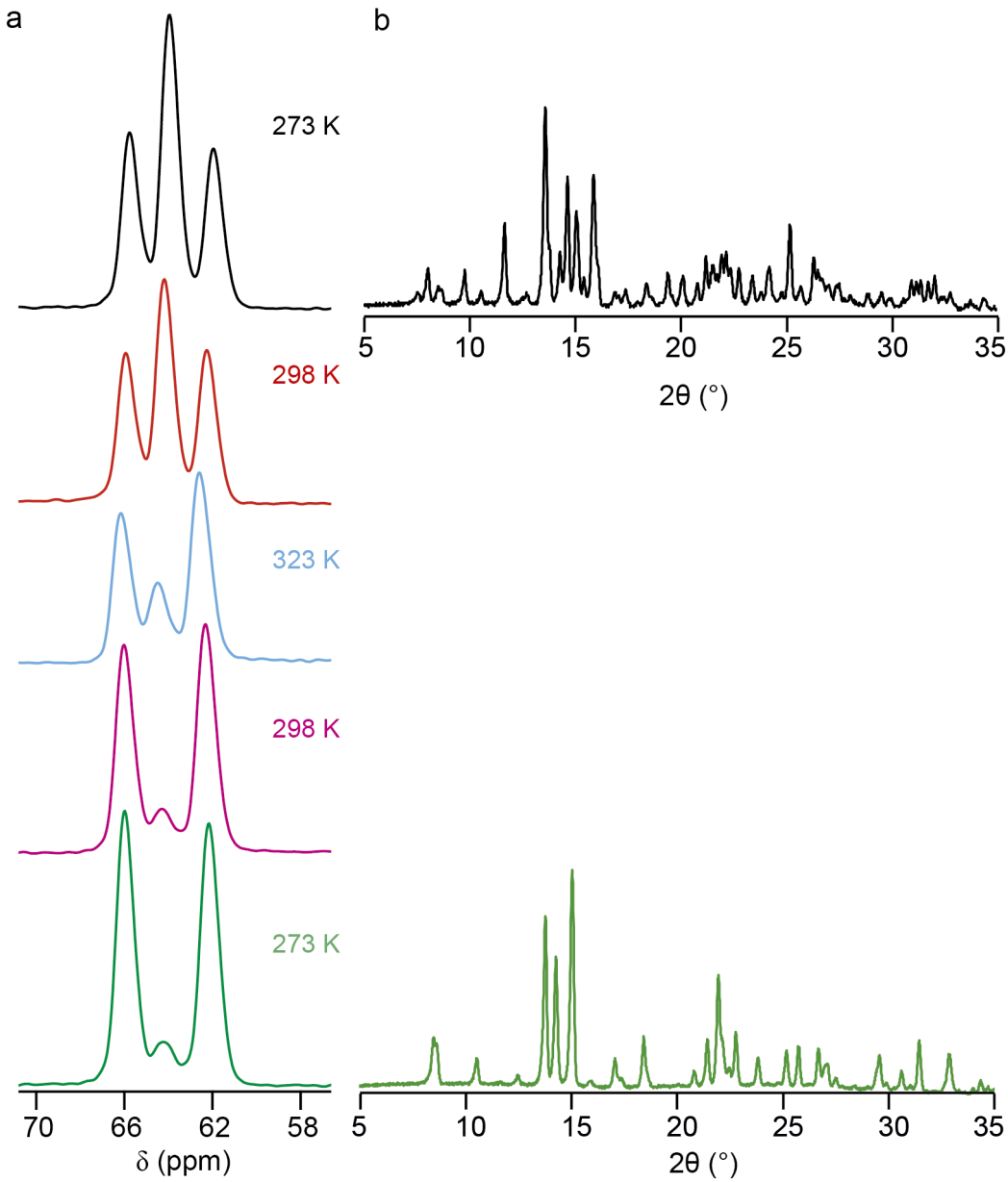

Figure 5.4. (a) ^{31}P solid-state NMR VT spectra of **5.2** recorded at 14.1 T and 55 kHz MAS. Only the isotropic centreband is shown for clarity. (b) Experimental powder XRD pattern of **5.2** before (black) and after (green) doing the VT NMR experiment.

Upon heating, polymorphs **5.2b** and **5.2c** appear to transform to a more stable phase, in this case **5.2a**. The discrepancy between experiment

and DFT calculations will be discussed later in this chapter, along with all the calculations for the rest of compounds.

The total energy of the three polymorphs can be compared to obtain some insight into their stability. In many cases, the energy difference between polymorphs is usually small, less than 1 kcal/mol (4.18 kJ/mol). However, conformational polymorphs are capable of differing by larger values, up to 2.5 kcal /mol (10.46 kJ/mol).[20] Therefore, in order to understand the stability of the three crystal structures for **5.2**, the energies obtained after geometry optimization using the CASTEP 7 code, were compared. The energy values from CASTEP calculations for **5.2a**, **5.2b** and **5.2c**, are given in Table 5.4. The energy was normalized to the number of molecules in the unit cell in order to compare the energy per molecule between polymorphs. It can be seen that the most stable polymorph is **5.2a**, with the less energy while **5.2b** and **5.2c** have higher energies, suggesting that these are less stable forms. This is in agreement with the observation of only **5.2a** in the sample after the VT experiment.

Table 5.4. Energies for the three polymorphs calculated using CASTEP 7

Polymorph	P sites	Energy / eV	Energy/molecule eV	Energy/molecule kJ/mol	ΔE kJ/mol
5.2a	8	–27055.9	–3381.987	–326312.12	0
5.2b	4	–13527.6	–3381.911	–326304.76	7.36
5.2c	4	–13527.7	–3381.938	–326307.41	4.71

Two crystal structures were obtained for **5.3**, *i.e.,* **5.3a** which has one molecule in the asymmetric unit, while two molecules are found in the asymmetric unit of **5.3b**. The asymmetric unit and crystal motifs for both polymorphs are shown in Figure 5.5a. Both polymorphs were found in different batches and obtained using different solvent mixtures, a

DCM/ethanol mixture was used for **5.3a** and hexane/DCM for **5.3b**. Only the bulk sample from which crystal structure **5.3b** was determined, was analysed by solid-state NMR. Attempts to crystallise a bulk sample using the other solvent mixture DCM/ethanol to obtain **5.3a** were unsuccessful, yielding only **5.3b**. This suggests that **5.3b** crystallise better from both solvent systems. The powder XRD patterns for the two polymorphs are quite different. Comparison of the experimental powder XRD pattern from the bulk sample and that simulated for each polymorph suggests that the bulk correspond to **5.3a**, as shown in Figure 5.5b. The ^{31}P solid-state NMR spectrum of the bulk sample is shown in Figure 5.5c. A major resonance is observed at 54.8 ppm with what seems to be ^{77}Se satellites possibly arising from the J(^{77}Se=P). This is in agreement with the single isolated molecule present in **5.3a**. Additional peaks can be observed in the spectrum also with a sideband manifold, suggesting that a possible second polymorph is present, possibly **5.3b**, as this is the only other crystal structure that was found for this sample. Moreover, the low intensity peak appears to contain two sideband manifolds, possibly reflecting the two P sites present in **5.3b** (*i.e.,* two molecules are present in the asymmetric unit, and each molecule has a P site). ^{77}Se solid-state NMR spectra of **5.3** at 9.4 T and 14.1 T, shown in Figure 5.6a and 5.6b, respectively, exhibit a doublet centred at –311.8 ppm with a ^{1}J (^{31}P-^{77}Se) couplings of 779 Hz, similar to that in solution. This is again in agreement with the presence of a single molecule in the asymmetric unit. Additional peaks can also be observed in the ^{77}Se solid-state NMR spectrum at 9.4 T and more clearly at 14.1 T, exhibiting a sideband manifold. These can be tentatively assigned to polymorph, **5.3b**, which represents a minor component of the bulk, as shown by the intensity of the resonances.

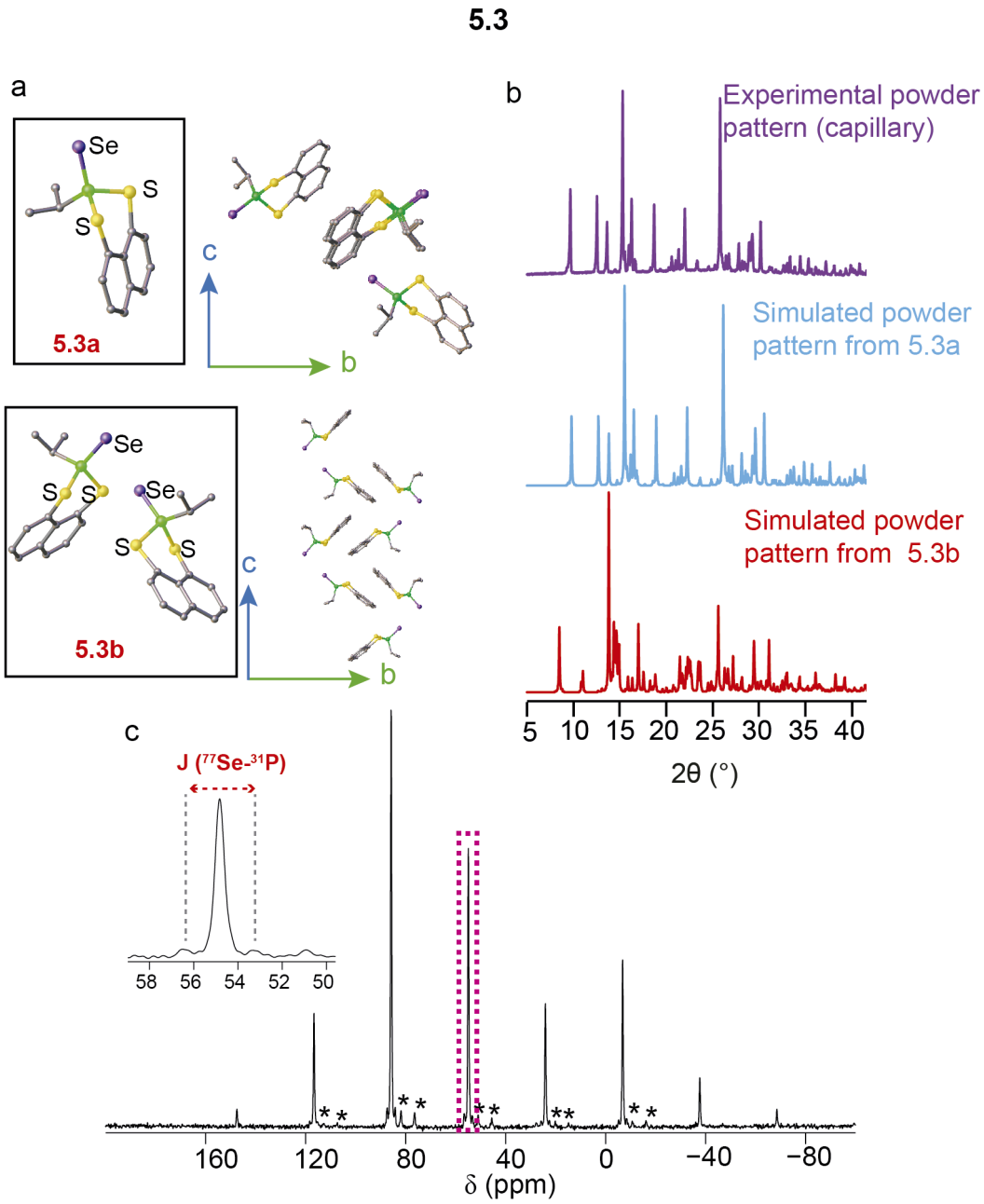

Figure 5.5. (a) Assymetric unit (black box) and crystal packing motifs showing the unit cell for **5.3** along a axis. (b) Comparison of the experimental and calculated powder XRD patterns for **5.3**. (c) ^{31}P NMR spectrum of **5.3** acquired at 14.1 T and 7.5 kHz MAS. Insets show the isotropic resonance and the * represents the additional peaks (possibly resulting from a second polymorph)

However, if these additional peaks correspond to polymorph **5.3b**, it might be expected that two doublets should be observed in the ^{77}Se spectra (*i.e.,* there are two molecules in the asymmetric unit, thus two Se site coupled to ^{31}P (100% abundance)). However, this is not observed, only one doublet can be seen in the ^{77}Se spectra. It is possible that the other doublet appears overlapped with the main resonance of **5.3a** and cannot be resolved, or the two Se species in 5.3b have very similar shifts.

Figure 5.6c shows the ^{77}Se solid-state NMR spectrum acquired with ^{31}P decoupling. It is unclear whether a single resonance is presented in the spectrum owing to the resonance broadening. To clarify that, a longer experiment (for better sensitivity) with higher decoupling power was performed and is shown in Figure 5.6d. Small splitting is still observed in the spectrum shown in Figure 5.6d, however, the splitting is different to that in the un-decoupled spectrum. It is possible that a residual coupling is still remaining as a result of the low power decoupling used (owing to the hardware available only CW between 15 – 25 kHz, being allowed for this experiment). Another possibility is the presence of two very similar Se sites, which will suggest the presence of **5.3b** in a majority of the sample. This assumption, however, does not agree with the powder XRD data and the ^{31}P NMR spectrum of **5.3**.

As performed previously with polymorphs in **5.2**, the energies calculated from CASTEP 7, can be compared between polymorphs to obtain insight into their relative stability. The energy is shown in Table 5.5. Again, the energy was normalized taking into account the number of molecules in the unit cell in order to compare the energy per molecule between polymorphs.

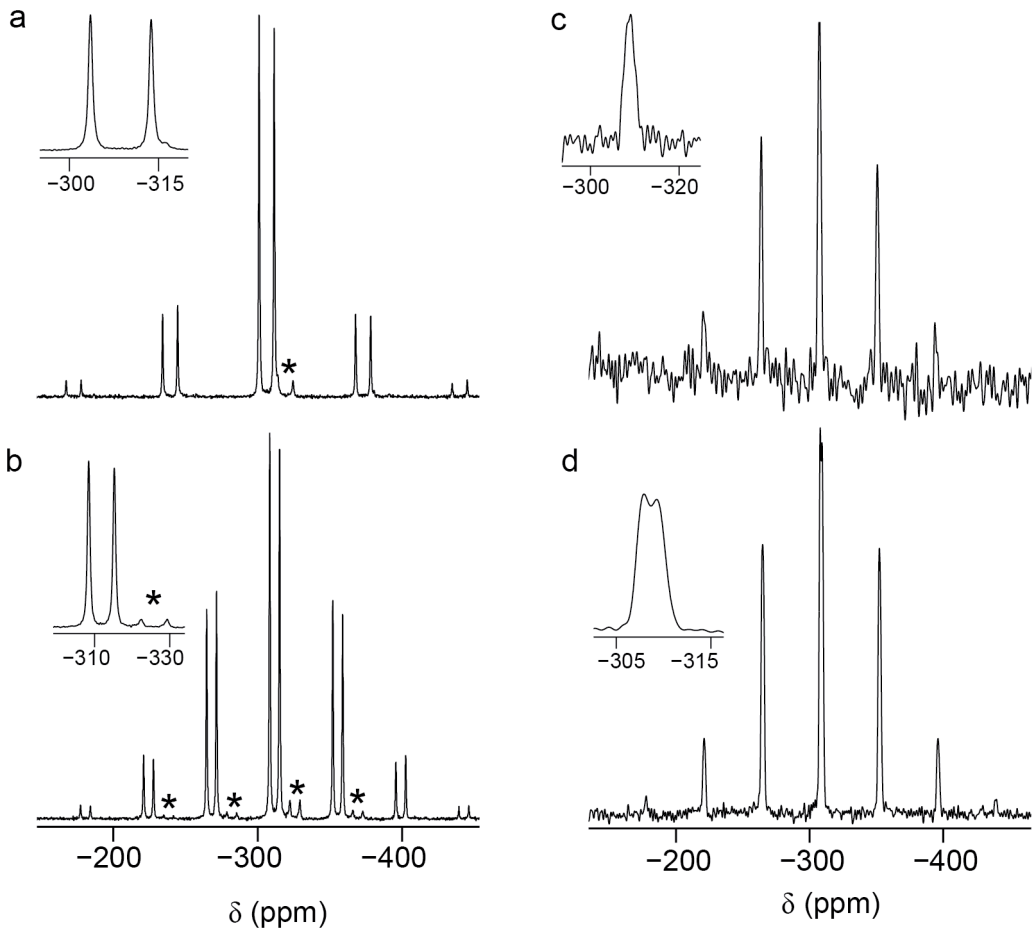

Figure 5.6. ^{77}Se CP NMR spectra of **5.3**, acquired at 5 kHz MAS and at (a) 9.4 T, (b) 14.1 T and (c, d) 14.1 T, with ^{31}P decoupling of 15 and 25 kHz, respectively. Insets show an expansion of the isotropic peak and the * denotes the additional peaks.

Table 5.5. Energies for the two polymorphs calculated using CASTEP 7

Polymorph	P sites	Energy / eV	Energy/molec eV	Energy/molec kJ/mol	ΔE kJ/mol
5.3a	4	–14232.66	–3558.16	–343310.62	0
5.3b	8	–28465.93	–3558.24	–343318.02	7.4

It can be observed that the more stable polymorph is **5.3a**, which has a lower energy, while **5.3b** has higher energy, with a difference of 7.4 kJ/mol between the two. This assumption is in agreement with the suggestion that **5.3a** forms the majority of the bulk and **5.3b** corresponds to a minor component of the sample, and is also consistent with the powder XRD pattern comparison and the ^{31}P solid-state NMR data, even if the only crystal structure determined from the sample measured is **5.3b**.

The synthesis of **5.4** was very challenging, and purification by column chromatography was not possible owing to decomposition, as mentioned previously. However, a crystal structure of **5.4**, was obtained from a DCM/hexane mixture. The asymmetric unit contains one crystallographically-independent molecule as seen in Figure 5.7a. The experimental powder XRD pattern of the bulk sample was compared with the simulated powder XRD pattern from the crystal structure, as shown in Figure 5.7b, with a clear difference between the two observed. This suggests that there is another polymorph present in the bulk that forms the majority of the bulk sample, while molecules with the crystal structure found correspond to only a minor component of the sample. Further crystallisations were carried out from different solvents mixtures in attempts to obtain the missing polymorph. However these crystallisations were unsuccessful.

The ^{31}P NMR MAS spectrum shown in Figure 5.7c, exhibits a main resonance centred at 13.8 ppm, a very different chemical shift in comparison with the rest of the P=O oxidised compounds, (which tend to appear between 35.9 – 47.5 ppm) and also very different to the ^{31}P solution-state NMR shift (40.4 ppm). Additional peaks can also be observed, none of which exhibit a sideband manifold. These peaks could arise from polymorphs present in the bulk or residual impurities. This

latter suggestion is perhaps less likely as solution-state NMR and microanalysis confirmed the purity of the sample. Another possibility is that they result from a decomposition product, which is possible owing to the instability of the sample.

The ^{77}Se solid-state NMR spectrum recorded at 9.4 T, is shown in Figure 5.7d, and exhibits two doublets centred at 486.6 ppm and 474.2 ppm with a J (^{31}P-^{77}Se) of 378 and 389 Hz, respectively. The presence of two selenium sites was confirmed in the ^{77}Se solid-state NMR spectrum acquired with ^{31}P decoupling, as shown in Figure 5.7e. At very low intensity is also possible to observe additional peaks in the ^{77}Se MAS NMR spectrum recorded at 9.4 T, as shown in Figure 5.7d, possibly corresponding to a polymorph present in the sample. Although, the known crystal structure does not seems to correspond to the majority of the bulk, as seen in the powder XRD patterns, it seems that the crystal forming the majority of the sample, also contains an isolated molecule in the asymmetric unit, as shown by the NMR spectrum. Therefore, both polymorphs could have similar asymmetric units but the packing between both must be different.

For **5.5**, only one polymorph has been determined, with an asymmetric unit that contains two crystallographically-independent molecules, as shown in Figure 5.8a. The comparison of simulated and experimental powder XRD patterns from the crystal structure and from the bulk are in good agreement, as shown in Figure 5.8b. The ^{31}P MAS NMR spectrum of **5.5** is shown in Figure 5.8c. Two resonances centred at 40.6 and 44.4 ppm are observed in agreement with the presence of two independent molecules in the asymmetric unit. The ^{77}Se solid-state NMR spectra of **5.5** were recorded at 9.4T and 14.1 T. Multiple fields are necessary for this sample, owing to the complexity of the spectrum, as

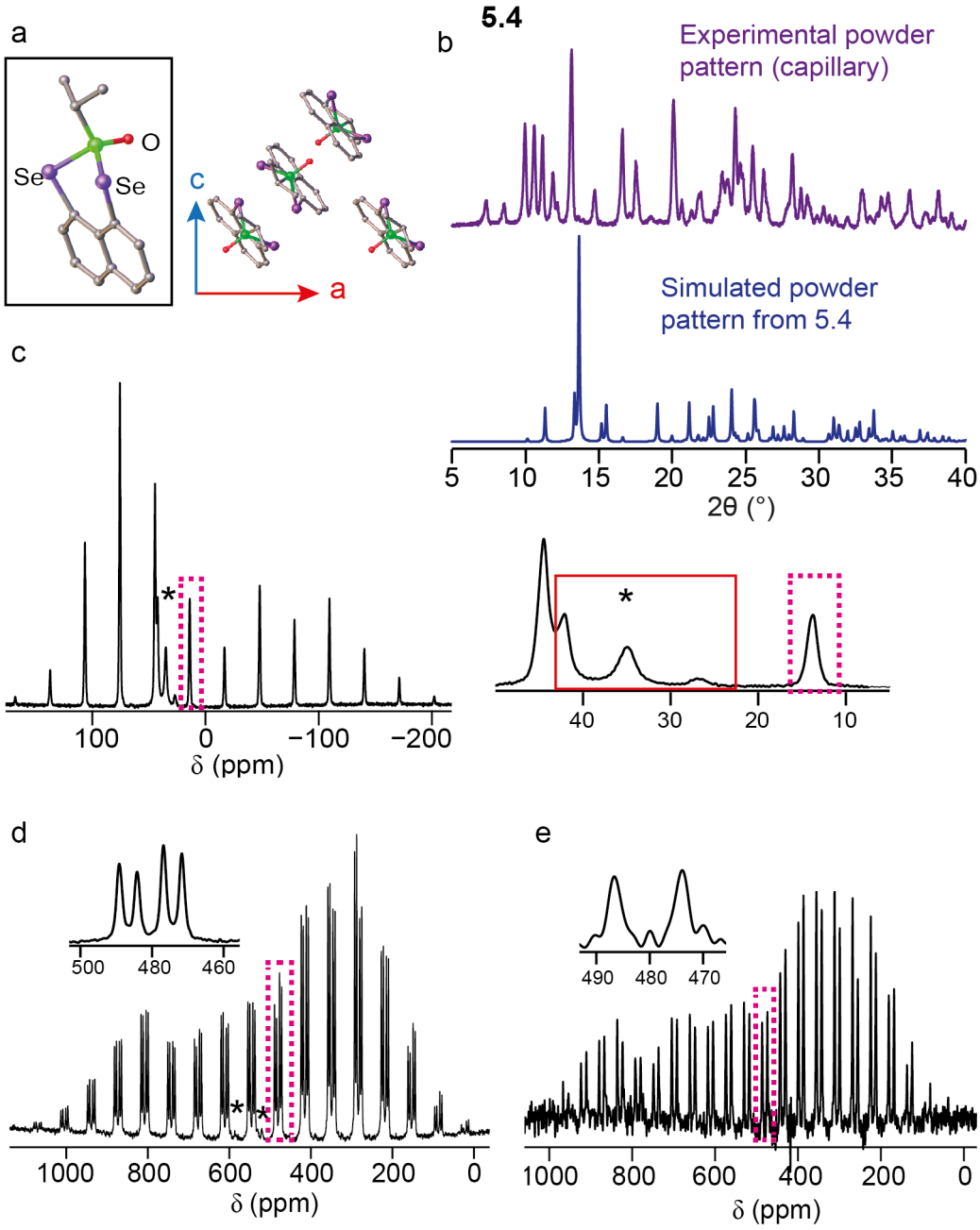

Figure 5.7. (a) Asymmetric unit (black box) and crystal packing motif showing the unit cell of **5.4** along b axis. (b) Comparison of the experimental and simulated powder XRD patterns for **5.4**. (c) ^{31}P MAS NMR spectrum of **5.4** acquired at 14.1 T and 7.5 kHz MAS. ^{77}Se CP MAS NMR spectra of **5.4**, acquired at 5 kHz MAS at (d) 9.4 T and (e) 14.1 T with ^{31}P decoupling. Insets show the isotropic resonances and the *represents the additional peaks.

four selenium sites are present and therefore, in principle, four doublets (owing to the J coupling with ^{31}P) should be observed. At 9.4 T, as shown in Figure 5.8d, a complex lineshape is observed, with overlapping resonances. However at 14.1 T, shown in Figure 5.8e, three distinct regions between ~ 410 – 440 ppm, with different apparent multiplicities are observed. Clear doublets can be distinguished centred at ~ 412.1 ppm and ~ 432.4 ppm, possible resulting from two selenium sites with a *J* (^{77}Se-^{31}P) coupling between ~ 377–391 Hz. The resonance at higher shift shows what appears to be a "triplet" centred at ~ 440.7 ppm, which may correspond to two very closely-spaced doublets from two very similar selenium sites. ^{77}Se solid-state NMR spectrum acquired with ^{31}P decoupling, is shown in Figure 5.8f, and confirmed the presence of four distinct resonances at ~410, 430, 338 and 440 ppm, in agreement with the presence of two molecules in the asymmetric unit. It must be noted that this spectrum shows broader resonances in comparison to the un-decoupled one, possibly as the poorer resolution obtained with the low decoupling power available for this experiment, as mention previously.

Two crystal structures were determined for **5.6** (*e.g.*, **5.6a** and **5.6b**), and their asymmetric unit and crystal packing motifs are shown in Figure 5.9a. Crystal structure **5.6a** contains a single crystallographically-distinct molecule in the asymmetric unit, while two crystallographically-distinct molecules are present in the asymmetric unit of **5.6b**. Both polymorphs were found in different batches of the same material and using different solvent systems for crystallisation (*i.e.*, DCM/ethanol for **5.6a** and DCM/hexane for **5.6b**).

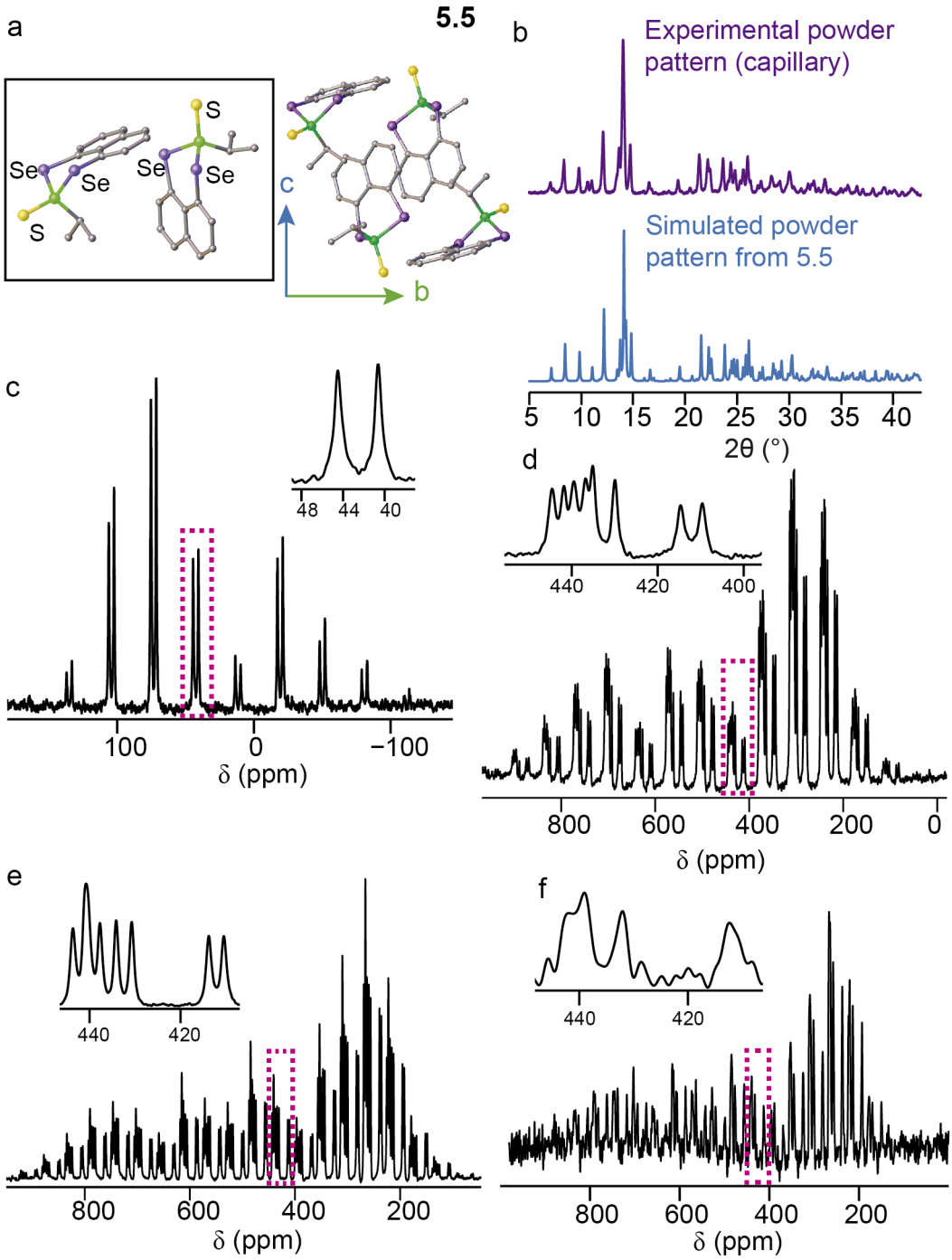

Figure 5.8. (a) Asymmetric unit (black box) and crystal packing motif showing the unit cell for **5.5** along a axis. (b) Comparison of the experimental and simulated powder XRD patterns for **5.5**. (c) ^{31}P MAS NMR spectrum of **5.5** acquired at 14.1 T and 7.5 kHz MAS. ^{77}Se CP MAS NMR spectra of **5.5** acquired at 5 kHz MAS at (d) 9.4 T, (e) 14.1 T and (f) 14.1 T with ^{31}P decoupling. Insets show the isotropic resonances

The first attempt to synthesise **5.6**, yielded **5.6b,** along with other impurities present in the solution-state NMR spectra. No solid-state NMR spectra were recorded at that point, as the reaction had not completed and quite a lot of starting material was still present in the reaction mixture. Instead, a second batch of the same compound was synthesised this time with different conditions to afford the target compound. Crystallisation of this batch yielded a second polymorph (**5.6a**) determined by single-crystal XRD. The comparison of the simulated and experimental powder XRD patterns from the bulk material are shown in Figure 5.9b, and good agreement is observed with **5.6a,** suggesting little or no evidence of the first polymorph (**5.6b**) present in the sample.

The ^{31}P MAS NMR spectrum of **5.6** is shown in Figure 5.9c. A main resonance centred at 25.8 ppm is observed, with the presence of a small additional peak, probably corresponding to an impurity due to the lack of sideband manifold. The ^{77}Se solid-state NMR spectrum of **5.6**, recorded at 9.4 T, is shown in Figure 5.9d. Three distinct selenium sites centred at ~409 and ~442 (probably corresponding to the selenium sites in the *peri* position) and –258.9 ppm resulting from the P=Se, are observed. At all fields, the multiplicity of the centrebands is a clear doublet for all Se sites as a result of the "through-bond" *J* coupling to ^{31}P (note 100% abundance), in relatively good agreement with the $^{1}J(^{31}P\text{-}^{77}Se)$ couplings observed in solution. A ^{77}Se solid-state NMR spectrum acquired with ^{31}P decoupling is shown in Figure 5.9e, confirming the presence of three distinct selenium sites, suggesting one isolated molecule in the unit cell. This supports the proposal that polymorph **5.6a** forms the majority of the sample. No additional peaks were found in the ^{77}Se solid-state NMR spectra suggesting that no further polymorphs are present, not even polymorph **5.6b**, that was found in different batch.

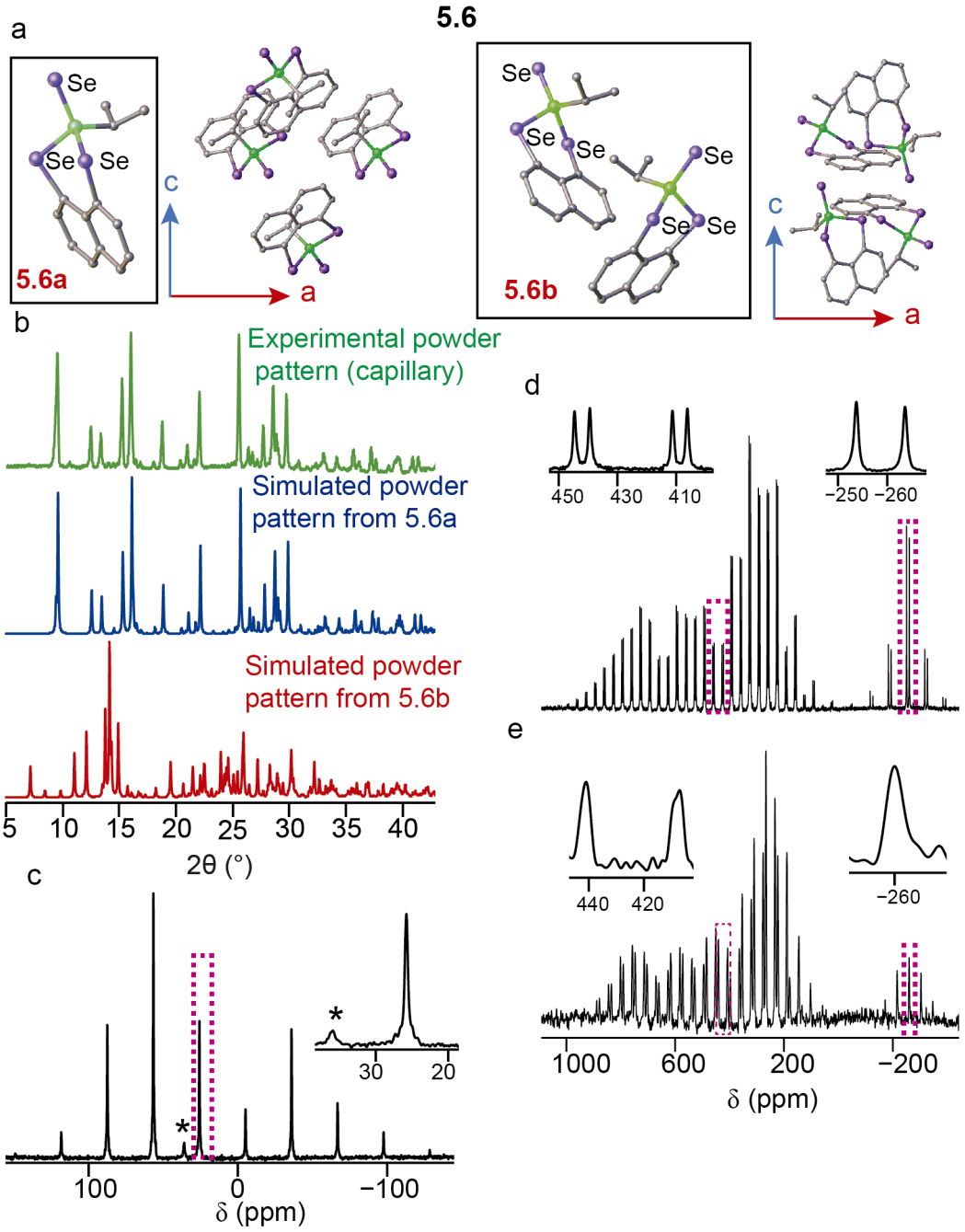

Figure 5.9. (a) Asymmetric unit (black box) and crystal packing motif showing the unit cell for **5.6** along b axis. (b) Comparison of the experimental and simulated powder XRD patterns for **5.6**. (c) ^{31}P MAS NMR spectra of **5.6** acquired at 14.1 T and 7.5 kHz MAS. ^{77}Se CP MAS NMR spectra of **5.6** acquired at 5 kHz MAS and at (d) 9.4 T, (e) 14.1 T with ^{31}P decoupling. Insets show the isotropic resonances and the * shows the additional peaks.

For **5.7** and **5.8**, only one polymorph was found, with the asymmetric unit and crystal packing motifs shown in Figures 5.10a and 5.10d, respectively. An isolated molecule is seen in the asymmetric unit of **5.7**, while two molecules are present for **5.8**. Comparison of the experimental and simulated powder XRD patterns are in very good agreement in both cases, as shown in Figures 5.10b and 5.10e, suggesting that no further polymorphs or impurities are present in the bulk samples. The ^{31}P MAS NMR spectra of **5.7** and **5.8**, shown in Figures 5.10c and 5.10f, are in good agreement with the crystal structures and no further resonances appear in the spectra (*i.e.*, a main resonance is observed for **5.7** centred at 47.5 ppm, while two resonances centred at 71.9 and 70.7 ppm are observed in **5.8**, consistent with the presence of one molecule and two molecules in the asymmetric unit, respectively).

Compound **5.9** exhibits two polymorphs, **5.9a** and **5.9b**, both containing two molecules in the asymmetric unit, but with different crystal packing motifs, as shown in Figure 5.11a. Both polymorphs were found in the same synthetic batch but under slightly different conditions, **5.9a** crystallised from a DCM/ethanol mixture while **5.9b** crystallised from a DCM/methanol. The simulated powder XRD patterns for each polymorph appear very similar, as shown in Figure 5.11b. However, a more detailed look into the relative intensities reveals some differences between them. Comparison of the simulated XRD patterns with the experimental pattern, suggests the closest similarity is to **5.9b** but, owing to the very similar patterns observed, it is difficult to distinguish the proportions of the polymorphs in the sample. The ^{31}P MAS spectrum shown in Figure 5.11c, exhibits two main resonances centred at 55.6 and 53.8 ppm, possibly corresponding to the two crystallographically-inequivalent phosphorus sites of one polymorph.

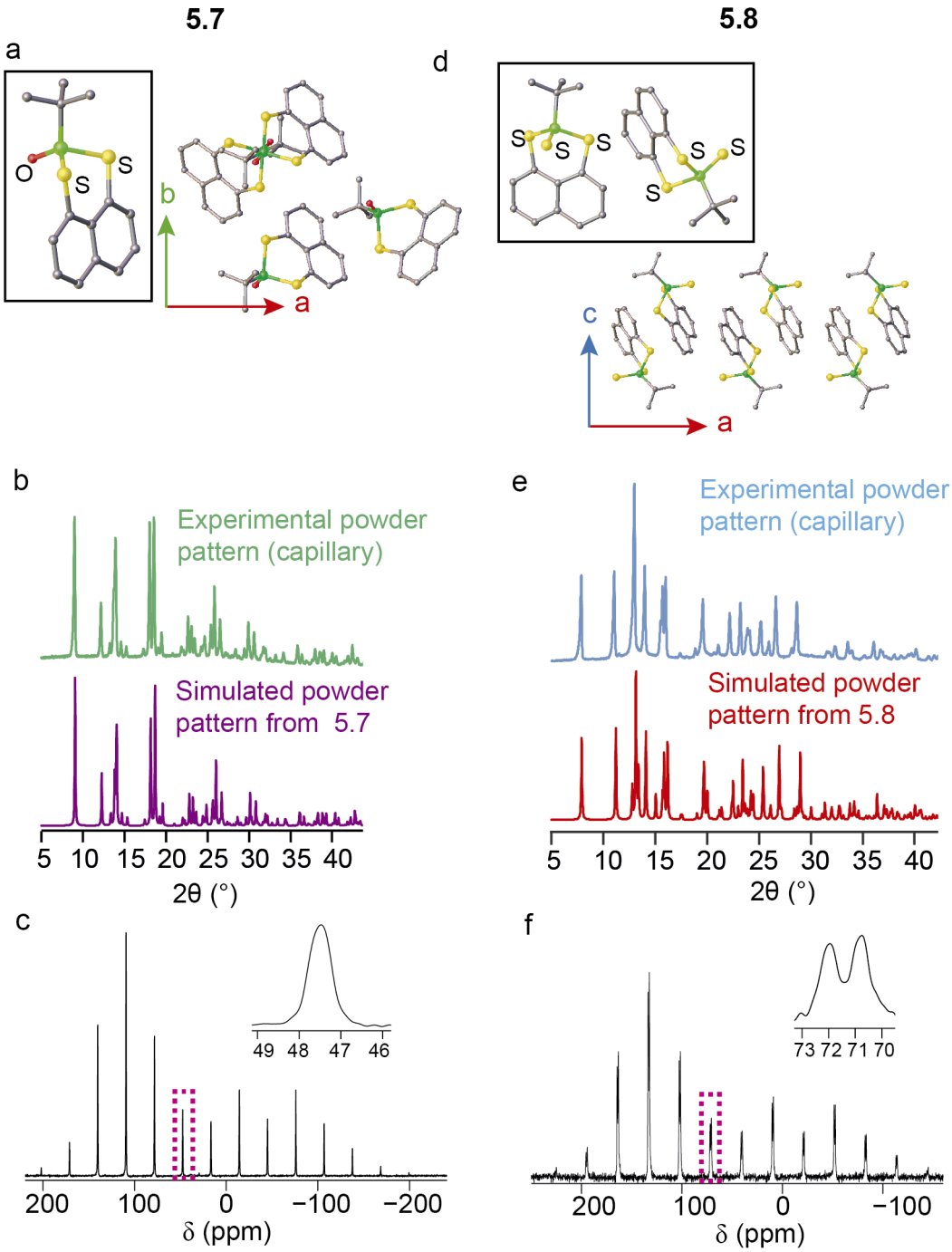

Figure 5.10. (a and d) Asymmetric unit (black box) and crystal packing motifs showing the unit cell for **5.7** and **5.8** along c and b axis, respectively. (b and e) Comparison of the experimental and calculated powder XRD patterns for **5.7** and **5.8**, respectively. (c and f) ^{31}P MAS NMR spectra acquired at 14.1 T and 7.5 kHz MAS for **5.7** and **5.8**, respectively. Insets show the isotropic resonances.

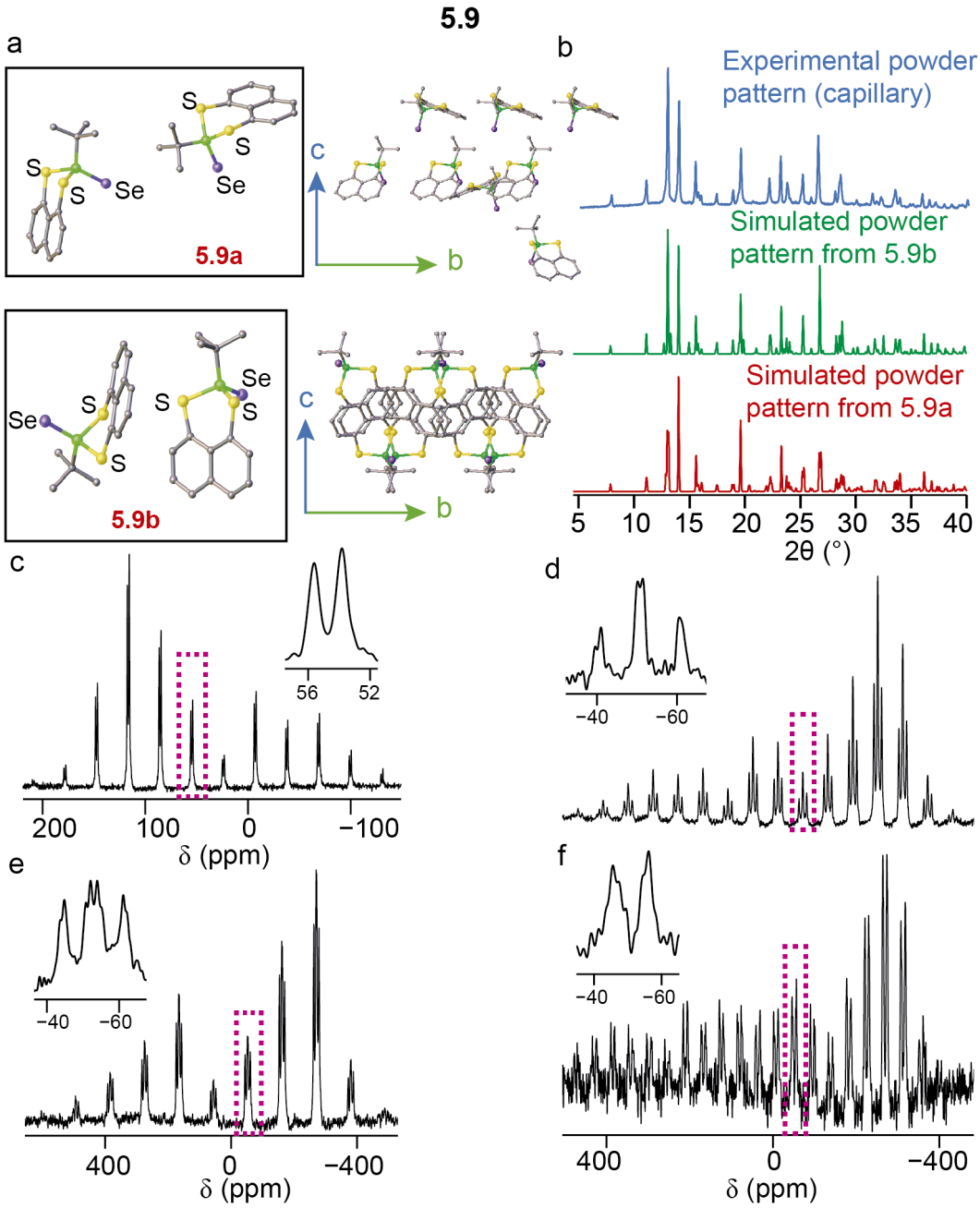

Figure 5.11. (a) Asymmetric unit (black box) and crystal packing motif showing the unit cell for **5.9** along a axis. (b) Comparison of the experimental and simulated powder XRD patterns for **5.9**. (c) ^{31}P MAS NMR spectrum of **5.9** acquired at 14.1 T and 7.5 kHz MAS. ^{77}Se CP MAS NMR spectra of **5.9** acquired at 5 kHz MAS and at (d) 9.4 T, (e) 14.1 T and (f) 14.1 T, with ^{31}P decoupling. Insets show the isotropic resonances.

No additional peaks from the other phase are found in the spectrum, possibly due to the similarity in the phosphorus environment between both polymorphs. The ^{77}Se solid-state NMR spectra of **5.9** acquired at 9.4 T and 14.1 T, exhibit two doublets centred at –46.1 and –55.6 ppm with ^{1}J (^{31}P-^{77}Se) couplings of 835 and 826 Hz, as shown in Figure 5.11d and 5.11e, respectively. These two doublets are more clearly distinguished at higher field, confirming they arise from coincidental overlap and not multiple couplings. At 14.1 T, additional peaks are also observed as shoulders on each resonance. This might arise from the second polymorph present in the sample. Based on the above data we propose that a mixture of both polymorphs could be present in the sample in an almost equal amount (as seen from the intensity of the peaks). The ^{77}Se solid-state NMR spectrum acquired with ^{31}P decoupling, shown in Figure 5.11f, suggests the presence of four selenium sites (although the low decoupling power available does limit resolution), only possible as a result of two different polymorphs in the sample each with two molecules in the asymmetric unit. Although this is not very clear from the isotropic peak, which is less intense owing to the large CSA, and the level of noise could contribute to the analysis, it is possible to distinguish the four resonances, from the more intense peak of the sideband manifold, as shown in Figure 5.12c. In order to investigate the polymorphism in this sample, where both phases seems to correspond to 50% of the bulk, a different temperature was used in the reaction (*i.e.*, 80 °C rather than 100 °C), to see if the temperature has an effect on the polymorph formation. The new sample was again crystallised but using different solvent mixtures and both polymorphs are still obtained. Polymorph **5.9a** was found from a hexane/DCM mixture, while **5.9b** was obtain from a DCM/ethanol mixture. The experimental powder XRD pattern of both samples, the new one and the old one, are completely

identical (shown in Figure C2 of Appendix C). The ^{77}Se solid-state NMR spectrum was again recorded for the new sample at 14.1 T. The spectrum is shown in Figure 5.12b and the ^{77}Se solid-state NMR spectrum acquired with ^{31}P decoupling is shown in Figure 5.12d. For the new sample, it is more difficult to distinguish additional peaks probably because of the broadening of the spectra as more resolution is required in order to distinguish the shoulders seen in Figure 5.12a. Note that the experiments were very time consuming, (*i.e.*, the spectrum shown in Figure 5.12a was obtained after 22 h while spectrum shown in Figure 5.12b was obtained after 27 h). Despite the longer experiment, the spectrum with best resolution is still that shown in Figure 5.12a (the 14.1 T ^{77}Se spectrum from the old sample). This difference could possibly arise from different CP match obtained as both spectra were recorded on different days. It is also possible that in the new sample, although both polymorphs are present, the proportions of them in the bulk are slightly different, and they cannot be resolved as well as for the old sample. Another possibility is that the nature of both samples is different hence different resolution of the same spectrum is observed.

Only one crystal structure was determined for **5.10**, which contains one crystallographically-independent molecule in the asymmetric unit, as shown in Figure 5.13a, and surprisingly, a single crystallographic selenium site, as a consequence of symmetry. As for **5.4** (the *iso*propyl version of **5.10**), the experimental and calculated powder XRD pattern do not agree well, suggesting that there may be another more abundant polymorph in the bulk that has not yet been identified. The ^{31}P MAS NMR spectrum, shown in Figure 5.13c, exhibits one resonance centred at 30.1 ppm, and a $^{1}J(^{31}P\text{-}^{77}Se)$ coupling of ~378 Hz can also be observed.

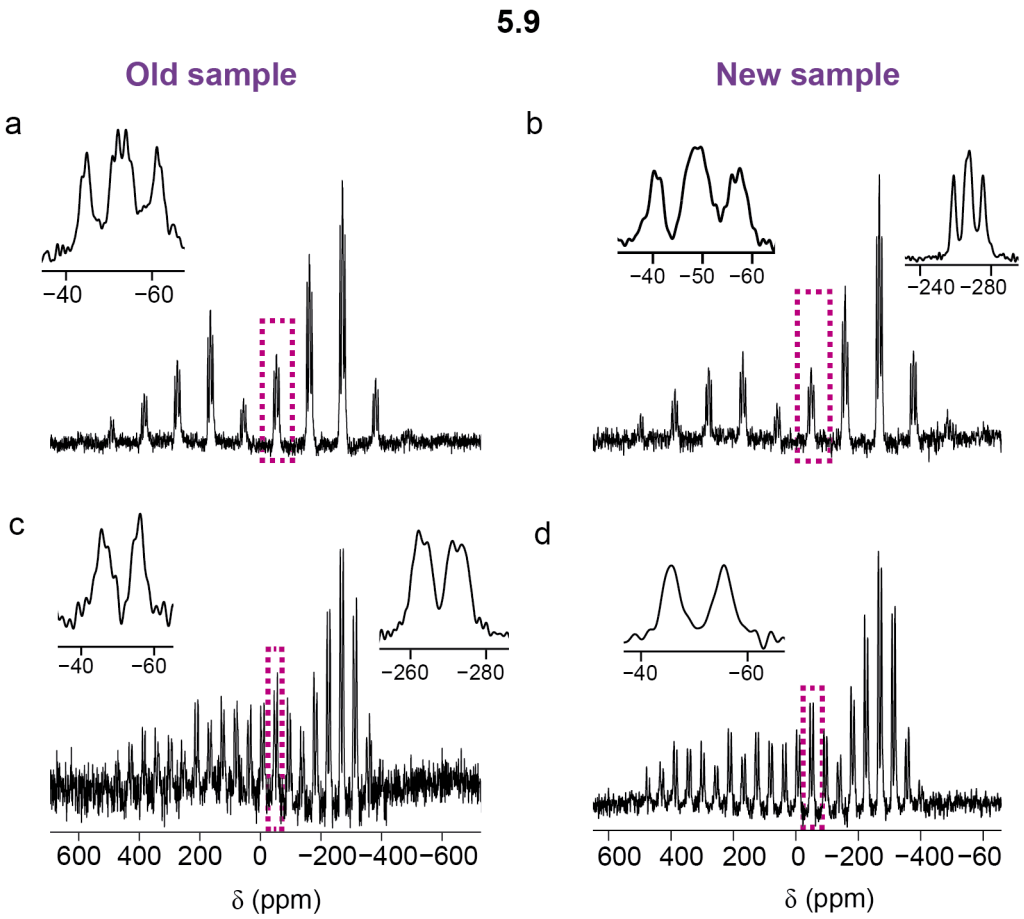

Figure 5.12. ^{77}Se CP MAS NMR spectra of **5.9** acquired at 14.1 T with 5 kHz MAS for (a, b) the old sample and new sample, respectively, and acquired with ^{31}P decoupling for(c, d) the old sample and new sample, respectively. Insets shows the isotropic resonances and the higher intensity sideband is also show in the inset, when necessary.

The ^{77}Se solid-state NMR spectrum recorded at 9.4 T is shown in Figure 5.13d. Two clear doublets centred at 422.8 and 442.8 ppm can be easily distinguished and no evidence of further polymorphs is found. The two resonances must arises from two distinct selenium sites that results from two crystallographically-inequivalent Se in the asymmetric unit that are coupled with ^{31}P with a *J* coupling between 384–386 Hz, respectively.

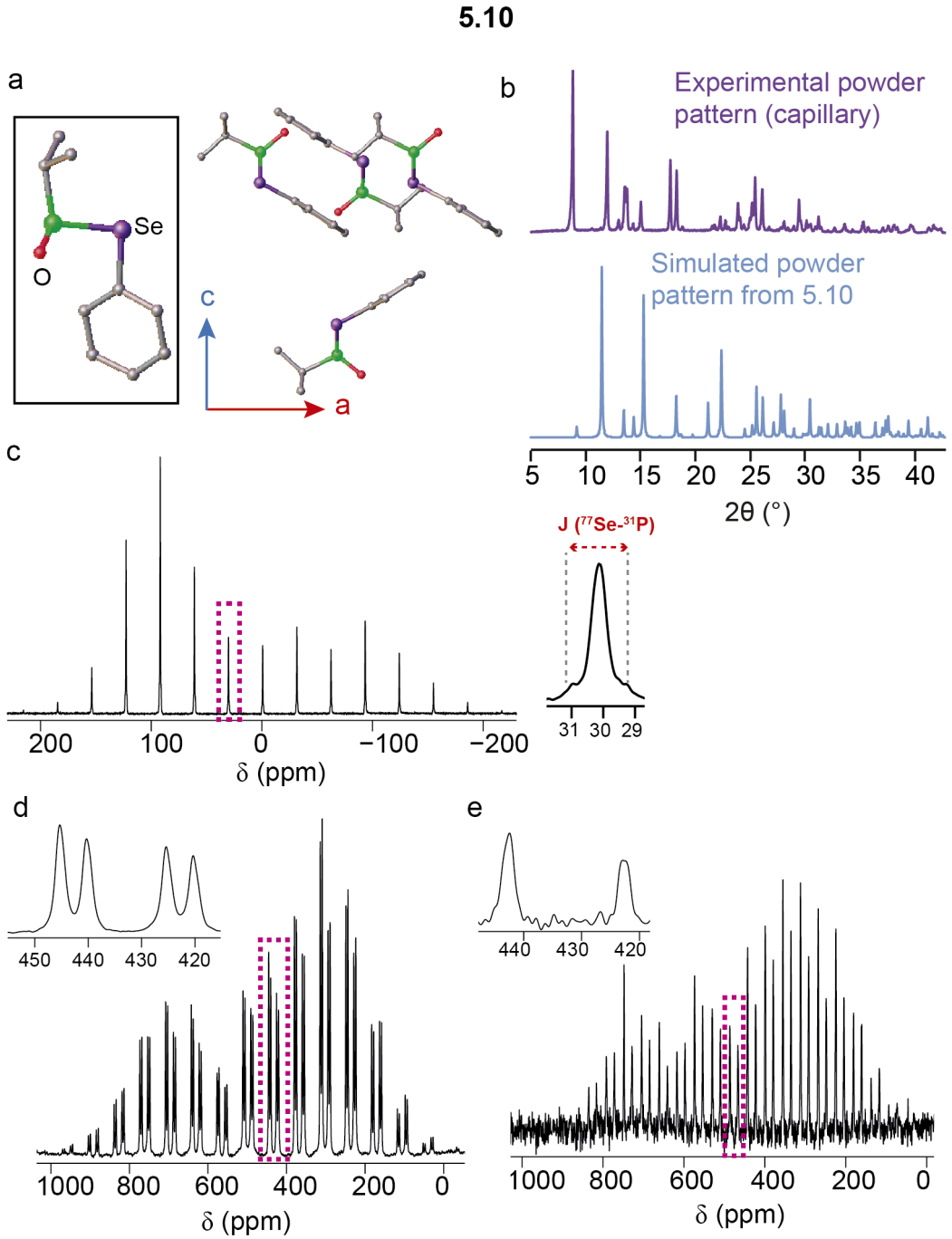

Figure 5.13. (a) Asymmetric unit (black box) and crystal packing motif showing the unit cell for **5.10** along b axis. (b) Comparison of the experimental and simulated powder XRD patterns for **5.10**. (c) ^{31}P MAS NMR spectrum of **5.10** acquired at 14.1 T and 7.5 kHz MAS. ^{77}Se CP MAS NMR spectra of **5.10** acquired at 5 kHz MAS at (d) 9.4 T and (e) 14.1 T with ^{31}P decoupling. Insets show the isotropic resonances.

The ^{77}Se solid-state NMR spectrum with ^{31}P decoupling confirms the presence of two selenium sites, as shown in Figure 5.13e. Therefore, the missing polymorph that may correspond to the majority of the bulk might contain a single molecule in the asymmetric unit and the symmetry must be different in comparison to the polymorph determined (*i.e.*, one P site and two Se sites must be present in the asymmetric unit).

Only one crystal structure has been determined for **5.11**, and it contains one crystallographically-independent molecule in the asymmetric unit, as shown in Figure 5.14a. Experimental powder XRD patterns of the bulk sample were compared with the simulated powder XRD pattern from the crystal structure, as shown in Figure 5.14b, and good agreement is observed. The ^{31}P MAS NMR spectrum exhibits a single resonance at 43.1 ppm. The ^{77}Se solid-state NMR spectrum, recorded at 9.4 T, is shown in Figure 5.14d. A single resonance at ~364 ppm can be observed, which appears to be a "triplet". However, at 14.1 T, two clear doublets at ~364 and ~357.8 ppm can be easily distinguished, as can be shown in Figure 5.14e. This confirms the presence of two distinct selenium sites, as a result of the crystal packing, as expected from the crystal structure. The ^{77}Se solid-state NMR spectrum with ^{31}P decoupling shown in Figure 5.14f, shows two distinct resonances at ~ 364.0 and 358.1 ppm, in agreement with the presence of one molecule in the unit cell.

Two crystal structures were determined for **5.12**, one containing a single crystallographically-independent molecule (**5.12a**) and the other containing two independent molecules (**5.12b**) in the asymmetric unit. The asymmetric unit and packing motifs of both polymorphs are shown in Figure 5.15a. Both polymorphs were obtained from same batch under same conditions, *i.e.*, crystallisation from a DCM/methanol mixture.

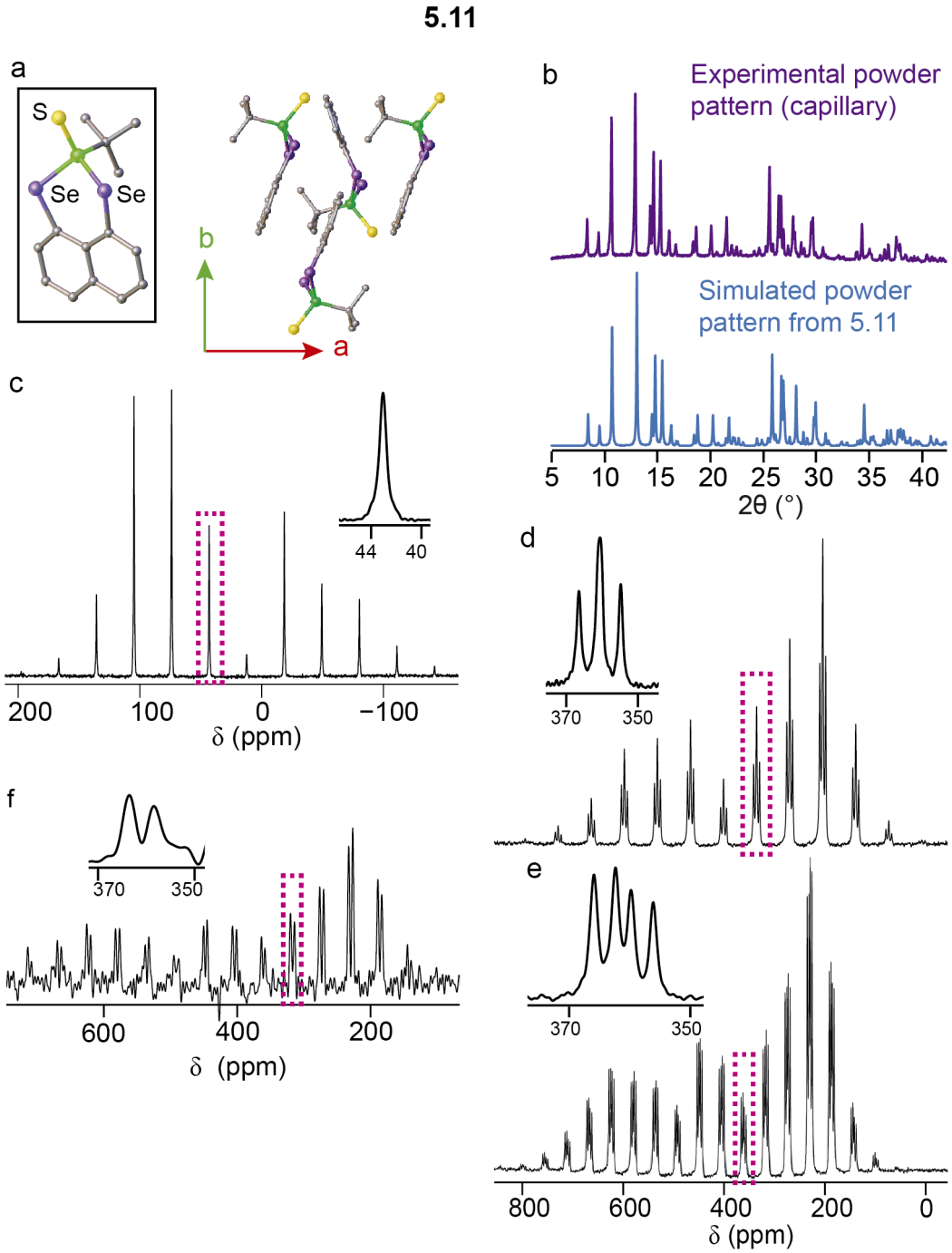

Figure 5.14. (a) Asymmetric unit (black box) and crystal packing motif showing the unit cell for **5.11** along c axis. (b) Comparison of the experimental and simulated powder XRD patterns for **5.11**. (c) ^{31}P MAS NMR spectrum of **5.11** acquired at 14.1 T and 7.5 kHz MAS. ^{77}Se CP MAS NMR spectra of **5.11** acquired at 5 kHz MAS at (d) 9.4 T, (e) 14.1 T and (f) 14.1T with ^{31}P decoupling. Insets show the isotropic resonances.

A powder XRD pattern of the bulk sample were obtained and compared to the two simulated powder XRD patterns for each crystal structure, as shown in Figure 5.15b. Both polymorphs seem to have very similar XRD patterns, which makes the detection of both polymorphs in the bulk difficult. The ^{31}P MAS spectrum, shown in Figure 5.15c, exhibits two resonances at 22.7 and 20.9 ppm, most likely corresponding to the two independent molecules present in the unit cell, rather than a mixture of polymorphs. The ^{77}Se solid-state NMR spectrum recorded at 9.4 T, exhibits a complicated lineshape, as shown in Figure 5.15d. The ^{77}Se solid-state NMR spectrum recorded at 14.1 T, is shown in Figure 5.15e and here two isotropic regions, one between 370–350 ppm and the other between –140 to –180 ppm, can be observed, each of them with the corresponding sideband manifold. The presence of overlapped resonances could arise from the presence of two independent molecules, *i.e.,* six selenium sites present in the asymmetric unit, or from the presence of polymorphs **5.12a** and **5.12b** presence in a 50-50 % in the same sample. This latter assumption is less likely to happen and should result in more Se resonances. In order to clarify the origin of the resonances, ^{77}Se NMR of a single large crystal (crushed to powder) of known structure (**5.12b**) was recorded resulting in the same spectrum as the bulk sample, thus potentially confirming the presence of a single phase rather than a mixture of two polymorphs in equal amounts. The two resonances at ~ –152.1 and ~ –165.2 ppm can be easily assigned to the P=Se group. The four remaining selenium sites are presumed to appear in the region between 370 – 350 ppm. However, without the removal of the *J* coupling coming from ^{31}P, any assignment can be certain. The ^{77}Se solid-state NMR spectrum acquired with ^{31}P decoupling is shown in Figure 5.15f and exhibits three distinct resonances, one at 368.7 ppm, one at ~358.8 ppm that present

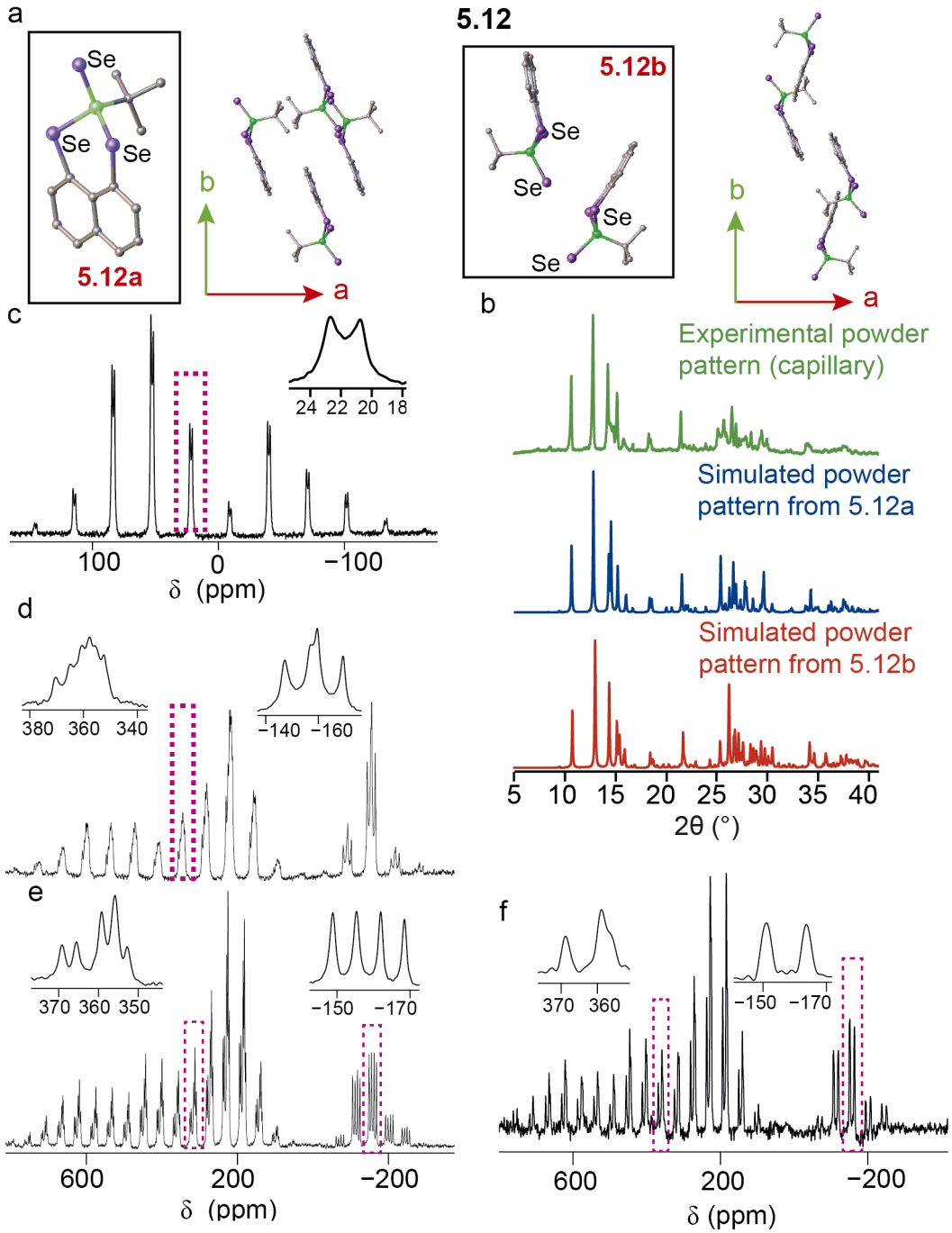

Figure 5.15. (a) Asymmetric unit (black box) and crystal packing motif showing the unit cell for **5.12** along c axis. (b) Comparison of the experimental and simulated powder XRD patterns for **5.12**. (c) ^{31}P MAS NMR spectrum of **5.12** acquired at 14.1 T and 7.5 kHz MAS. ^{77}Se CP MAS NMR spectra of **5.12** acquired at 5 kHz MAS at (d) 9.4 T, (e) 14.1 T and (f) 14.1T with ^{31}P decoupling. Insets show the isotropic resonances.

higher intensity indicating the possibility of corresponding to more than one Se site, and the last resonance appear at ~356.3 ppm, with the same intensity that the resonance at higher shift. The four Se sites must present similar environment resulting in coincidental overlapping of resonances and small chemical shift difference observed in the spectrum.

5.6.4 Crystal structure analysis

All crystallographic data including splay angles, torsion angles of the backbone and out-of-plane displacements are given in Tables C1-C5 of the Appendix C. As for the un-oxidised series, the splay angles increase on moving from sulfur to selenium compounds, around 5° through the series, with the *tert*butyl analogues generally having larger values than the *iso*propyl materials. The chalcogen oxidation has a small effect on the splay angles, less than 1°, and varies in the order of S > Se > O > un-oxidised, for the series of compounds, except the sulfur *tert*butyl ones, which order is un-oxidised > S >O > Se. For the out-of-plane displacements there is general increase going from sulfur to selenium compounds, however, is difficult to tell as the values also vary between different molecules in the asymmetric unit. The distance of the different chalcogen-atom (P=X) to the naphthalene plane was also estimated. Two different positions are observed. When the chalcogen (X atom) is in the plane of the naphthalene values between 0.007 to 1.015 Å are observed, and when the chalcogen (X atom) is perpendicular to the plane of the naphthalene, values between 2.387 to 3.032 Å are observed. For the compounds crystallising in this latter conformation, the out-of-plane displacement increases in the sulfur *tert*butyl analogues as the size of the chalcogen increases (Se > S > O). Unfortunately, this cannot be compared for the rest

of compounds as only the oxygen-sulfur and selenium *iso*propyl derivatives crystallise in this conformation. The distortion of the backbone is similar through the series, with torsion angles ranging from 170 – 179°, suggesting that the oxidation with the different chalcogens does not affect the planarity of the naphthalene. The *peri*-distance varies from 3.135 – 3.438 Å through the series, with the selenium analogues having larger values.

5.6.5 General trends

In this section, the NMR data of the un-oxidised (*i.e.,* **4.1** – **4.6**, except **4.2**) and the oxidised (*i.e.,* **5.1** – **5.12**) will be compared to obtain a better understanding of the changes in the ^{31}P and ^{77}Se environment as a result of oxidation by different chalcogens. The ^{31}P and ^{77}Se NMR parameters for the solid-state NMR spectra for all compounds are given in Table 5.6. The order of the ^{31}P chemical shifts does not vary compared to that seen in solution-state NMR spectra, with the sulfur and the *tert*butyl analogues being the most deshielded of the series, except for **5.6** and its *tert*butyl analogue, **5.12**. The range of the ^{31}P chemical shift can then be estimated on the basis of the local chalcogen atom attached. For example, the S-oxidised version always appears at higher chemical shift than the O-oxidised and Se-oxidised analogues, as shown in Figure 5.16a. In this figure, the chemical shift in solution and in the solid state is compared for all compounds described in this chapter (**5.1** – **5.12**), and for compounds from Chapter 4, the un-oxidised version, (**4.1** – **4.6,** except **4.2**). Three distinct regions can be distinguished. A first region, between –20 – 10 ppm for the un-oxidised (P^{III}) compounds, a second region, between 20 – 50 ppm, for the selenium-*peri* oxidised compounds and a last region, between 50 – 70

Table 5.6. ^{77}Se and ^{31}P solid-state NMR data

	4.1	**5.1**	**5.2**	**5.3**	**4.4**	**5.4**	**5.5**	**5.6**	**4.3**
E,R,X group	S, iso	S, iso,O	S, iso, S	S, iso, Se	Se, iso	Se,iso, O	Se,iso,S	Se,iso, Se	S, Ph
$\delta_{iso}(^{31}P)$	643	36	66 64 62	55	–2	14	41 44	26	0.5 –3
$\delta_{iso}(^{77}Se)$	–	–	–	–309	280	487 474	441 439 432 412	409 442 –259	–
$^{1}J(^{31}P–^{77}Se)$	–	–	–	–	300	378 389	349 332 391 378	392 382	–
$^{1}J(^{31}P=^{77}Se)$	–	–	–	779	–	–	–	749	–
	4.2	**5.7**	**5.8**	**5.9**	**4.5**	**5.10**	**5.11**	**5.12**	**4.6**
E,R,X group	S, iso	S, tert, O	S, tert, S	S,tert, Se	Se, tert	Se,tert,O	Se, tert, S	Se, tert,Se	Se, Ph
$\delta_{iso}(^{31}P)$	–	47	72 71	54 56	6	30	43	21 23	–22
$\delta_{iso}(^{77}Se)$	–	–	–	–46 –56	213 179	443 423	364 358	369 359 356 –152 –165	350 231
$^{1}J(^{31}P–^{77}Se)$	–	–	–	–	340/270 319	384 386	396 423.7	411 382 347	335/278 328
$^{1}J(^{31}P=^{77}Se)$	–	–	–	835 826	–	–	–	740 746	–

δ (ppm), J (Hz).

ppm, for the sulfur-*peri* oxidised compounds.

For the case of ^{77}Se NMR, the substitution of the chalcogen also has an influence on the order of the chemical shift, with that from solution and solid-state spectra being different. In solution, the analogues appear as Se ≥ S > O, while is solids the order is the reverse, O > S ≥ Se, as shown in the Figure 5.16b. ^{77}Se NMR is also very sensitive to changes in the molecular environment and different ranges of shift are also shown in Figure 5.16b.

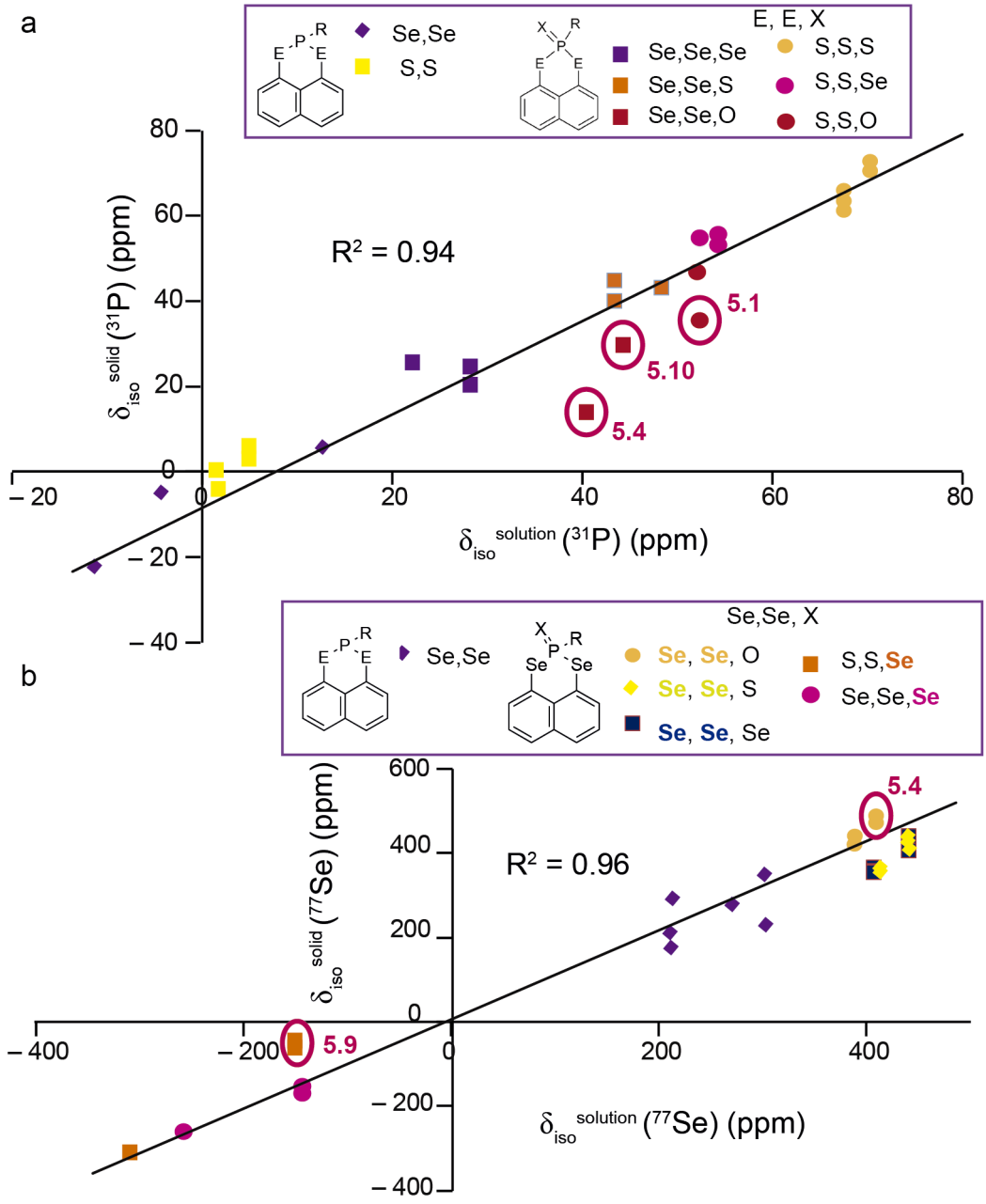

Figure 5.16. Plots of (a) $\delta_{iso}^{solid}(^{31}P)$ against $\delta_{iso}^{solution}(^{31}P)$ and (b)$\delta_{iso}^{solid}(^{77}Se)$ against $\delta_{iso}^{solution}(^{77}Se)$, for **4.1 – 4.6**, (except **4.2)** and **5.1 – 5.12.**

Two regions are clearly observed, depending on the type of selenium attached to phosphorus, a first region between –400 to 0 ppm for the Se=P and a second region between 0 to 400 ppm for the seleniums in the *peri*-position (P-Se). The chalcogen substitution has a minimum impact on the

selenium environment in the *peri*-position while, the type of selenium (*i.e.*, P=Se or P-Se) has a dramatic effect in the chemical shifts. In contrast, the chalcogen substitution has more influence on the ^{31}P NMR environment, as it is directly bonded to this nucleus.

In Figure 5.16a, although a good correlation (R^2 = 0.94) is found between ^{31}P chemical shifts in solution and in the solid state, there are some chemical shifts differences (*i.e.*, between ~14 – 27 ppm) for some compounds, e.g., **5.1**, **5.4** and **5.10**, that are circled in the figure. Figure 5.16b also shows a good correlation (R^2 = 0.96) between the ^{77}Se chemical shift in solution and in the solid state, with the exception of **5.9** and **5.4** , where a difference of ~106 and ~82 ppm respectively, is observed. As discussed in previous chapters, the difference between solution and solid state chemical shifts could, in principle, arise from crystal packing effects or from averaging or changes in conformations. As this is difficult to demonstrate experimentally, a way of investigating this effect in the systems studied will be the use of DFT calculations. Comparison of the chemical shift predicted for an isolated molecule that predicted for the whole crystal could give an indication of the magnitude of the crystal packing effect. This is an analogy for the comparison of solution-state and solid-state NMR parameters, as the first one should be closer to the isolated molecule and the latter to the crystal structure, assuming no significant changes in conformation are presented. Therefore, in order to study this effect, DFT calculations using CASTEP 7 were performed on the full crystal structure and compared to calculations for isolated molecules of **5.1** – **5.12**. The comparison of $\sigma_{iso}^{molecule}(^{31}P)$ against $\sigma_{iso}^{crystal}(^{31}P)$, is shown in Figure 5.17. The compounds that differ the most are **5.10** and one of the ^{31}P environments in **5.5** and **5.12b**, with differences of ~12 ppm. For these three compounds, only **5.10** reveals an experimentally similar

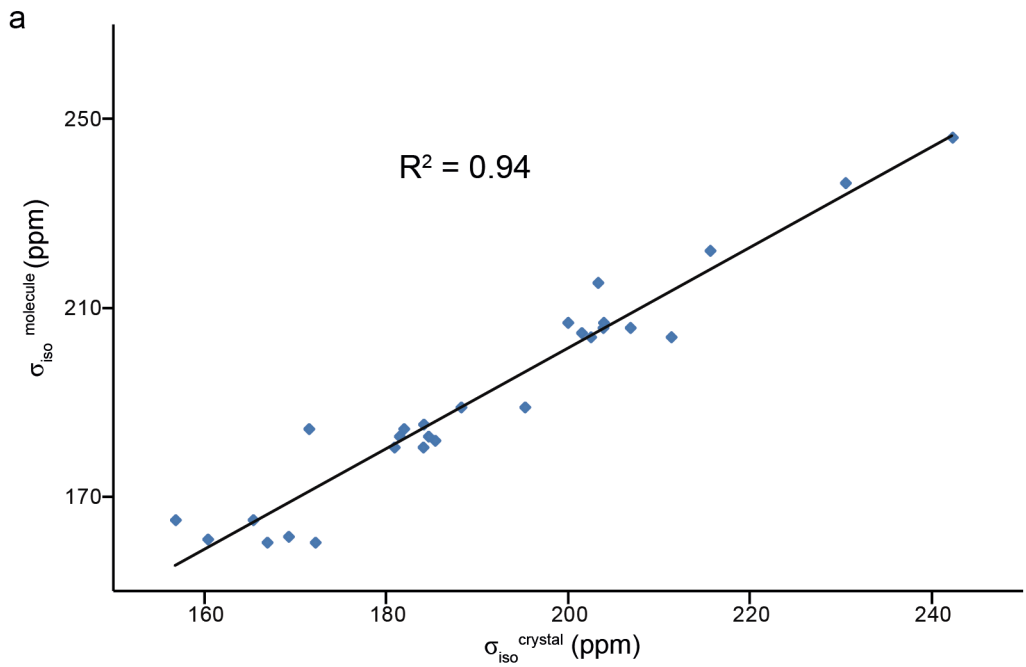

Figure 5.17. Plot of DFT calculated $\sigma_{iso}^{molecule}(^{31}P)$ against $\sigma_{iso}^{crystal}(^{31}P)$ for **5.1** – **5.12**.

difference between the chemical shift found in solution and solid (~ 14 ppm), suggesting that there might be a significant crystal packing effect for this compound. In contrast, **5.1** and **5.4**, which show larger chemical shift differences (14 – 26 ppm) between solution- and solid-state NMR, have much smaller difference computationally (*i.e.*, only 3 – 6 ppm difference in found between $\sigma_{iso}^{molecule}$ against $\sigma_{iso}^{crystal}$ for these two compounds). This suggests that it might be other effects *e.g.*, conformational changes imposed by crystal packing present in these compounds that might explain that difference.

For the solid-state NMR spectra, the experimental CSA parameters were also extracted and compared for all compounds (those described in this chapter, and those from Chapter 4), in order to obtain additional information about the local structure around ^{31}P and ^{77}Se. Table 5.7 summarises the CSA information through the series for ^{31}P and ^{77}Se NMR.

The full CSA tensors are given for all compounds in Tables C6-C8 in the Appendix C. Ω (^{31}P) varies from ~140 to 320 ppm. The *tert*butyl analogues possess larger Ω(^{31}P) than the *iso*propyl analogues, with the exception of **5.1** and **5.7**, and with significant differences *(i.e.,* from 27 to 255 ppm). Generally, the selenium *peri*- substituted compounds exhibit larger spans than the sulfur *peri*-substituted analogues, and the substitution of different chalcogens at the phosphorus atom has relatively small influence on the Ω(^{31}P) values, which increase, as the polarizability of the chalcogen increases: O > S > Se. The range of Ω(^{77}Se) varies from ~124 to 978 ppm. Generally, the *iso*propyl compounds possess larger Ω(^{77}Se), than the *tert*butyl analogues, with the exception of **5.3** and **5.9**. The chalcogen substitution on the P atom, has a small effect on Ω(^{77}Se), with the O-derivatives possessing the larger spans of the whole series. It is also clear from the table that the two types of selenium atoms, *i.e.,* those in the *peri*-positions and those double bounded to phosphorus (P=Se) have very different Ω. Those in the *peri*-position vary between 550 – 906 ppm, while the magnitude and range of Ω(^{77}Se) for P=Se, is much smaller, between ~124 – 197 ppm, with the exception of **5.9**, that has a Ω very similar to the selenium in the *peri*-positions. Figure 5.18 shows the correlation between the experimental span and chemical shift for ^{31}P and ^{77}Se. Although, no good correlation is found for ^{31}P (Figure 5.18a), which indicates that for a particular chemical shift the span cannot be easily predicted, it is possible to observe a better correlation in the ^{77}Se, with the exception of **5.9** that appears at very different chemical shift compared to the selenium atoms that possess similar span values. In order to understand this difference a closer look into the crystal structures and molecular conformation is needed.

Table 5.7. ^{77}Se and ^{31}P experimental CSA parameters the spectra recorded at 14.1 T and at 5 kHz MAS and 7.5 kHz MAS for ^{77}Se and ^{31}P, respectively.

	4.1	**5.1**	**5.2**[a]	**5.3**	**4.4**	**5.4**[a]	**5.5**[a]	**5.6**[a]	**4.3**
E,R,X group	S, iso	S, iso,O	S, iso, S	S, iso, Se	Se, iso	Se,iso, O	Se,iso,S	Se,iso,Se	S, Ph
Ω(^{31}P)	169 184 209	303	141 177 187	159	198	282	207 221	202	197 193
κ(^{31}P)	0.9 0.4 0.3	0.8	0.9 0.8 0.8	0.9	0.4	1.0	0.9 0.7	0.8	0.2 0.2
Ω(^{77}Se)	–	–	–	188	589	866 906	745 703 804 732	696 736 197	–
κ(^{77}Se)	–	–	–	–0.0	–1.0	–0.6 –0.4	–0.8 –1.0 –0.8 –0.8	–0.9 –1.0 –0.9	–
	4.2	**5.7**	**5.8**	**5.9**[a]	**4.5**[a]	**5.10**[a]	**5.11**[a]	**5.12**[a]	**4.6**[a]
E,R,X group	S, tert	S, tert, O	S, tert, S	S,tert, Se	Se, tert	Se,tert,O	Se, tert, S	Se, tert,Se	Se, Ph
Ω(^{31}P)	–	301	303 302	283 282	231	320	243	229 242	203
κ(^{31}P)	–	0.9	0.9 0.9	0.9 0.9	0.5	0.8	0.9	0.8 0.7	0.3
Ω(^{77}Se)	–	–	–	850 978	447 470	721 782	592 560	642 628 554 142 124	593 569
κ(^{77}Se)	–	–	–	–0.9 –0.9	–0.9 –1.0	–0.4 –0.3	–0.9 –1.0	–0.8 –0.9 –0.9 0.4 0.9	–0.0 –1.0

[a] The values are summarised from the most deshielded to more shielded site.

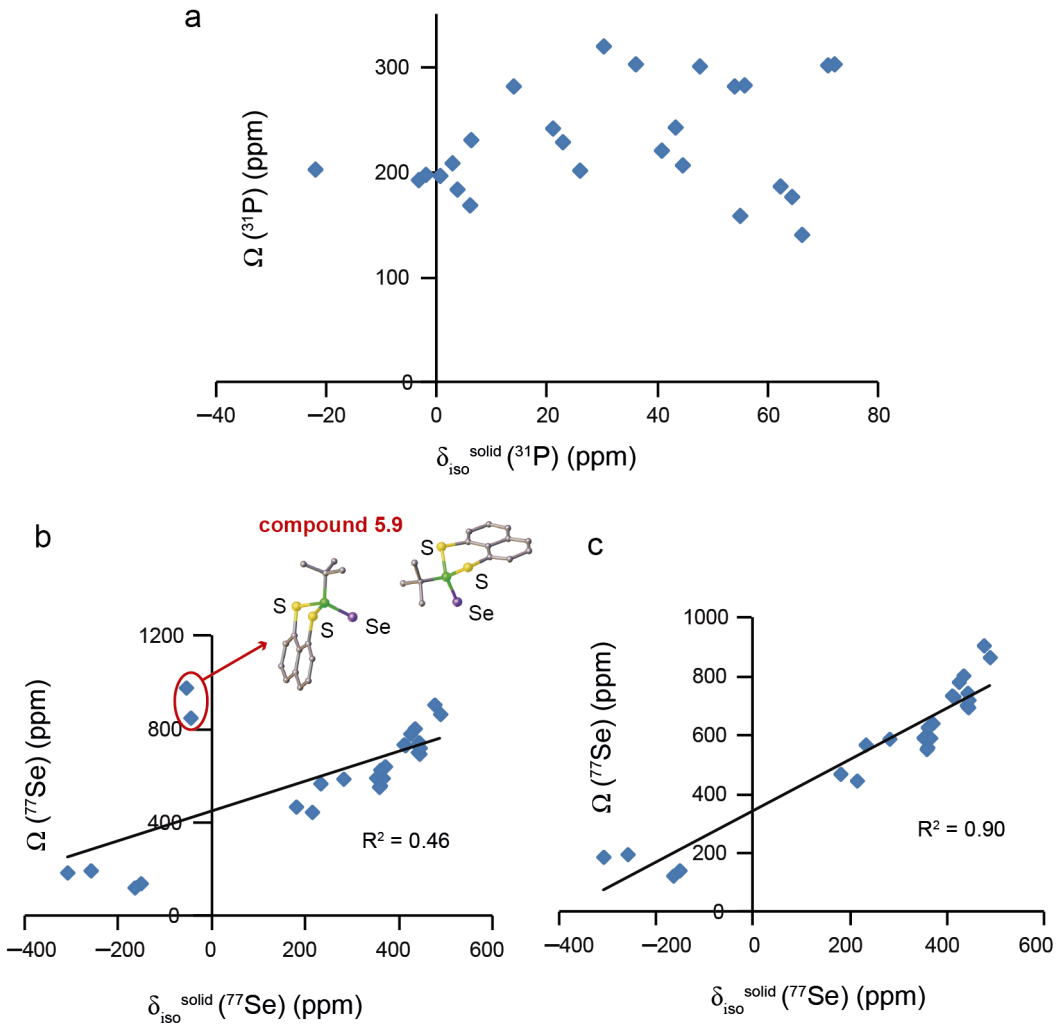

Figure 5.18. Plots of (a) Ω(^{31}P) against δ_{iso}^{solid} (^{31}P) and (b) Ω(^{77}Se) against δ_{iso}^{solid} (^{77}Se), for **4.1** – **4.6**, (except **4.2)** and **5.1** – **5.12**. (c) Same as (b) with the values for **5.9** removed.

5.6.6 Conformational difference

The molecular conformations in crystal structures of the oxidised compounds were compared and it was noted that these did differ for some compounds. In some cases, the chalcogen (X) double bonded to phosphorus (P=X), appears almost in the plane of the naphthalene ring, adopting a B conformation as shown in Figure 5.19. This conformation has

been found for **5.2**, **5.3**, **5.5**, **5.6**, **5.11** and **5.12**. In contrast, the rest of compounds exhibit a different conformation of the chalcogen-phosphorus double bond (P=X), which has an almost perpendicular arrangement with respect to the naphthalene plane, denotes as A conformation in Figure 5.19. This conformation is seen in **5.1**, **5.4**, **5.7**, **5.8**, **5.9** and **5.10**. It must be noted that all the O-oxidised derivatives prefer this orientation rather than the parallel conformation. This different conformation could arise as a consequence of the different sterics or different intermolecular interactions present in the compounds studied.

Generally, except for **5.7** and **5.8**, the compounds that adopt an A conformation, exhibit some differences in the NMR parameters (chemical shifts and CSA) in comparison to the compounds that adopt a B conformation. As previously discussed, **5.4**, **5.1** and **5.10**, show different ^{31}P chemical shifts in solution and in the solid-state (*i.e.*, $\delta_{iso}^{Solution}(^{31}P)$ = 40 ppm, while $\delta_{iso}^{Solid}(^{31}P)$ = 14 ppm for **5.4**) as was shown in Figure 5.16a, while **5.9** and **5.4** exhibit differences between the ^{77}Se chemical shift in solution and in the solid-state as shown in Figure 5.16b. It is also clear from the previous section that **5.9** also exhibits very different $\Omega(^{77}Se)$ which could result from the different conformation. Therefore, in order to investigate if the molecular conformation has an impact on the chemical shift and span for these compounds to account for the differences observed experimentally, the NMR parameters for an isolated molecule in different conformations were calculated using CASTEP 7, as described in the experimental section. These calculations were performed for only three compounds, **5.9**, **5.10** and **5.12**, in order to gain some insight into the origin of the NMR parameters. The values for both conformations for each of the three compounds are summarised in Table 5.8.

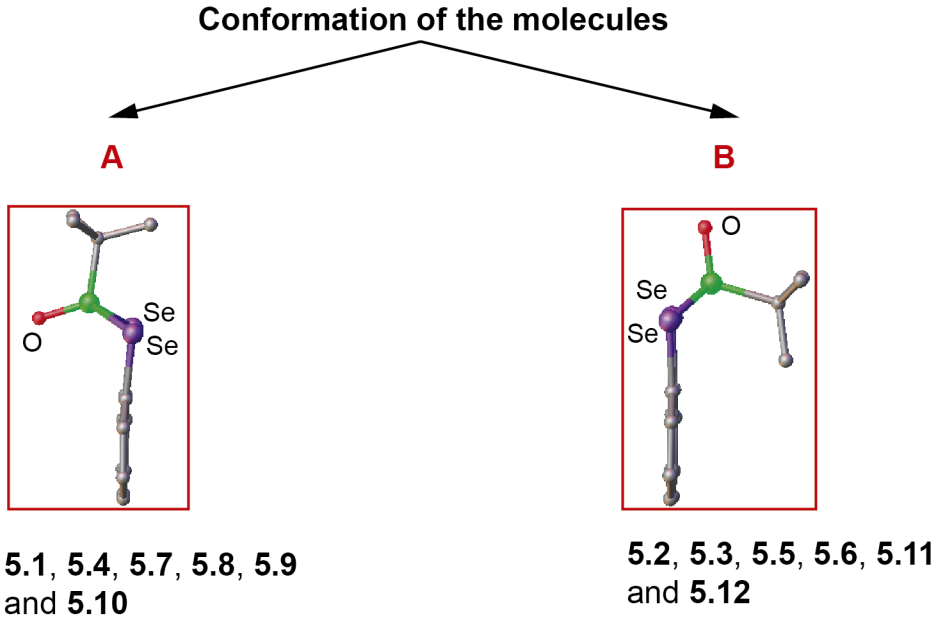

Figure 5.19. Schematic representation of the two conformations observed for **5.1** – **5.12**.

Table 5.8. ^{77}Se and ^{31}P calculated NMR parameters for isolated molecules of three compounds in different conformations.

Compound	Geometry	$\sigma_{iso}(^{31}P)$	$\Omega(^{31}P)$	$\sigma_{iso}(^{77}Se)$	$\Omega(^{77}Se)$
5.10	**A**	214	439	1136	903
5.10	**B**	197	256	1271	576
5.12	**A**	165	507	909[a] 1463	1329[a] 1415
5.12	**B**	166	295	1232[a] 1808	721[a] 236
5.9	**A**	182	491	1628	1337
5.9	**B**	193	293	1877	225

[a] Is the Se in peri position. Note that both Se atoms have very similar Ω and σ_{iso} and so only one value is given. The rest of Ω and σ_{iso} for the three compound are for the Se in P=Se.

For ^{31}P, there are differences between the three compounds studied for both conformations. $\sigma_{iso}{}^{solid}(^{31}P)$ varies for the different conformations between 1 (**5.12**) and 17 (**5.10**) ppm, while differences in $\Omega(^{31}P)$ between conformations are much bigger (*i.e.,* differences in $\Omega(^{31}P)$ vary between

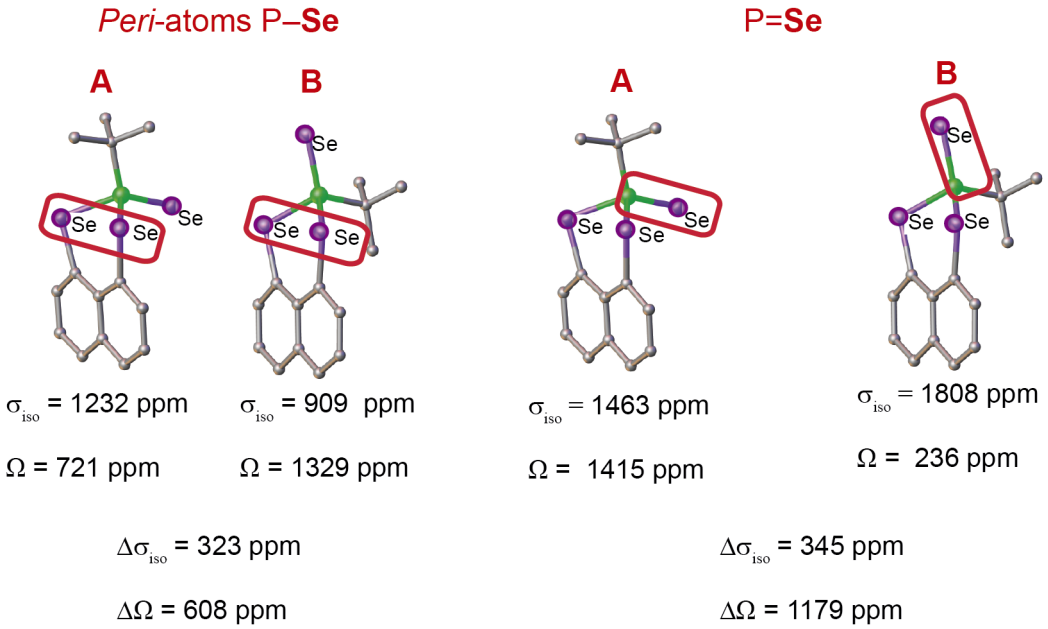

Figure 5.20. Schematic representation of the difference in the ^{77}Se calculated NMR parameters (σ_{iso} and Ω) between conformation A and B, for the two types of selenium atoms in **5.12** (*i.e.*, selenium in the *peri*-position and P=Se).

183 –212 ppm). However, the bigger differences are clearly found for the selenium environment. $\sigma_{iso}^{solid}(^{77}Se)$ between conformations varies much less than the $\Omega(^{77}Se)$ between the two conformations, (*i.e.*, 135 (**5.10**) to 345 (**5.12**) ppm difference is found for $\sigma_{iso}^{solid}(^{77}Se)$ for P=Se, while $\Omega(^{77}Se)$ differences are between 327 (**5.10**) and ~1179 (**5.12**) ppm, for the P=Se). This suggests that although there is a variation of the isotropic chemical shift, the span experiences more significant changes between conformations. Between the two types of Se atoms (*peri*-Se and Se=P), the different conformations (A and B) have similar influence on $\sigma_{iso}^{solid}(^{77}Se)$ with 323 ppm difference observed for the *peri*-Se, while 345 ppm difference is observed for the P=Se. In contrast, the difference observed in the $\Omega(^{77}Se)$ between the two conformation is greater for the Se=P than for

the *peri*-Se, (*i.e.*, 608 ppm difference is observed in the P-Se, while 1179 ppm difference is observed for the P=Se). This is shown schematically in Figure 5.20.

5.6.7 Calculation of NMR parameters

To gain insight into the structural origin of the ^{77}Se and ^{31}P magnetic shielding tensors, periodic first-principles GIPAW calculations were performed on geometry-optimized crystal structures initially obtained from single crystal X-ray diffraction data for each compound. The ^{31}P and ^{77}Se magnetic shielding tensors were calculated using CASTEP 7, and the value of the isotropic chemical shift and span are given in Tables 5.9 and 5.10. For full chemical shift tensor components see Tables C9-C11 in the Appendix C.

The values of σ_{ref} can be determined by linear regression from a plot of $\delta_{iso}{}^{exp}$ against $\sigma_{iso}{}^{calc}$ for a range of compounds, as discussed previously. Normally, this plot should yield a gradient of 1, and the value of the σ_{ref} is taken from the intercept. However, this ideal situation does not often happen, and the scaling factor can be required to determine σ_{ref}. In Chapter 4, it was not possible to determine σ_{ref} owing to the variation in values seen and limited range of compounds studied. In this section all compounds, including those in Chapter 4 (except **4.2**) will be considered to obtain a better idea of the agreement between calculation and experiments and to establish a σ_{ref} value for ^{31}P and ^{77}Se. A plot of the $\delta_{iso}{}^{exp}(^{31}P)$ against $\sigma_{iso}{}^{calc}(^{31}P)$ for all compounds, is shown in Figure 5.21a. However, poor agreement (R^2 = 0.46) is found when all compounds are considered. It was seen in Chapter 4 that the sulfur and selenium compounds have different differences between experiment and calculated

values and so it may be that two different σ_{ref} values should be determined, one for the sulfur compounds and one for the selenium analogues. Plots of experimental $\delta_{iso}^{exp}(^{31}P)$ against calculated $\sigma_{iso}^{calc}(^{31}P)$ for selenium and sulfur compounds separately are shown in Figures 5.21b and 5.21c, respectively, and better agreement is found with $R^2 = 0.68$ and 0.83, for selenium and sulfur. The values of σ_{ref} for selenium and sulfur, taking these scaling factors into account, can be estimated using these plots to be 243.1 and 292.6 ppm, respectively. A plot of ^{31}P δ_{iso}^{exp} against δ_{iso}^{calc} is shown in Figure 5.21d, and when using different σ_{ref} for the selenium and sulfur compounds, relatively better agreement ($R^2 = 0.81$) is found for all compounds. It is known from previous chapters that many of the compounds exhibit some motional behaviour, probably related to the R groups attached to P, as shown in Chapter 4 for the un-oxidised compounds. As this effect is not considered in the calculation of these systems, (that are carried out at 0 K), this may contributes to discrepancies between calculations and experiments. The Ω values for ^{31}P were also calculated, as were the components of the CSA tensor. Figures 5.22a and 5.22b, show plots of Ω^{exp} against Ω^{calc} and δ_{ii}^{exp} against δ_{ii}^{calc}, respectively, for all compounds studied in Chapter 4 and 5. Although, the agreement is moderate for $\Omega(^{31}P)$, with $R^2 = 0.76$, a poor agreement is found for the components of the tensors ($R^2 = 0.35$). All calculated values for $\Omega(^{31}P)$ were generally overestimated in comparison to the experimental values, while a different behaviour is seen for the components of the CSA, δ_{ii}^{calc}. The δ_{22}^{calc} was generally overestimated while, δ_{11}^{calc} and δ_{33}^{calc} were underestimated in comparison to the experimental values. Figure 5.23a shows a plot of ^{77}Se δ_{iso}^{exp} against σ_{iso}^{calc}, which reveals a better correlation ($R^2 = 0.98$) compared to the ^{31}P data. In this case, a much better determination of σ_{ref} is possible as better agreement is obtained

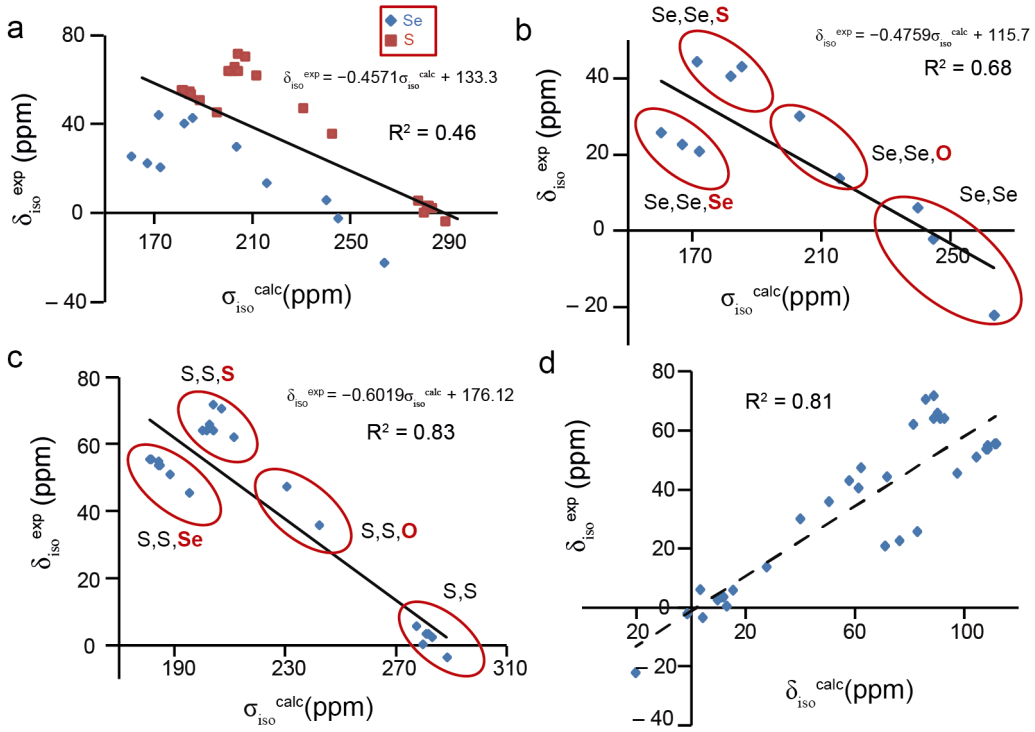

Figure 5.21. Plot of ^{31}P δ_{iso}^{exp} against σ_{iso}^{calc} (a) for all compounds studied in this chapter and in Chapter 4, (b) for selenium compounds, (c) for sulfur compounds. (d) Plot of ^{31}P δ_{iso}^{exp} against δ_{iso}^{calc} for all compounds studied in this chapter and in Chapter 4. The dashed line represents the perfect agreement between calculated and experimental results.

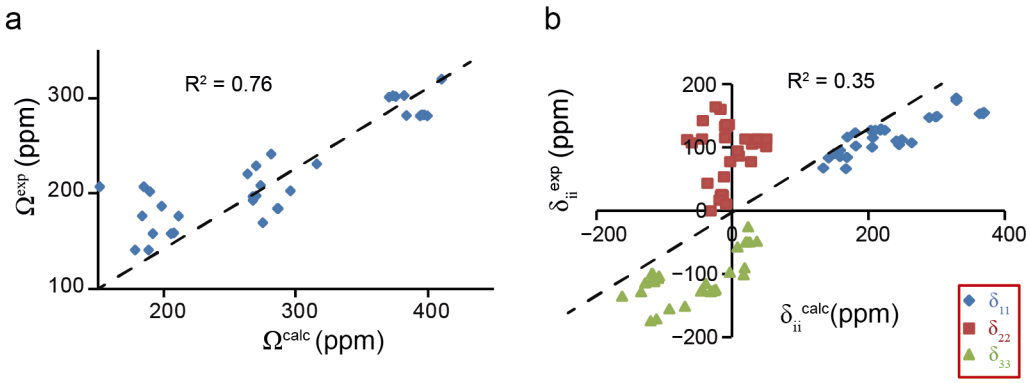

Figure 5.22. Plot of (a) ^{31}P Ω^{exp} against Ω^{calc} and (b) ^{31}P δ_{ii}^{exp} against δ_{ii}^{calc} for compounds studied in Chapter 4 and 5. Dashed lines represent perfect agreement between calculated and experimental results.

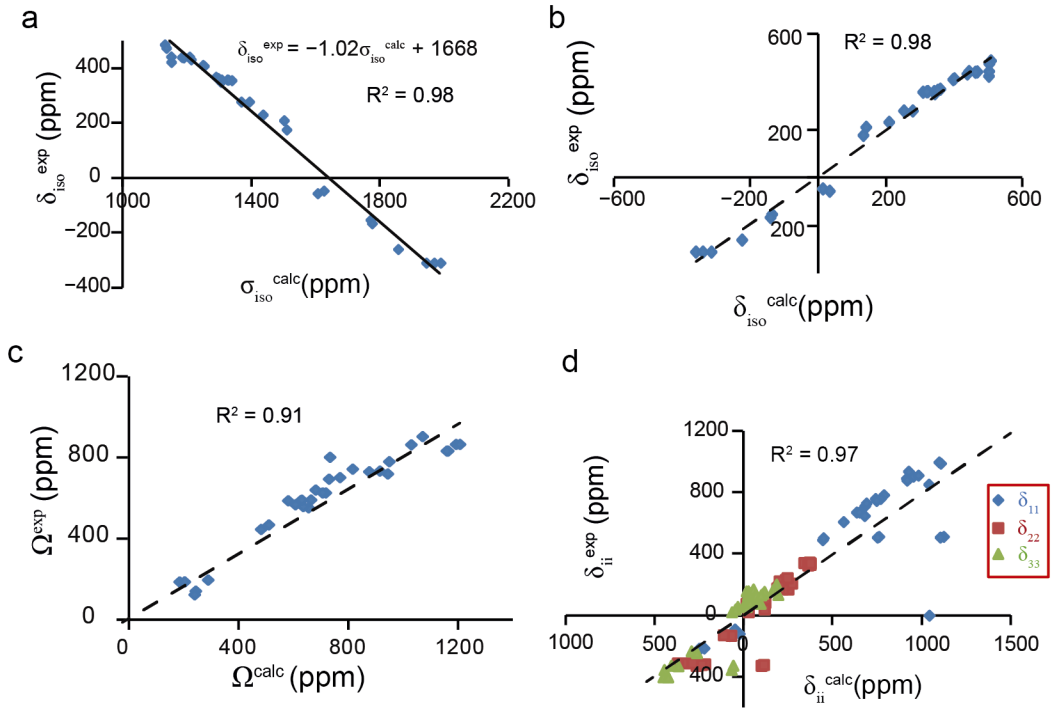

Figure 5.23. Plot of (a) ^{77}Se δ_{iso}^{exp} against σ_{iso}^{calc} and (b) ^{77}Se δ_{iso}^{exp} against δ_{iso}^{calc} and (c) ^{77}Se Ω^{exp} against Ω^{calc} and (d) ^{77}Se δ_{ii}^{exp} against δ_{ii}^{calc}, for compounds studied in Chapter 4 (**4.1** – **4.6**, except **4.2**) and **5.1** – **5.12**. Dashed lines represent perfect agreement between calculated and experimental results.

The gradient is 1, and σ_{ref} can be determined from the y-intercept without any scaling factor, and a value of 1668 ppm was obtained. A very good agreement ($R^2 = 0.98$) is then found between δ_{iso}^{exp} against δ_{iso}^{calc}, as shown in Figure 5.23b. Figures 5.23c and 5.23d, shows plots of the ^{77}Se Ω^{exp} against Ω^{calc} and δ_{ii}^{exp} against δ_{ii}^{calc}, respectively, for all compounds and better agreement ($R^2 = 0.91$ and 0.97) is found, compared to the ^{31}P data. Calculated values for $\Omega(^{77}Se)$ and for the components of the CSA, δ_{ii}^{calc}, were in some cases overestimated and underestimated, depending on the compound, in comparison to the experimental values.

Table 5.9. Calculated ^{31}P NMR parameters (isotropic chemical shift, δ_{iso}^{calc} and span Ω^{calc} for compounds **4.1** – **4.6** and **5.1** – **5.12**.

	4.1	**5.1**	**5.2a**	**5.2b**	**5.2c**	**5.3a**	**5.3b**	**4.4**	**5.4**	**5.5**	**5.6**
δ_{iso}^{calc}	15 12 11 9	50	90 81	92 88	91	108	104 98	–2	27	72 61	83
Ω^{calc}	274 285 286 273		211 183	198	178 188	205	207 191	269	383	151 184	189
	4.2	**5.7**	**5.8**	**5.9a**	**5.9b**	**4.3**	**4.5**	**5.10**	**5.11**	**5.12**	**4.6**
δ_{iso}^{calc}	–	62	89 86	108 111	108 111	41 13	3	40	58	76 71	–20
Ω^{calc}	–	370	373 375	399 397	394 395	267 267	315	410	263	269 281	295

All values are quoted in ppm.

Table 5.10. Calculated ^{77}Se NMR parameters (isotropic chemical shift, δ_{iso}^{calc} and span Ω^{calc} for compounds **4.1** – **4.6** and **5.1** – **5.12**.

	4.1	**5.1**	**5.2a**	**5.2b**	**5.2c**	**5.3a**	**5.3b**	**4.4**	**5.4**	**5.5**	**5.6**
δ_{iso}^{calc}	–	–	–	–	–	–275	–319 –299	300 275	524 519	485 479 456 419	461 416 –187
Ω^{calc}	–	–	–	–	–	203	183 203	581 626	1030 1071	770 816 733 876	730 915 289
	4.2	**5.7**	**5.8**	**5.9a**	**5.9b**	**4.3**	**4.5**	**5.10**	**5.11**	**5.12**	**4.6**
δ_{iso}^{calc}	–	–	–	63 44	66 47	–	167 159	518 518	372 341	379 362 344 330 –106 –102	364 233
Ω^{calc}	–	–	–	1159 1207	1164 1193	–	482 510	944 949	630 636	681 706 718 655 240 244	664 607

All values are quoted in ppm.

5.6.8 Phase transitions in the solid state

In order to probe motional behaviour in **5.1** – **5.12**, as described in Chapter 4 for **4.1** – **4.6**, ^{31}P NMR experiments at three different temperatures were performed. These were carried out a reasonable time after the compounds were synthesised, and surprisingly additional peaks had appeared in the NMR spectra of the three compounds studied (**5.4**, **5.5** and **5.6**). The origin of which are not immediately clear. It must be noted that owing to the change in the samples and additional peaks observed in the NMR spectra, VT experiment was finally not carried out.

Figure 5.24a shows the original ^{31}P NMR spectrum of **5.4** at 14.1 T and 14 kHz MAS. As previously discussed, the additional peaks that appear with lower intensity were believed to possibly arise from different polymorphs present in the bulk sample. Although several attempts to crystallise the sample always yielded crystals with the same structure, this does not appear to correspond to the majority of the bulk as shown previously from the comparison of the experimental and simulated XRD patterns. Figure 5.24b shows the spectrum of the same sample recorded a few months later. It can be seen that the additional peaks have significantly increased in intensity, which in principle, indicates that the "impurity" now corresponds to the majority of the sample. Note that the intensity in this case can be a poor indicator of the proportion of the phases present, if there are significant differences in T_1 relaxation times, as was seen for **4.6**. ^{31}P solution-state NMR spectra were recorded for the same sample in order to see if additional peaks were present. Figure 5.24c shows the ^{31}P NMR spectrum at 6.35 T, recorded in $CDCl_3$, and additional peaks can also be observed in the same region (~45 ppm).

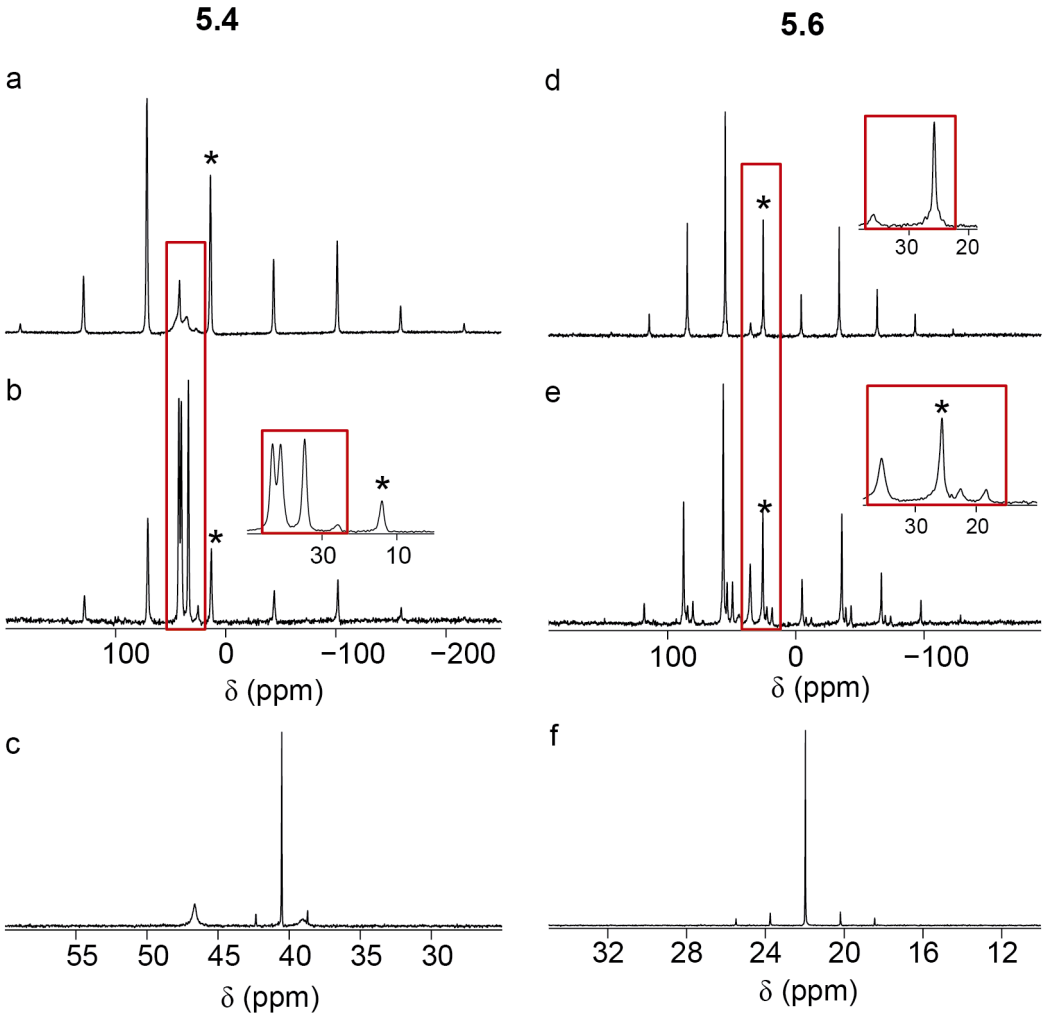

Figure 5.24. ^{31}P MAS NMR spectra acquired for **5.4** and **5.6**, respectively at 14.1 T (a, d) at 14 kHz MAS and at 7.5 kHz MAS. (b, e) as (a, d) but the spectrum were recorded a few months later. (c, d) ^{31}P solution-state NMR spectrum of **5.4** and **5.6**, respectively recorded at 6.35 T, in $CDCl_3$, after the spectra in (b, e).

This suggests that the additional peaks do not arise from a polymorph, and owing to the tendency of **5.4** to decompose, it is likely that the extra peaks arise from a decomposition product.

As for **5.4**, additional peaks were also found in the ^{31}P solid-state NMR spectrum of **5.6** that were not present in the original spectrum recorded a few months earlier (Figure 5.24d). Figure 5.24e shows two sets of extra peaks, one at ~35 ppm and two resonances with lower intensity at ~20 ppm. The resonance at 35 ppm was in the original spectrum in Figure 5.24c, while the two resonances at 20 ppm are new in the spectrum. In order to determine if any of those resonances arise from a decomposition product, ^{31}P solution-state NMR of the same sample was measured at 6.35 T, in $CDCl_3$. Figure 5.24f, shows the ^{31}P solution-state NMR of **5.6**, and no additional peaks are observed suggesting that, in contrast to **5.4**, the extra peaks shown in the ^{31}P solid-state NMR spectrum of **5.6**, probably arise from different polymorphs present in the sample. The two resonances at around ~ 20 ppm could correspond to polymorph **5.6b**, that was found in a different batch of the same compound, while the resonance at 35 ppm could arise from another polymorph not previously found.

Figure 5.25a shows the original spectrum of **5.5** at 14.1 T and 14 kHz MAS. For this compound, only one crystal structure was determined, as discussed previously. The ^{31}P solid-state NMR of the same compound was recorded again after few months, and additional peaks again appear in the spectrum, as shown in Figure 5.25b. ^{31}P solution-state NMR spectra of the same sample of **5.5**, recorded at at 6.35 T, in $CDCl_3$ confirmed the absence of these additional resonances, as shown in Figure 5.25c. This suggests that the new resonance must arise from a new polymorph. This is confirmed by crystallisation of the sample measured in the solid-state NMR experiment, yielding a new polymorph, **5.5b**, whose asymmetric unit has only a single molecule as shown in Figure 5.25d. Figure 5.25e shows the simulated powder XRD patterns for the two polymorphs and the original experimental data.

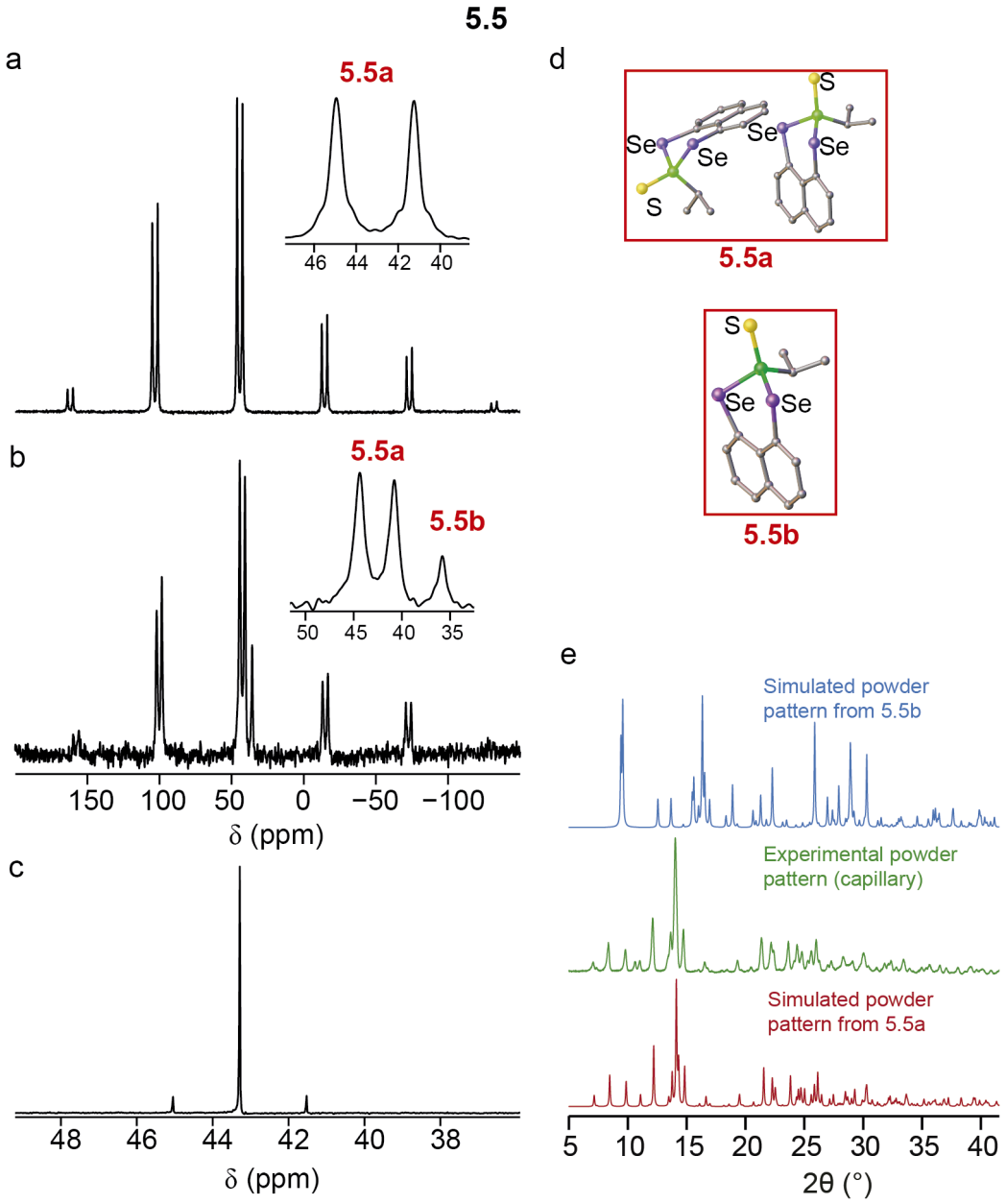

Figure 5.25. ^{31}P MAS NMR spectrum of **5.5** acquired (a) at 14.1 T and 14 kHz MAS. (b) As (a) but recorded after few months. (c) ^{31}P NMR spectrum acquired at 6.35 T, in $CDCl_3$ recorded after the spectrum in (b), for **5.5**. Insets show the isotropic peak. (d) Asymmetric units (red square) for the two polymorphs determined for **5.5** (**5.5a** and **5.5b**). (e) Comparison of the experimental and simulated powder XRD patterns for crystal structures of **5.5a** and **5.5b**.

It is clear that both crystal structures are in fact very different. Unfortunately, because of the loss of the sample measured in the solid-state NMR after a number of experiments, it was not possible to re-record the experimental powder pattern to see if there were any changes between the original and the sample studied later.

5.7 Conclusions

In this chapter a series of twelve new oxidised P-S and P-Se heterocycles has been successfully synthesised using a similar route to that reported in the literature.[10] The compounds were fairly stable upon exposure to air in the solid form for few months, while in solution they decomposed to the naphtho[1,8-cd]1,2-dithiole and naphtho[1,8-cd]1,2-selenole quite rapidly. As solids, after a few months the samples undergo phase transitions, as observed by the appearance of new peaks in the solid-state NMR spectra of some of the compounds studied. This phase transition occurs spontaneously, as no heat was intentionally applied to the sample, except perhaps the grinding of the sample before packing it in the rotor and the heat arising from the MAS NMR experiments performed (*i.e.,* frictional heating). For the oxygen derivatives a decomposition reaction is favored in comparison to the phase transition. The *iso*propyl oxygen derivatives (**5.1** and **5.4**), were the most unstable compounds of the series.

The strain in the system was analyzed for the series of compounds and it is clear that oxidation with different chalcogens does not affect the planarity of the aromatic backbone, which exhibits similar torsion angles and splay angles through the series. However, a bigger difference is found in the distance of the different chalcogens (X) from the naphthalene plane, where for some compounds the P=X bond was co-linear with the ring and

for others, it was far from it, adopting a pseudo perpendicular position. This different arrangement of the chalcogen (X) was defined as conformation A and B. It was shown that the NMR parameters (*i.e.,* the isotropic chemical shift and the span), especially for ^{77}Se, were sensitive to the change in conformation, giving very different values for the two conformations. This was also confirmed by NMR calculations using periodic DFT for an isolated molecule in the two different arrangements. Comparison of the isotropic chemical shifts in solution and solid, reflect some differences for some of the compounds. DFT calculations confirm that the differences do not generally arise as crystal packing effect, but probably as a result of the different conformation found in solid and in liquids. In solution there is more motion of the molecules, and it is even possible that there is an equilibrium between conformation A and B, while in solids the motion is restricted by crystal packing. However, further computational work is needed in order to confirm this.

The presence of polymorphism was confirmed by using single-crystal and powder XRD techniques together with solid-state NMR. It was clear that although single-crystal X-ray diffraction was essential for the determination of the different polymorphs, it is very insensitive to the proportion of these in the bulk sample and techniques such as powder XRD or solid-state NMR are required. Powder XRD provides a good indication of the polymorphs present in the majority of the bulk, except in cases where the powder XRD patterns are very similar or there is a mixture of several polymorphs, as occurs for **5.2**. In contrast, ^{31}P and ^{77}Se solid-state NMR spectra, were very sensitive to changes in the local environment, even between polymorphs with structures that were quite similar, as for **5.9**. Furthermore, they provide a quantitative indication of the proportions of each polymorph in the bulk sample by analysis of the

intensity of the observed resonances. The tendency to exhibit polymorphism seems to increase as the content of more polarizable atoms increases, *i.e.*, the two compounds that possess three Se atoms in the structure, **5.6** and **5.12**, exhibit more polymorphs. In the sulfur derivatives, those that possess a Se atom, **5.3** and **5.9**, also exhibit polymorphism. In the case of sulfur derivatives, apart from the ones containing Se, polymorphism was only found in **5.2**, which undergoes a phase transition upon heating in the rotor. Only one crystal structure is known for all of the oxygen derivatives. However, the disagreement between the simulated XRD pattern and the experimental measurement, as for **5.4** and **5.10**, suggest that further unidentified polymorphs may be present, and indeed form the bulk of the material.

DFT calculations were a good indicator of the relative stability of the different crystal structures, by comparison of the different calculated energies of each polymorph. However, DFT NMR calculations for ^{31}P for these compounds were poorly reproduced in the system studied experimentally. The disagreement between calculations and experimental values probably arises as a consequence of the motion of the R group, as previously shown in Chapter 4. Moreover, another important factor that might contribute to the disagreement is that the calculations were performed for a single crystal structure that did not in fact correspond to the bulk sample, for **5.4** and **5.10**. In contrast, calculations of ^{77}Se NMR parameters were in very good agreement with the experimental values.

This study provides a starting point for understanding polymorphism in the systems studied, which is of vital importance for molecular materials, where the properties of the materials could be related to the solid-state structure and ultimately define the applicability and uses of these materials.

5.8 Future work

A further investigation into the spontaneous phase transitions that occur in some of the compounds studied could be carried out for all compounds in order to identify all possible polymorphs not yet found in the systems studied. Similarly, crystal structure prediction could help in determining new crystal structures and provide insight into their relative stability.

In terms of the DFT calculations, the temperature effects could be studied to see if better agreement is then found for the ^{31}P NMR parameters between calculations and experiments. Moreover, further work on the conformational equilibrium in these systems could also be performed to understand the difference observed between the chemical shift in solid and in solution.

5.9 References

1. S. L. Morissette, Ö. Almarsson, M. L. Peterson, J. F. Remenar, M. J. Read, A. V. Lemmo, S. Ellis, M. J. Cima and C. R. Gardner, *Adv. Dru. Deliv. Rev.*, **2004**, 56, 275-300.

2. D. E. Sands, *Introduction to Crystallography*, Dover Publications Inc, New York, **1969**.

3. W. I. F. David and K. Shankland, *Structure Determination from Powder Diffraction Data, Vol.* 64., Oxford University Press, UK, New York, **2008,** 1-331.

4. R. K. Harris, *J. Pharm. Pharmacol.*, **2007**, 59, 225-239.

5. B. A. Demko and R. E. Wasylishen, *Inorg. Chem.*, **2008**, 47, 2786-2797.

6. J. R. Smith, W. Xu and D. Raftery, *J. Phys. Chem. B.*, **2006**, 110, 7766-7776.

7. C. Bonhomme, C. Gervais, F. Babonneau, C. Coelho, F. Pourpoint, T. Azaïs, S. E. Ashbrook, J. M. Griffin, J. R. Yates, F. Mauri and C. J. Pickard, *Chem. Rev.*, **2012**, 112, 5733-5779.

8. S. Price and L. Price, *Intermolecular Forces and Clusters I, Vol. 115*, Springer-Verlag, Berlin, **2005**, 81-123.

9. D. Mangin, F. Puel and S. Veesler, *Org. Process. Res. Dev.*, **2009**, 13, 1241-1253.

10. A. Karaçar, M. Freytag, H. Thönnessen, J. Omelanczuk, P. G. Jones, R. Bartsch and R. Schmutzler, *Z. Anorg. Allg. Chem.*, **2000**, 626, 2361-2372.

11 F. R. Knight, A. L. Fuller, M. Bühl, A. M. Z. Slawin and J. D. Woollins, *Chem. Eur. J.*, **2010**, 16, 7617-7634.

12. P. Kilian, A. M. Z. Slawin and J. D. Woollins, *Dalton Trans.*, **2003**, 3876-3885.

13. M. D. Segall, P. J. D. Lindan, M. J. Probert, C. J. Pickard, P. J. Hasnip, S. J. Clark and M. C. Payne, *J. Phys. Condens. Matter.*, **2002**, 14, 2717-2744.

14. M. D. Segall, S. J. Clark, C. J. Pickard, P. J. Hasnip, M. I. J. Probert, K. and R. A. M. C. Payne, *Z. Kristallogr.*, **2005**, 220, 567-570.

15. C. J. Pickard and F. Mauri, *Phys. Rev. B*, **2001**, 63, 1-12.

16. J. P. Perdew, K. Burke and M. Ernzerhof, *Phys. Rev. Lett.*, **1996**, 77, 3865-3868.

17. J. R. Yates, C. J. Pickard and F. Mauri, *Phys. Rev. B*, **2007**, 76, 1-12.

18. S. Grimme, *J. Comput. Chem.*, **2006**, 27, 1787-1799.

19. A. Karaçar, M. Freytag, H. Thönnessen, J. Omelanczuk, P. G. Jones, R. Bartsch and R. Schmutzler, *Heteroatom. Chem.*, **2001**, 12, 102-113.

20. A. J. Cruz-Cabeza, S. M. Reutzel-Edens and J. Bernstein, *Chem. Soc. Rev.*, **2015**, 44, 8619-8635.

Chapter 6: Experimental procedures

6.1 General considerations

All experiments were carried out under an oxygen- and moisture-free nitrogen atmosphere using standard Schlenk techniques and glassware. Reagents were obtained from commercial sources and used as received. Dry solvents were collected from an MBraun solvent purification system. Elemental analyses were performed by Stephen Boyer at the London Metropolitan University. Infrared spectra were recorded for solids as KBr discs and oils on NaCl plates in the range 4000-300 cm^{-1} on a Perkin-Elmer System 2000 Fourier transform spectrometer. Electron Impact (EI^+), Atmospheric Pressure Chemical Ionisation ($APCI^+$), Atmospheric Solids Analysis Probe ($ASAP^+$) and Nano-electrospray (NSI) mass spectra were carried out by the EPSRC National Mass Spectrometry Service, Swansea. ^1H and ^{13}C solution-state NMR spectra were recorded on a Bruker Avance 400 MHz or a Bruker Avance 300 MHz spectrometer with chemical shifts (reported in ppm) referenced to residual solvent peaks. ^{77}Se and ^{31}P NMR spectra were recorded on a Jeol GSX 270 MHz spectrometer with chemical shifts (reported in ppm) referenced to external $(CH_3)_2Se$ and 85% H_3PO_4, respectively. Assignments of ^{13}C and ^1H NMR spectra were made with the help of ^1H-^1H COSY, ^1H-^{13}C HSQC and ^1H-^{13}C HSBC experiments. Coupling constants (J) are given in Hertz (Hz). The naphtho[1,8-*cd*]1,2-dithiole and naphtho[1,8-*cd*]1,2-diselenole precursor were prepared using standard literature procedures.[1]

6.2 Experimental procedures of Chapter 4

6.2.1 Synthesis of compound 4.1

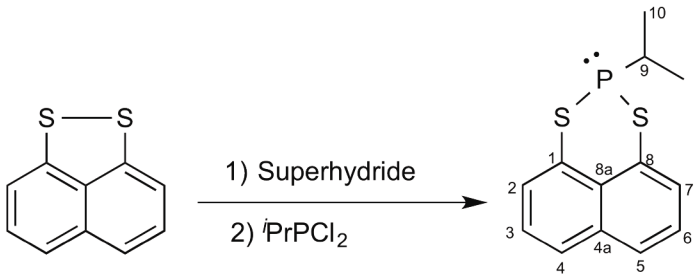

To a solution of naphtho[1,8-cd]1,2-dithiole (1.3 g, 6.8 mmol) in THF (100 mL) was added dropwise a 1 M solution of lithium triethylborohydride (superhydride) in THF (11.2 mL, 11.2 mmol). The mixture was stirred at room temperature for 15 min, after which a solution of dicholoro*iso*propylphosphine (1.5 mL, 10.2 mmol) in THF (10 mL) was added dropwise to the mixture. The resulting mixture was heated to ~66 °C and left overnight. After the solvent was removed *in vacuo*, the reaction mixture was extracted with hexane (125 mL), washed with distilled water (200 mL) and the organic layer was dried with magnesium sulfate and concentrated under reduced pressure. Column chromatography on silica gel (hexane) was performed to afford the purified target compound as a white solid. Crystals suitable for X-ray diffraction were grown in hexane. (1.2 g, 66%); **IR** (KBr disk) : ν_{max} cm^{-1} : 2951w, 2916, 2956w, 1548s, 1494s, 1463w, 1360s 1317w, 1232w, 1203vs, 1192s, 1148w, 1082w, 1030s, 888w, 868w, 813vs, 755vs, 639s, 546w, 533w, 508s, 498s; **^{1}H {^{31}P} NMR** (300 MHz, $CDCl_3$) δ (ppm) = 7.8 (dd, $^{3}J_{HH}$ = 8.3 Hz, $^{4}J_{HH}$ = 1.2 Hz, 2H ArH–4, 5) 7.6 (dd, $^{3}J_{HH}$ = 7.3 Hz, $^{4}J_{HH}$ = 1.4 Hz, 2H, ArH–2, 7) 7.4 (t, $^{3}J_{HH}$ = 7.8 Hz, 2H, ArH–3, 6) 1.9 (m, 1H, CH, H9) 1.1 (d, $^{3}J_{HH}$ = 7.0 Hz , 2 × CH_3, 6H, H10); **^{13}C {^{1}H} NMR** (75.4 MHz, $CDCl_3$) δ (ppm) = 135.4 (d, $^{4}J_{CP}$ = 3.1 Hz, Cq, ArC–4a) 131.0 (d,

$^{3}J_{CP}$ = 3.2 Hz, 2 × CH, ArC–2, 7) 129.6 (s, 2 × CH, ArC–4, 5) 127.7 (d, $^{3}J_{CP}$ = 4.2 Hz, Cq, ArC–8a) 125.7 (s, 2 × CH, ArC–3, 6) 124.4 (d, $^{2}J_{CP}$ = 9.0 Hz, 2 x Cq, ArC–1, 8) 28.8 (d, $^{1}J_{CP}$ = 31 Hz, CH, C–9) 18.9 (d, $^{2}J_{CP}$ = 18.5 Hz, 2 × CH_3, C10); **^{31}P {^{1}H} NMR** (109.3 MHz, $CDCl_3$) δ (ppm) = 4.72 (s); **MS** (APCI^{+}): m/z (%) 265.02 (100) $[M+H]^{+}$; **elemental analysis** calculated (%) for $C_{13}H_{13}PS_2$ (264.35) : C 59.07, H 4.96. Found C 59.21, H 4.87.

6.2.2 Synthesis of compound 4.2

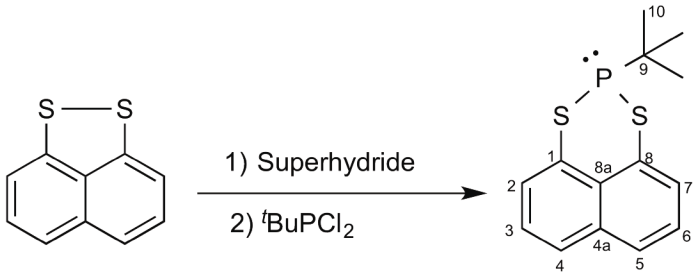

To a solution of naphtho[1,8-cd]1,2-dithiole (1.3 g, 6.8 mmol) in THF (100 mL) was added dropwise a 1 M solution of superhydride in THF (14.0 mL, 14.0 mmol). The mixture was stirred at room temperature for 15 min, after which a solution of dicholoro*tert*butylphosphine (1.1 g, 6.83 mmol) in THF (10 mL) was added dropwise to the mixture. The resulting mixture was warmed to ~66 °C and left overnight. After the solvent was removed *in vacuo*, the reaction mixture was extracted with hexane (125 mL), washed with distilled water (200 mL) and the organic layer dried with magnesium sulfate and concentrated under reduced pressure. Column chromatography on silica gel (hexane) was performed to afford the purified target compound as a yellowish sticky solid. Crystals suitable for X-ray diffraction were grown in hexane. (1,2 g, 72%); **^{1}H {^{31}P} NMR** (300 MHz, $CDCl_3$) δ (ppm) = 7.7 (dd, $^{3}J_{HH}$ = 8.1 Hz, $^{4}J_{HH}$ = 1.2 Hz, 2H ArH–4, 5) 7.6 (dd, $^{3}J_{HH}$ = 7.5 Hz, $^{4}J_{HH}$ = 1.0 Hz, 2H, ArH–2, 7) 7.3 (t, $^{3}J_{HH}$ = 7.3 Hz, $^{3}J_{HH}$ =

7.2 Hz, 2H, ArH–3, 6) 1.1 (d, $^{2}J_{CP}$ = 15.7 Hz, 3 × CH_3, 6H, H10); **^{13}C {^{1}H} NMR** (75.4 MHz, $CDCl_3$) δ (ppm) = 135.2 (d, $^{4}J_{CP}$ = 2.8 Hz, Cq, ArC–4a) 129.8 (d, $^{3}J_{CP}$ = 2.6 Hz, 2 × CH, ArC–2, 7) 129.1 (s, 2 × CH, ArC–4, 5) 128.3 (d, $^{3}J_{CP}$ = 4.4 Hz, Cq, ArC–8a) 125.8 (d, $^{2}J_{CP}$ = 10.3 Hz, 2 x Cq, ArC–1, 8) 125.5 (s, 2 × CH, ArC–3, 6) 39.6 (d, $^{1}J_{CP}$ = 38.8 Hz, CH, C–9) 27.4 (d, $^{2}J_{CP}$ = 18.0 Hz, 2 × CH_3, C10); **^{31}P {^{1}H} NMR** (109.3 MHz, $CDCl_3$) δ (ppm) = 24.1 (s); **MS** (EI^+): m/z (%) 278.0 (10) $[M^{\bullet}]^+$, 189 (100) $[C_{10}H_6S_2\text{-}H]^+$; **elemental analysis** calculated (%) for $C_{14}H_{15}PS_2$ (278.3) : C 60.4, H 5.43. Found C 60.55, H 5.35

6.2.3 Synthesis o compound 4.3

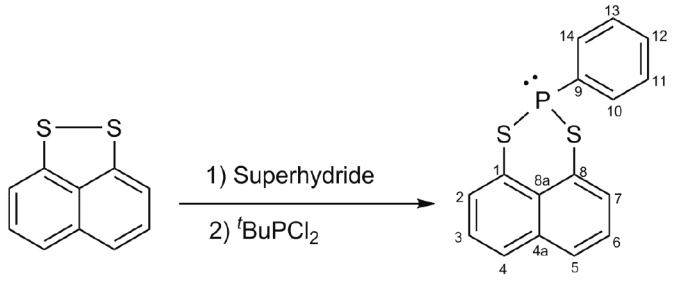

To a solution of naphtho[1,8*cd*]1,2-dithiole (0.5 g, 2.6 mmol) in THF (50 mL) was added dropwise a 1M solution of superhydride in THF (5.2 mL, 5.2 mmol) at 0 °C while stirring. The solution turned from orange to yellow. Quickly afterwards dichlorophenylphosphine (0.4 mL, 2.6 mmol) was added dropwise while stirring at –78 °C with no colour change. The solvent was evaporated leaving a white-yellow solid, which was dissolved in toluene. After filtration, the solvent was removed *in vacuo* and the resulting colourless solid was re-crystallised from toluene resulting in colourless crystals. The compound was further purified by column chromatography on silica gel (hexane/toluene 1:1) to afford the purified target compound as a yellowish solid. (0.6 g, 73%); **mp**: 94 °C; **IR** (KBr

disk) : ν_{max}/cm^{-1} 1544.3 s, 1492.7 s, 1475.0 s, 1429.1 s, 1359.9 s, 1316.1 s, 1192.5 s, 1150.6 s, 1081.8 s, 1024.1 s, 885.9 s, 813.7 vs, 756.1 vs, 741.6 vs, 693.1 s, 533.5 s, 490.7 s, 472.7 s, 400.5 s, 305.9 s; **^{1}H {^{31}P} NMR** (400 MHz, C_6D_6) δ (ppm) = 7.6 (dd, $^{4}J_{HH}$ = 1.3 Hz, $^{3}J_{HH}$ = 7.9 Hz, 2H, H-10, H-14), 7.3 (dd, $^{3}J_{HH}$ = 1.3 Hz, $^{3}J_{HH}$ = 7.3 Hz, 2H, H-2, H-7), 7.1 (dd, $^{4}J_{HH}$ = 1.1 Hz, $^{3}J_{HH}$ = 8.1 Hz, 2H, H-4, H-5), 6.8 (dd, $^{3}J_{HH}$ = 7.3 Hz, $^{3}J_{HH}$ = 7.4 Hz; 2H, H-3, H-6), 6.7 (t, $^{3}J_{HH}$ = 7.4 Hz, 2H, H-11, H-13), 6.6 (m, 1 H, H-12); **^{13}C {^{1}H} NMR** (100.6 MHz, C_6D_6) δ (ppm) = 137.2 (d, $^{1}J_{CP}$ = 39.2 Hz; Cq, C-9), 135.6 (d, $^{3}J_{CP}$ = 3.1 Hz; Cq, C-4a), 131.6 (d, $^{2}J_{CP}$ =18.2 Hz; 2 × CH, C-10, C-14), 131.1 (d, $^{3}J_{CP}$ = 3.0 Hz; 2 × CH, C-2, C-7), 129.9 (s; 2 × CH, C-4, C-5), 128.8 (s; 1 CH, C-12), 128.5 (d, $^{3}J_{CP}$ = 4.5 Hz; 2 × CH, C-13, C-11), 127.6 (Cq, C-8a), 125.4 (s, 2 × CH, C-3, C-6), 125.3 (s, 2 × Cq, C-1, C-8); **^{31}P {^{1}H} NMR** (161.9 MHz, C_6D_6) δ (ppm) = 1.3 (s, 1 P); **MS** (ASAP^{+}) : m/z (%) 299.01 (40) $[M+H]^{+}$; **elemental analysis** calculated (%) for $C_{16}H_{11}PS_2$ (298.36) : C 64.41, H 3.72. found : C 64.57, H 3.63.

6.2.4 Synthesis of compound 4.4

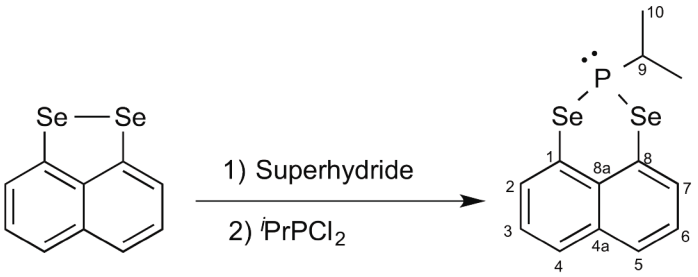

To a solution of naphtho[1,8-cd]1,2-diselenole (2.0 g, 12.6 mmol) in THF (60 mL) was added dropwise a 1 M solution of superhydride in THF (25.3 mL, 25.3 mmol). The mixture was stirred at room temperature for 15 min, after which a solution of dicholoro*iso*propylphosphine (2.0 mL, 16.4 mmol) in THF (10 mL) was added dropwise to the mixture. The resulting

mixture was warmed to ~66 °C and left overnight. After the solvent was removed *in vacuo*, the reaction mixture was extracted with hexane (250 mL), washed with distilled water (100 mL) and the organic layer dried with magnesium sulfate and concentrated under reduced pressure. Column chromatography on silica gel (hexane) was performed to afford the purified target compound as a brown-light solid. Crystals suitable for X-ray diffraction were grown in hexane. (2.0 g, 45%); **mp** 83-91 °C; **IR** (KBr disk) : ν_{max} cm^{-1} : 3422w, 2959w, 2854w, 1539w, 1487w, 1352w, 1191s, 1019w, 806vs, 750vs, 636w, 427s, 279w, 251s, 223s; **^{1}H {^{31}P} NMR** (400 MHz, $CDCl_3$) δ (ppm) = 7.6 (m, 4H, ArH–2, 7, 4, 5) 7.2 (dd, $^{3}J_{HH}$ = 7.1 Hz, $^{3}J_{HH}$ = 7.2 Hz, 2H, ArH–3, 6) 1.8 (m, 1H, CH, H–9) 1.0 (d, J = 7.0 Hz , 2 × CH_3, 6H, H–10); **^{13}C {^{1}H} NMR** (100.6 MHz, $CDCl_3$) δ (ppm) = 135.1 (d, $^{4}J_{CP}$ = 3 Hz, Cq, ArC–4a) 133.0 (d, $^{3}J_{CP}$ = 4.0 Hz, 2 × CH, ArC–2, 7) 130.6 (s, 2 × CH, ArC–4, 5) 129.5 (d, $^{3}J_{CP}$ = 3.6 Hz, Cq, ArC–8a) 125.5 (s, 2 × CH, ArC–3, 6) 123.3 (d, $^{2}J_{CP}$ = 8.7 Hz, 2 x Cq, ArC–1, 8) 30.2 (d, $^{1}J_{CP}$ = 35.3 Hz, CH, C9) 19.3 (d, $^{2}J_{CP}$ = 21.9 Hz, 2 × CH_3, C10); **^{31}P {^{1}H} NMR** (109.3 MHz, $CDCl_3$) δ (ppm) = –3.4 (s, ^{1}J (^{31}P, ^{77}Se) = 276 Hz); **^{77}Se {^{1}H} NMR** (51.52 MHz, $CDCl_3$) δ (ppm) = 270.2 (s,^{1}J (^{31}P, ^{77}Se) = 276 Hz); **MS** (EI^+): m/z (%) 359.9 (12) $[M+H]^+$, 285.8 (100) $[C_{10}H_6Se_2^{\bullet}]^+$, 236.9 (82) $[C_{10}H_6SeP^{\bullet}]^+$, 205.9 (32) $[C_{10}H_6Se^{\bullet}]^+$, 126.0 (48) $[C_{10}H_6{}^{\bullet}]^+$; **elemental analysis** calculated (%) for $C_{13}H_{13}PSe_2$ (358.14) : C 43.60, H 3.66. Found C 43.68, H 3.74.

6.2.5. Synthesis of compound 4.5

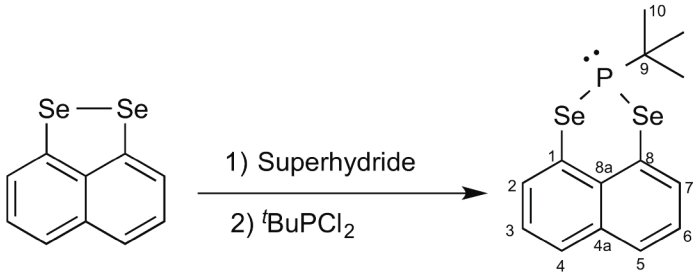

To a solution of naphtho[1,8-cd]1,2-diselenole (2.0 g, 12.0 mmol) in THF (80 mL) was added dropwise a 1 M solution of superhydride in THF (24.0 mL, 24.0 mmol). The mixture was stirred at room temperature for 15 min after which a solution of *tert*butyldichlorophosphine (2.6 g, 16.4 mmol) in THF (15 mL) was added dropwise to the mixture. The resulting mixture was warmed to ~66 °C and left overnight. After the solvent was removed *in vacuo*, the reaction mixture was extracted with hexane (250 mL), washed with distilled water (100 mL) and the organic layer dried with magnesium sulfate and concentrated under reduced pressure. The residue was passed through a shallow plug of dry silica and washed through with hexane to afford the purified target compound as a brown-purple solid. Crystals suitable for X-ray diffraction were grown in hexane. (2.3 g, 48%); **mp** 85-88 °C; **IR** (KBr disk) : υ_{max} cm^{-1} : 2933s, 2852w, 2363s, 1655w, 1540s, 1455s, 1350s, 1192s, 804vs, 752vs, 565s, 439w, 420s; **^{1}H {^{31}P} NMR** (400 MHz; $CDCl_3$)) δ (ppm) = 7.8 (dd, $^{3}J_{HH}$ = 7.2 Hz, $^{4}J_{HH}$ = 1.3 Hz, 2H, ArH–2, 7), 7.7 (dd, $^{3}J_{HH}$ = 8.3 Hz, $^{4}J_{HH}$ = 1.2 Hz, 2H, ArH–4, 5), 7.3 (dd, $^{3}J_{HH}$ = 8.0 Hz, $^{3}J_{HH}$ = 7.3 Hz, 2H, ArH–3, 6), 1.2 (s, 9H, H10, 3 × CH_3); **^{13}C {^{1}H} NMR** (100.6 MHz; $CDCl_3$) δ (ppm): 134.9 (d, $^{4}J_{CP}$ = 3.2 Hz, Cq, ArC–4a), 131.4 (d, $^{3}J_{CP}$ = 4.5 Hz, 2 × CH, ArC–2, 7), 130.2 (s, 2 × CH, Ar–C–4, 5), 125.5 (s, 2 × CH, Ar–C–3, 6), 124.8 (d, $^{2}J_{CP}$ = 10.6 Hz, 2 x Cq, Ar–C–1, 8), 38.4 (d, $^{1}J_{CP}$ = 44.3 Hz, Cq, C9) 27.7 (d, $^{2}J_{CP}$ = 18.3 Hz, 3 × CH_3, C10); **^{31}P {^{1}H} NMR** (109.4 MHz $CDCl_3$) δ (ppm)= 12.3 (t, ^{1}J (^{31}P,^{77}Se) = 302 Hz); **^{77}Se {^{1}H} NMR** (51.5 MHz, $CDCl_3$) δ

(ppm)= 210.2 (d, ^{1}J (^{31}P,^{77}Se) = 302 Hz); **MS** (EI^{+}): m/z (%) 373.9 (15) $[M+H]^{+}$, 285.9 (85) $[C_{10}H_6Se_2^{\bullet}]^{+}$, 236.9 (100) $[C_{10}H_6SeP^{\bullet}]^{+}$, 205.6 (23) $[C_{10}H_6Se^{\bullet}]^{+}$, 126.0 (30) $[C_{10}H_6^{\bullet}]^{+}$, **elemental analysis** calculated (%) for $C_{14}H_{15}PSe_2$ (372.16) : C 45.18, H 4.06. Found C 45.29, H 4.15.

6.2.5. Synthesis of compound 4.6

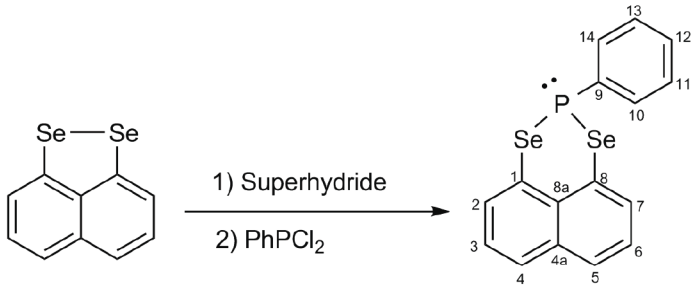

To a solution of naphtho[1,8-*cd*]-1,2-diselenole (0.5 g, 1.8 mmol) in THF (50 mL) was added dropwise a 1M solution of superhydride in THF (3.5 mL, 3.5 mmol) at room temperature while stirring. The solution turned from purple to yellow. Afterwards dichlorophenylphosphine (0.2 mL, 1.8 mmol) was added dropwise while stirring at –10 °C. The reaction was slowly warmed up to room temperature changing the colour over orange to red. The solvent was evaporated leaving a brown-red solid. The residue was dissolved in toluene (50 mL) and after filtration the solvent was removed *in vacuo* and re-crystallised from DCM/hexane (0.2 g, 28%); **mp** = 71°C; **IR** (KBr): ν_{max} (cm^{-1}) = 3423 (w), 3043 (vw), 1539 (s), 1479 (s), 1430 (s), 1317 (m), 1195 (s), 1078 (m), 853 (w), 812 (s), 794 (s), 755 (vs), 742 (s), 693 (s), 485 (m), 423 (m), 411 (s), 358 (w); **$^{1}H\{^{31}P\}$ NMR** (400.1 MHz, C_6D_6): δ (ppm) = 7.6 (m, $^{3}J_{HH}$ = 8.3 Hz, $^{4}J_{HH}$ = 1.3 Hz; 2 H, H-10, H-14), 7.5 (dd, $^{3}J_{HH}$ = 7.2 Hz, $^{4}J_{HH}$ = 1.3 Hz; 2 H, H-2, H-7), 7.2 (dd, $^{3}J_{HH}$ = 8.3 Hz, $^{4}J_{HH}$ = 1.2 Hz; 2 H, H-4, H-5), 6.7 (t, $^{3}J_{HH}$ = 7.4 Hz; 2 H, H-3, H-6), 6.7 (m, $^{3}J_{HH}$ = 7.3 Hz, $^{4}J_{HH}$ = 1.6 Hz; 2 H, H-11, H-13), 6.6 (t, $^{3}J_{HH}$ = 7.4 Hz, $^{4}J_{HH}$ = 1.2 Hz; 1 H, H-12); **^{13}C NMR** (100.6 MHz, C_6D_6): δ (ppm) = 138.0 (d, $^{3}J_{CP}$ = 48.6 Hz;

C-9), 135.5 (d, $^{3}J_{CP}$ = 3.3 Hz; C-8a), 133.1 (d, $^{3}J_{CP}$ = 3.9 Hz; C-2, C-7), 132.3 (d, $^{2}J_{CP}$ = 19.1 Hz; C-10, C-14), 130.8 (s; C-4, C-5), 129.9 (s; C-4a), 128.6 (d, $^{3}J_{CP}$ = 17.2 Hz; C-11, C-13), 128.4 (d, $^{4}J_{CP}$ = 8.7 Hz; C-12), 125.4 (s; C-3, C-6), 124.7 (d, $^{2}J_{CP}$ = 10.0 Hz; C-1, C-8); **^{31}P{^{1}H} NMR** (162.0 MHz, C_6D_6): δ (ppm) = –13.6 (s, ^{1}J = 288.4 Hz); **^{77}Se NMR** (270.1 MHz, $CDCl_3$): δ (ppm) = 315.4 (d, ^{1}J = 287.1 Hz); **MS** (APCI^{+}): *m*/*z* = 285.8799 (100) [$C_{10}H_6Se_2$+H], 394.9003 (5) [M+2H]$^{+}$; **elemental analysis** for $C_{16}H_{11}PSe_2$(392.15) calculated (%): C 49.00, H 2.83, found (%): C 49.20, H 2.87;.

6.3 Experimental procedures of Chapter 5

6.3.1 Synthesis of compound 5.1

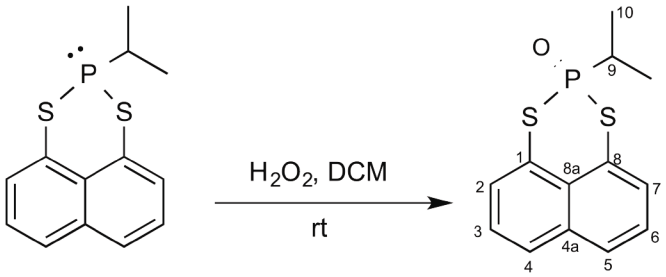

To solution of naphtho[1,8-cd]1,2-dithiole isopropylphosphine (**4.1**) (0.1 g, 0.4 mmol) in dichloromethane (40 mL) was added hydrogen peroxide (30% in water) (0.2 mL, 2.0 mmol) and the stirring continue for 5 h. Removal of the volatiles afforded a pale yellow solid. Crystals suitable for X-ray diffraction were grown by layering a hexane solution of **5.1** with dichloromethane (0.1 g, 93%); **mp** 114–118 °C; **IR (KBr disk)** : ν_{max} cm^{-1} : 2966w, 2362w, 1546w, 1460w, 1365w, 1213vs, 1035s, 877s, 820vs, 758vs, 667s, 571vs, 554vs, 535s; **^{1}H {^{31}P} NMR** (300 MHz; $CDCl_3$) δ (ppm) = 7.8 (dd, $^{3}J_{HH}$ = 8.3 Hz, $^{4}J_{HH}$ =1.2 Hz, 2H, ArH–4, 5), 7.6 (dd, $^{3}J_{HH}$ = 7.3 Hz, $^{4}J_{HH}$ =1.2 Hz, 2H, ArH–2, 7), 7.4 (dd, $^{3}J_{HH}$ = 7.5 Hz, $^{3}J_{HH}$ = 7.4 Hz, 2H, ArH–3, 6), 2.3 (m, 1H, CH, H9), 1.4 (d, $^{3}J_{HH}$ = 7.2 Hz, 6H, 2 x CH_3, H10); **^{13}C {^{1}H} NMR** (75.4 MHz; $CDCl_3$) δ (ppm): 136.2 (s, Cq, ArC–4a), 132.3 (d, $^{3}J_{CP}$ = 8.3 Hz, 2

x CH, ArC–2, 7), 130.1 (s, 2 x CH, ArC–4, 5), 127.0 (d, $^{3}J_{CP}$ = 6.6 Hz, Cq, ArC–8a), 126.7 (d, $^{2}J_{CP}$ = 3.5 Hz, 2 x Cq, ArC–1, 8), 126.4 (s, 2 x CH, ArC–3, 6), 34.8 (d, $^{1}J_{CP}$ = 70 Hz, CH, C9), 15.5 (d, $^{2}J_{CP}$ = 3.4 Hz, 2 x CH_3, C10); **^{31}P {^{1}H} NMR** (109.3 MHz, $CDCl_3$) δ (ppm)= 52.0 (s); **MS (APCI^{+}):** m/z (%) 281.0223 (56) $[M+H]^{+}$, 220.9647 (100) $[C_{10}H_6PS_2]$, 189.9909 (67) $[C_{10}H_6PS]^{+}$; **Elemental analysis** calculated (%) for $C_{13}H_{13}OPS_2$ (280.34) : C 55.7, H 4.7. Found C 55.5, H 4.7.

6.3.2 Synthesis of compound 5.2

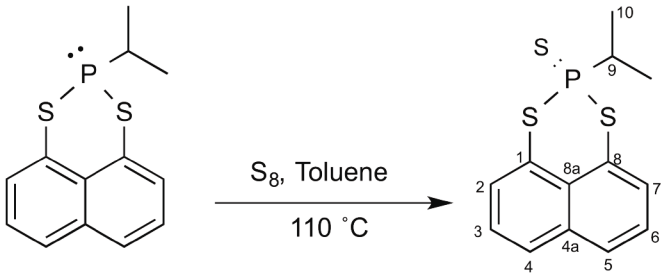

A solution of naphtho[1,8-cd]1,2-dithiole isopropylphosphine (**4.1**) (0.15 g, 0.56 mmol) and sulfur flowers (0.07 gr, 2.34 mmol) in toluene (50 mL) was heated at 110 ˚C for 48 h. The resulting solution was allowed to cool to room temperature, after removal of the volatiles column chromatography on silica gel hexane/DCM 1:1 was performed to afford a pale pink solid. Crystals suitable for X-ray diffraction were grown in diethyl ether (0.1 g, 56%); **mp** 175–177 °C; **IR (KBr disk)** : ν_{max} cm^{-1} : 2965w, 2922w, 2862w, 1546s, 1494w, 1447w, 1361w, 1326w, 1262s, 1200s, 1092vs, 1031vs, 878w, 817vs, 757vs, 715vs, 614vs, 566s, 483w; **^{1}H {^{31}P} NMR** (300 MHz; $CDCl_3$) δ (ppm) = 7.8 (dd, $^{3}J_{HH}$ = 8.2 Hz, $^{4}J_{HH}$ =1.1 Hz, 2H, ArH–4, 5), 7.6 (dd, $^{3}J_{HH}$ = 7.3 Hz, $^{4}J_{HH}$ =1.2 Hz, 2H, ArH–2, 7), 7.4 (t, $^{3}J_{HH}$ = 8.0 Hz, 2H, ArH–3, 6), 2.3 (m, 1H, CH, H9), 1.4 (s, 6H, 2 x CH_3, H10); **^{13}C {^{1}H} NMR** (75.4 MHz; $CDCl_3$) δ (ppm): 136.1 (s, Cq, ArC–4a), 131.2 (d, $^{3}J_{CP}$ = 7.9 Hz, 2 x CH, ArC–2, 7), 130.5 (s, 2 x CH, ArC–4, 5), 128.1 (d, $^{2}J_{CP}$ = 4.8 Hz, 2 x Cq, ArC–1, 8), 126.5

(s, 2 x CH, ArH–3, 6), 35.6 (d, $^{1}J_{CP}$ = 47.8 Hz, CH, C9), 15.5 (s, 2 x CH_3, C10); **^{31}P {^{1}H} NMR** (109.3 MHz, $CDCl_3$) δ (ppm)= 67.2 (s); **MS (APCI^{+}):** m/z (%) 296.9992 (100) $[M+H]^{+}$.

6.3.3 Synthesis of compound 5.3

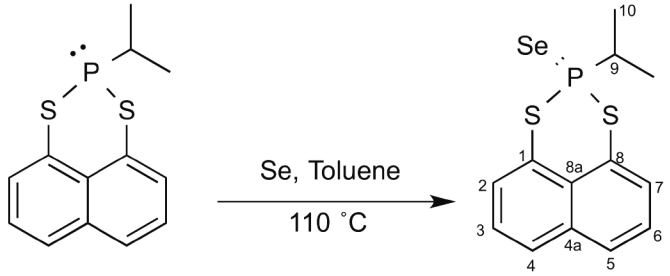

A solution of naphtho[1,8-cd]1,2-dithiole isopropylphosphine (**4.1**) (0.1 g, 0.6 mmol) and elemental selenium (0.1 gr, 0.7 mmol) in toluene (50 mL) was heated at 110 ˚C and left overnight. The resulting solution was allowed to cool to room temperature and was filtered through a silica plug with hexane (250 mL) and dichloromethane (250 mL). Removal of the volatiles afforded a pink solid. Crystals suitable for X-ray diffraction were grown by layering a hexane solution of **5.3** with in dichloromethane (0.2 g, 93%); **mp** 191-197 °C; **IR** (KBr disk) : ν_{max} cm^{-1} : 2964s, 2922w, 1949w, 1546w, 1493w, 1443w, 1360w, 1261vs, 1202s, 1094vs, 1030vs, 877w, 814vs, 819.1vs, 751s, 664s, 564vs, 428w; **^{1}H {^{31}P} NMR** (300 MHz; $CDCl_3$) δ (ppm) = 7.8 (dd, $^{3}J_{HH}$ = 8.2 Hz, $^{4}J_{HH}$ =1.1 Hz, 2H, ArH–4, 5), 7.6 (dd, $^{3}J_{HH}$ = 7.3 Hz, $^{4}J_{HH}$ =1.2 Hz, 2H, ArH–2, 7), 7.4 (dd, $^{3}J_{HH}$ = 8.0 Hz, $^{3}J_{HH}$ = 7.5 Hz, 2H, ArH–3, 6), 2.4 (m, 1H, H9), 1.2 (d, $^{3}J_{HH}$ = 6.9 Hz, 6H, 2 x CH_3, H10); **^{13}C {^{1}H} NMR** (75.4 MHz; $CDCl_3$) δ (ppm): 136.1 (s, Cq, ArC–4a), 130.8 (d, $^{3}J_{CP}$ = 7.0 Hz, 2 x CH, ArC–2, 7), 130.5 (s, 2 x CH, ArC–4, 5), 127.8 (d, $^{2}J_{CP}$ = 5.5 Hz, 2 x Cq, ArC–1, 8), 126.5 (s, 2 x CH, ArH–3, 6), 126.3 (d, $^{3}J_{CP}$ = 7.0 Hz, Cq, ArC–8a), 35.2 (d, $^{1}J_{CP}$ = 37.0 Hz, CH, C9), 16.0 (s, 2 x CH_3, C10); **^{31}P {^{1}H} NMR** (109.3 MHz, $CDCl_3$) δ (ppm)= 51.6 (s, ^{1}J (^{31}P,^{77}Se) = 797 Hz); **^{77}Se {^{1}H} NMR** (51.5

MHz, $CDCl_3$) δ (ppm)= –310.6 (d, ^1J (^{31}P,^{77}Se) = 797 Hz); **MS (APCI$^+$):** m/z (%) 343.9350 (3) $[M]^+$, 220.9641 (100) $[C_{10}H_6S_2P]^+$, 189.9904 (82) $[C_{10}H_6S_2]^+$; e**lemental analysis** calculated (%) for $C_{13}H_{13}SePS_2$ (343.3) : C 45.5, H 3.8. Found C 45.4, H 3.9.

6.3.4 Synthesis of compound 5.4

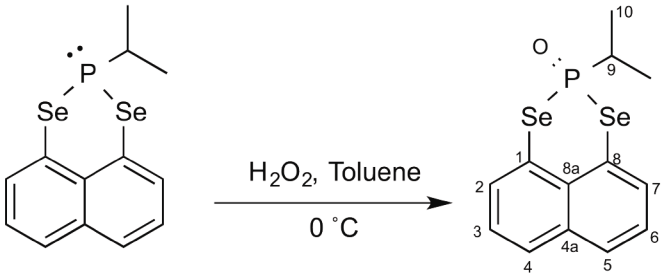

To a solution of naphtho[1,8-cd]1,2-diselenole isopropylphosphine (**4.4**) (0.2 g, 0.7 mmol) in toluene (80 mL) in an ice bath, H_2O_2 (30% solution in water) (0.8 mL, 8.4 mmol) was added dropwise (60 μL per 20 min). Stirring was continued until complete consumption of the starting material, monitored by ^{31}P NMR. The reaction mixture was washed with water (100 mL), and the organic layer dried with magnesium sulfate and concentrated under reduced pressure. Crystals suitable for X-ray diffraction were grown by layering a dichloromethane solution of **5.4** with in hexane. (0.1 g, 60%); **mp** 79-82 °C; **IR** (KBr disk) : ν_{max} cm^{-1} : 3433.6 s, 2964s, 1639.5s, 1538.8s, 1460.5s, 1349.6s, 1261.6vs, 1195.6vs, 1096.5vs, 1028.6vs, 874s, 798.3vs, 754.5vs, 653.7s, 498vs, 383.9s, 340.4s, 309.2s, 294.8s, 260.2vs; **^{1}H {^{31}P} NMR** (400 MHz; $CDCl_3$) δ (ppm) = 7.8 (dd, $^3J_{HH}$ = 8.3 Hz, $^4J_{HH}$ = 1.3 Hz, 2H, ArH– 4, 5), 7.7 (dd, $^3J_{HH}$ = 7.3 Hz, $^4J_{HH}$ =1.3 Hz, 2H, ArH– 2, 7), 7.3 (dd, $^3J_{HH}$ = 8.2 Hz, $^3J_{HH}$ = 7.3 Hz, 2H, ArH– 3, 6), 2.37 (m, CH, H9), 1.4 (d, $^3J_{HH}$ = 7.2 Hz, 3x CH_3, H10); **^{13}C {^{1}H} NMR** (100.6 MHz; $CDCl_3$) δ (ppm): 136.5 (s, Cq, ArC–4a), 134.3 (d, $^3J_{CP}$ = 7.7 Hz, 2 x CH, ArC–2, 7), 131.0 (s, 2 x CH, ArC–4, 5), 128.6 (d, $^2J_{CP}$ = 3.1 Hz, 2 x Cq, ArC–1, 8), 126.4

(s, 2 x CH, ArH–3, 6), 38.9 (d, $^{1}J_{CP}$ = 52.9 Hz, CH, C9), 16.1 (s, 3 x CH_3, C10); **^{31}P {^{1}H} NMR** (109.3 MHz, $CDCl_3$) δ (ppm)= 40.4 (s, ^{1}J (^{31}P,^{77}Se) = 398.4 Hz); **^{77}Se {^{1}H} NMR** (51.5 MHz, $CDCl_3$) δ (ppm)= 403.8 (d, ^{1}J (^{31}P,^{77}Se) = 396.6 Hz));**MS** (APCI^{+}): m/z (%) 376.9107 (100) $[M+2H]^{+}$, 286.8873 (67) $[C_{10}H_6Se_2+H]^{+}$; **elemental analysis** calculated (%) for $C_{13}H_{13}OPSe_2$ (374.1) : C 41.7, H 3.5. Found C 41.6, H 3.4.

6.3.5 Synthesis of compound 5.5

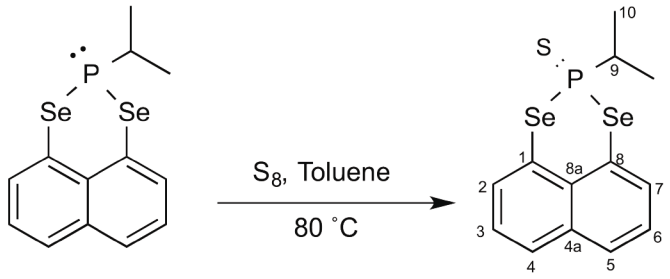

A solution of naphtho[1,8-cd]1,2-diselenole isopropylphosphine (**4.4**) (0.4 g, 1.0 mmol) and elemental sulfur (0.03 gr, 1.0 mmol) in toluene (30 mL) was heated at 80 ˚C for several hours. The resulting solution was allowed to cool to room temperature and after the solvent was removed in vacuo. Column chromatography on silica gel hexane/DCM 4:1 was performed to afford the purified target compound as a purple-orange solid. Crystals suitable for X-ray diffraction were grown by layering a dichloromethane solution of **5.5** with in methanol. (0.2 g, 61%); **mp** 147-150 °C; **IR** (KBr disk) : ν_{max} cm^{-1} : 3424w, 2921w, 1655w, 1539s, 1488w, 1441w, 1357s, 1315w, 1192s, 1032s, 816vs, 753s, 700vs, 590vs, 482s, 384w; **^{1}H {^{31}P} NMR** (400 MHz; $CDCl_3$) δ (ppm) = 7.8 (dd, $^{3}J_{HH}$ = 8.3 Hz, $^{4}J_{HH}$ = 1.2 Hz, 2H, ArH-4, 5), 7.8 (dd, $^{3}J_{HH}$ = 7.3 Hz, $^{4}J_{HH}$ = 1.3 Hz, 2H, ArH-2, 7), 7.4 (dd, $^{3}J_{HH}$ = 8.1 Hz, $^{3}J_{HH}$ = 7.2 Hz, 2H, ArH-3, 6), 2.4 (m, 1H, CH, H9), 1.3 (m, 6H, 2x CH_3, H10); **^{13}C {^{1}H} NMR** (100.6 MHz; $CDCl_3$) δ (ppm): 136.3 (s, Cq, ArC-4a), 132.9 (d, $^{3}J_{CP}$ = 6.9 Hz, 2 x CH, ArC-2, 7), 131.2 (s, 2 x CH, ArC-4, 5), 128.3 (d, $^{2}J_{CP}$ = 5.5

Hz, 2 x Cq, ArC-1, 8), 128.0 (d, $^{3}J_{CP}$ = 3.5 Hz, 2 x Cq, ArC-8a), 126.3 (s, 2 x CH. ArC-3, 6) 39.1 (d, $^{1}J_{CP}$ = 35.1 Hz, P-CH, C9) 15.8 (s, 2x CH_3, C10); **^{31}P {^{1}H} NMR** (109.3 MHz, $CDCl_3$) δ (ppm)= 43.3 (s, ^{1}J (^{31}P,^{77}Se) = 385 Hz); **^{77}Se {^{1}H} NMR** (51.5 MHz, $CDCl_3$) δ (ppm)= 438.7 (d, ^{1}J (^{31}P,^{77}Se) = 385 Hz); **MS** (EI^+): m/z (%) 391.9 (15) $[M+H]^+$, 285.8 (100) $[C_{10}H_6Se_2]^+$, 237.9 (33) $[C_{10}H_6SeP^{\bullet}]^+$, 205.9 (33) $[C_{10}H_6Se^{\bullet}]^+$, 126.0 (32) $[C_{10}H_6{}^{\bullet}]^+$; **elemental analysis** calculated (%) for $C_{13}H_{13}SPSe_2$ (390.20) : C 40.02, H 3.36 Found C 40.14, H 3.31.

6.3.6 Synthesis of compound 5.6

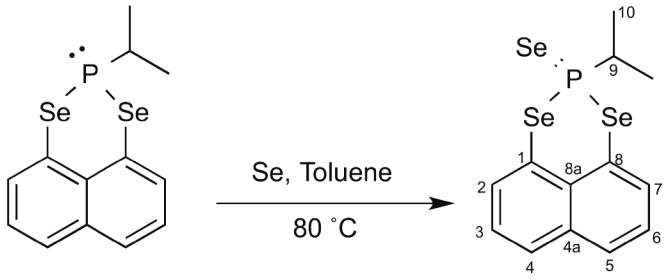

A solution of naphtho[1,8-cd]1,2-diselenole isopropylphosphine (**4.4**) (0.5 g, 1.4 mmol) and elemental selenium (0.1 gr, 1.7 mmol) in toluene (30 mL) was heated to 80 ˚C and left overnight. The resulting solution was allowed to cool to room temperature and after the solvent was removed *in vacuo*. Column chromatography on silica gel hexane/DCM 4:1 was performed to afford the purified target compound as an orange-pink solid. Crystals suitable for X-ray diffraction were grown by layering a dichloromethane solution of **5.6** with in methanol (0.6 g, 77%); **mp** 150-153 °C; **IR** (KBr disk) : ν_{max} cm^{-1} : 3450w, 2962w, 2858w, 1539s, 1487w, 1438s, 1355s, 1312w, 1237w, 1191s, 1135w, 1084w, 1027s, 871w, 845w, 812vs, 750vs, 686w, 648vs, 515vs, 475vs, 424w, 374w; **^{1}H {^{31}P} NMR** (400 MHz; $CDCl_3$) δ (ppm) = 7.9 (dd, $^{3}J_{HH}$ = 8.3 Hz, $^{4}J_{HH}$ = 1.2 Hz, 2H, ArH-4, 5), 7.8 (dd, $^{3}J_{HH}$ = 7.3 Hz, $^{4}J_{HH}$ = 1.3 Hz, 2H, ArH-2, 7), 7.4 (dd, $^{3}J_{HH}$ = 8.1 Hz, $^{3}J_{HH}$ = 7.3 Hz, 2H, ArH-3,

6), 2.5 (m, 1H,CH, H9), 1.2 (d, $^{3}J_{HH}$ = 6.9 Hz, 6H, 2x CH_3, H10); **^{13}C {^{1}H} NMR** (100.6 MHz; $CDCl_3$) δ (ppm): 136.3 (s, Cq, ArC-4a), 132.5 (d, $^{3}J_{CP}$ = 6.2 Hz, 2x CH, ArC-2, 7), 131.3 (s, 2x CH, ArC-4, 5), 128.3 (d, $^{2}J_{CP}$ = 6.1 Hz, 2 x Cq, ArC-1, 8), 127.9 (d, $^{3}J_{CP}$ = 3.7 Hz, 2 x Cq, ArC-8a), 126.3 (s, 2x CH, ArC-3, 6), 38.2 (d, $^{1}J_{CP}$ = 26.3 Hz, P-CH, C9) 16.3 (s, 2x CH_3, C10); **^{31}P {^{1}H} NMR** (109.3 MHz, $CDCl_3$) δ (ppm)= 22.0 (s, ^{1}J (^{31}P,^{77}Se) = 391 Hz, ^{1}J (^{31}P,^{77}Se) = 773 Hz); **^{77}Se {^{1}H} NMR** (51.5 MHz, $CDCl_3$); δ (ppm)= 439.2 (d, ^{1}J (^{31}P,^{77}Se) = 391 Hz), -260 (d, ^{1}J (^{31}P,^{77}Se) = 773 Hz); **MS** (APCI^{+}): m/z (%) 438.8339 (53) $[M+H]^{+}$, 360.9161 (38) $[C_{13}H_{13}PSe_2]^{+}$; **elemental analysis** calculated (%) for $C_{13}H_{13}PSe_3$ (437.1) : C 35.7, H 3.0. Found C 35.7, H 2.9.

6.3.7 Synthesis of compound 5.7

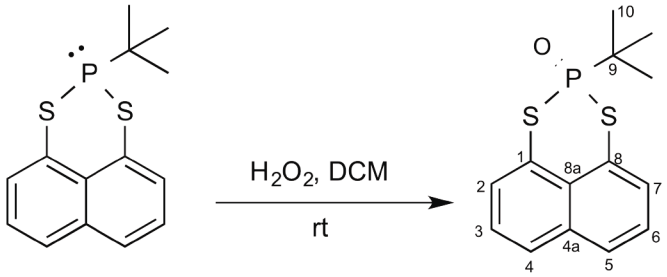

To a solution of naphtho[1,8-cd]1,2-dithiole tertbutylphosphine (**4.2**) (0.3 g, 1.0 mmol) in dichloromethane (50 mL) was added hydrogen peroxide (30% in water) (0.1 mL, 9.8 M). The mixture was stirred overnight giving a yellowish solution. Removal of the volatiles afforded a pale yellow solid. Crystals suitable for X-ray diffraction were grown by layering a hexane solution of **5.7** with in dichloromethane. (0.3 g, 93%); **mp** 230–236 °C (decomp); **IR** (KBr disk) : ν_{max} cm^{-1}: 2962w, 2926w, 2857w, 2361w, 1546w, 1457w, 1362w, 1262w, 1206vs, 1185vs, 1146s, 883w, 822vs, 761vs, 624vs, 572vs, 510s, 488w, 406w; **^{1}H {^{31}P} NMR** (300 MHz; $CDCl_3$) δ (ppm) = 7.7 (dd, $^{3}J_{HH}$ = 8.3 Hz, $^{4}J_{HH}$ =1.1 Hz, 2H, ArH–4, 5), 7.6 (dd, $^{3}J_{HH}$ = 7.3 Hz, $^{4}J_{HH}$ =1.2 Hz, 2H, ArH–2, 7), 7.4 (t, $^{3}J_{HH}$ = 7.4 Hz, 2H, ArH–3, 6), 1.4 (s, 9H, 3 x

CH_3, H10); **^{13}C {^{1}H} NMR** (75.4 MHz; $CDCl_3$) δ (ppm): 136.1 (s, Cq, ArC–4a), 132.5 (d, $^3J_{CP}$ = 7.0 Hz, 2 x CH, ArC–2, 7), 130.0 (s, 2 x CH, ArC–4, 5), 127.1 (d, $^3J_{CP}$ = 6.3 Hz, Cq, ArC–8a), 126.3 (s, 2 x CH, ArH–3, 6), 125.6 (d, $^2J_{CP}$ = 4.1 Hz, Cq, ArC–1, 8), 40.5 (d, $^1J_{CP}$ = 67.6 Hz, Cq, C9), 24.8 (s, 3 x CH_3, C10); **^{31}P {^{1}H} NMR** (109.3 MHz, $CDCl_3$) δ (ppm)= 51.7 (s); **MS (APCI$^+$):** m/z (%) 295.0375 (100) $[M+H]^+$.

6.3.8 Synthesis of compound 5.8

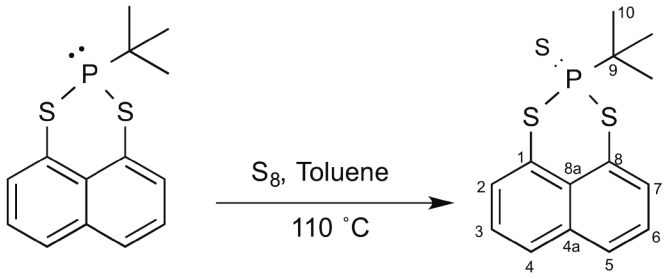

Compound **5.8** was prepared following the procedure described previously for compound **5.2** with naphtho[1,8-cd]1,2-dithiole tertbutylphosphine (**4.2**) (0.27 g, 0.97 mmol) and sulfur flowers (0.04 gr, 1.16 mmol) heated at 90 ˚C for 72 h. A pinkish-orange solid was afforded. Crystals suitable for X-ray diffraction were grown by layering a hexane solution of **5.8** with in dichloromethane (0.13 g, 43%); **mp** 198–203 °C; **IR** (KBr disk) : ν_{max} cm^{-1} : 2957s, 2922w, 2859s, 1550w, 1495w, 1470w, 1456w, 1365w, 1324w, 1261w, 1203s, 1094br, 1015w, 883w, 813vs, 755vs, 689vs, 601vs, 551vs, 472w; **^{1}H {^{31}P} NMR** (300 MHz; $CDCl_3$) δ (ppm) = 7.8 (dd, $^3J_{HH}$ = 8.2 Hz, $^4J_{HH}$ =1.1 Hz, 2H, ArH–4, 5), 7.6 (dd, $^3J_{HH}$ = 7.3 Hz, $^4J_{HH}$ =1.2 Hz, 2H, ArH–2, 7), 7.4 (t, $^3J_{HH}$ = 8.0 Hz, 2H, ArH–3, 6), 1.4 (s, 9H, 3 x CH_3, H10); **^{13}C {^{1}H} NMR** (75.4 MHz; $CDCl_3$) δ (ppm): 134.8 (s, Cq, ArC–4a), 130.0 (d, $^3J_{CP}$ = 7.3 Hz, 2 x CH, ArC–2, 7), 129.2 (s, 2 x CH, ArC–4, 5), 127.05 (d, $^2J_{CP}$ = 4.9 Hz, 2 x Cq, ArC–1, 8), 125.3 (d, $^3J_{CP}$ = 6.8 Hz, 2 x Cq, ArC–8a), 125.1 (s, 2 x CH, ArC–3, 6), 44.8 (d, $^1J_{CP}$ = 44.1 Hz, Cq, C9), 24.2 (d, $^2J_{CP}$ = 2.0 Hz, 3 x

CH_3, C10); **^{31}P {^{1}H} NMR** (109.3 MHz, $CDCl_3$) δ (ppm)= 70.2 (s); **MS** (APCI$^+$): m/z (%) 311.0145 (100) $[M+H]^+$, 279.0425 (48) $[C_{14}H_{15}PS_2]^+$; **elemental analysis** calculated (%) for $C_{14}H_{15}PS_3$ (310.43) : C 54.2.1, H 4.9. Found C 53.8, H 5.0.

6.3.9 Synthesis of compound 5.9

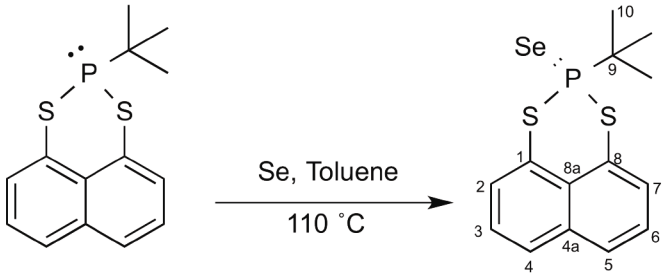

Compound **5.9** was prepared following the procedure described previously for compound **5.3**, with naphtho[1,8-cd]1,2-dithiole tertbutylphosphine (**4.2**) (0.3 g, 1.0 mmol) and elemental selenium (0.1 gr, 1.1 mmol) yielding a white solid. Crystals suitable for X-ray diffraction were grown by layering a hexane solution of **5.9** with in dichloromethane (0.3 g, 97%); **mp** 203–206 °C; **IR** (KBr disk) : ν_{max} cm^{-1} : 2964s, 2921w, 1548w, 1494w, 1469w, 1454s, 1364w, 1261vs, 1202s, 1170w, 1094vs, 1016vs, 882w, 812vs, 754s, 614s, 578vs, 548vs, 445w; **^{1}H {^{31}P} NMR** (300 MHz; $CDCl_3$) δ (ppm) = 7.8 (dd, $^3J_{HH}$ = 8.0 Hz, $^4J_{HH}$ =1.0 Hz, 2H, ArH–4, 5), 7.6 (dd, $^3J_{HH}$ = 7.3 Hz, $^4J_{HH}$ =1.0 Hz, 2H, ArH–2, 7), 7.4 (t, $^3J_{HH}$ = 7.8 Hz, 2H, ArH–3, 6), 1.4 (s, 9H, 3 x CH_3, H10); **^{13}C {^{1}H} NMR** (75.4 MHz; $CDCl_3$) δ (ppm): 135.9 (s, Cq, ArC–4a), 130.6 (d, $^3J_{CP}$ = 6.8 Hz, 2 x CH, ArC–2, 7), 130.4 (s, 2 x CH, ArC–4, 5), 128.3 (d, $^2J_{CP}$ = 5.5 Hz, 2 x Cq, ArC–1, 8), 126.3 (s, 2 x CH, ArH–3, 6), 126.0 (d, $^3J_{CP}$ = 6.8 Hz, Cq, ArC–8a), 46.3 (d, $^1J_{CP}$ = 33.0 Hz, Cq, C9), 25.6 (d, $^2J_{CP}$ = 2.7 Hz, 3 x CH_3, C10); **^{31}P {^{1}H} NMR** (109.3 MHz, $CDCl_3$) δ (ppm)= 53.8 (s, ^{1}J (^{31}P,^{77}Se) = 794 Hz); **^{77}Se {^{1}H} NMR** (51.5 MHz, $CDCl_3$) δ (ppm)= –

1520.5 (d, ^{1}J (^{31}P,^{77}Se) = 794 Hz); **MS** (APCI^{+}): m/z (%) 358.9588 (100) $[M+H]^{+}$, 279.0427 (64) $[C_{14}H_{15}S_2P]^{+}$; **Elemental analysis** calculated (%) for $C_{14}H_{15}SePS_2$ (357.3) : C 47.1, H 4.2. Found C 47.2, H 4.3.

6.3.10 Synthesis of compound 5.10

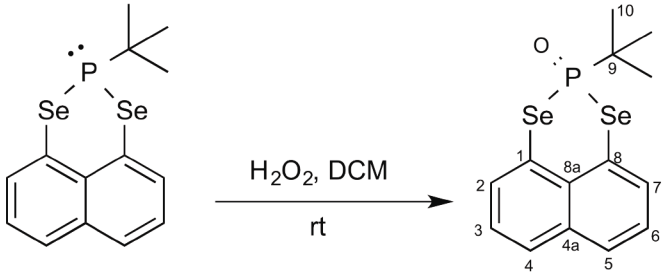

To a solution of naphtho[1,8-cd]1,2-diselenole tertbutylphosphine (**4.5**) (0.2 g, 0.7 mmol) in dichloromethane (40 mL), H_2O_2 (30% solution in water) (0.14mL, 1.34 mmol) was added dropwise and the stirring continue for 1 hour. The reaction mixture was washed with water (100 mL), and the organic layer dried with magnesium sulfate and concentrated under reduced pressure. Crystals suitable for X-ray diffraction were grown in dichloromethane. (0.2 g, 88%); **mp** 199-201 °C; **IR** (KBr disk) : ν_{max} cm^{-1} : 3422.9s, 2957.2s, 1592.5w, 1541.6s, 1490.2w, 1455.7s, 1362s, 1317.3w, 1196.6vs, 1175vs, 1137.9s, 1008.6w, 819.1vs, 804s, 758.3vs, 689.1w, 616.1s, 505.5vs, 468.3vs, 396.1w, 318.6w, 286.6w, 259.7vs; **^{1}H {^{31}P} NMR** (400 MHz; $CDCl_3$) δ (ppm) = 7.8 (m, 4H, ArH–2, 7, 4, 5), 7.3 (dd, $^{3}J_{HH}$ = 8.0 Hz, $^{3}J_{HH}$ =7.4 Hz, 2H, ArH–3, 6), 1.4 (m, 9H, 3 x CH_3, H10); **^{13}C {^{1}H} NMR** (100.6 MHz; $CDCl_3$) δ (ppm): 136.3 (s, Cq, ArC–4a), 134.0 (d, $^{3}J_{CP}$ = 6.9 Hz, 2 x CH, ArC–2, 7), 130.8 (s, 2 x CH, ArC–4, 5), 128.6 (d, $^{2}J_{CP}$ = 3.1 Hz, 2 x Cq, ArC–1, 8), 126.3 (s, 2 x CH, ArH–3, 6), 44.0 (d, $^{1}J_{CP}$ = 50.5 Hz, Cq, C9), 25.0 (s, 3 x CH_3, C10); **^{31}P {^{1}H} NMR** (109.3 MHz, $CDCl_3$) δ (ppm)= 44.1 (s, ^{1}J (^{31}P,^{77}Se) = 406.7 Hz); **^{77}Se {^{1}H} NMR** (51.5 MHz, $CDCl_3$) δ (ppm)= 392.9 (d, ^{1}J (^{31}P,^{77}Se) = 406.7 Hz); **MS** (APCI^{+}): m/z (%) 390.9268 (28) $[M+H]^{+}$, 316.8537 (42)

$[C_{10}H_6Se_2P]^+$, 285.8798 (84) $[C_{10}H_6Se_2]^+$, 253.9396 (100) $[C_{10}H_6SePO]^+$, 236.9370 (82) $[C_{10}H_6SeP]^+$, 206.9710 (31) $[C_{10}H_6Se]^+$, 128.0620 (24) $[C_{10}H_8]^+$; **elemental analysis** calculated (%) for $C_{14}H_{15}OPSe_2$ (388.2) : C 43.3, H 3.9. Found C 43.2, H 3.8.

6.3.11 Synthesis of compound 5.11

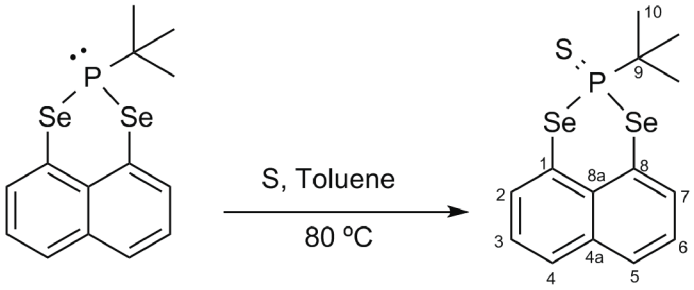

Compound **5.11** was prepared following the procedure described previously for compound **5.5**, with naphtho[1,8-cd]1,2-diselenole tertbutylphosphine (0.5 g, 1.3 mmol) and elemental sulfur (0.04 gr, 1.4 mmol) yielding a white-green solid. Crystals suitable for X-ray diffraction were grown by layering a dichloromethane solution of **5.11** with hexane. (0.4 g, 69%); **mp** 199-202 °C; **IR** (KBr disk) : ν_{max} cm^{-1} : 3417w, 2965w, 1638w, 1538w, 1491w, 1455w, 1356s, 1191s, 1013w, 847w, 808s, 750s, 669vs, 581s, 489s, 430w; **^{1}H {^{31}P} NMR** (400 MHz; $CDCl_3$) δ (ppm) = 7.8 (dd, $^3J_{HH}$ = 8.25 Hz, $^4J_{HH}$ = 1.1 Hz, 2H, ArH–4, 5), 7.8 (dd, $^3J_{HH}$ = 7.3 Hz, $^4J_{HH}$ = 1.2 Hz, 2H, ArH–2, 7), 7.4 (dd, $^3J_{HH}$ = 8.0 Hz, $^3J_{HH}$ = 7.4 Hz, 2H, ArH–3, 6), 1.3 (s, 9H, 3 x CH_3, H10); **^{13}C {^{1}H} NMR** (100.6 MHz; DMSO) δ (ppm): 135.8 (s, Cq, ArC–4a), 131.3 (d, $^3J_{CP}$ = 6.6 Hz, 2x CH, ArC–2, 7), 130.7 (s, 2xCH, ArC–4, 5), 128.9 (d, $^2J_{CP}$ = 5.9 Hz, 2 x Cq, ArC–1, 8,), 126.8 (d, $^3J_{CP}$ = 3.1 Hz, 2 x Cq, ArC–8a), 125.8 (s,2xCH, ArC–3, 6), 47.6 (d, $^1J_{CP}$ = 30.3 Hz, C9), 24.2 (s, 3x CH_3, C10); **^{31}P {^{1}H} NMR** (109.3 MHz, $CDCl_3$) δ (ppm)= 48.6 (s, ^{1}J (^{31}P,^{77}Se) = 398 Hz); **^{77}Se {^{1}H} NMR** (51.5 MHz, $CDCl_3$) δ (ppm)= 413.2 (d, ^{1}J (^{31}P,^{77}Se) = 398 Hz); **MS** (EI^+): m/z (%) 405.8 (44) $[M^\bullet]^+$, 285.8 (100) $[C_{10}H_6Se_2^\bullet]^+$, 205.9

(28) $[C_{10}H_6Se^{\bullet}]^+$, 126.0 (40) $[C_{10}H_6^{\bullet}]^+$; **elemental analysis** calculated (%) for $C_{14}H_{15}SPSe_2$ (404.23) : C 41.6, H 3.7. Found C 41.7, H 3.6.

6.3.12 Synthesis of compound 5.12

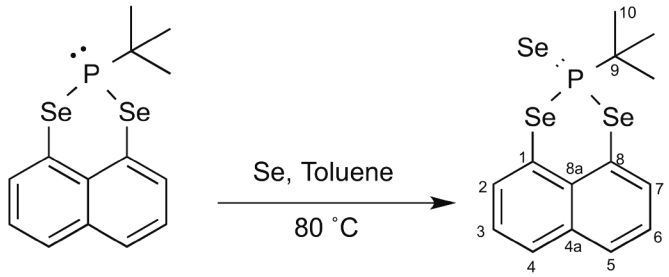

Compound **5.12** was prepared following the procedure described previously for compound **5.6**, with naphtho[1,8-cd]1,2-diselenole tertbutylphosphine (**4.5**) (0.2 g, 1.1 mmol) and elemental selenium (0.1 gr, 1.4 mmol) yielding a light-purple solid. Crystals suitable for X-ray diffraction were grown by layering a dichloromethane solution of **5.12** with methanol. (0.4g, 78%); **mp** 182-185 °C; **IR** (KBr disk) : ν_{max} cm^{-1} : 3423.7s, 2967s, 2283.9w, 1537.6s, 1490.6w, 1453.4s, 1355.6s, 1327.7s, 1190.3s, 1164.6s, 1012.3s, 846.1w, 807.8vs, 749.1vs, 593.7s, 556.4w, 534.8vs, 520.7vs, 482.2s, 417.4s, 375.4s; **^{1}H {^{31}P} NMR** (400 MHz; $CDCl_3$) δ (ppm) = 7.9 (dd, $^3J_{HH}$ = 8.3 Hz, $^4J_{HH}$ = 1.2 Hz, 2H, ArH-4, 5), 7.8 (dd, $^3J_{HH}$ = 7.3 Hz, $^4J_{HH}$ = 1.3 Hz, 2H, ArH-2, 7), 7.4 (dd, $^3J_{HH}$ = 8.1 Hz, $^3J_{HH}$ = 7.3 Hz, 2H, ArH-3, 6), 1.3 (s, 9H, 3 x CH_3, H10); **^{13}C {^{1}H} NMR** (100.6 MHz; $CDCl_3$) δ (ppm): 136.1 (s, Cq, ArC-4a), 131.1 (s, 2 x CH, ArC-4, 5), 130.8 (d, $^3J_{CP}$ = 6.01 Hz, 2 x CH, ArC-2, 7), 130.3 (d, $^2J_{CP}$ = 6.5 Hz, 2 x Cq, ArC-1, 8), 127.4 (d, $^3J_{CP}$ = 3.5 Hz, 2 x Cq, ArC-8a), 126.1 (s, 2 x CH. ArC-3, 6) 48.2 (d, $^1J_{CP}$ = 20.1 Hz, P-Cq, C9) 25.3 (s, 3 x CH_3, C10); **^{31}P {^{1}H} NMR** (109.3 MHz, $CDCl_3$) δ (ppm)= 27.3 (s, ^{1}J (^{31}P,^{77}Se) = 407 Hz, ^{1}J (^{31}P,^{77}Se) = 752 Hz); **^{77}Se {^{1}H} NMR** (51.5 MHz, $CDCl_3$) δ (ppm)= 406.1 (d, ^{1}J (^{31}P,^{77}Se) = 407 Hz), -143.7 (d, ^{1}J (^{31}P,^{77}Se) = 752 Hz); **MS** (NSI^+): m/z (%) 919.7195 (10) [2M+NH_4–H] 452.8489 (100) $[M+H]^+$;

elemental analysis calculated (%) for $C_{14}H_{15}PSe_3$ (453.8) : C 37.3, H 3.3. Found C 37.4, H 3.3.

6.4 References

1. A. L. Fuller, F. R. Knight, A. M. Z. Slawin, J. D. Woollins, *Eur. J. Inorg. Chem.*, **2010**, 2010, 4034-4043.

This page intentionally left blank.

General conclusions

In this thesis a range of chalcogen-containing heterocycles have been synthesised and studied by a range of techniques. Special attention has been given to understanding the solid-state nature of the compounds, and so bulk techniques have been used for this purpose. It was demonstrated that ^{31}P, ^{77}Se and ^{125}Te solid-state NMR spectra contain much more information than the solution-state analogue (which was used just to probe the purity of the compounds). Single-crystal X-ray diffraction has been used to determine the conformation of the molecules studied but, in some cases, several conformations were present in the same bulk sample, and, by the use of powder X-ray diffraction, solid-state NMR spectroscopy and screening of the crystallisation processes, polymorphism could be demostrated. DFT calculations were also used to help with the spectral assignment and understanding how the NMR parameters relate to the structure. However, in some cases, discrepancies were found, probably as dynamic behaviour was present in all the heterocycles studied and also since relativistic effects, not included in calculations, were important in order to study heavy atoms, as was demonstrated in this thesis.

In the first chapter of results, Chapter 3, a series of nine mixed Se and Te acenaphthenes systems was studied, with the aryl group attached to Te varied through the series. Solid-state NMR spectroscopy proved to be very sensitive to conformational changes, as observed by the difference in chemical shift and CSA found between the polymorphs. A difference in chemical shift between solution- and solid-state NMR spectra was observed for these materials. Initially, the differences were attributed to crystal packing, however, in Chapter 5 it was demonstrated that crystal

packing has little effect on the chemical shifts in comparison to a conformation change, as the latter affects the local environment. This is expected, as NMR is not a long-range technique and so is less sensitive to changes in crystal packing than more localized effects. Therefore, the difference in chemical shift between solution and solid, observed in compounds studied in Chapter 3, might arise from the different conformation in the solid state, imposed by crystal packing while, in solution, an average conformation is observed.

In Chapter 4, a series of six P-S and P-Se heterocycles was studied and some unusual interactions were observed by solid-state NMR spectroscopy. A heteronuclear J coupling between ^{77}Se and ^{31}P of another molecule though-space occurs for compounds **4.5** and **4.6**, thus explaining the strange multiplicity observed in the ^{77}Se NMR spectra. However, this interaction is not observed for compound **4.4**, as the packing is different in the three compounds, and the P-Se distance is greater. The second unusual interaction is a homonuclear through-space J coupling in **4.5**, which occurs between crystallographically-equivalent ^{31}P, which are magnetically inequivalent owing to the presence of a heteronuclear J coupling to ^{77}Se. This was demonstrated by a 2D J-resolved experiment with ^{77}Se decoupling. These interactions seem to enable stabilization of the solid-state structures of the heterocycles studied, and when they are not present, polymorphism is observed.

In Chapter 5, the P atom of the compounds in Chapter 4, is oxidised with different chalcogens. The stability of the oxidised derivatives decreases with respect to their parent compounds and polymorphism and phase transitions phenomena are observed. This is probably as a consequence of the possibility of forming other interactions between the polarisable atoms in the nucleation processes, leading to different

metastable phases. It was further demonstrated in this chapter that ^{77}Se and ^{31}P are very sensitive to conformation, as discussed previously. In this chapter all calculated and experimental NMR parameters were compared for all heterocycles studied. In Chapter 3, ^{77}Se and ^{125}Te NMR parameters were calculated by DFT for a mixed series of heterocycles resulting in the ^{77}Se NMR parameters poorly reproduced. However, for the P-Se heterocycles studied in Chapter 5, the ^{77}Se NMR parameters were well reproduced. This confirms that the poor agreement found in Chapter 3 is owing to the presence of Te in very close proximity to Se, and the presence of an interaction between the two atoms. It is clear from these studies that relativistic effects not accounted in calculations, are important for compounds studied in Chapter 3 but, not so much for those in Chapter 5, where the atoms bonded to Se are lighter (P). The poor agreement found between the calculated and experimental ^{31}P NMR parameters was attributed to the motion present in the heterocycles, as it is the R group attached to P atom that could have the most mobility in the system. Although, DFT provided very useful information, such as the mechanism and pathway of the through-space interactions observed, and could help establish the relationship between structure and NMR parameters, it is clear that further work in needed in compounds containing heavy atoms.

This work represents a contribution to the less explored area of chalcogen-containing materials with a solid-state NMR perspective. This work has provided valuable insight into weak interactions, polymorphism and phase transitions.

This page intentionally left blank.

Appendices

A Chapter 3

Table A1. ^{77}Se CP MAS (9.4 T, 5 kHz MAS) solid-state NMR experimental parameters performed for samples **3.1 – 3.9**.

Sample	Number of transients	Recycle interval / s	Contact time / ms
3.1	592	90	20
3.2	1560	35	12
3.3	3040	3	8
3.4	1656	3	8
3.5	4656	20	5
3.6	5568	10	8
3.7	17248	3	8
3.8	352	38	8
3.9	1792	10	8

Table A2. ^{125}Te CP MAS (9.4 T, 10.5 kHz MAS) solid-state NMR experimental parameters performed for samples **3.1 – 3.9**.

Sample	Number of transients	Recycle interval / s	Contact time / ms
3.1	1878	90	20
3.2	4632	35	12
3.3	28904	3	8
3.4	46560	3	8
3.5	24576	20	5
3.6	7280	10	8
3.7	54264	3	8
3.8	3740	38	8
3.9	7552	10	8

Table A3. ^{13}C CP MAS (14.1 T, 12.5 kHz MAS) solid-state NMR experimental parameters performed for samples **3.1 – 3.9**.

Sample	Number of transients	Recycle interval / s	Contact time / ms
3.1	442	90	20
3.2	1608	35	8
3.3	640	3	8
3.4	640	3	8
3.5	128	90	20
3.6	128	7	8
3.7	640	3	8
3.8	104	38	8
3.9	1024	10	8

Table A4. X-ray diffraction data of **3.1a**, **3.1b** and **3.1c**.

Compound	**3.1a**	**3.1b**	**3.1c**
Empirical formula	$C_{24}H_{18}SeTe$	$C_{24}H_{18}SeTe$	$C_{24}H_{18}SeTe$
Formula weight	512.97	512.97	512.97
Crystal color,Habit	colorless, prism	colorless, prism	Orange, needles
Crystal system	monoclinic	orthorhombic	Triclinic
Space group	$P2_1/n$	$Pca2_1$	P–1
Lattice parameters	a = 5.641(2) Å	a = 22.488(3) Å	a = 9.7470(18) Å
	b = 22.249(10) Å	b = 5.2755(6) Å	b = 9.907(2) Å
	c = 15.272(7) Å	c = 15.7835(18) Å	c = 11.960(2) Å
	α = 90°	α = 90°	α = 160.4500(17)°
	β = 100.477(18)°	β = 90°	β = 97.557(3)°
	γ = 90°	γ = 90°	γ = 116.347(3)°
***Peri*-atoms**	Te, Se	Te, Se	Te, Se
Peri-region-distances			
Te(1)···Se(1)	3.2479(19)	3.2178(9)	3.2432(19)
$\%\Sigma r_{vdW}$[a]	81	81	81
Peri-region bond lengths			
Te(1)-C(1)	2.152(10)	2.133(8)	2.133(17)
Te(1)-C(13)	2.142(11)	2.123(7)	2.148(15)
Se(1)-C(9)	1.943(11)	1.911(9)	1.928(18)
Se(1)-C(19)	1.942(12)	1.929(9)	1.941(13)
Peri-region bay angles			
Te(1)-C(1)-C(10)	123.1(7)	123.3(6)	123.6(12)
C(1)-C(10)-C(9)	130.6(9)	130.3(8)	129.8(16)
Se(1)-C(9)-C(10)	123.4(8)	124.0(7)	123.0(12)
Σ of bay angles	377.1	377.6	376.4(15)
Splay angle[b]	17.1	17.6	16.4
Out-of-plane displacement			
Te(1)	–0.403	–0.195	0.335
Se(1)	0.032	0.137	–0.361
Peri- torsion angles			
Te(1)-C(1)-C(10)-C(5)	171.98	176.0(4)	170.4(7)
Se(9)-C(9)-C(10)-C(5)	177.25	174.7(5)	170.7(6)
Te(1)-C(1)- C(9)-Se(9)	–9.10	–7.85	16

Selected bond lengths (Å) and angles (°). [a] van der Waals radii used for calculations: rdW(Se) 1.90 Å and rdW(Te) 2.06 Å [b] Splay angle: ∑ of the three bay region angles – 360

Table A5. X-ray diffraction data of **3.7a** and **3.7b**.

Compound	**3.7a**	**3.7b**
Empirical formula	$C_{24}H_{26}SeTe$	$C_{24}H_{26}SeTe$
Formula weight	569.07	569.07
Crystal color,Habit	colorless, chunk	orange, platelet
Crystal system	triclinic	monoclinic
Space group	P–1	$P2_1/c$
Lattice parameters	a = 9.656(1) Å	a = 10.6293(15) Å
	b = 10.492(2) Å	b = 10.2353(14) Å
	c = 12.795(2) Å	c = 21.535(3) Å
	α = 79.476(6)°	α = 90°
	β = 73.922(6)°	β = 92.093(4)°
	γ = 70.177(5)°	γ = 90°
***Peri*-atoms**	Te, Se	Te, Se
Peri-region-distances		
Te(1)···Se(1)	3.233	3.247
$\%\Sigma r_{vdW}$[a]	82	82
Peri-region bond lengths		
Te(1)-C(1)	2.142(4)	2.128(7)
Te(1)-C(13)	2.134(3)	2.145(7)
Se(1)-C(9)	1.919(3)	1.907(7)
Se(1)-C(23)	1.926(4)	1.923(8)
Peri-region bay angles		
Te(1)-C(1)-C(10)	123.4(3)	125.8(6)
C(1)-C(10)-C(9)	129.93	127.98
Se(1)-C(9)-C(10)	123.1(2)	124.2(5)
Σ of bay angles	376.43	377.98
Splay angle[b]	16.43	17.98
Out-of-plane displacement		
Te(1)	0.332	0.244
Se(1)	–0.924	0.304
Peri- torsion angles		
Te(1)-C(1)-C(10)-C(5)	–171.6(2)	174.3(4)
Se(1)-C(9)-C(10)-C(5)	–170.7(3)	169.9(4)
Te(1)-C(1)- C(9)-Se(9)	15	–13.12

Selected bond lengths (Å) and angles (°). [a] van der Waals radii used for calculations: rdW(Se) 1.90 Å and rdW(Te) 2.06 Å [b] Splay angle: ∑ of the three bay region angles – 360

Figure A1. ^{13}C CP MAS NMR spectra for compounds **3.1** – **3.9**.

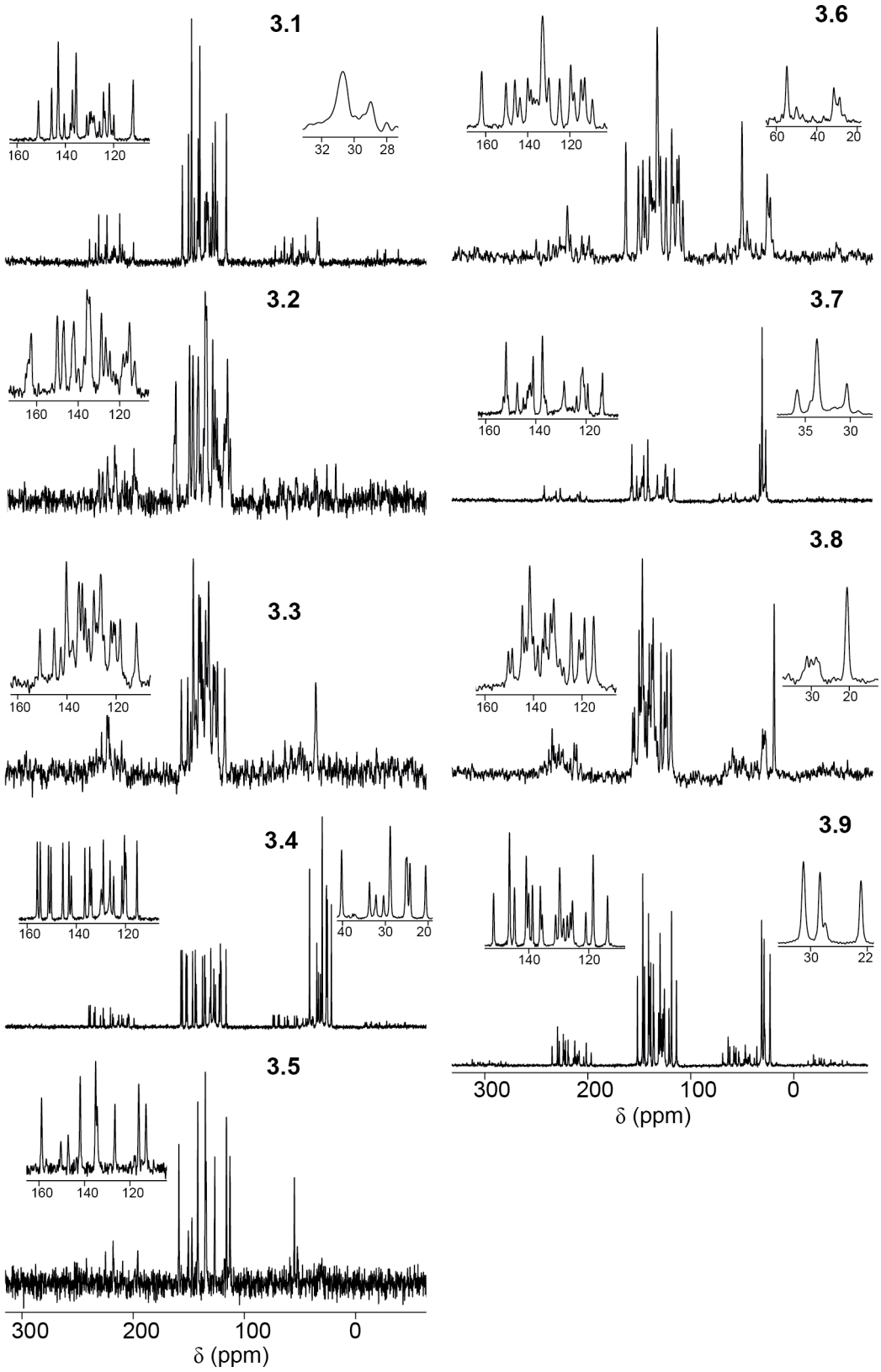

B Chapter 4

Table B1. X-ray diffraction data of polymorphs of **4.1**.

Compound	**4.1 a**	**4.1 b**	**4.1c**
Empirical formula	$C_{13}H_{13}PS_2$	$C_{13}H_{13}PS_2$	$C_{13}H_{13}PS_2$
Formula weight	264.34	264.34	264.34
Crystal color,Habit	colorless, chunk	colorless, prism	colorless, prism
Crystal system	monoclinic	monoclinic	triclinic
Space group	$P2_1/c$	$P2_1$	P–1
Lattice parameters	a = 18.0397(17) Å	a = 16.406(5) Å	a = 8.682(3) Å
	b = 9.8619(10) Å	b = 10.006(2) Å	b = 12.082(4) Å
	c = 15.5876(15) Å	c = 16.711(5) Å	c = 12.671(5) Å
	α = 90°	α = 90°	α = 104.580(6)°
	β = 114.111(8)°	β =111.495(7)°	β = 105.706(7)°
	γ = 90°	γ = 90°	γ = 91.914(3)°
***Peri*-atoms**	S, S	S, S	S, S
Peri-region-distances			
E(1)···E(9)	3.162	3.135 [3.156]	3.170
$\%\Sigma r_{vdW}$[a]	87	87 [87]	88
Peri-region bay angles			
S(9)-C(9)-C(10)	125.9(3) [125.6(3)]	124.4(11) [124.7(8)]	125.80(15)
S(49)-C(49)-C(50)		[125.1(11)]	
S(1)-C(1)-C(10)	126.5(3) [126.2(2)]	124.1(9) [126.6(11)]	126.45(16)
S(41)-C(41)-C(50)		[122.9(9)]	
C(9)-C(10)-C(1)	126.90 [127.29]	129.5(10)	127.13 [127.02]
		[129.9(10)]	
Σ of bay angles	379.3 [379.1]	378 [378.8]	379.38 [379.33]
		[377.9] [378.4]	
Splay angle[b]	19.3 [19.1]	18 [18.8]	19.38 [19.33]
		[17.9] [18.4]	
Out-of-plane displacement			
S(1) / S(21)	0.093 [0.063]	0.312 [0.153]	0.007 [0.275]
S(41) / S(61)		[0.278] [0.065]	
S(9) / S(29)	0.214 [0.227]	0.095 [0.226]	0.222 [0.039]
S(49) / S(69)		[0.075] [0.203]	
Peri-torsion angles			
S(1)-C(1)-C(10)-C(5)	177.48(19) [176.33(19)]	170.2(6) [173.9(7)]	179.59(10) [170.93(12)]
S(41)-C(41)-C(50)-		[170.9(6)] [178.4(7)]	
S(9)-C(9)-C(10)-C(5)	172.42(19)	175.0(7) [173.1(7)]	173.20(10)
S(49)-C(49)-C(50)-		[176.1(7)] [175.1(7)]	
S(1)-C(1)-C(9)-S(9)	4.13 [2.88]	–3.96 [0.85]	5.25 [5.83]
S(41)-C(41)-C(49)-		[–4.37] [2.73]	

Selected bond lengths (Å) and angles (°). [a] van der Waals radii used for calculations: rdW(S) 1.80 Å, [b] Splay angle: ∑ of the three bay region angles – 360. [] denotes data for the second molecule in the asymmetric unit, and for the case of **4.1b**, is also denotes the third and four molecule.

Table B2. X-ray diffraction data of **4.2** and **4.3**.

Compound	**4.2 (tert)**	**4.3 (Ph)**
Empirical formula	$C_{14}H_{15}PS_2$	$C_{16}H_{11}PS_2$
Formula weight	278.37	298.36
Crystal color, Habit	colorless, block	colorless, prism
Crystal system	monoclinic	monoclinic
Space group	$P2_1/c$	$P2_1/n$
Lattice parameters	a = 21.259(3) Å	a = 9.1545(19) Å
	b = 7.2032(9) Å	b = 12.826(3) Å
	c = 20.189(3) Å	c = 23.488(5) Å
	α = 90°	α = 90°
	β = 116.264(8)°	β = 92.945(5)°
	γ = 90°	γ = 90°
***Peri*-atoms**	S, S	S, S
***Peri*-region-distances**		
E(1)···E(9)	3.186	3.169 [3.184]
$\%\Sigma r_{vdW}$[a]	88	88 [88]
***Peri*-region bay angles**		
S(9)-C(9)-C(10)	126.2(4) [127.7(4])	126.45 [125.38]
S(1)-C(1)-C(10)	126.5(4) [126.8(5)]	126.03 [126.93]
C(9)-C(10)-C(1)	126.8(5) [126.16]	127.25 [126.97]
Σ of bay angles	379.5 [380.66]	379.73 [379.28]
Splay angle[b]	19.5 [20.66]	19.73 [19.28]
Out-of-plane displacement		
S(1)	0.032 [0.277]	0.233 [0.011]
S(9)	0.277 [0.040]	0.047 [0.285]
***Peri*- torsion angles**		
S(1)-C(1)-C(10)-C(5)	178.5(4) [171.0(4)]	172.32 [178.80]
S(9)-C(9)-C(10)-C(5)	171.1(4) [177.9(4)]	177.75 [170.83]
S(1)-C(1)-C(9)-S(9)	6.07 [–5.57]	4.46 [–6.42]

Selected bond lengths (Å) and angles (°). [a]van der Waals radii used for calculations: rdW(S) 1.80 Å, [b] Splay angle: ∑ of the three bay region angles – 360.[] denotes data for the second molecule in the asymmetric unit.

Table B3. X-ray diffraction data of **4.4**, **4.5**and **4.6**.

Compound	**4.4(iso,Se)**	**4.5(tert,Se)**	**4.6(Ph,Se)**
Empirical formula	$C_{13}H_{13}PSe_2$	$C_{14}H_{15}PSe_2$	$C_{16}H_{11}PSe_2$
Formula weight	358.14	372.17	392.15
Crystal color,Habit	purple, block	colorless, platelet	
Crystal system	triclinic	triclinic	monoclinic
Space group	P–1	P–1	$P2_1/c$
Lattice parameters	a = 7.6709(17) Å	a = 7.3880(15) Å	a = 12.526(2) Å
	b = 9.404(2) Å	b = 10.3745(19) Å	b = 12.864(2) Å
	c = 10.484(2) Å	c = 10.8099(19) Å	c = 9.2830(16) Å
	α =106.421(8)°	α = 107.355(8)°	α = 90°
	β = 104.690(7)°	β = 107.255(8)°	β = 108.644(3)°
	γ = 106.308(8)°	γ = 107.255(8)°	γ = 90°
***Peri*-atoms**	Se, Se	Se, Se	Se, Se
Peri-region-distances			
Se(1)···Se(1)	3.351	3.389	3.375
$\%\Sigma r_{vdW}$[a]	88	89	89
Peri-region bay angles			
Se(2)-C(9)-C(10)	127.9(3)	130.1(4)	127.65
Se(1)-C(1)-C(10)	128.3(3)	128.0(3)	128.58
C(9)-C(10)-C(1)	126.9(3)	126.2(4)	127.34
Σ of bay angles	383.1(	384.3()	383.57
Splay angle[b]	23.1	24.3	23.57
Out-of-plane displacement			
Se(1)	0.139	0.372	0.274
Se(2)	0.143	0.032	0.117
Peri- torsion angles			
Se(1)-C(1)-C(10)-C(5)	175.57(14)	168.4(3)	171.42
Se(2)-C(9)-C(10)-C(5)	175.16(14)	177.6(3)	175.50
Se(1)-C(1)-C(9)-S(9)	0.36	7.39	–3.33

Selected bond lengths (Å) and angles (°). [a] van der Waals radii used for calculations: rdW(Se) 1.90 Å, [b] Splay angle: ∑ of the three bay region angles – 360.

Figure B1. Comparison of experimental and simulated powder XRD patterns for compound **4.3**.

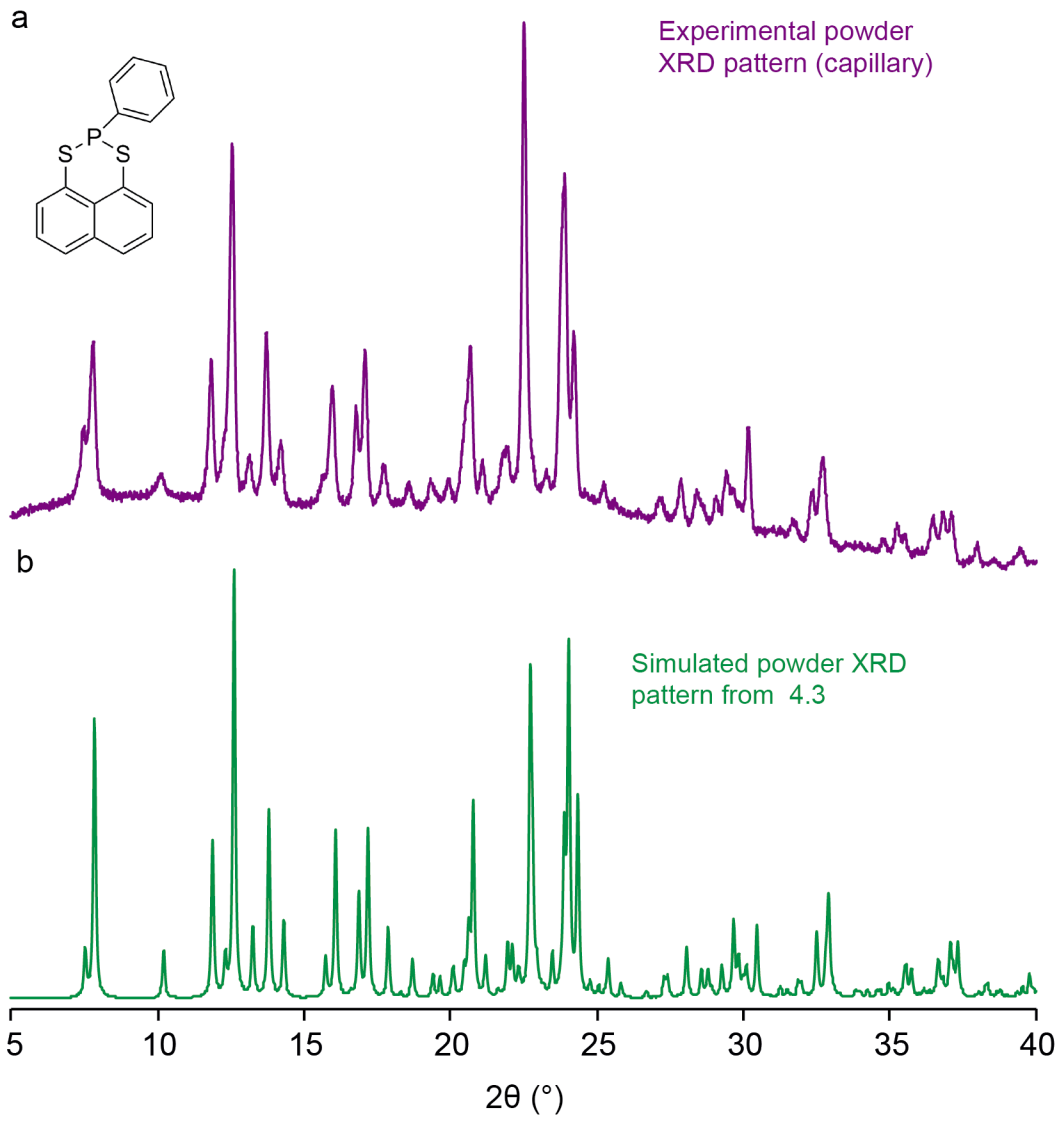

Figure B2. Comparison of experimental and simulated powder XRD patterns for compound **4.4**.

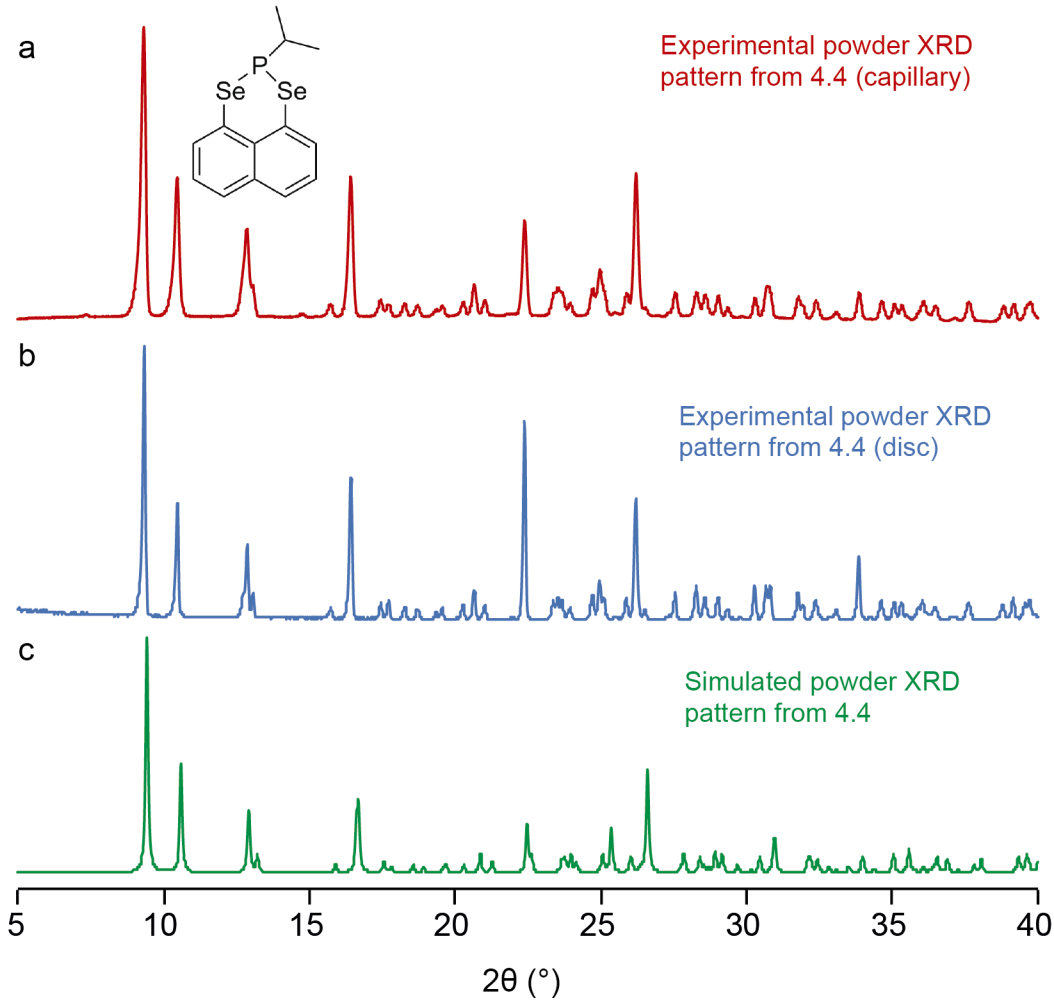

Figure B3. Comparison of experimental and simulated powder XRD patterns for compound **4.5**.

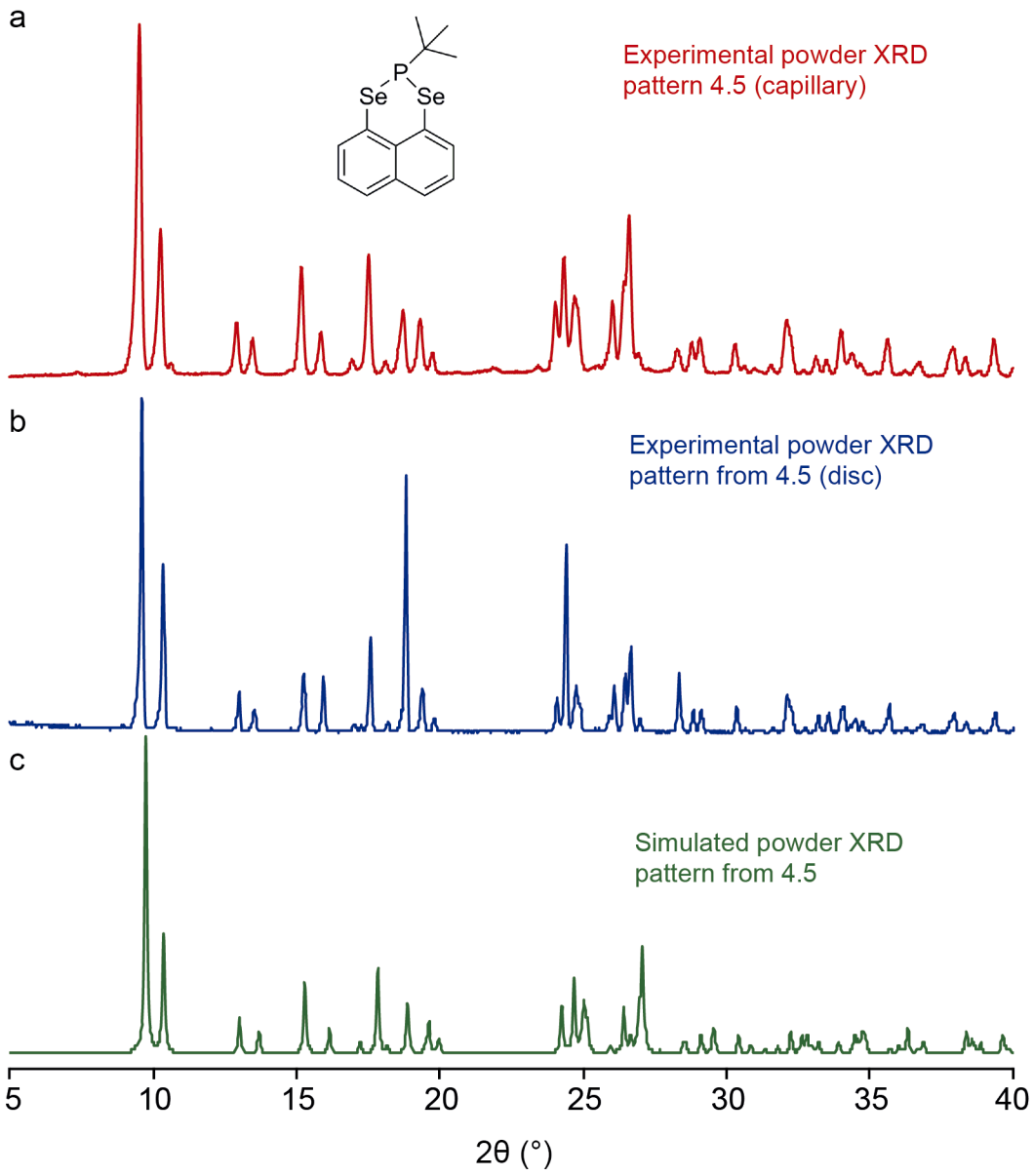

Figure B4. Comparison of experimental and simulated powder XRD patterns for compound **4.6**.

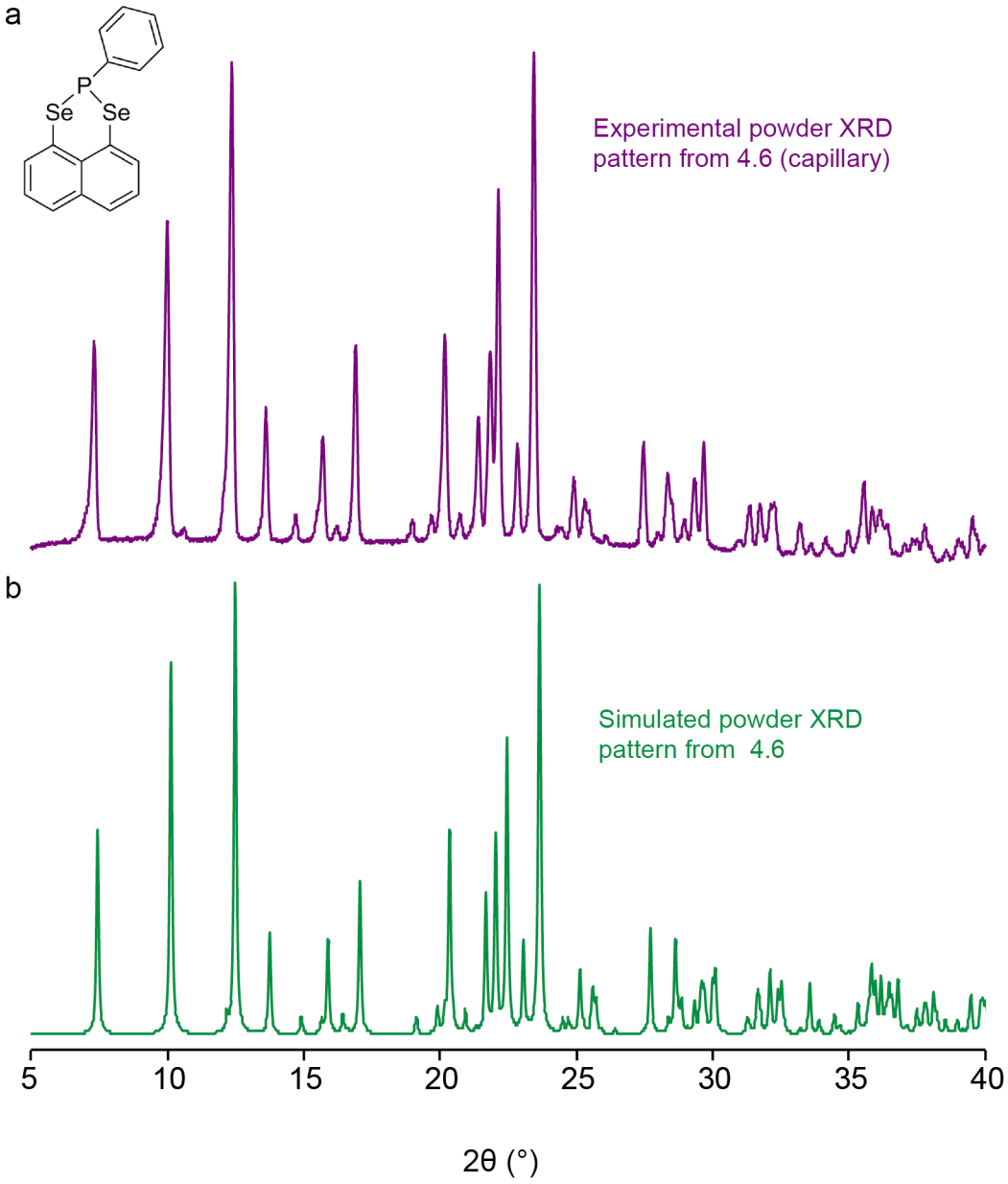

Table B3. Variable-temperature ^{31}P solid-state NMR of **4.1**, **4.3**, **4.4** and **4.5**.

Compound	Temperature	δ_{iso}	Ω	κ	δ_{11}	δ_{22}	δ_{33}
		1.9	217.9	0.2	105.1	13.5	–112.8
		2.8	165.4	1.0	59.0	56.0	–106.6
4.1	273	5.5	174.8	0.8	68.2	55.0	–106.7
		2.9	211.7	0.3	98.3	23.9	–113.4
		3.9	172.0	0.6	73.4	37.3	–98.8
4.1	298	6.1	195.2	0.2	95.6	22.5	–99.6
		3.7	214.5	0.3	100.5	24.8	–114.6
		4.9	142.8	0.9	53.7	50.1	–89.1
4.1	323	6.9	199.4	0.3	95.5	29.1	–103.9
		–0.1	193.2	0.3	88.2	16.4	–105.0
4.3	273	–4.2	193.6	0.2	84.7	11.5	–108.9
		0.5	154.8	0.9	55.3	45.7	–99.5
4.3	298	–3.4	181.2	0.2	80.2	10.5	–101.0
		1.1	180.2	0.3	82.7	18.0	–97.4
4.3	323	–2.7	176.2	0.03	84.3	–0.7	–91.8
4.4	273	–2.5	206.7	0.5	84.7	29.5	–121.9
4.4	298	–2.05	180.3	0.9	60.9	52.3	–119.4
4.4	323	–1.5	189.3	0.5	75.7	33.4	–113.6
4.5	273	5.0	231.3	0.5	101.6	43.2	–129.7
4.5	298	6.1	231.7	0.5	102.9	44.0	–128.8
4.5	323	7.1	230.9	0.5	104.4	43.4	–126.6

All values are quoted in δ (ppm), Ω(ppm).

Figure B5. ^{13}C CP MAS NMR spectra of **4.2**, **4.3**, **4.4**, **4.5** and **4.6** recorded at 9.4 T (**4.1**, **4.3**) or 14.1 T (**4.4**, **4.5**) and 12.5 kHz MAS.

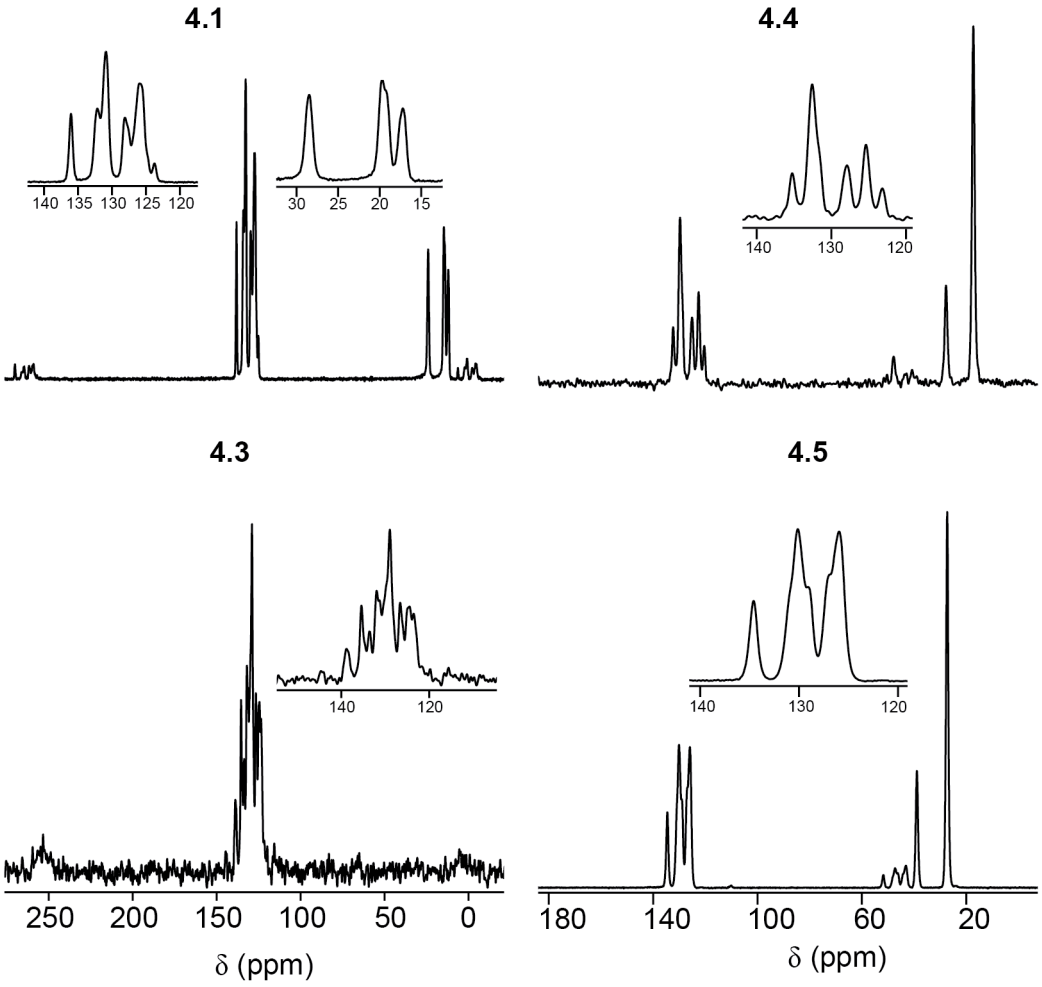

C Chapter 5

Figure C1. Comparison of the experimental and simulated powder XRD patterns for **5.2**.

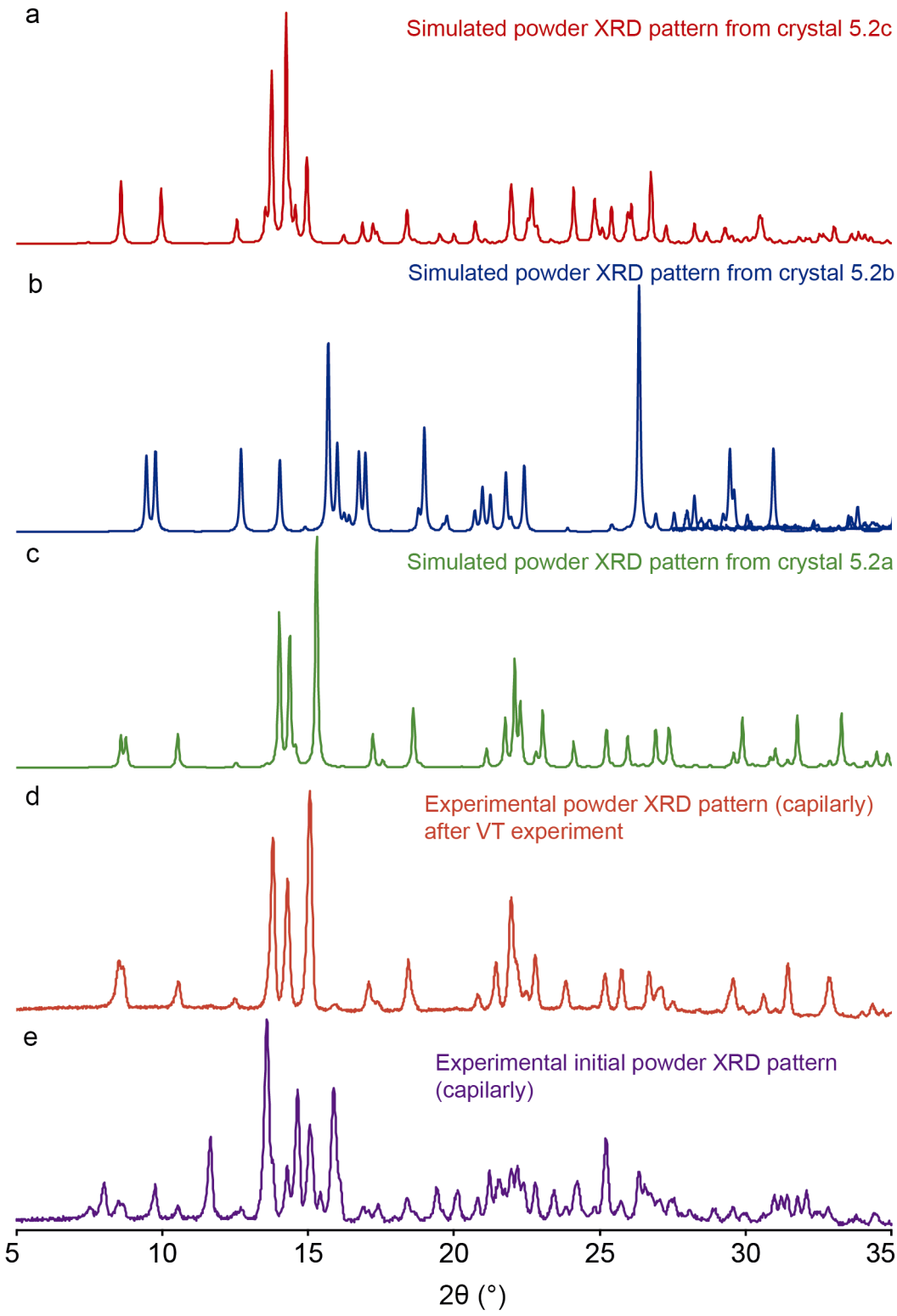

Figure C2. Comparison of the experimental powder XRD pattern for **5.9** of different batches.

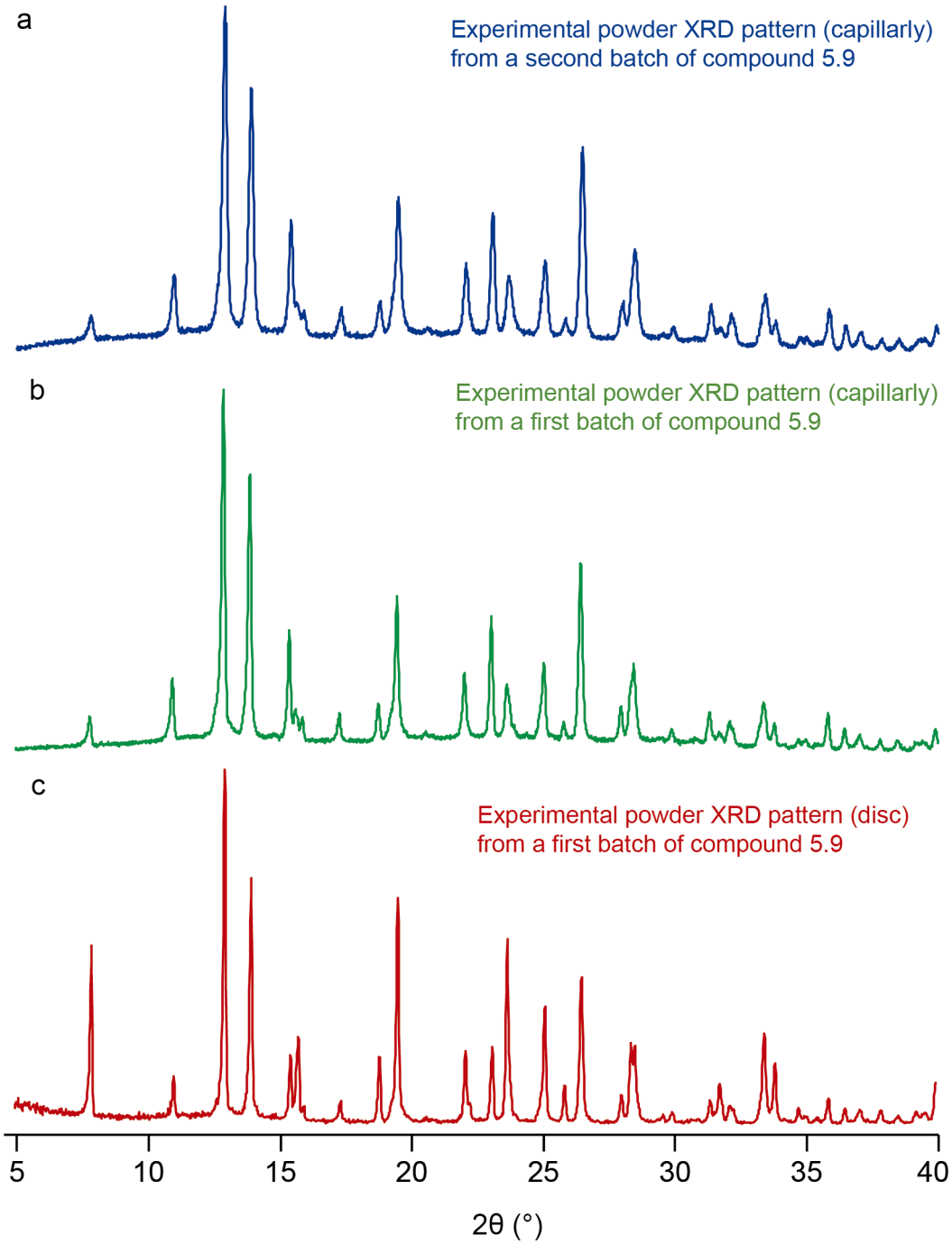

Table C1. X-ray diffraction data of **5.1** and polymorphs of **5.2**.

Compound	**5.1**	**5.2a**	**5.2b**	**5.2c**
Empirical	$C_{13}H_{13}OPS_2$	$C_{13}H_{13}PS_3$	$C_{13}H_{13}SPS_2$	$C_{13}H_{13}SPS_2$
Formula weight	280.34	296.40	296.40	296.40
Crystal color, Habit	yellow, prism	colorless, prism	colorless, prism	colorless, prism
Crystal system	monoclinic	orthorhombic	monoclinic	triclinic
Space group	$P2_1/n$	Pnma	$P2_1/n$	P–1
Lattice parameters [a]	a = 8.6246(16) b = 11.3834(13) c = 13.218(3) α = 90° β = 100.875(4)° γ = 90°	a = 13.0269(14) b = 12.6244(16) c = 16.782(2) α = 90° β = 90° γ = 90°	a = 6.74886(16) b = 18.091(4) c = 10.942(3) α = 90° β =94.530(4)° γ = 90°	a = 9.034(6) b = 12.6786(10) c = 12.835(9) α = 108.135(14)° β =91.561(8)° γ = 99.768(19)°
***Peri*-atoms**	S, S	S, S	S, S	S, S
***Peri*-region-distances**				
E(1)···E(9)	3.188	3.197 [3.156]	3.209	3.226 [3.217]
$\%\Sigma r_{vdW}$ [b]	88	89 [88]	89	90 [89]
***Peri*-region bay angles**				
S(9)-C(9)-C(10)	126.32(14) [125.6(3)]	125.97 [126.29]	125.96(10)	126.0(5) [126.4(4)]
S(1)-C(1)-C(10)	125.84(14) [126.2(2)]	125.97 [126.29]	126.74(10)	126.9(4) [126.5(5)]
C(9)-C(10)-C(1)	127.61(17)	127.90 [127.44]	127.48	127.52 [127.77]
S(1)-P(1)-X(1)	114.74	110.89 [111.88]	110.56	111.43 [111.64]
S(9)-P(1)-X(1)	115.10	110.89 [111.88]	111.99	111.33 [111.49]
Σ of bay angles	379.77	379.84 [380.02]	380.18	380.42 [380.67]
Splay angle [c]	19.77	19.84 [20.02]	20.18	20.42
Out-of-plane displacement				
S(1) / S(21)	0.130	0.155 [0.190]	0.019	0.062 [0.144]
S(9) / S(29)	0.124	0.155 [0.190]	0.217	0.205 [0.158]
X(1)	2.404	0.749 [0.653]	0.881	0.785 [0.784]
***Peri*-torsion angles**				
S(1)-C(1)-C(10)-C(5)	175.18(13)	174.76(11) [173.29(10)]	179.51(8)	177.5(4) [174.9(3)]
S(9)-C(9)-C(10)-C(5)	–175.76(12)	174.76(11) [173.29(10)]	–173.50(8)	–172.7(4) [–174.6(3)
S(1)-C(1)-C(9)-	–0.48	0.00 [0.00]	4.96	3.92 [0.19]

Selected bond lengths (Å) and angles (°). [a] a, b and c in Å, [b] van der Waals radii used for calculations: rdW(S) 1.80 Å, [c] Splay angle: ∑ of the three bay region angles – 360. [] denotes data for the second molecule in the asymmetric unit.

Table C2. X-ray diffraction data of polymorphs of **5.3** and compound **5.4**.

Compound	**5.3a**	**5.3b**	**5.4**
Empirical formula	$C_{13}H_{13}SePS_2$	$C_{13}H_{13}SePS_2$	$C_{13}H_{13}OPSe_2$
Formula weight	343.30	343.30	374.14
Crystal color,Habit	yellow,prism	colorless,platelet	colorless,prism
Crystal system	monoclinic	monoclinic	monoclinic
Space group	$P2_1/c$	$P2_1/n$	$P2_1/n$
Lattice parameters[a]	a = 12.8212(16)	a = 6.8698(18)	a = 8.655(3)
	b = 16.3306(18)	b = 18.060(4)	b = 11.659(3)
	c = 13.5472(15)	c = 10.995(3)	c = 13.302(4)
	α = 90°	α = 90°	α = 90°
	β = 91.217(3)°	β = 94.374(5)°	β = 100.116(9)°
	γ = 90°	γ = 90°	γ = 90°
***Peri*-atoms**	S, S	S, S	S, S
Peri-region-distances			
E(1)···E(9)	3.194 [3.204]	3.211	3.387
$\%\Sigma r_{vdW}$[b]	88.7 [89]	89.2	94.1
Peri-region bay angles			
S(9)-C(9)-C(10)	126.7(2)/126.2(2)	125.89(19)	127.8(2)
S(1)-C(1)-C(10)	126.0(2)/ 126.40(19)	126.83(19)	128.1(2)
C(9)-C(10)-C(1)	127.17/127.62	127.38	127.99
S(1)-P(1)-X(1)	110.32/111.31	110.14	115.28
S(9)-P(1)-X(1)	111.36/110.99	112.25	115.19
Σ of bay angles	379.87/380.22	380.1	383.89
Splay angle[c]	19.87/20.22	20.1	23.89
Out-of-plane displacement			
S(1) / S(21)	0.191/0.126	0.042	0.172
S(9) / S(29)	0.115/0.239	0.223	0.098
X(1)	0.664/0.645	0.914	2.490
Peri-torsion angles			
S(1)-C(1)-C(10)-C(5)	174.02(16)/175.05(15)	–179.65(15)	174.5(2)
S(9)-C(9)-C(10)-C(5)	–175.78(16)/–171.73(16)	–173.59(15)	–176.3(2)
S(1)-C(1)-C(9)-S(9)	–1.49/2.74	5.57	–1.41

Selected bond lengths (Å) and angles (°). [a] a, b and c in Å, [b] van der Waals radii used for calculations: rdW(S) 1.80 Å, [c] Splay angle: ∑ of the three bay region angles – 360. [] denotes data for the second molecule in the asymmetric unit.

Table C3. X-ray diffraction data of **5.5** and polymorphs of **5.6**.

Compound	**5.5**	**5.6a**	**5.6b**
Empirical formula	$C_{13}H_{13}SPSe_2$	$C_{13}H_{13}PSe_3$	$C_{13}H_{13}PSe_3$
Formula weight	390.20	437.10	437.10
Crystal color,Habit	colorless,prism	colorless,prism	colorless,block
Crystal system	triclinic	moniclinic	triclinic
Space group	P–1	$P2_1/n$	P–1
Lattice parameters[a]	a = 9.1569(8)	a = 7.0610(10)	a = 9.2010(11)
	b = 12.8590(9)	b = 18.453(3)	b = 12.8611(14)
	c = 13.0712(11)	c = 10.9373(13)	c = 13.1260(18)
	α = 71.491(4)°	α = 90°	α = 70.831(8)°
	β = 89.991(5)°	β = 93.549(8)°	β = 89.618(6)°
	γ = 79.021(5)°	γ = 90°	γ = 78.617(7)°
***Peri*-atoms**	Se, Se	Se, Se	Se, Se
Peri-region-distances			
E(1)···E(2)	3.413/3.396	3.412	3.418/3.402
$\%\Sigma r_{vdW}$[a]	89.8	89.8	89.9/89.5
Peri-region bay angles			
Se(2)-C(9)-C(10)	127.47(19)/127.6(2)	128.0(2)	127.3(3)/128.0(2)
Se(1)-C(1)-C(10)	127.91(16)/127.87(18)	126.8(2)	128.8(2)/127.5(3)
C(9)-C(10)-C(1)	128.84/128.37	129.04	128.32/128.49
Se(1)-P(1)-X(1)	111.36/112.06	112.75	111.41/112.19
Se(9)-P(1)-X(1)	111.65/112.43	110.12	111.29/111.77
Σ of bay angles	384.22	383.84	384.42/383.99
Splay angle[b]	24.22	23.84	23.42/23.99
Out-of-plane displacement			
Se(1) / Se(21)	0.007/0.187	0.301	0.032/0.166
Se(2) / Se(29)	0.279/0.148	0.114	0.264/0.186
X(1)	0.900/0.924	1.015	0.889/0.907
Peri-torsion angles			
Se(1)-C(1)-C(10)-C(5)	179.30(17)/173.51(13)	171.68(17)	178.5(2)/174.84(18)
Se(2)-C(9)-C(10)-C(5)	–171.09(17)/–175.14(13)	177.67(18)	–171.6(2)/–173.69(18)
Se(1)-C(1)-C(9)-S(2)	6.67/–1.29	–8.68	5.62/0.92

Selected bond lengths (Å) and angles (°). [a] a, b and c in Å, [b] van der Waals radii used for calculations: rdW(Se) 1.90 Å, [c] Splay angle: ∑ of the three bay region angles – 360. [] denotes data for the second molecule in the asymmetric unit.

Table C4. X-ray diffraction data of **5.7**, **5.8** and polymorphs of **5.9**.

Compound	**5.7**	**5.8**	**5.9a**	**5.9b**
Empirical formula	$C_{14}H_{15}OPS_2$	$C_{14}H_{15}PS_3$	$C_{14}H_{15}SePS_2$	$C_{14}H_{15}SePS_2$
Formula weight	294.37	310.43	357.33	357.33
Crystal color,Habit	yellow,prism	colorless,	yellow, prism	colorless, prism
Crystal system	orthorhombic	orthorhombic	monoclinic	orthorhombic
Space group	$P2_12_12_1$	$Pca2_1$	$P2_1/c$	$Pca2_1$
Lattice	a = 7.1542(9)	a = 16.880(3)	a = 23.979(4)	a = 17.0295(18)
parameters[a]	b = 13.2648(17)	b = 7.5882(13)	b = 7.6450(9)	b = 7.6358(7)
	c = 14.4394(14)	c = 22.354(5)	c = 17.077(3)	c = 22.455(2)
	α = 90°	α = 90°	α = 90 °	α = 90 °
	β = 90°	β = 90°	β =110.470(3)°	β = 90°
	γ = 90°	γ = 90°	γ = 90°	γ = 90°
***Peri*-atoms**	S, S	S, S	S, S	S, S
Peri-region-distances				
E(1)···E(9)	3.194	3.179/3.176	3.170/3.175	3.157/3.166
$\%\Sigma r_{vdW}$[b]	88.7	88.3/88.2	88/88.2	87.7/87.9
Peri-region bay angles				
S(9)-C(9)-C(10)	126.58(14)	125.8(5)	125.3(6)	125.6(11)
S(29)-C(29)-C(30)		126.3(4)	125.1(5)	124.5(10)
S(1)-C(1)-C(10)	125.70(14)	127.2(5)	126.7(5)	126.8(11)
S(21)-C(21)-C(30)		124.9(5)	126.5(5)	127.2(11)
C(9)-C(10)-C(1)	127.56	127.01/128.06	127.62/127.31	127.22/127.63
Se(1)-P(1)-X(1)	114.83	114.39/115.96	114.34/115.22	113.79/114.37
Se(9)-P(1)-X(1)	114.83	115.73/115.16	115.91/115.76	116.57/116.16
Σ of bay angles	379.84	380.01/379.26	379.62/378.91	379.62/379.33
Splay angle[c]	19.84	20.01/19.26	19.62/18.91	19.62/19.33
Out-of-plane displacement				
S(1) / S(21)	0.291	0.075/0.231	0.060/0.019	0.094/0.021
S(9) / S(29)	0.027	0.146/0.008	0.146/0.213	0.175/0.230
X(1)	2.387	2.884/2.872	3.032/3.021	3.008/2.999
Peri-torsion angles				
S(1)-C(1)-C(10)-C(5)	170.80(11)	–176.9(4)	178.1(4)	–176.6(8)
S(21)-C(21)-C(30)-		173.5(4)	178.0(5)	–179.2(8)
S(9)-C(9)-C(10)-C(5)	–179.51(11)	175.3(4)	–175.1(3)	174.0(8)
S(29)-C(29)-C(30)-		–180.0(4)	–173.1(5)	174.0(8)
S(1)-C(1)-C(9)-S(9)	–7.16	–1.34/–5.38	2.52/4.12	–2.28/–4.37

Selected bond lengths (Å) and angles (°). [a] a, b and c in Å, [b] van der Waals radii used for calculations: rdW(S) 1.80 Å, [c] Splay angle: ∑ of the three bay region angles – 360. [] denotes data for the second molecule in the asymmetric unit.

Table C5. X-ray diffraction data of **5.10**, **5.11** and polymorphs of **5.12**.

Compound	**5.10**	**5.11**	**5.12a**	**5.12b**
Empirical formula	$C_{14}H_{15}OPSe_2$	$C_{14}H_{15}SPSe_2$	$C_{14}H_{15}PSe_3$	$C_{14}H_{15}PSe_3$
Formula weight	388.17	404.23	451.13	451.13
Crystal color,Habit	colorless, platelet	colorless, prism	colorless, needle	colorless, prism
Crystal system	orthorhombic	moniclinic	monoclinic	triclinic
Space group	Pnma	$P2_1/n$	$P2_1/n$	P–1
Lattice parameters[a]	a = 7.2589(16)	10.9763(14)	11.043(3)	7.3255(11)
	b = 12.309(3)	7.2894(9)	7.4326(19)	10.9412(14)
	c = 15.422(3)	19.316(3)	19.487(6)	19.468(3)
	α = 90°	α = 90°	α = 90 °	α = 74.016(4)
	β = 90°	β =	β = 106.043(6)	β = 89.372(6)
	γ = 90°	γ = 90°	γ = 90 °	γ = 86.742(5)°
***Peri*-atoms**	Se, Se	Se, Se	Se, Se	Se, Se
Peri-region-distances				
E(1)···E(2)	3.367	3.434	3.425	3.432/3.438
$\%\Sigma r_{vdW}$[b]	88.6	90.3	90.1	90.3/90.5
Peri-region bay angles				
Se(9)-C(9)-C(10)	127.8(2)	128.2(3)	128.1(9)	128.01(19)
Se(29)-C(29)-C(30)				127.7(2)
Se(1)-C(1)-C(10)	127.8(2)	128.0(4)	127.8(11)	128.1(2)
Se(21)-C(21)-C(30)				128.32(19)
C(9)-C(10)-C(1)	127.77	128.71	128.57	128.74/128.58
Se(1)-P(1)-X(1)	115.11	109.73	109.60	109.43/108.62
Se(9)-P(1)-X(1)	115.11	109.55	109.79	110.14/110.06
Σ of bay angles	383.37	384.91	384.47	384.85/384.6
Splay angle[c]	23.37	24.91	24.47	24.84/24.6
Out-of-plane displacement				
Se(1) / Se(21)	0.178	0.224	0.261	0.173/0.181
Se(2) / Se(29)	0.178	0.233	0.202	0.247/0.337
X(1)	2.461	0.014	0.007	0.114/0.130
Peri-torsion angles				
Se(1)-C(1)-C(10)-C(5)	174.03(17)	172.0(3)	170.8(10)	173.73(14)
Se(21)-C(21)-C(30)-				173.19(15)
Se(9)-C(9)-C(10)-C(5)	174.03(17)	–171.7(3)	–173.6(10)	–171.98(14)
Se(29)-C(29)-C(30)-				–169.08(16)
Se(1)-C(1)-C(9)-S(2)	0.00	0.18	–2.14	1.42/3.39

Selected bond lengths (Å) and angles (°). [a] a,b and c in Å, [b] van der Waals radii used for calculations: rdW(S) 1.80 Å, [c] Splay angle: ∑ of the three bay region angles – 360. [] denotes data for the second molecule in the asymmetric unit.

Table C6. ^{31}P experimental NMR data for compounds **4.1** – **4.6** and **5.1** – **5.12**.

	4.1	**5.1**	**5.2**[a]	**5.3**	**4.4**	**5.4**	**5.5**[a]	**5.6**	**4.3**
E,R,X group	S, iso	S, iso,O	S, iso, S	S, iso, Se	Se,iso	Se,iso, O	Se,iso,S	Se,iso,Se	S,Ph
δ_{iso}	6 4 3	36	66 64 62	55	–2	14	44 41	26	0.5 –3
Ω	169 184 209	303	141 177 187	159	198	282	207 221	202	197 193
κ	0.9 0.4 0.3	0.8	0.9 0.8 0.8	0.9	0.4	1.0	0.9 0.7	0.8	0.2 0.2
δ_{11}	67 85 96	148	116 128 130	111	84	108	117 124	101	91 86
δ_{22}	54 26 24	114	108 114 114	102	24	108	106 95	78	17 11
δ_{33}	–103 –99 –112	–155	–25 –49 –57	–48	–114	–174	–90 –97	–101	–106 –107
	4.2	**5.7**	**5.8**	**5.9**[a]	**4.5**	**5.10**	**5.11**	**5.12**[a]	**4.6**
E,R,X group	S, tert	S, tert, O	S, tert, S	S,tert, Se	Se,tert	Se,tert,O	Se, tert, S	Se, tert,Se	Se,Ph
δ_{iso}	–	47	72 71	56 54	6	30	43	23 21	–22
Ω	–	301	303 302	283 282	231	320	243	229 242	203
κ	–	0.9	0.9 0.9	0.9 0.9	0.5	0.8	0.9	0.8 0.7	0.3
δ_{11}	–	150	179 175	156 154	103	149	128	105 113	68
δ_{22}	–	143	161 165	137 134	44	113	116	87 78	0.1
δ_{33}	–	–151	–124 –127	–126 –127	–128	–171	–115	–124 –128	–135

All values are quoted in δ (ppm), Ω(ppm). [a] The values are summarised for the most deshielded to more shielded site.

Table C7. ^{77}Se experimental NMR data for compounds **4.1** – **4.3** (except **4.2**) and **5.1** – **5.6.**

	4.1	**5.1**	**5.2**[a]	**5.3**	**4.4**	**5.4**	**5.5**[a]	**5.6**[a]	**4.3**
E,R,X group	S, iso	S, iso,O	S, iso, S	S, iso, Se	Se, iso	Se,iso, O	Se,iso,S	Se,iso,Se	S, Ph
δ_{iso}	–	–	–	–309	280	486 474	441 439 432 412	442 408 –260	–
$\Omega(^{77}Se)$	–	–	–	188	589	866 906	745 703 804 732	696 736 197	–
$\kappa(^{77}Se)$	–	–	–	–0.03	–1.0	–0.6 –0.4	–0.8 –1.0 –0.8 –0.8	–0.9 –1.0 –0.9	–
$\delta_{11}(^{77}Se)$	–	–	–	–214	672	1000 991	913 906 939 880	893 894 –133	–
$\delta_{22}(^{77}Se)$	–	–	–	–311	84	327 346	245 209 223 207	233 171 –317	–
$\delta_{33}(^{77}Se)$	–	–	–	–402	83	133 85	168 203 135 148	197 158 –330	–

All values are quoted in δ (ppm), Ω(ppm). [a] The values are summarised for the most deshielded to more shielded site.

Table C8. ^{77}Se experimental NMR data for compounds **4.5** – **4.6** and **5.7** – **5.12.**

	5.7	**5.8**	**5.9**[a]	**4.5**	**5.10**	**5.11**	**5.12**[a]	**4.6**
E,R,X group	S, tert, O	S, tert, S	S,tert, Se	Se, tert	Se,tert,O	Se, tert, S	Se, tert,Se	Se, Ph
δ_{iso}	–	–	–46 –56	213 179	443 423	364 358	368 359 356 –152 –165	350 231
$\Omega(^{77}Se)$	–	–	850 979	447 470	721 782	592 560	642 628 554 142 124	593 569
$\kappa(^{77}Se)$	–	–	–0.9 –0.9	–0.9 –1.0	–0.4 –0.3	–0.9 –1.0	–0.9 –0.8 –0.9 0.4 0.9	–0.03 –1.0
$\delta_{11}(^{77}Se)$	–	–	515 516	505 492	854 859	748 731	785 761 713 –90 –119	649.6 610.2
$\delta_{22}(^{77}Se)$	–	–	–318 –321	77 23	341 331	188 172	178 182 196 –131 –127	343 41
$\delta_{33}(^{77}Se)$	–	–	–335.3 –361.7	58 23	132.9 77.6	155.7 171.2	143 133 159 –232 –243	57 11

All values are quoted in δ (ppm), Ω(ppm). [a] The values are summarised for the most deshielded to more shielded site.

F

Figure C3. ^{13}C CPMAS NMR spectra of **5.1 – 5.12** recorded at 9.4 T or 14.1 T (**5.1**, **5.3** and **5.8**) and 12.5 kHz MAS.

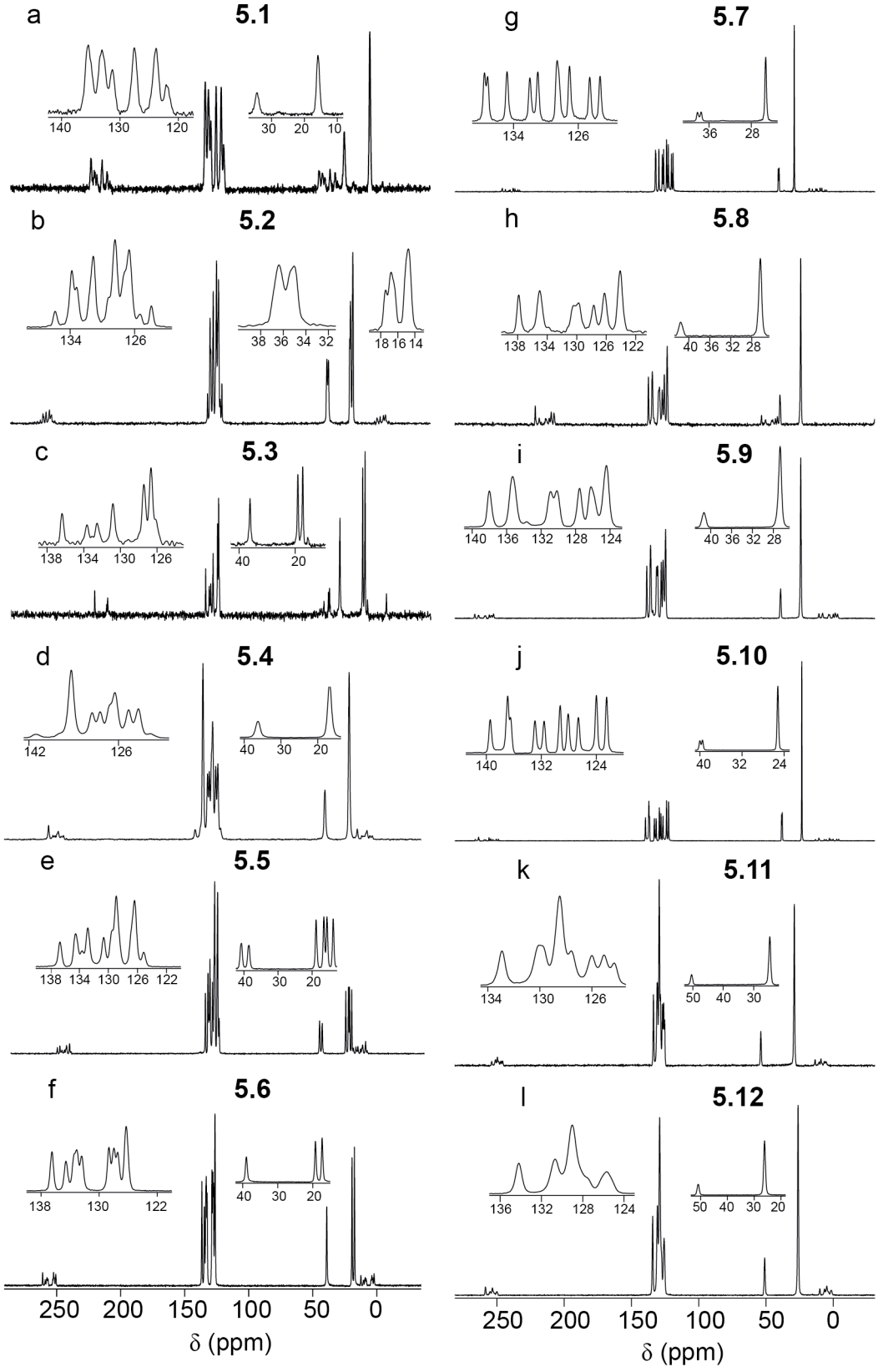

Table C9. Calculated ^{31}P NMR parameters (isotropic chemical shift, δ_{iso}, span Ω, skew κ and chemical shift tensor components, δ_{ii} for compounds **4.1** – **4.6**, and **5.1** – **5.12**.

	4.1	**5.1**	**5.2a**	**5.2b**	**5.2c**	**5.3a**	**5.3b**	**4.4**	**5.4**	**5.5**	**5.6**
E,R,X	S, iso	S, iso,O	S, iso, S	S, iso, S	S, iso, S	S, iso, Se	S, iso, Se	Se, iso	Se,iso, O	Se,iso,S	Se,iso,Se
δ_{iso}	15 12 11 9	50	90 81	92 88	91	108	104 98	–2	27	72 61	83
Ω	274 285 286 273	382	211 183	198	178 188	205	207 191	269	383	151 184	189
κ	0.31 0.29 0.29 0.26	0.75	0.89 0.79	0.82	0.73 0.86	0.87	0.86 0.77	0.18	0.68	0.85 0.87	0.88
δ_{11}	166 168 168 158	36	62 66	64	64 64	55	231 224	141	263	168 180	205
δ_{22}	–13 –15 –16 –14	289	218 206	217	203 209	241	38 56	–17	–60	29 7	27
δ_{33}	–108 –117 –119 –155	–45	19 42	37	49 35	49	24 33	–128	–120	18 -4	16
	4.2	**5.7**	**5.8**	**5.9a**	**5.9b**	**4.3**	**4.5**	**5.10**	**5.11**	**5.12**	**4.6**
E,R,X group	S, tert	S, tert, O	S, tert, S	S,tert, Se	S,Ph	S,Ph	Se, tert	Se,tert,O	Se, tert, S	Se, tert,Se	Se, Ph
δ_{iso}	–	62	89 86	108 111	108 111	4 13	3	40	58	76 71	–20
Ω	–	370	373 375	399 397	394 395	267 267	315	410	263	269 281	295
κ	–	0.86	0.86 0.89	0.90 0.89	0.89 0.92	0.26 0.25	0.38	0.78	0.78	0.75 0.80	0.12
δ_{11}	–	300	72 71	368 369	363 369	149 158	181	298	224	244 249	133
δ_{22}	–	–44	329 329	–11 –5	–8 –9	–19 –10	–37	–67	–11	9 –3	–32
δ_{33}	–	–70	–18 –25	–31 –28	-31 -26	-118 -109	–134	–112	–39	–25 –32	–162

All values are quoted in δ (ppm), Ω(ppm).

Table C10. Calculated ^{77}Se NMR parameters (isotropic chemical shift, δ_{iso}, span Ω, skew κ and chemical shift tensor components, δ_{ii} for compounds **4.4**, and **5.3 – 5.6**.

	5.3a	**5.3b**	**4.4**	**5.4**	**5.5**	**5.6**
E,R,X	S, iso, Se	S, iso, Se	Se, iso	Se,iso, O	Se,iso,S	Se,iso,Se
δ_{iso}	–275	–319 –299	300 275	524 519	485 479 456 419	461 416 –187
Ω	203	185 203	581 626	1030 1071	770 816 733 876	730 915 289
κ	0.35	–0.10 –0.20	–0.82 –0.65	–0.43 –0.38	–0.77 –0.80 –0.98 –0.53	–0.86 –0.49 0.04
δ_{11}	–185	–204 –211	671 656	1112 1122	969 997 943 935	–45 948 931
δ_{22}	–251	–306 –333	141 140	376 384	286 261 217 265	–183 267 252
δ_{33}	–289	–389 –414	90 30	82 51	199 181 209 58	–334 33 201

All values are quoted in δ (ppm), Ω(ppm).

Table C11. Calculated ^{77}Se NMR parameters (isotropic chemical shift, δ_{iso}, span Ω, skew κ and chemical shift tensor components, δ_{ii} for compounds **4.5** – **4.6**, and **5.9** – **5.12**.

	5.9a	**5.9b**	**4.5**	**5.10**	**5.11**	**5.12**	**4.6**
E,R,X group	S,tert, Se	S,tert,Se	Se, tert	Se,tert,O	Se, tert, S	Se, tert,Se	Se, Ph
δ_{iso}	63 44	66 47	167 159	518 518	372 341	379 362 344 330 –106 –102	364 233
Ω	1159 1207	1164 1193	482 510	944 949	630 636	681 706 718 655 240 244	664 607
κ	–0.71 –0.70	–0.70 –0.72	–0.80 –0.63	–0.41 –0.41	–0.74 –0.48	–0.76 –0.62 –0.48 –0.40 0.26 0.83	–0.02 –0.46
δ_{11}	779 788	784 786	472 468	1055 1057	765 709	806 788 760 701 8 –18	698 583
δ_{22}	–210 –238	–208 –238	39 51	390 389	216 239	206 215 229 242 –81 –39	359 139
δ_{33}	–380 –418	–380 –407	9 42	111 108	134 73	125 82 42 46 –232 –262	34 –24

All values are quoted in δ (ppm), Ω(ppm).